Novel diesel particulate filters containing fine ceramic fibres

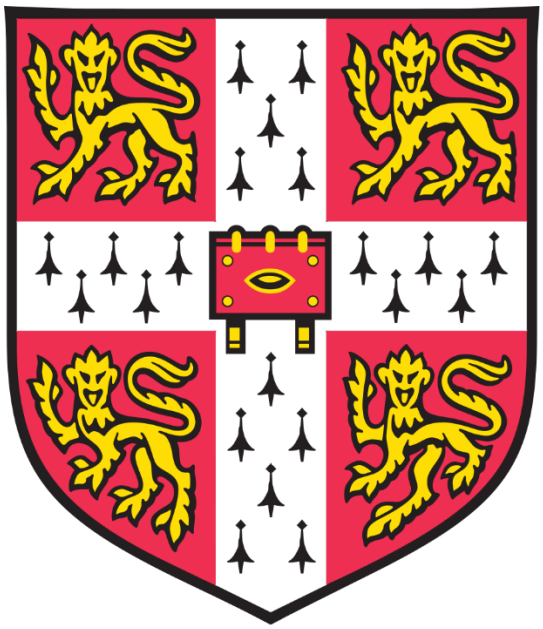

Alastair James Houston

Department of Materials Science and Metallurgy
University of Cambridge

This dissertation is submitted for the degree of
Doctor of Philosophy

Robinson College March 2019

I wish to dedicate this thesis to my parents,
John and Amanda, for all their support.

Declaration

I hereby declare that except where specific reference is made to the work of others, the contents of this dissertation are original and have not been submitted in whole or in part for consideration for any other degree or qualification in this, or any other university. This dissertation is my own work and contains nothing which is the outcome of work done in collaboration with others, except as specified in the text and acknowledgements. This dissertation contains fewer than 60 000 words including appendices, bibliography, footnotes, tables and equations and has fewer than 150 figures.

Alastair James Houston

March 2019

Acknowledgements

I gratefully acknowledge the financial support provided by the Engineering and Physical Science Research Council (EPSRC). Thanks are also due to Prof. Mark Blamire and Prof. Paul Midgley for provision of office, laboratory and workshop facilities at the Department of Materials Science and Metallurgy, University of Cambridge.

I would particularly like to thank my supervisor, Prof. Bill Clyne, for his guidance, support and advice throughout my research. Thanks also go to Dr. James Dean for encouragement and without whom I would have spent a lot more time trying to figure out how to use various modelling software.

I would also like to thank everyone who has provided technical support including Kevin Roberts, Keith Page and Sue Gymer for help with the VPS, Jenny Shepherd for tomography, and Bob Stearn and Giovanni Orlando for general equipment help around the Gordon lab.

Special thanks go out to my Gordon lab fam, who have made this PhD an unforgettable experience. To Gordon lab members past and present: Megan, Julia, Rob T, Max, Matt, Sam, Jimmy, Eleanor, Tom, Eleonore, Noel, Nashid, Yi, Fernando, Catalina, Rob J, Joe and Amy (sitting in our office definitely makes you part of our lab!) – every one of you has made my time in Cambridge so much more fun, with regular pub trips, formals, BBQs at Bill's and outings to spoons. In particular, thank you to Megan, with whom I shared all of my first-year undergraduate supervisions and now share a desk. Thanks for being there through all the ups and downs of the last seven years of Cambridge!

I am also grateful for a long list of Part III students and summer students that I have had the pleasure to supervise over the past three years. Thanks to Eleanor, August, Hannah, Katie and Joe, all of whom might recognise small parts of our work included in this thesis.

Thanks to my friends outside of materials science who have kept me sane over the years. In particular, to Finlay, for following me all over Europe for various juggling conventions and to Douglas, whose knowledge of statistics proved very useful and contributed in part to the analysis in Chapter 6.

Finally, thanks to my family, who have supported me all the way through my Cambridge journey.

Abstract

Ongoing concerns about the adverse health effects of carbon particulates in diesel engine exhausts continue to drive the quest for improved performance from Diesel Particulate Filter (DPF) systems. Two of the main areas in which improvements are being sought are in enhanced filtration efficiency of very fine particles (<50 nm), particularly immediately after regeneration (the periodic removal of accumulated particulate via combustion), and in improved thermal shock resistance. To contribute to these aims, this work focuses on creating novel composite materials through the introduction of fine ceramic fibres.

Filtration efficiency is considered by experimental measurement of porosity and permeability. Porosity of the material is shown to increase with fibre content, providing a larger volume for soot collection. The permeability is shown to slightly decrease due to the fine nature of the fibres. However, these small fibre diameters, in comparison to the larger particles, offer an increased surface area and scope for an improved soot trapping capability.

A simulation, modelling the particles and fibres as simplified spheres and cylinders, allows an understanding into the effect of porosity, fibre proportion, and the sizes of the particles and fibres on the permeability. An empirical equation linking these factors is suggested. A model of this type, on a hybrid particle-fibre-void composite material, has not been studied in the literature, and so offers a novel insight into the complex behaviour of such materials, practicable not only to DPFs, but to any other applications of such composites systems. The model is shown to have good agreement with the experimentally derived data.

Finally, the effect of fibres on the thermal shock resistance is investigated. The fibres show improved fracture toughness, and variability in the stiffness which suggests, via a derived figure of merit, that thermal shock resistance improves with increased fibre proportion. Thermal shock is induced experimentally using a vacuum plasma sprayer, and the experimental results, measured as a decrease in stiffness as a consequence of micro-cracking, are comparable to those of the merit index.

The study concludes that there appears to be a significant benefit to adding fine ceramic fibres into current DPF materials. The increased porosity, whilst also significantly increasing the specific surface area, suggests the filter could offer a higher soot loading capacity, thus lengthening the time between regenerations. The inclusion of small diameter fibres predicts that the period of initially low filtration efficiency of a clean filter could be shortened, with little impact on the permeability. Fibres also offer significant advantages for the thermal shock resistance. Fibres are well-known for their toughening ability and this remains true for these hybrid particle and fibre composites.

Table of Contents

List of Figures

List of Tables

Nomenclature

Roman Symbols

a_0	Crack length (m)
A	Surface area of filter (m^2)
A_c	Surface area of a cylinder (m^2)
A_{crack}	Crack surface area (m^2)
A_f	Surface area of fluxmeter in thermal conductivity rig (m^2)
A_s	Surface area of a sphere (m^2)
A_{test}	Surface area of sample to be tested in thermal conductivity rig (m^2)
Bi	Biot number (-)
c	Volumetric heat capacity (J m^{-3} K^{-1})
c_{D_c}	Constant offset of the cylinder diameter term in S correction (-)
c_{D_s}	Constant offset of the sphere diameter term in S correction (-)
c_L	Constant offset of the cylinder length term in S correction (-)
c_λ	y-intercept of linear dependence of lambda on porosity (-)
d	Thickness of filter (m)
D	Diameter of fibre (m)
D_c	Diameter of a cylinder (m)
D_{eq}	Diameter of equivalent cylinders in Carman-Kozeny derivation (m)
D_p	Diameter of particles (m)
D_s	Diameter of a sphere (m)
E	Young's modulus (GPa)
E_f	Fibre stiffness (GPa)
E_n	Stiffness of fibre network (GPa)

f	Fibre volume fraction (volume ratio of fibres to particles) (-)
f_r	Fundamental resonance frequency (Hz)
F	Load applied during 4-point bend test (N)
$\underline{F}$	Internal and external force contribution in Navier-Stokes equation (N)
g	Acceleration due to gravity (≈ 9.81…) (m s^{-2})
G_c	Fracture energy (J)
h	Height of 4-point bend test sample (m)
h_i	Interfacial heat transfer coefficient (W m^{-2} K^{-1})
k	Thermal conductivity (W m^{-1} K^{-1})
k_f	Thermal conductivity of fluxmeter (W m^{-1} K^{-1})
k_{test}	Thermal conductivity of sample to be tested (W m^{-1} K^{-1})
K	Bayes factor (-)
l	Length between furthest points on 4-point bend test (Figure 3.5) (m)
L	Length of a cylinder (m)
L_p	Length of pendulum arm (m)
L_s	Length of sample (m)
m	Mass of filter (kg)
m_0	Theoretical mass of filter instantaneously upon submersion (kg)
m_{dry}	Mass of dry filter (kg)
m_{f,D_c}	Gradient of linear dependence of cylinder diameter term on fibre volume fraction in S correction (-)
m_{f,D_s}	Gradient of linear dependence of sphere diameter term on fibre volume fraction in S correction (-)
$m_{f,L}$	Gradient of linear dependence of cylinder length term on fibre volume fraction in S correction (-)
m_{sub}	Mass of filter having been submerged for around 72 hours (kg)
m_{ε,D_c}	Gradient of linear dependence of cylinder diameter term on porosity in S correction (-)
m_{ε,D_s}	Gradient of linear dependence of sphere diameter term on porosity in S correction (-)

$m_{\varepsilon,L}$	Gradient of linear dependence of cylinder length term on porosity in S correction (-)
m_λ	Gradient of linear dependence of lambda on porosity (-)
M	Mass of pendulum arm (kg)
M_{TS}	Merit index of thermal shock resistance (J $m^{-3/2}$ $s^{-1/2}$)
n	Number of cylinders in Carman-Kozeny derivation (-)
n_c	Number of cylinders (-)
n_s	Number of spheres (-)
P	Power (W)
ΔP	Pressure difference over filter (Pa)
Q	Gas flux (m^3 m^{-2} s^{-1})
Q_h	Heat flux (W m^2)
Re	Reynolds number (-)
s	Distance between opposing contact points in 4-point bend test (m)
S	Specific surface area (m^2 m^{-3})
Stk	Stokes number (-)
t	Time (s)
T	Temperature (K)
T_1	Correction factor in RFDA (-)
ΔT_i	Temperature drop at interface (K)
u	Speed of fluid (m s^{-1})
V	Volume of water displaced in permeability experiment (m^3)
V_c	Volume of a cylinder (m^3)
V_f	Fibre volume fraction (in equation by Markaki and Clyne) (-)
V_{filter}	Volume of filter (m^3)
V_s	Volume of a sphere (m^3)
V_T	Total volume of cube in sphere and cylinder model (m^3)
w	Width of 4-point bend test sample (m)
Δx	Distance over which pressure gradient is formed in Darcy's Law (m)
z	Thickness (m)
Z	Evidence (-)

Greek Symbols

δ	Deflection of centre of sample in 4-point bend test (m)
ε	Porosity (fraction) (-)
ε_r	Strain released (-)
η	Dynamic viscosity (Pa s)
θ_1	Angle of release of pendulum (°)
θ_2	Final angle of pendulum, having fractured sample (°)
κ	Permeability (m^2)
κ_{meas}	Measured value of permeability from COMSOL (m^2)
κ_{pred}	Predicted value of permeability from model (m^2)
λ	Tortuosity constant in Carman-Kozeny equation (-)
λ_{laser}	Wavelength of laser light (m)
ν	Poisson's ratio (-)
$\bar{v}$	Average velocity in a channel ($m\ s^{-1}$)
v_s	Superficial velocity ($m\ s^{-1}$)
π	≈ 3.141… (-)
ρ	Density of a fluid ($kg\ m^{-3}$)
ρ_{filter}	Density of porous filter ($kg\ m^{-3}$)
ρ_p	Density of particle ($kg\ m^{-3}$)
ρ_{water}	Density of water (=1000 $kg\ m^{-3}$ at room temperature) ($kg\ m^{-3}$)
σ_r	Stress released (Pa)
σ_S	Standard deviation of measured specific surface area about a plane of predicted specific surface area (m^{-1})
σ_κ	Standard deviation of measured permeability about a plane of predicted permeability (m^2)
Φ_s	Sphericity of particle (-)

Other Symbols

$\frac{dT}{dx}$	Thermal gradient (K m^{-1})
$\left(\frac{dT}{dx}\right)_f$	Thermal gradient of fluxmeters (K m^{-1})
$\left(\frac{dT}{dx}\right)_{test}$	Thermal gradient of sample being tested (K m^{-1})

Acronyms / Abbreviations

CCRT	Catalysed Continuously Regenerating Trap
CDPF	Catalysed Diesel Particulate Filter
CFD	Computational Fluid Dynamics
CI	Compression Ignition
CK	Carman-Kozeny
CMC	Ceramic Matrix Composite
CRT	Continuously Regenerating Trap
CT	Computerised Tomography
CTE	Coefficient of Thermal Expansion
DOC	Diesel Oxidation Catalyst
DPF	Diesel Particulate Filter
EBP	Exhaust Back Pressure
EDX	Energy Dispersive X-ray Spectroscopy
EU	European Union
FBC	Fuel Borne Catalyst
GPF	Gasoline Particulate Filter
LB	Lattice Boltzmann
MCMC	Markov chain Monte Carlo
PM	Particulate Matter
$PM_{2.5}$	Classification for PM <2.5 µm
PM_{10}	Classification for PM <10 µm
PVA	Polyvinyl Alcohol
RFDA	Resonance Frequency Damping Analysis
SEM	Scanning Electron Microscope
SOF	Soluble Organic Fraction

TEM	Transmission Electron Microscope
T_g	Glass transition temperature
TSR	Thermal Shock Resistance
US EPA	United States Environmental Protection Agency
VPS	Vacuum Plasma Sprayer
WHO	World Health Organization
XRD	X-ray Diffraction

1. Background

1.1. Introduction

Diesel cars have been gaining popularity in Europe over recent years, offering many benefits over petrol engines, such as a high efficiency correlating with the reduction of CO_2, low operating cost, high durability and reliability. Europe's rise in diesel cars has been encouraged by the efforts of national governments to reduce carbon dioxide emissions from the transportation sector. Countries that signed the 1997 Kyoto Protocol agreed to reduce their greenhouse gas emissions in the manner of their choosing and, in order to meet these targets relatively cheaply, EU countries motivated the purchase of diesel cars with tax breaks on diesel fuel [1]. In response to these incentives, in the 12 years between 2001 and 2013 the market share of diesel cars in the EU increased from 36 % to 53 % [2].

There are two main internal combustion engine types: Spark ignition engines (petrol) and compression ignition engines (diesel). In a spark ignition engine, the air and fuel are mixed before being injected into the combustion chamber and then ignited with a spark, allowing time for good mixing between the air and fuel, and a relatively clean burn. On the other hand, in a compression ignition (CI) engine it is much more difficult to control the ignition, due to the heterogeneity of the combustion process because air and fuel must mix in the combustion chamber. CI engines offer a relatively high combustion efficiency (>98 %). However, the small fraction of unburnt fuel and lubricating oil yields a great number of incomplete combustion products [3]. This leads to the big problem with diesel engines: whilst the levels of CO_2 are considerably lower than that of their petrol counterparts (due to a leaner burn), there is instead a problem of significantly increased

emission of NO_x (NO and NO_2) gases and particulate matter (PM), with emissions from diesel engines being two orders of magnitude higher than petrol engines [4].

These problems with diesel engines have become widely publicised due to recent news stories. In March of 2015, Europe witnessed a dense smog cloud that hung over major cities. The cloud was comprised of diesel exhaust pollutants, and, for a short period of time, the Parisian air pollution levels were higher than any city in the world, including those infamous for high smog levels, such as Delhi and Beijing. More bad press for diesel engines followed in September 2015, where Volkswagen officials announced that an estimated 11 million cars, sold mostly in Europe, contained an illegal "defeat device", such that certain models complied with the emissions standards for NO_x only under laboratory testing conditions. In real driving situations, taking into account individual driving habits and road conditions, the NO_x emissions from the affected 2.0 L engine cars could increase up to 40 times the U.S standard of 70 mg/mile, the United States Environmental Protection Agency (US EPA) found [5]. The defeat device software was able to detect when the vehicle was being subjected to a standard drive cycle test, and changed the performance of the car such that it appeared to meet the emission standards. Following this scandal, there is now a demand for roadside emission testing, which is currently being phased in by the EU.

To meet these new requirements, the NO_x and PM levels must be controlled and reduced. The work described in this thesis is focused on PM.

1.2. Diesel particulate matter

1.2.1. Composition and structure

The complete combustion of hydrocarbon fuel in an internal combustion engine should yield CO_2 and H_2O as the only products. However, in the very short time allowed for chemical oxidation processes in combustion chambers, the lack of homogeneity in the fuel-air mixture, and the heterogeneity and rapid variations in the temperature are such that this state of ideal thermodynamic equilibrium is not reached [6]. This leads to the formation of carbonaceous diesel particulate matter (PM).

Diesel PM is estimated to contain 20,000 different chemical compounds [7], of which 700 have been positively identified [8]. The particulates consist mostly of soot with a formula given approximately by C_8H [9], with minor components of volatile organic compounds from unburnt fuel and evaporated lubrication oil, generally described as the soluble organic fraction (SOF). SOF emissions are highest during a fuel-rich burn at light engine loads, when exhaust temperatures are low [6]. Metal compounds from fuel additives and wear of the engine are also present and lead to a small amount of inorganic ash. Diesel PM is the only pollutant regulated by the US EPA that is not chemically defined [10]. The exact composition of PM varies considerably and will depend on many factors, for example the processing of the emissions after combustion, the engine operating conditions (speed, load, injection timing), the type of fuel and lubricants used. A typical particle composition for a heavy-duty diesel engine tested in a heavy-duty transient cycle is shown in Figure 1.1.

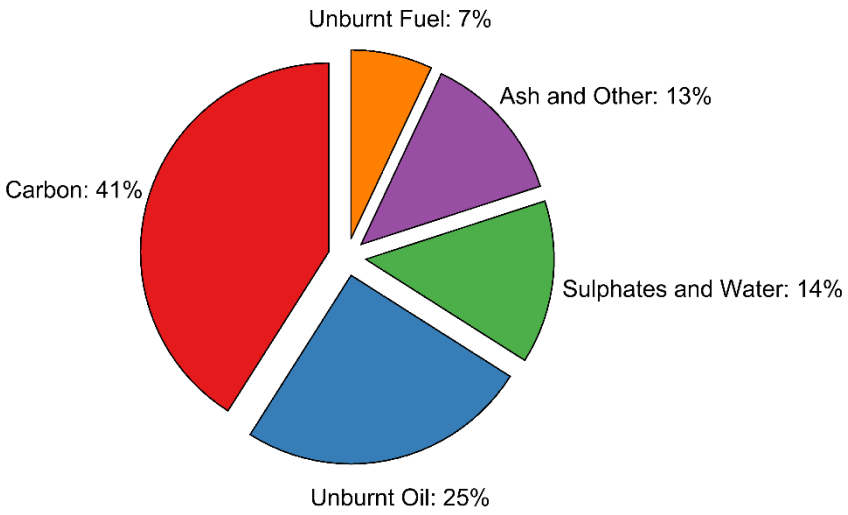

Figure 1.1: Typical composition of diesel particulate from a heavy-duty diesel engine, tested on an engine test bench in a transient cycle. Data taken from Kittelson [4].

Since the chemical composition of PM is impossible to regulate, PM is instead regulated by its physical size. The simplest and most commonly-used metric in air pollution studies is the mass of particles in a given volume of air. Particles are classified into two categories, labelled PM_{10} and $PM_{2.5}$, which represent particles of size less than

10 µm and 2.5 µm respectively. Almost all particulates are smaller than 10 µm, and the size distribution is typically trimodal, as seen in Figure 1.2.

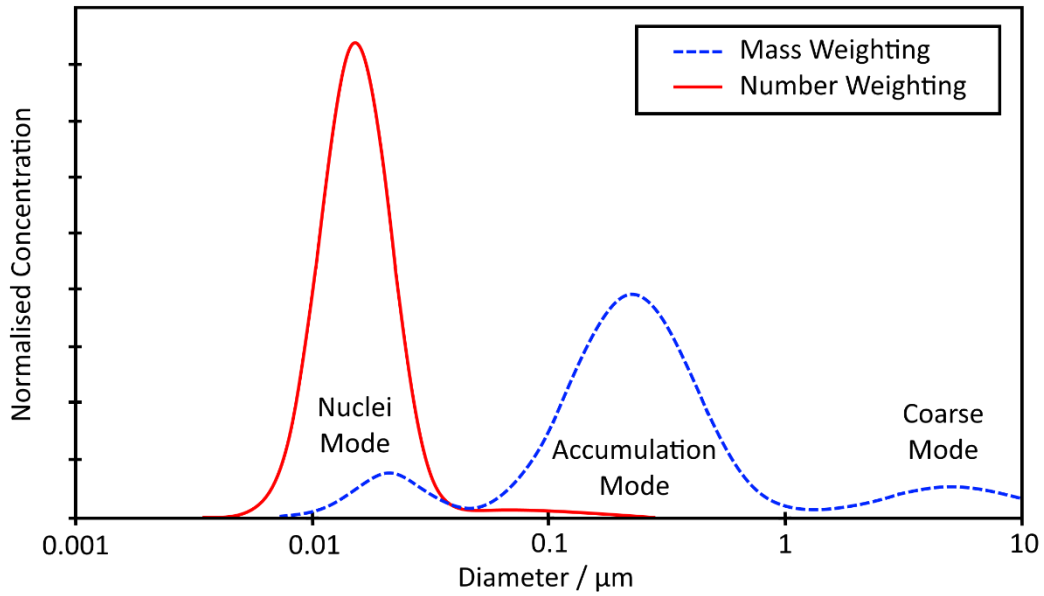

Figure 1.2: Particle Size Distribution of typical engine exhaust. Both mass and number weightings are included. Graph reproduced from Kittelson [4].

The smallest particles are nanoscale, with diameters in the range of 5–20 nm. These particles are said to be in the nuclei mode, and are simple volatile organic and sulphur compounds, with some carbon particles and metallic ash. The nuclei mode contains 1–20 % of the particle mass, but more than 90 % of the particle number. The nuclei mode particles can agglomerate into chains or clusters and form a complex fractal-like morphology with other adsorbed or condensed species. These new agglomerate particles form the accumulation mode (0.1–1 µm in diameter); an example of such a particle is illustrated in Figure 1.3. The accumulation mode dominates the particulate mass emitted by an engine, but accounts for less than 10 % of the total number of particles [4].

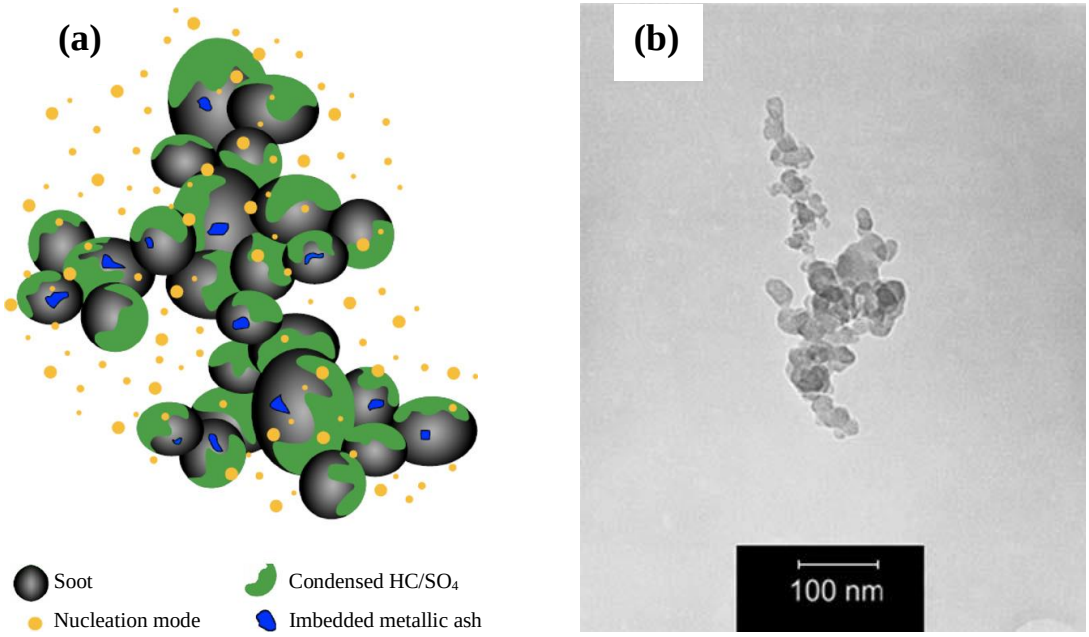

Figure 1.3: *(a) An illustration of an accumulation mode particle. The structure is formed of agglomerated carbon particles with condensed species of metallic ash and sulphates. Figure reproduced from Maricq [10]. (b) TEM image of diesel PM taken from a modern diesel engine, from Ristovski et al. [11].*

The third peak on the particle size distribution is the coarse mode. This accounts for 5–20 % of the particle mass, and consists of accumulation mode particles which have been deposited on the surfaces of the exhaust system, and then later re-entrained into the gas flow [4].

1.2.2. Health effects

PM occurs naturally, for example as volcanic ash, terrestrial dust and bio aerosols, such as fungal spores and pollen. However, in the urban environment, vehicle emissions are the predominant source of fine PM [12]. As of 2014, 54 % of the world population was classified as living in an urban environment [13], and so these diesel pollutants are emitted at ground level close to where billions of people live and work [6]. Even those living in rural environments will be affected by diesel pollution, since $PM_{2.5}$ may remain in the atmosphere for weeks and so can be transported over long distances.

Epidemiological studies have shown indisputable links between diesel PM and respiratory morbidity and mortality, despite its low percentage in relation to the amount of overall particulate matter [11]. Chemically, PM can lead to effects on health by providing a mechanism for the introduction of toxic compounds into the body during respiration, via adsorption and condensation of such compounds onto the surface of the PM. As the number of particles deposited in the lungs increases, their coagulation and growth can lead to adverse reactions. The mechanism by which diesel PM causes physical irritation in the lungs is via the release of inflammatory cytokines, and is covered in detail in research by Ristovski *et al.* [11]. There is a 0.6–2.2 % increase in respiratory mortality risk for a 10 µg m^{-3} increase in ambient PM [14].

More than 90 % of diesel exhaust derived PM is smaller than 1 µm in diameter [4]. Size determines where diesel PM deposits in the respiratory tract; the smaller the particles, the deeper they are able to penetrate into the lungs [15]. As such, smaller particles are proposed to be more harmful to human health [15-17]. As mentioned in Section 1.2.1, particulate matter measurements in an urban location yielded a portion of 1 % of the particle mass for size class 0.01–0.1 µm, but 73 % in terms of particle count. Since 2011, emissions have therefore been legislated not only in mass, but also in number.

In addition to inflammation of the lungs, studies have shown that diesel PM can cause DNA damage [18] and induce carcinogenic mutations [19]. Diesel PM has been listed as a Group 1 (confirmed) human carcinogen by the International Agency for Research on Cancer, a part of the World Health Organization (WHO) [20-22]. A report by the UK government [23] quantified the effect of PM on health as being responsible for an average loss of life expectancy of 3–4 months in Scotland and Northern Ireland and 6–7 months in England and Wales; this is equivalent to 340 000 life years lost.

1.2.3. Environmental effects

The residence time of particles in the atmosphere is longest for particles in the 0.1–10 µm diameter range and is typically about 10 days, being removed from the lower atmosphere by rain rather than by sedimentation. Larger particles are removed by settling (dry deposition), and smaller particles are removed by diffusion and coagulation. Hence

the material is not lost from the atmosphere, but leads to increased number of particles in the accumulation mode [24].

The effect of diesel PM on global warming is relatively unknown, with the exact composition determining its contribution. PM high in elemental carbon absorbs sunlight and has a high global warming potential [4, 6, 25], with atmospheric PM being 2000 times more influential on the global climate (based on mass) than CO_2 [26]. On the other hand, if the PM is rich in sulphates (which is unlikely due to widespread use of ultra-low sulphur diesel), this has the opposite effect of reflecting sunlight [27].

Soot can have a large influence on the environment, even once it has been deposited out of the atmosphere. Soot settling on glaciers or ice in arctic regions absorbs solar heat directly, contributing to the retreat of glaciers, and leading to rising sea levels [6]. The settling soot can also have a significant effect on vegetation, with deposited soot particles on leaves hindering photosynthesis. Diesel PM in the atmosphere can lead to acid rain, which adversely affects the health of ecological systems such as agricultural crops, lakes and forests [6].

Soot deposition can also have a deleterious effect on the appearance of buildings and structures, some of which will be aesthetically appealing or culturally significant. Due to their carbon content, diesel particles are black and stick to surfaces effectively, re-soiling cleaned London buildings over a period of eight years [28]. Soot particles can also cause significant damage to such landmarks, since they contain acidic substances and these enhance corrosion of stone and metal building materials. Damage to the Acropolis in Athens has received much attention, with damage seeming to correlate with the increasing reliance on cars. The PM carries with it sulphates and nitrates that can be extremely harmful to stone, with nitrogen oxides converting sulphites on the building to sulphuric acid, and making the surface nitrogen-rich (enhancing biodegradation) [28].

As observed in March 2015 in major cities over Europe, diesel exhaust particles can also cause a smog. The smog reduces visibility, and can be smelled, making it unpleasant to live in such places. The smog caused such alarm in Paris that, between the hours of

11:00 a.m. and 6:00 p.m. on 27 September 2015, officials imposed the first ever car-free day in 30 % of the city [1].

1.2.4. Emission limits

In a diesel engine exhaust, in addition to diesel PM, nitrogen oxides (NO_x) form substances that are harmful to the environment and health. Internal engine alterations can reduce particulate emission, but at the cost of increased NO_x emissions and vice versa; this is known as the NO_x–PM trade-off. Consequently, the laws limit both exhaust components simultaneously. Emissions of NO_x and PM in Europe are regulated by a set of standards that have been regularly updated. Since the introduction of EURO 1 emission limits in 1992, the particle limits have been lowered from 0.14 g/km to 0.005 g/km, and the NO_x limits from 0.97 g/km to 0.08 g/km [29]. Figure 1.4 shows how the limits have decreased for each iteration of the regulations.

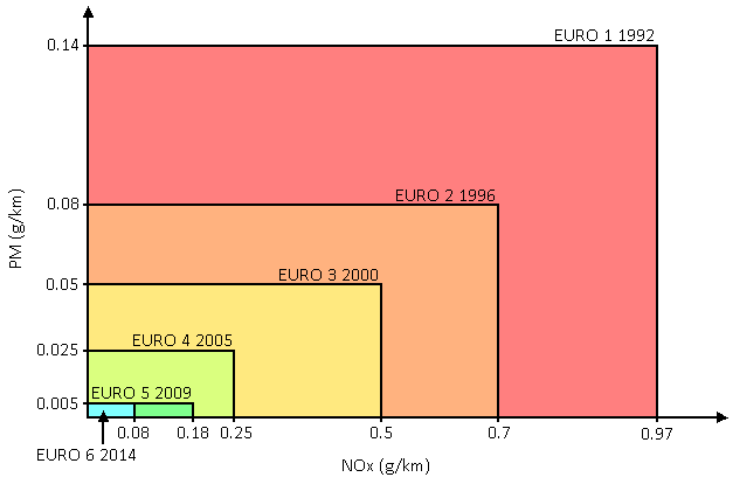

Figure 1.4: The incremental change in the PM and NO_x emission standards between EURO 1 (1992) and EURO 6 (2014). Data taken from EU regulations, summarised by the Automobile Association [30].

Because the smaller particles are deemed particularly hazardous to health, a particle number-based limit of 6 x10^{11} particles/km was introduced with the EURO 5b emission standards [29].

The PM emission limits from EURO 5 and later are below what can be achieved by internal engine alterations alone. A particulate filter and DeNO$_x$ aftertreatment, whilst not prescribed by law, are necessary to meet the new strict emission requirements.

The current emission standard is the EURO 6 standard, which came into effect in January 2015 for the approval and sale of new vehicles. PM limits have always been focussed on diesel engines, due to the fact they produce 10–100 times more particulate matter than petrol engines. However, improvements in engine performance and efficient filtration techniques mean that the PM emission limits for diesel engines are comparable to those from a petrol engine [31]. Limits for petrol engines in the EURO 6 standard mean that gasoline particulate filters (GPFs) are now required on some spark-ignition engines [29]. A recent report from the UK government [32] highlights that between 1970 and 2016, the emissions of $PM_{2.5}$ fell by 78 %. Looking towards the future, they state their goals of reducing $PM_{2.5}$ emissions against the 2005 baseline by 30 % by 2020 and 46 % by 2030.

To ensure a new car passes the emission limits, it is tested in a controlled environment in a laboratory, such that all vehicles are exposed to the same drive cycle, and the results can therefore be easily compared. This testing procedure is the source of the recent scandal involving Volkswagen, who used "defeat device" software, such that a car would recognise the prescribed drive cycle conditions and change the engine performance such that the car met the emission standards. In real driving conditions on the road, emissions could in fact be up to 40 times higher than the standards [5]. It has long been acknowledged that laboratory emissions and real-world emissions differ, but they have been assumed to be proportional to one another. Hence, a decrease observed in laboratory tests would result in a comparable reduction in the real world. However, whilst test-cycle NO_x emissions have decreased by 80 % since 1992, the real-driving NO_x emissions have not significantly decreased, with on-road EURO 5 diesel vehicles exceeding emission limits by an average of 320 % [33]. In response to these revelations, the EU has introduced roadside testing of vehicle emissions. Member states have agreed that since September 2017 these new real driving emissions tests will determine whether a new car model is allowed to be put on the market. Since there will be technical limitations in reducing the emissions significantly, a "conformity factor" has been introduced, by which new cars

produced after September 2017 are allowed to produce road-side emissions 110 % over the limit; this will be reduced to 50 % by January 2020 [34].

1.3. Exhaust after-treatment

1.3.1. Introduction

Since the introduction of the EURO 5 emissions limits for passenger cars, it has not been possible to obtain emissions below these levels via engine design alone. Instead, the emissions must be lowered using exhaust after-treatment, in the form of active removal of diesel pollutant from the exhaust gases after combustion. The first contribution to the reduction of particulate mass emission was the Diesel Oxidation Catalyst (DOC), and such devices have been mandatory on all new diesel cars sold in Europe since 1998 [6].

A DOC is a non-filter based open monolith system resembling a catalytic converter, but optimised for lean conditions. It contains platinum and palladium, which are impregnated into a highly porous washcoat about 20–40 µm thick that is applied to the passageway walls [6]. As the exhaust gases flow past, this effectively promotes oxidation of unburnt hydrocarbons, carbon monoxide (CO) and the soluble organic fraction of diesel PM. The DOC also oxidises nitric oxide (NO) to the more toxic nitrogen dioxide (NO_2), which is in itself a disadvantage. However, high NO_2 levels can be used to continuously catalyse the oxidation of the carbonaceous fraction of PM on a Diesel Particulate Filter (DPF) [6, 17]. Further problems involving unwanted oxidation arise when there is a high sulphur content in the exhaust gases. This is uncommon nowadays, since the introduction of ultra-low sulphur diesel, but there is a risk that the sulphur will oxidise over the DOC, forming sulphates, and actually increase the total PM emissions [6].

In addition to a DOC, another system is needed to trap the solid carbonaceous component of the diesel PM. This has been achieved with a Diesel Particulate Filter (DPF), which first entered series production in 2000 with the launch of the Peugeot 607 HDI [35]. DPFs are considered to be the only diesel after treatment technology that can meet the more strict PM requirements, being not only able to reduce the emissions of

coarse particles (1–10 µm) but also particles in the accumulation mode (0.1–1 µm) and nanoparticles in the nuclei mode (<50 nm) [17].

The basic design of a DPF is an extruded cylindrical porous ceramic honeycomb structure, with thousands of small parallel channels in the longitudinal direction of the exhaust system. Adjacent channels are alternately plugged at each end, forcing the exhaust gases to flow through the porous substrate walls, which act as a mechanical filter [6, 17]. The overall size of the filter will depend on the exhaust volume of the engine; a standard for passenger cars is 144 mm diameter and 152 mm in length, approximately 2.5 L volume and having a filter wall surface area of about 1.9 m^2 (assuming a typical 200 cells per square inch, cpsi, the standard unit of cell density for honeycomb structures). The weight of such a filter is around 1.5 kg, depending on the material chosen [35]. Filtration occurs as incoming gas is forced to pass through the wall between the inlet and outlet channels in order to escape from the exhaust system. The wall material must be highly permeable in order to maintain a low back-pressure, but also have a high filtration efficiency, such that the gas is able to easily pass through the structure, but the soot particles become trapped. The filter material must capture PM by interception, impaction and diffusion and hold them until they can be removed by active or passive regeneration [17]. The honeycomb structure and an indication of how the gas flows through the filter are shown in Figure 1.5.

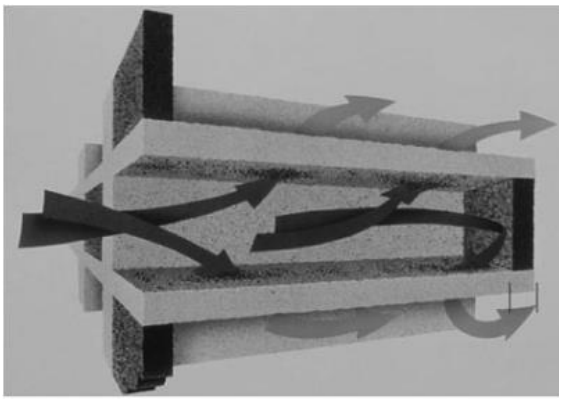

Figure 1.5: The honeycomb structure of a DPF. Exhaust fumes entering through the inlet channel must first pass through the wall of the DPF material before they are emitted to the atmosphere. The length of each channel is typically 152 mm, with a width of approximately 1 mm. Image reproduced from Adler [35].

Since the DPF material will be exposed to exhaust gases and internal heating during regeneration, they must be able to maintain structural stability at high temperatures, as well as being able to withstand a chemically corrosive environment. It is also important for the materials to provide a high specific surface area for filtration and to possibly act as a scaffold for catalysts.

1.3.2. Pore-scale filtration

DPFs are designed to have optimum pore architecture, enabling exhaust gases to pass through without much hindrance, and to be sufficiently impervious to PM. Although nano-scale filters are available for liquid filtration [36], it is not useful to use them for gases in a DPF scenario because of the high pressure drop that this would create. Instead, filter materials with large pore sizes can be used, such that filtration occurs by deep-bed filtration or by forming a soot cake [35], as opposed to sieving, see Figure 1.6.

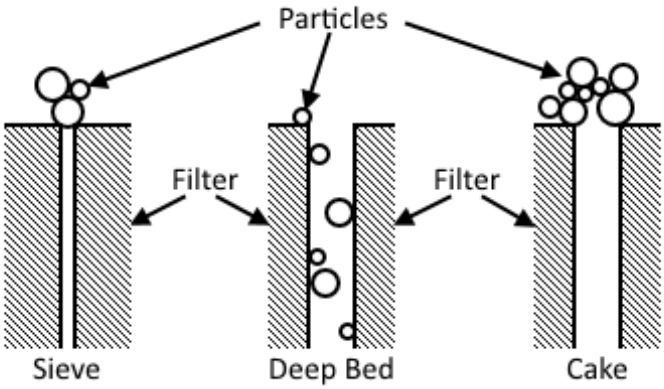

Figure 1.6: Modes of filtration. Although sieving is most effective this leads to an unacceptably large back-pressure. Hence DPFs exploit deep bed filtration and cake formation, such that the back-pressure is minimised. Modified from Olson and Martins [37].

For a soot cake layer to develop, the PM must strike and adhere onto the filter surface. Whether a particle will impact on the filter can be determined by the magnitude of the (dimensionless) Stokes number (Stk):

$$Stk \approx \frac{\rho_p {D_p}^2 u}{18\eta D} \qquad (1.1)$$

where ρ_p is the density of the particle, D_p is the diameter of the particle, u is the speed of the fluid, η is the viscosity of the fluid and D is the diameter of the obstacle.

The Stokes number is the ratio of the characteristic time needed for the particle to change its velocity to that needed for it to pass an obstacle. If Stk >>1, then particles will strike the obstacle, while Stk <<1 means that most particles are expected to follow the fluid stream around the obstacle. This is shown schematically in Figure 1.7a.

By assuming values for an accumulation mode particulate (density of ~2000 kg m^{-3}, diameter of ~100 nm) flowing in air (viscosity of ~30 µPa s) at 0.1 m s^{-1}, the variation of the Stokes number with the obstacle diameter can be plotted. This is shown in Figure 1.7b.

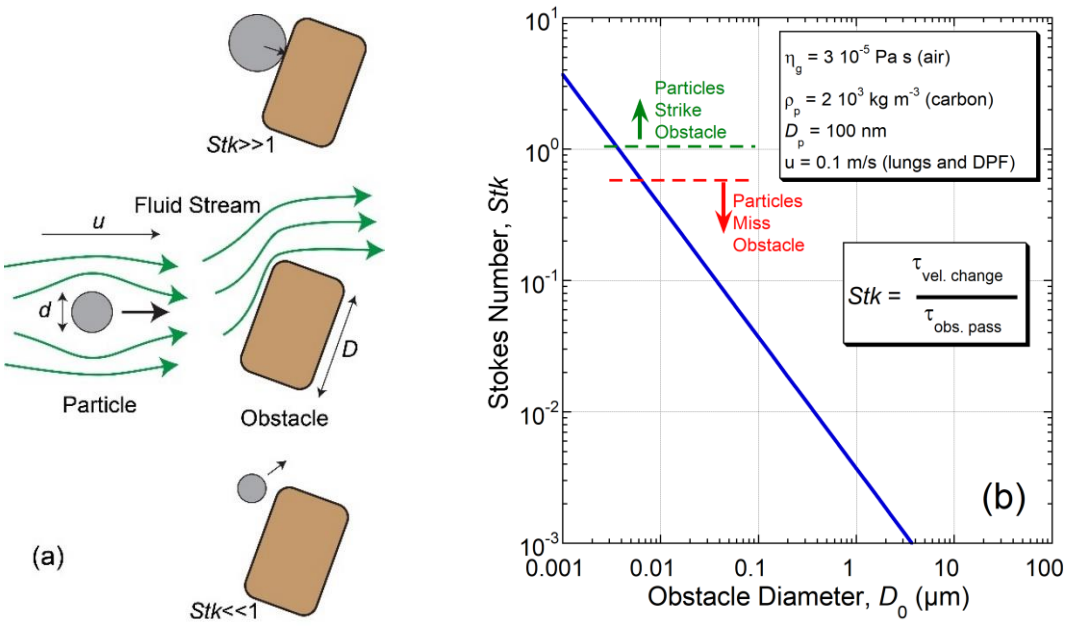

Figure 1.7: (a) Schematic of the variation of Stokes number. (b) Dependence of Stokes number on obstacle diameter.

Figure 1.7b shows that for the particles to strike the filter surface, the obstacle diameter should be smaller than 100 nm. However, having features of this size returns to the sieving regime, leading to large back-pressures. For deep-bed filtration and soot cake formation, the pore channels are significantly wider, >10 µm, and the low Stokes number indicates that these alternative methods initially provide a low filtration efficiency when

the filter is clean, but significantly improve to almost 100 % efficiency after a small amount of soot loading at the expense of an increased back-pressure.

1.3.3. Back-pressure

As the filters accumulate PM, the soot blocks pores and impedes gas flow, raising the back-pressure in the exhaust system. This exhaust back-pressure (EBP) can lead to negative responses from the engine. Most noticeably, a higher EBP requires the engine to do extra p-V work, and so extra fuel is required, corresponding to a decrease in the fuel economy [38]. In serious conditions, a large EBP can lead to a large increase in the exhaust temperature, leading to failure of the pistons, cylinder heads and valves via the processes of torch erosion and thermal fatigue cracking [39].

Back-pressure can be decreased by careful DPF design choices. It has been found that increasing the diameter of the inlet cell relative to the exit cell increases ash loading by 50 %, whilst maintaining the same EBP [40]. So-called asymmetrical cell technology filters become more beneficial at higher soot and ash loads, due to larger inlet channels and capacity to hold more ash and soot. Low EBP sensitivity can also be obtained by using a larger open frontal area and a higher porosity.

Whilst soot accumulation leads to an increase in EBP, it does offer some advantages over a perfectly clean DPF. Soot very quickly forms loose and relatively permeable layers (porosity > 90 % [41]), known as a soot cake, allowing for very good filtration efficiencies (up to 99.9 %) to be achieved quickly over the entire particle size range, even for filters with micrometre-scale pores [17, 29]. The stages of soot cake formation, as well as its effect on the pressure drop is shown in Figure 1.8, and the effect of soot load on the filtration efficiency is shown in Figure 1.9. This is a considerable advantage over filters with pore sizes in the nanometre range, which can be manufactured to remove the diesel PM using a sieve effect, but the low permeability of such a filter leads to an unreasonably high EBP in the exhaust system. Before a soot cake layer has formed, the low initial filtration efficiency is one of the weaknesses of a DPF [42, 43].

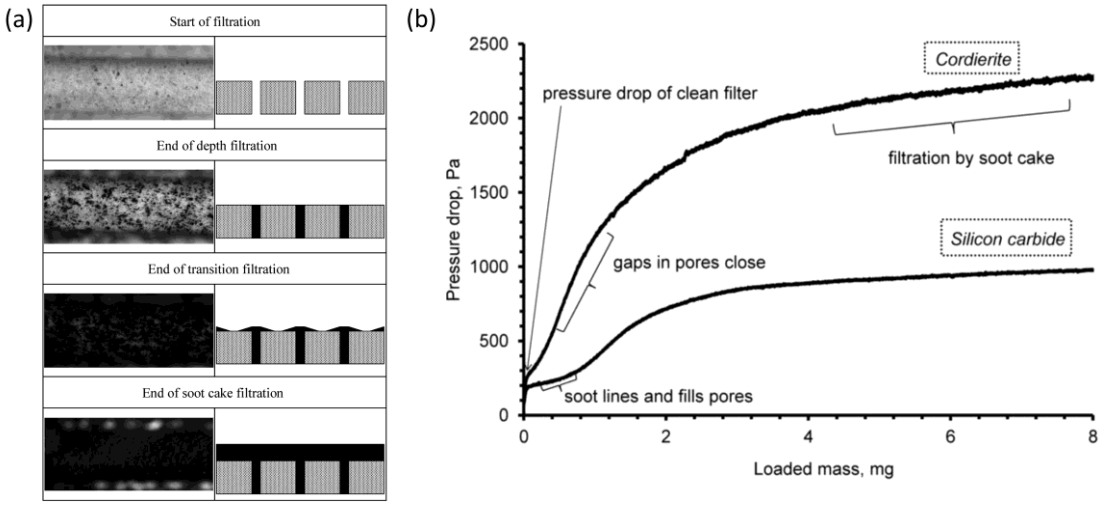

Figure 1.8: *(a) microstructures and diagrams of the soot loading in a DPF during operation [44] and (b) experimental data for the pressure drop across DPFs as a function of their mass gain during deposition of PM [43].*

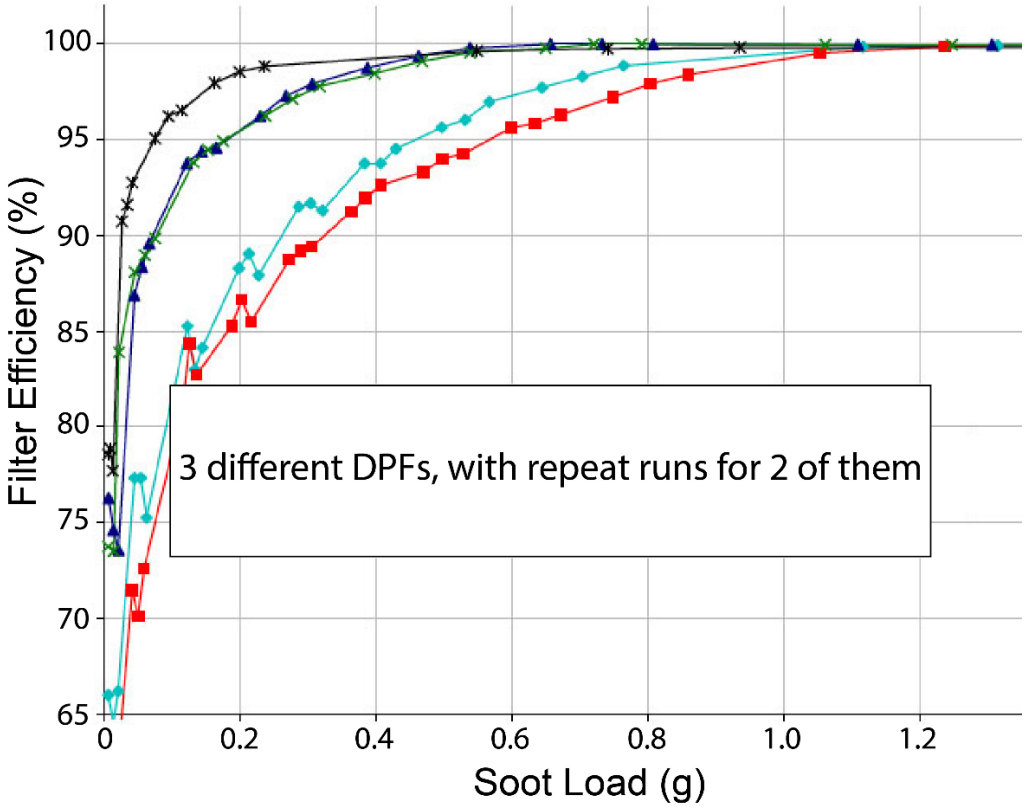

Figure 1.9: *Filtration efficiency of DPFs as a function of soot load, measured at Cambustion [45]. The filtration efficiency is initially very low but increases to almost 100 % after 1.2 g of soot has accumulated.*

Filtration efficiency can be measured as either the fraction of mass or number of PM collected. Konstandopoulos *et al.* [46] predicted the filtration efficiency for different sized soot particles and showed that the most difficult size to trap was around 300 µm, corresponding to the accumulation mode peak (Figure 1.2). However, even though the filters struggled initially to filter the accumulation mode particles, after 20 minutes the soot cake had formed, and filtration efficiency was equally high for all particle sizes.

By considering the effects of deep-bed filtration and soot cake formation, an optimum pore size could be estimated. The minimum usable pore size is given by Darcy's law which relates the pressure drop over the filter to the pore size [47].

$$Q = \frac{\kappa}{\eta}\frac{\Delta P}{\Delta x} \qquad (1.2)$$

where Q is the gas flux through the filter ($m^3\ m^{-2}\ s^{-1}$), ΔP is the pressure drop over the filter (Pa), η is the viscosity of the gas (Pa s), Δx is the thickness of the filter (m^2) and κ is the specific permeability (m^2), found using the Carman-Kozeny equation [48]:

$$\kappa = \frac{\varepsilon^3}{\lambda S^2} \qquad (1.3)$$

where ε is the porosity level, S is the specific surface area of the filter ($m^2\ m^{-3}$), and λ is a dimensionless constant, approximately equal to 5 [48]. By using appropriate figures for these values, and by assuming that a pressure drop of over 30 mbar can be assumed to be unacceptable, the minimum pore size, D_{eq}, can be predicted to be just under 10 µm, where D_{eq} is calculated from S by assuming the pores are equivalent to parallel channels. The result is shown in Figure 1.10.

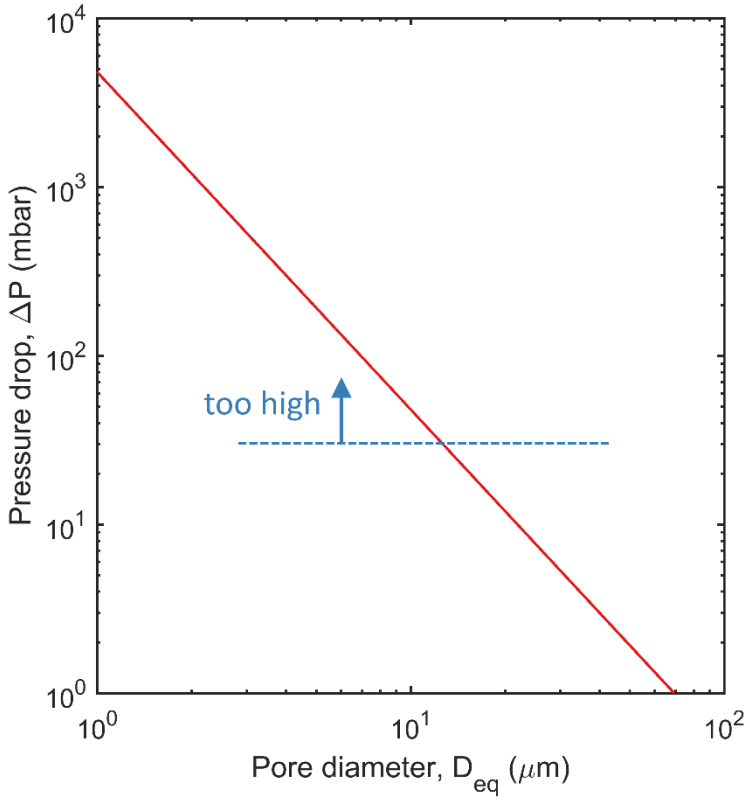

Figure 1.10: Predicted pressure drop across a DPF of wall thickness Δx = 1 mm as a function of pore size. Predicted using Darcy's equation and the Carman-Kozeny equation, based on a honeycomb structure DPF with 50 % porosity, $\eta = 3 \times 10^{-5}$ Pa s and $Q = 0.1\ m^3\ m^{-2}\ s^{-1}$.

Merkel *et al.* suggested in a patent [49] that the optimum pore size had a narrow distribution and median pore size of < 25 µm.

1.3.4. Regeneration

As DPFs accumulate PM, the EBP will increase. Eventually this EBP will noticeably begin to negatively impact the engine performance, and the PM trapped in the DPF must be removed. Carbon particulate has the fortunate characteristic that its oxides are gases, so this can be done by oxidation in a process called regeneration, which can be classified into two types. In passive regeneration, particulates can be removed continuously during regular operation or, alternatively, in active regeneration removal can occur periodically

after a pre-determined quantity of soot has accumulated and the back-pressure has reached a certain level.

Passive Regeneration

Thermal regeneration is the cleanest and most attractive method for regenerating DPFs, necessitating either the exhaust gas temperature to be increased or the soot ignition temperature to be lowered by a catalyst. During regeneration, the collected particulate is oxidised by O_2 and/or NO_2 to produce primarily CO_2. A minimum temperature and adequate gas supply are required [17]. Oxidation is possible using O_2, but this requires temperatures above 600 °C, much higher than a typical exhaust gas temperature of ~250 °C. In such a reaction CO_2 is the preferred product, but CO emission may occur if O_2 is depleted in the reaction zone. NO_2 is a stronger oxidiser than O_2 and thus allows regenerations at much lower temperatures (approximately 260 °C). NO_2 concentrations can be increased by oxidising NO, typically over a DOC.

In passive regeneration, PM trapped in the DPF is continuously in a dynamic equilibrium between the soot being captured and the soot being oxidised. Since carbon will not oxidise until temperatures much hotter than the normal exhaust temperature are reached, catalysts must be used to lower the oxidation temperature of the accumulated PM. The simplest way to do this is by using a component called a catalysed DPF (CDPF), whereby the surfaces of a DPF are coated with a catalytic material, commonly containing Pt-group metals.

CDPFs are effective in lowering the PM oxidation temperature, and so passive regeneration becomes possible at exhaust operating temperatures and very high filtration efficiency is maintained. However, coating all the surfaces with a catalyst can raise the EBP by reducing the mean pore size. In some applications, this problem is addressed by modifying the DPF structure to accommodate the thin catalytic layer on all surfaces. Another problem associated with the introduction of a catalytic layer is that, in high sulphur conditions, it can promote the formation of sulphates and therefore reduce the trapping efficiency. Effectiveness and durability of CDPFs is maximised by using ultra-low sulphur diesel fuel [17].

Another method of promoting passive regeneration is via a component called the continuously regenerating trap (CRT). A CRT is a two-stage and full time passive regeneration system, where an uncatalysed DPF is regenerated using the powerful oxidative NO_2 generated over an upstream DOC. A CRT puts significant limitations on the exhaust system: the NO_x:C ratio must be greater than 8:1 by mass, and ideally above 20:1, and the exhaust gas temperature must be >260 °C for at least 40 % of the engine duty cycle [17]. For these reasons, a CRT is often used in heavy duty diesel engines, where exhaust temperatures tend to be high for the majority of their use.

By combining the ideas of the CDPF and the CRT, Johnson Matthey created a catalysed CRT (CCRT) [17], formed of a CDPF downstream of a DOC, providing the benefit of the highly oxidative NO_x [46] in addition to Pt-group catalysts which reduces the PM oxidation temperature down to 210 °C. This is commonly reached in a typical exhaust system. CCRTs are particularly useful for urban buses, where low engine speeds can make high exhaust temperatures difficult to attain. In general, CCRTs are more effective than a CRT, and this in turn is better than a CDPF for passive regeneration. The disadvantage of using DOCs in the CRT and CCRT is the increase in NO_2 emissions.

The major disadvantage with all passive regeneration systems is that, in idle operation or light-load conditions with low exhaust gas temperature, the soot ignition temperature cannot be reached, even with a catalyst. An excessive EBP can then build up, damaging the filter and engine. To monitor this situation, DPFs must be fitted with a back-pressure monitor. Current passive regeneration systems can only be successful by maintaining an average exhaust gas temperature at the filter inlet above that of the soot ignition temperature and the rate of PM generated by the engine must not greatly exceed the rate of oxidation of PM in the filter.

Active regeneration

For engines subjected to light-loads or high PM emissions, passive regeneration is currently unacceptable, and the filter must be actively regenerated instead. Active DPFs are less dependent on the engine duty cycle, and so they have a much broader range of applications. Active DPF regeneration systems operate by periodically raising the DPF

temperature sufficiently such that the accumulated PM can oxidise without the use of a catalyst; the ignition temperature that must be reached is around 600 °C. This temperature can be attained by means such as extra fuel injection or electrical heaters.

Regeneration is initiated when the soot loading of the DPF reaches a back-pressure threshold determined by DPF control software, measured using a differential pressure sensor. The frequency of active regeneration is determined by the engine's duty cycle, PM emission rate and filter technology, but generally occurs every 500–1000 km [35] and takes approximately 20 minutes to complete. The DPF temperature can become very high (>1000 °C) during regeneration.

The main method of active regeneration is late-cycle injection (post-injection), which is the preferred system for light-duty passenger cars. In this situation, the first post-injection of fuel retards combustion and increases the temperature of the exhaust gas. A second post-injection occurs when the engine piston is at top dead centre. This fuel partly combusts in the cylinder, but introduces a small amount of unburnt fuel into the exhaust gases, which oxidises exothermically over a DPF, raising the temperature. The disadvantage of this particular method of active regeneration is that fuel can leak into the crankcase leading to dilution of lubricant, which consequently requires more frequent oil changes [17].

Another active regeneration method is known as a catalytic burner. In this process, diesel fuel is introduced directly into the exhaust through an in-exhaust injector. It evaporates, mixes with the exhaust gases, and is combusted over an upstream DOC. This is used in heavy duty applications, where lubrication dilution makes post-injection unfavourable. By avoiding post-injection, regeneration is safer, has no lubricant dilution issues and has no critical exothermic reactions [17].

Electric heating systems have also been employed to induce active regeneration. This has been unfavourable in the past, because it puts a substantial load on the vehicle's electrics, leading to a significant fuel consumption penalty. However, brake energy recuperation is a technology that has been advancing, meaning that electric heating of

DPFs could become much more efficient [17]. It is the most flexible regeneration method and works with a wide range of filter substrates.

Finally, rather than heating or catalysing the carbon oxidisation reaction, methods of loosening and then collecting the trapped particulate have been trialled. The removal of particulate from the filter requires the flow of air through the filter to be reversed, either by redirecting the exhaust gases to briefly flow in the opposite direction or by using an electric blower (operated whilst the vehicle is stationary or, for the case of hybrid cars, running on batteries). Loosening of the particulate can be achieved simply by pulsed reverse air flow [50]. However, for more efficient regeneration, the soot can be dislodged via shock waves created by rapid pulse electric discharges [51]. Such systems do not lead to complete regeneration, but maintain a steady-state "clean" soot-loading of ~2 g L^{-1} after a few regenerations [52]. This retention of the deep-bed carbon but removal of the soot cake has been considered to be a desirable effect for maintaining a high filtration efficiency [53]. These systems have shown promise for regenerating filters with very high soot loadings (up to 17 g L^{-1} [52]) and have the advantage of collecting the soot rather than releasing it as CO_2. Similar to the electric heating systems, these regeneration methods can require substantial amounts of electricity.

The disadvantage of active regeneration systems is that there is an increase in fuel consumption of approximately 2 % [17]. Active regeneration can also lead to uncontrolled regeneration, where the DPF temperature increases to a much higher temperature than necessary, reaching temperatures in excess of 1000 °C. The most common reason is excess PM loading, in combination with a high O_2 concentration and a low exhaust flow rate; this occurs when an engine drops to idle during a regeneration [54]. Hot spots can also form due to uneven soot loading in the filter leading to incomplete regeneration, locally reaching temperatures as high as the melting point of the material. Uncontrolled regeneration is the most common reason for DPF failure, since the filter is damaged by cracking (under thermal shock) or melting at high temperatures.

In addition to modifying the design of the exhaust system, catalysts can be added via the fuel. This is known as fuel borne catalyst (FBC) assisted regeneration. Very small quantities of fuel additives can be used to substantially lower the oxidation temperature

of trapped particles; a tank of FBCs will cover 240,000 km before refill [55]. FBCs can be used in conjunction with both passive and active filter systems and make regeneration faster, more complete, easier and safer. Examples of additives that are used include transition and precious metals eg. Ce, Fe, Cu, Sr, Pt. There are unfortunately a few issues associated with the use of FBCs, such as the cost of precious metals and the deposition of CeO_2/Fe_2O_3 residue in the DPF which can only be removed by ash cleaning.

1.3.5. Ash problem

Regeneration is effective in removing the majority of the PM in the filter, although a few non-combustible substances (ash) will remain. These inorganic species come from a variety of sources, such as additives in the fuel (including FBCs), oil, salts from environmental air, or wear debris from the engine. The composition is mainly of oxides, sulphates and phosphates of iron, calcium and zinc [35]. Over time, the accumulation of ashes leads to a rise in EBP and deterioration of the filter capacity [56], ultimately leading to the reduction of the lifetime of the filter. The first generation of DPFs required maintenance intervals of 80,000 km because of ash blocking, but this has been extended to over 250,000 km due to lower amounts of additives in the fuel [35]. Filters blocked with ash will generally need to be replaced, although they may be cleaned using deionised water, ultrasound and acid [57]. Of course, aggressive cleaning of this type imposes a requirement for the DPF to be mechanically robust, as well as resistant to high temperatures and thermal shock.

1.4. DPF design

1.4.1. Channel structure

At the largest DPF scale, the arrangement of channels must be decided. The most common channel cross-section is square, with the four neighbouring channels being plugged at alternate ends, such that the exhaust gases are forced to pass through the filter wall into an adjacent channel. This design provides good packing efficiency and a large available surface area for filtration. Other cell geometries have been considered, such as

equilateral triangles [58, 59] and hexagons [60-62]. The equilateral triangles can support the same alternating pattern between inlet and outlet channels as in the square cell case, but the sharper angles are less favourable for soot cake formation. The hexagonal cells improve on this problem, and Tsuneyoshi and Yamamoto claim an improved regeneration efficiency and a lower maximum regeneration temperature at the expense of a longer regeneration time [60]. However, the packing can no longer be alternating and consequently some inlet channels are required to touch; this reduces the effective total surface area for filtration (although Nakamura *et al.* acknowledge that a small amount of deposition does occur on these inlet/inlet walls [61]). Neither the triangular or hexagonal designs have made it through to DPF production.

Even for the square cross-sectional channels, there are choices to be made. For example, the optimum size of the channels was determined in some of the earliest work on DPFs by Howitt and Montierth in 1981 [63]. They found that for a given wall thickness, there is an ideal cell density (measured in cells per square inch, cpsi). For a wall thickness of 0.012 inches (300 μm) this was found to be 200 cpsi, and these values are still used in modern DPFs, over 35 years later.

As mentioned in Section 1.3.3, asymmetric geometries have also been considered, in which the inlet channels can be made larger than the outlet channels. This can either be by making the inlet channels form larger squares [40, 64, 65], or by introducing a wavy cell design, where inlet cells are squares with concave curvature, whereas the outlet cells have convex curvature [66, 67]. This is beneficial since, when in use, a soot cake will form on the surface of the inlet channel, and so as filtration proceeds the inlet channel width will decrease. A larger inlet channel also provides a larger surface area for soot collection, and so more soot can be trapped between regeneration cycles, and the filters are more tolerant to the accumulation of ash [40]. These channel designs are shown in Figure 1.11 below.

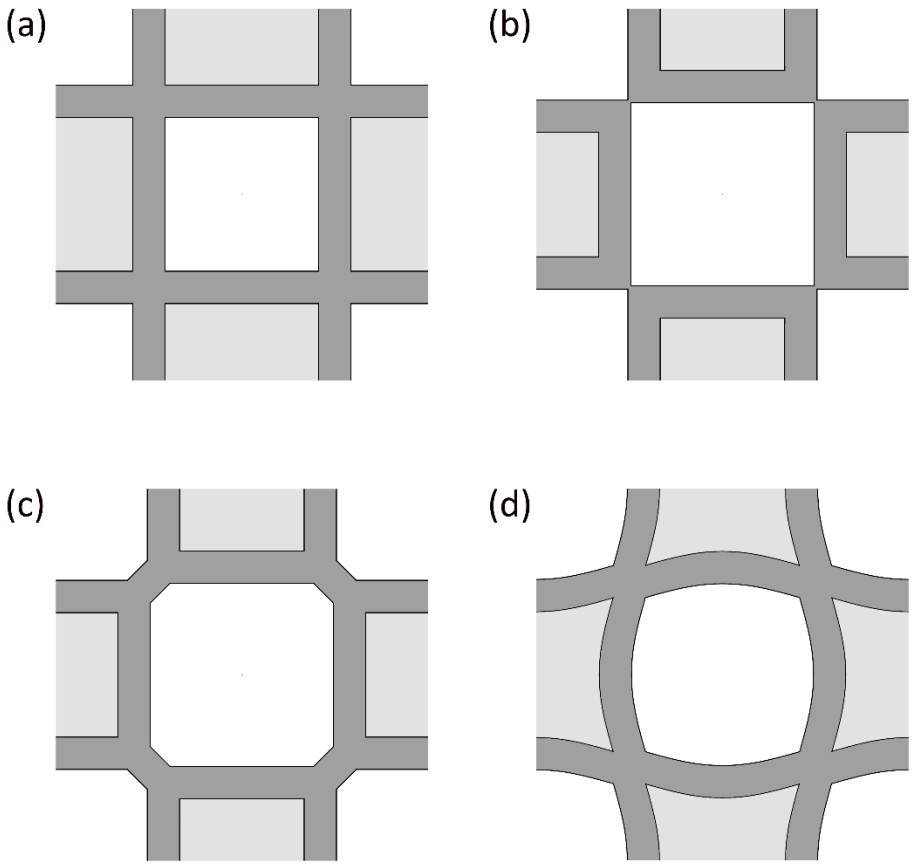

Figure 1.11: Different DPF channel configurations, the white areas represent the inlet channels, the light grey areas are the outlet channels and the dark grey area is the channel wall. (a) normal square channels, (b) enlarged inlet channel, (c) octagonal inlet channel, and (d) wavy cell design.

1.4.2. Materials requirements

There are a number of key requirements that a potential DPF material must satisfy to be viable:

1. High temperature stability is the most important requirement for a DPF. In general, the filter will be cycled between ambient temperature and 250 °C, although during a regeneration, temperatures of 600 °C will regularly be reached and spikes of over 1000 °C are not uncommon, especially in unfavourable

regeneration situations, for example a drop to idle during regeneration. The melting temperature should therefore be much higher than 1000 °C, and there should be no polymorphism over the entire temperature range. Materials should ideally be crystalline, rather than amorphous, such that there is no glass transition temperature.

2. Low coefficient of thermal expansion (CTE) is critical for a DPF. Since the material may be cycled over a temperature range of over 1000 °C, it is important that the material is not subjected to a large thermal strain which could cause damage to the filter which will be constrained in a container. The CTE should ideally be lower than 5 μK^{-1}.

3. High fracture energy is necessary, because if a brittle material fails it will be by fracture. Resistance to crack propagation is a key benefit, since any crack that runs through the length of the DPF will provide a low resistance path for the gas stream, resulting in poor filtration efficiency.

4. High thermal conductivity is important, to relieve thermal stresses in the structure. If there is a local spike in temperature, it will be beneficial to dissipate this energy to the surrounding material.

5. Low stiffness is important to increase the thermal shock resistance (TSR). A more compliant material will lead to lower stresses when accommodating a given thermal strain.

6. Corrosion resistance must be considered, since the DPF is exposed to a number of chemical species from the diesel itself, ash deposited from burnt lubricant oil, or wear and tear from the engine components.

7. Mechanical strength, whilst not critical, must be sufficient to allow the material to easily be handled without breaking, in addition to coping with vibrations and mechanical shocks when in use.

8. Durability is important during the useful lifetime of the DPF. Rather than the distance driven, this can be thought of as the number of regenerations, since the regeneration cycles will be the most demanding process during the lifetime of the filter.

9. Availability for mass production, and good mouldability, at low prices and low weight, are also prerequisites for automotive applications.

1.4.3. Currently-used materials

The category of materials that best fulfils these property requirements is that of porous ceramics. The porous structure can commonly be achieved by incorporating organic particulates, such as sawdust starch [68] or graphite [69], allowing for precise control of the pore size, shape, and distribution. These organic components can then be removed by combustion. Methods of production include leaching [70], fused deposition [71], gelcasting [72-74], reaction bonding [69], direct consolidation [68] and gel freeze drying [75]. Since some properties, including fracture toughness [76] and stiffness [77], are sensitive to porosity level and pore architecture, focussing entirely on the properties of the dense materials can be misleading. However, the fully-dense properties provide a suitable comparison between materials.

Cordierite ($2MgO.2Al_2O_3.5SiO_2$) is cheaply produced from natural raw materials kaolin and talc and is widely used as a DPF material, especially in heavy duty diesel applications. It offers the benefit of a very low CTE [78], as well as good mechanical strength, toughness and melt resistance [79], but its low thermal conductivity can lead to thermal spikes in unfavourable regeneration conditions, resulting in melting of the material [35]. In addition, the corrosion resistance of cordierite is not ideal, being particularly susceptible to damage from ash components, e.g. sodium [80, 81].

Another DPF material is silicon carbide, SiC, commonly used in low and medium duty applications. It offers the considerable advantages of a high heat capacity, excellent TSR, high thermal conductivity, thermal and chemical durability, and good handling strength. However, its high thermal expansivity requires the DPF to be broken down into

a segmented architecture, held together by low modulus cement consisting of alumina-silicate fibres [82], in order to keep the thermal stresses low during an uneven regeneration.

High density mullite can be manufactured by a reaction-bonding route from powders of Al_2O_3 and Si/SiC [69]. Despite its low thermal conductivity, mullite has been introduced due to its low CTE, good TSR and mechanical and chemical stability at elevated temperatures. Mullite has the disadvantages that it is difficult to achieve a high porosity due to easy densification [83], and the maximum temperature is limited to around 1550 °C, since mullite might decompose into Al_2O_3 and SiO_2 above this temperature [73].

Aluminium titanate, Al_2TiO_5, has been introduced into low and medium duty applications [17]. It offers excellent TSR, chemical and thermal durability and a higher mass-based filtration performance than SiC in a clean state, due to a lower porosity and smaller mean pore size [84]. However, one major limitation is the large thermal stresses that are generated by anisotropic thermal expansion [85].

Concept filters have been made out of metallic materials. Metal filters (e.g. made from sintered Fe-Cr-Ni metal particles) offer significant benefits of high strength and high thermal conductivity resulting in a fairly good thermal shock resistance. However, the disadvantages include a high CTE and higher density, in addition to problems with high temperature and corrosion and the price of special alloyed fibres [35].

1.4.4. Potential benefits of fibres

Most of the literature on DPFs concerns the aforementioned materials in powder form, resulting in granular structures; very little work has concentrated on the effect of incorporating fibres into the DPF substrate. Previous work on ceramic fibre based DPF materials [83] found that the addition of fibres produced a desirable combination of high porosity and high permeability, whilst maintaining adequate mechanical strength. The pore structure formed in a fibrous material is much more interconnected and exhibits an increased tortuosity when compared to simple sintered particles; all surfaces tend to be in contact with the gas flow, with no dead-end pores [36].

In addition to benefits of a more open pore structure, fibres can also be beneficial for the mechanical properties. Fibrous materials offer flexibility and compressibility advantages over granular materials [86], which will act to increase the thermal shock resistance of the material. Fibres may also act to improve the toughness of composite materials via the mechanisms of fibre pull-out and increased cross-linking [87, 88]. In such a process, the toughness is increased because a crack propagating through the material must first de-bond the interface between the fibres and particles, and then overcome the frictional force for the two surfaces to slide over one another [87]. This thermal shock resistance benefit of fibres has been employed elsewhere, e.g. in Space Shuttle tiles comprised from a network of silica fibres where thermal shock resistance is a critical property [89].

As mentioned in Section 1.4.2, a low stiffness is desirable for improving the thermal shock resistance, since it allows for higher thermal strains to be accommodated. Fibre networks have been shown to considerably reduce the stiffness [90, 91], and the reduction in stiffness is dependent on the fibre aspect ratio (length/diameter) in addition to the porosity (void content). An analytical model developed by Markaki and Clyne [91] predicts the stiffness of the fibre network, E_n, to be:

$$E_n = \frac{9\,E_f\,V_f}{32\left(\frac{L}{D}\right)^2} \tag{1.4}$$

where E_f is the stiffness of a single fibre (GPa), V_f is the volume fraction of fibres, and (L/D) is the aspect ratio of a fibre. This model shows good agreement with experimental data, where porosity was varied by changing the fibre length and consolidation procedure [92], and can also be applied to known anisotropic fibre orientation distributions [93].

This dependence of stiffness on fibre aspect ratio is shown below in Figure 1.12, reproduced from Clyne *et al.* [94]. Therefore, addition of fibres, in particular with a large aspect ratio, is expected to improve the thermal shock resistance.

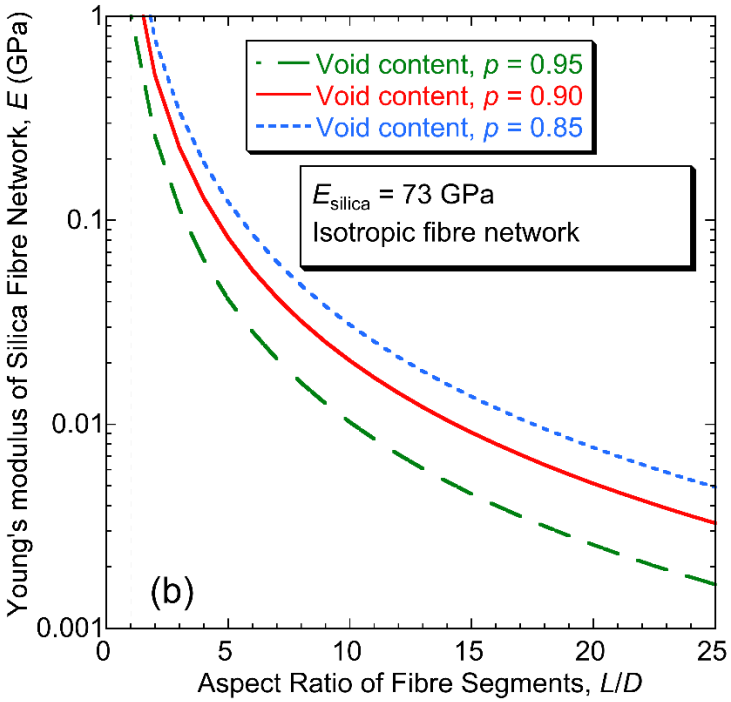

Figure 1.12: Dependence of stiffness on fibre aspect ratio and porosity for a fibre network.

Filtering efficiency is dependent on inter-fibre spacing. There is a general correlation between the scale of the fibre diameter and the scale of the particles removed [95, 96]. A study by Su *et al.* [86], on the filtration efficiency of dye molecules from an aqueous solution using a fibrous ceramic material, found that the inter-fibre spacing must be similar to the minimum particle size; this size dependence is also predicted by the Stokes number (Equation 1.1). In this case, filtering appeared to be by mechanical entrapment (modelled by Peri [97]), although surface electrical effects were found to play a significant role in filtration efficiency, due to the tendency of inorganic surfaces to become charged [36].

Fibres can also be bundled, as shown in Figure 1.13, which can stimulate a multi-scale pore architecture. A study using this technique to form filtration membranes showed that this structure displayed high permeability and good filtration efficiency, with flow predominantly through coarse inter-bundle pores, but with sufficient flow through fine intra-bundle pores to ensure good filtration efficiency [36]. Use of very fine ceramic fibres has previously been limited by high production costs. However, even ultra-fine alumina fibres are now becoming available at low cost and in large quantities [36, 86]. For example,

fibres produced in Estonia by Metallurg Engineering are grown from an Al melt and the production rate is fairly high, in the order of kg hr^{-1}. The growth process results in highly aligned fibres, with an extremely long aspect ratio. Fibres can be produced with diameters of between 5 nm and 20 nm, with a very uniform fibre diameter for a given batch [86]. Such fibres, with diameters on the same scale as diesel PM offer a potential material which could be incorporated into DPFs. However, the issue with fibres of this scale is the significant increase in back-pressure, as shown in Figure 1.10. Thus, it is preferable to use fibre with a diameter in the range of microns, rather than nanometers. In this current work, the effect of incorporating fibres into a DPF substrate is being investigated.

In commercial production of DPFs, the material must be extruded into its final shape. For a fibrous material this will result in anisotropic properties, because fibres will preferentially align in the extrusion direction. The orientation behaviour is controlled by fibre content, size, distribution and morphology [83].

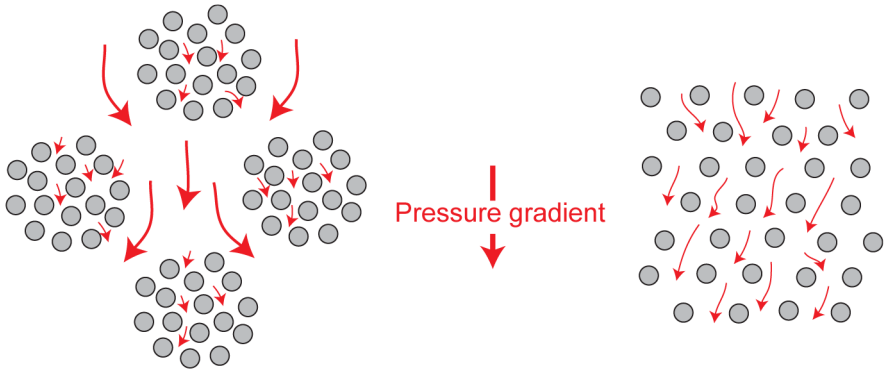

Figure 1.13: Schematic showing the effect of fibre bundles in a filtration scenario. Efficient filtration of fine particles is achieved by intra-bundle flow, whilst high permeability is maintained by flow between bundles. This effect was shown to efficiently filter a small dye molecule from an aqueous solution by Su and Clyne [36].

The inclusion of fine chopped ceramic fibres has been studied in detail by those working on ceramic matrix composites (CMCs). Often for CMCs the aim is to form a fully-dense structure, as opposed to the highly porous structures required for filtration. However, the methods of production are worthy of consideration. Ball-milling, with the inclusion of ethanol [98], can be used to break down fibres into smaller lengths. If it is

required to separate bundles of fibres, this can be achieved by dispersing the fibre agglomerates in water, followed by filtering and drying [99]. These fibres are then mixed with fine particulate; a common method for blending is via ball-milling, either in ethanol [100] or isopropyl alcohol [101]. Cold isostatic pressing is then used to form the material into the green compact, ready for sintering.

1.5. Simulation

1.5.1. Introduction

The structure of a DPF lends itself well to analysis by simulation. Experimentally, it is expensive and time-consuming to create novel DPF designs [102], especially if it requires temporarily halting the production of commercial DPFs. The wide variety of environments, engines and usage that a potential DPF material could be subject to are too large to be able to fully experimentally measure. Equally, it is not possible to computationally model all conditions, but in simulation there is a much wider scope for tailoring the model to specific cases.

1.5.2. Scales of simulation

Although there is a definite advantage to simulation, it is not without problems. The main difficulty is in the hierarchical structure of the DPF; it can be analysed at the entire macroscopic filter scale (tens of cm), the channel scale (mm) or the wall scale (μm) [103]. Since this spans several orders of magnitude, it is impossible to combine all of these into one model using current computing capabilities, and so simulations often focus on one particular scale.

Filter scale

At the entire filter scale, the main interests are in the effective thermal conductivity of the monolith and the effect of uneven soot loading. The entire filter cannot simulate every channel as this would be too time-consuming. Instead, the filter can be broken down into a smaller multi-channel model which considers either splitting up the filter into radial

sectors which repeat to form the whole structure [104], representing different areas of the filter by using representative channels in different regions of the filter [105, 106] or by assuming the filter to be one continuum model [107-109].

Kostoglou *et al.* [107] found that hot spots formed during regeneration were more significant when located near to the filter entrance. Hot spots found deeper in the filter could be dissipated via convection. Regeneration of catalysed DPFs was also found to be affected by non-uniformities in both the axial and radial catalyst distribution by Konstandopoulos *et al.* [108]. In addition, both authors acknowledged that radial temperature gradients at the inlet can also hinder regeneration, with simulations showing that by insulating the inlet cone to the filter a 30 % gain in regeneration efficiency could be obtained [107]. Galindo *et al.* showed that, in addition to insulation of the inlet cone, the effective radial conductivity also depended on the open frontal area of the monolith, the substrate porosity, the wall temperature and the existence of a soot cake layer [104].

The distribution of the soot cake layer can also be observed at the filter scale. Yi [106] found that the soot loading was concentrated towards the ends of the channels, showing an axial variation as well as a radial distribution. Hinterberger *et al.* [109] agreed with this observation but noted that the soot maximum occurs at the rear of the DPF at higher exhaust gas flow rates due to dominating inertial effects.

Channel scale

By limiting the simulation to a single channel, more detail can be observed in the soot cake formation. The channels can be analysed by either a one, two or three-dimensional model. Pioneering work at this scale of the DPF was carried out by Bissett [110], and much of the later literature built off the groundwork laid out in this paper. The major assumptions of Bissett's model are presented clearly in a review paper by Yang *et al.* [102]. This model was a simple 1D model, but it has been shown that 1D models are in strong agreement with 3D modelling [111]. By following the work of Bissett, several researchers used and improved the 1D channel model to simulate the effect of particulate oxidation on a catalytic coating [112, 113], the evolution of temperature gradients [114] and the effect of soot cake thickness [115, 116].

Wall scale

Finally, at the smallest scale, there is interest in the filtration phenomena occurring at the pore scale as the exhaust gases pass through the filter wall. For wall scale simulations, the pore architecture must be captured. Initially this was possible by highly complex and time-consuming methods of subsequent imaging and polishing through a DPF sample followed by extrapolation of the images to form a continuous digital three-dimensional representation of the pore structure [117]. Nowadays, micro computed tomography (micro-CT) has become a widely available technique, and current resolutions can be as low as 0.5 µm, making the study of DPF walls viable.

Pore scale simulation of DPF walls is uncommon, with the most extensive work being done in a series of papers by Yamamoto *et al.* [118-121] using the micro-CT method for generating a digital porous structure. In these papers, Yamamoto *et al.* acknowledge that the pressure distribution depends on the non-uniformity of the pore structure [119] and offer an insight into the effectiveness of NO_2 [119] and temperature dependence [120] under the process of continuous regeneration in a catalysed DPF. Additional work by Tsushima *et al.* focussed on the deposition properties of soot, observing that the small soot particles (around 1 nm) were not able to penetrate the DPF substrate, due to a higher diffusivity, and were captured on the front side. Contrariwise, larger particles were found to penetrate deeper into the substrate in the early stages of particle loading [122].

Looking further afield from DPFs shows that there is interest in pore scale simulations of general porous media, often concerning a liquid phase. Micro-CT can be a costly and time-consuming technique and the resolution can be limited. Rather than generating a structure through imaging techniques, idealised structures could be generated by filling a volume with spheres to represent sintered particles [123, 124] or cylinders to represent a fibrous network [125-128]. However, no evidence was found in the literature of combining both particles and fibres into a single model, and this will be covered in this work in Chapter 6. The various methods used in CFD packages to simulate fluid flow are described in the following section.

1.5.3. Simulation methods

For the first simulations of fluid flow through porous media, techniques known as lattice gas automata were used [129-132]. In such simulations, a homogeneous two-dimensional hexagonal grid (called the FHP model after Frisch, Hasslacher and Pomeau [133]) fills the pore space and is populated with particles, representing gas molecules. As the simulation advances, all these molecules travel to a neighbouring node where they are assigned a new path based on particle collision. This is a simplistic elastic collision model which is able to successfully reproduce the physics of incompressible fluid flow. The results are macroscopically indistinguishable from real fluids [131], thus can be considered to solve the Navier-Stokes equations for fluid flow, given a sufficiently fine lattice and large number of particles. The analysis can be extended to three-dimensional fluid flow, requiring a four-dimensional face-centred hypercube lattice to provide sufficient symmetry [134].

However, initial enthusiasm for the lattice gas automaton methods was dampened due to the presence of high levels of molecular noise requiring a huge number of particles for convergence to an acceptable average, in addition to the long computation times needed for discrete calculations [135]. These drawbacks were improved upon by the introduction of Lattice Boltzmann (LB) methods [136] which preserve the simplicity of the lattice gas automata but instead use a continuum method based on the statistical motion of gas molecules to overcome the problem of molecular noise. In the LB methods, all particles are assumed to be hard spheres interacting through fully elastic collisions and are described by precise three-dimensional position and velocity coordinates. Rather than evaluating each particle, they are evaluated as one function, the velocity distribution function, which provides the probability density for the presence of a molecule in a seven-dimensional phase space (the six dimensions associated with position and velocity, and an additional time dimension).

LB methods remain the popular choice for analysing the fluid flow through porous media, including DPFs [118-122, 137] although it is not without its limitations. One of the major drawbacks is that the lattice must have a uniform mesh spacing everywhere in the domain. Since fluids tend to have thin boundary layers close to surfaces, the resolution

required to accurately capture these thin layers would result in over-resolution elsewhere, and therefore slow solution times. Refinements in the lattice near boundaries have been implemented [138, 139] but a compromise is necessary between a fine enough resolution to be representative of the physics of fluid flow, and coarse enough resolution for a fast solution. Another potential issue is that LB methods are not derived for compressible flow; however, this can be accounted for, as shown by Alexander *et al.* [140].

A final method of simulation is by numerically solving the Navier-Stokes equations using a finite element solver with suitable boundary conditions. The form of the Navier-Stokes equations used for fluid flow through a small pore network are:

$$\rho \frac{d\underline{u}}{dt} = -\nabla p + \eta \nabla^2 \underline{u} + \underline{F} \tag{1.5}$$

$$\nabla . \underline{u} = 0 \tag{1.6}$$

where ρ is the density of the fluid, $\underline{u}$ is the velocity of the fluid, η is the coefficient of viscosity, p is the pressure acting on the fluid, and $\underline{F}$ represents the contributions of internal and external forces. Gravity can be ignored in such simulations due to the small size [141]. The results from such pore scale simulations have been shown to have good correlation with Darcy's Law at a macroscopic scale [142].

1.6. Structure of this thesis

This thesis begins by considering the materials and experimental techniques that were used, followed by preliminary work on a first-generation of materials focusing on processing conditions. The work then divides into considerations of filtration efficiency and thermal shock resistance. The former is divided into two chapters; one on experimental and tomographic results, and another on simulation.

2. Materials

2.1. Introduction

In this work the effect of fibre inclusion in DPFs is investigated. To create the samples, this necessitated each sample to be a composite formed by mixing of fibres and particles, which were then sintered to form the DPFs (with varying fibre contents).

This work focussed on two combinations of particles and fibres, labelled as first and second-generation materials. Neither combination contains the commonly used DPF materials of cordierite or silicon carbide, as detailed in Section 1.4.3, but it is hoped that conclusions about the effect of fibre inclusion in these materials can be transferred to commercial materials. This work therefore aims to study the effect of fibre inclusion, in terms of the filtration efficiency and thermal shock resistance, on a similar material to a DPF, but does not suggest that these materials are better than those used commercially.

The first-generation of materials was useful for running preliminary experiments on the effect of certain processing conditions. However, due to some of the properties that will be discussed later in this section, such as the amorphous nature of the fibres and the small particle size compared to the fibre size, it was necessary to switch subsequently to the second-generation of materials.

The second-generation materials provided a much better size compatibility between fibres and particles, and the crystalline nature allowed for effective sintering, rather than softening above a glass transition temperature.

2.2. Characterisation techniques

2.2.1. SEM

Two Scanning Electron Microscopes (SEMs) were used throughout this work. The first was a JEOL JSM-5500LV, which was used for quick analysis of samples, such as calculating the length or diameter distributions of the particles and fibres or performing an Energy Dispersive X-ray (EDX) spectroscopy scan to determine the elemental components and their approximate proportions. The second SEM was a FEI Nova NanoSEM, which was used not only for image analysis, but also for obtaining higher quality images. Both back-scattered and secondary electron images were used for these purposes.

Since the samples were non-conducting, it was also necessary to prepare the samples with a thin conductive coating in order to reduce the effect of charging when the samples were subjected to the electron beam within the SEM. The samples were fixed to a sample stub using carbon tape in the case of loose fibres or particles or using silver conductive paint in the case of sintered specimens. These samples could then be sputtered with a thin layer of gold for 2 minutes, producing a nanoscale conductive film. In addition to the sputtering, low accelerating voltages were used, which also alleviates the effect of sample charging.

2.2.2. XRD

X-Ray Diffraction (XRD) was another analysis technique used to characterise the fibres used in the composites. X-ray diffraction, in addition to EDX, is a useful tool for examination of the composition of the fibres. Whereas EDX just provides information about the elemental proportions in a sample, XRD offers information about the specific (crystalline) phases present. This technique therefore works only for crystalline materials, whereas amorphous materials will offer little information other than the fact they are amorphous.

XRD was used to analyse both the first and second-generation fibres. In both cases, the equipment used was a Bruker D8 theta/theta with LynxEye Position Sensitive Detector. The fibres were ground and packed into a shallow container such that the top surface was flat. It was then rotated during the scan as the source and detector scanned between 2θ values of 5° and 80°.

2.2.3. Particle size analysis

Although it is possible to measure the particle diameters by analysing SEM images, it is also convenient to affirm the measurements using a particle size analyser. A particle size distribution was acquired using a Malvern Mastersizer/E, which measures the scattering of laser light passing through an aqueous suspension of particles (continuously stirred to prevent sedimentation) using an array of photodiodes, shown schematically in Figure 2.1.

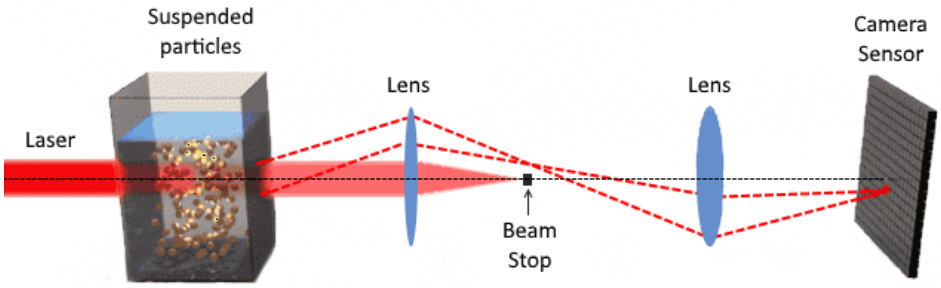

Figure 2.1: Schematic of set-up of particle size distribution measurement, the radial scattering pattern intensity is detected using an array of photodiodes. Figure adapted from LS Instruments [143].

The dependence of the scattering angle, θ, on the wavelength of the laser, λ_{laser}, and the particle diameter, D_p, is given by Equation 2.1 [144]. Hence, the particle size distribution can be determined by measuring the intensity of light as a function of scattering angle.

$$\sin\theta = \frac{1.22\,\lambda_{laser}}{D_p} \qquad (2.1)$$

2.3. First-generation materials

2.3.1. Fibres

The fibres used were supplied as a 2 cm thick fibre mat, which was a low-cost mass-produced material used for insulation in furnace applications. The fibre dimensions were measured by analysing SEM images. The fibres were found to have a distribution of diameters, ranging from 3 to 15 µm. Initially the fibre mat contained approximately 15 wt.% of "shot" particles. During processing, the fibres were teased apart by hand and then passed through a 250 µm sieve. This sieve broke the fibres up into appropriately-sized lengths, an aspect ratio of approximately 10–20, and also removed most of the larger shot particles that were left in the fibre mat from the fibre production process. A micrograph of some sieved fibres is shown in Figure 2.2.

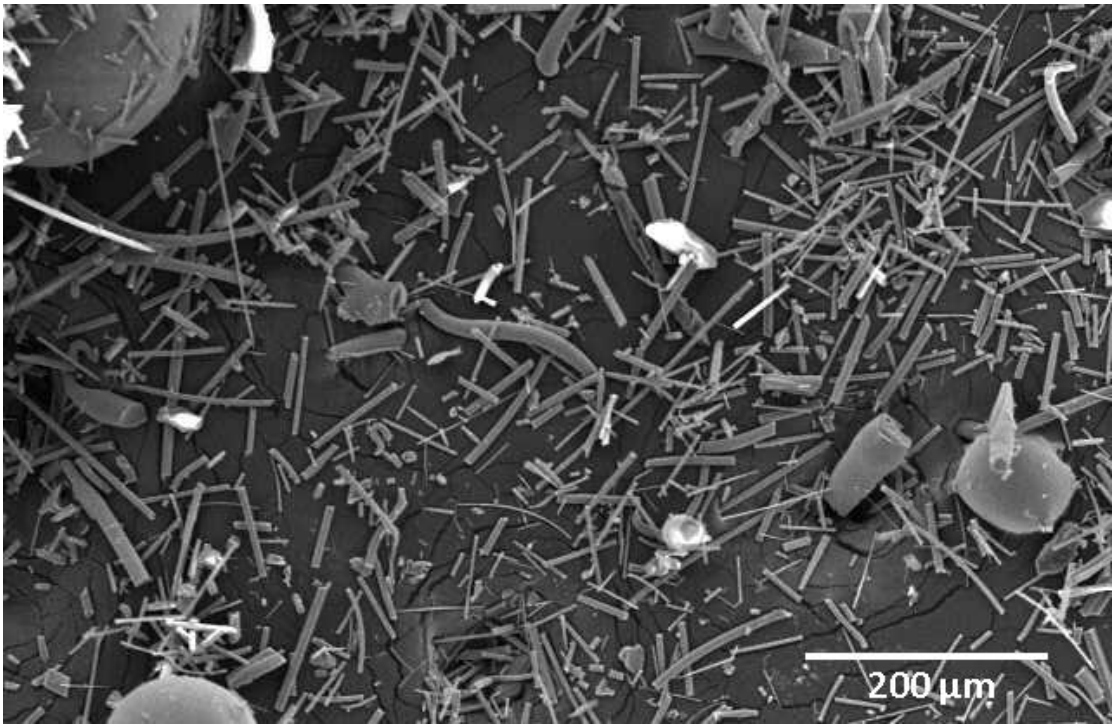

Figure 2.2: SEM image of the first-generation fibres, after being passed through a sieve. There is a distribution of fibre diameters and the larger particles, e.g. top left, are shot particles produced during the fibre manufacturing process.

To estimate the composition, the fibres were initially examined using XRD. However, it was apparent that the material was amorphous, since no crystalline peaks were observed, only a characteristic broad peak at ~ 20–30 ° (2θ), indicative of amorphous material. Figure 2.3 shows this trace.

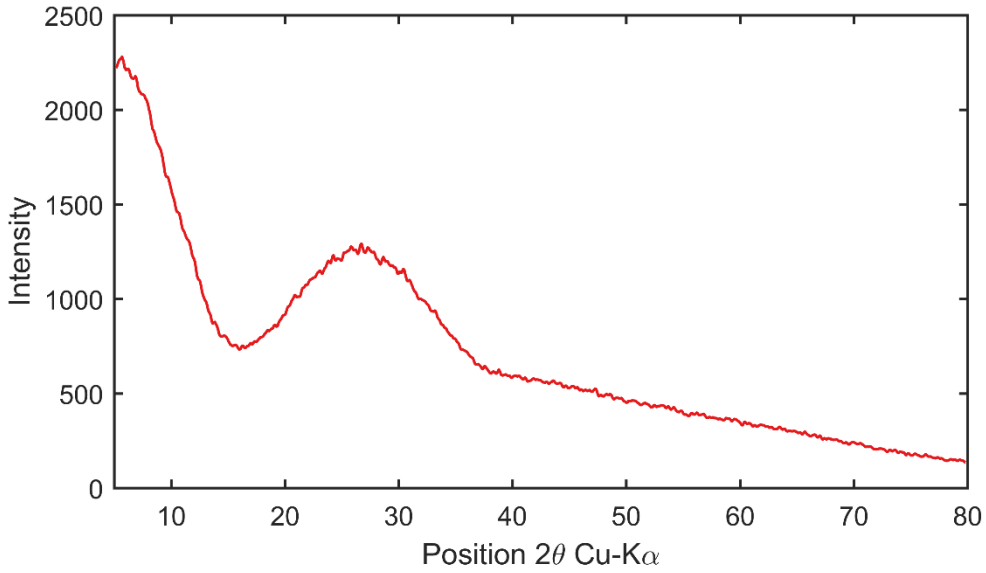

Figure 2.3: XRD trace of fibres between 5 and 80 °2θ. No crystalline peaks are observed.

Since there is no information to be gained from this trace, other than the amorphous nature of the fibres, EDX was used to investigate the composition. Using the JEOL JSM-5500LV SEM, the relative concentration of elements was found to approximate the proportions of 2Si:1Ca:1Mg, as well as a significant concentration of oxygen. This suggests the elements were present in a mixture of amorphous forms of the common oxide stoichiometry, SiO_2, CaO and MgO.

Since the fibres were found to be amorphous, another important property to consider is that of the glass transition temperature, T_g. At this point, the material will soften and become unusable. By measuring the elongation of a compacted sample of fibres (using a Netzsch DIL 402 C dilatometer) the T_g was found to be about 1150 °C, as shown in Figure 2.4. At this point, the compacted cylinder stopped getting longer, due to the thermal expansion of the fibres, and started getting smaller as a consequence of softening past T_g. A coefficient of thermal expansion was also measured to be 9.4 μK^{-1}.

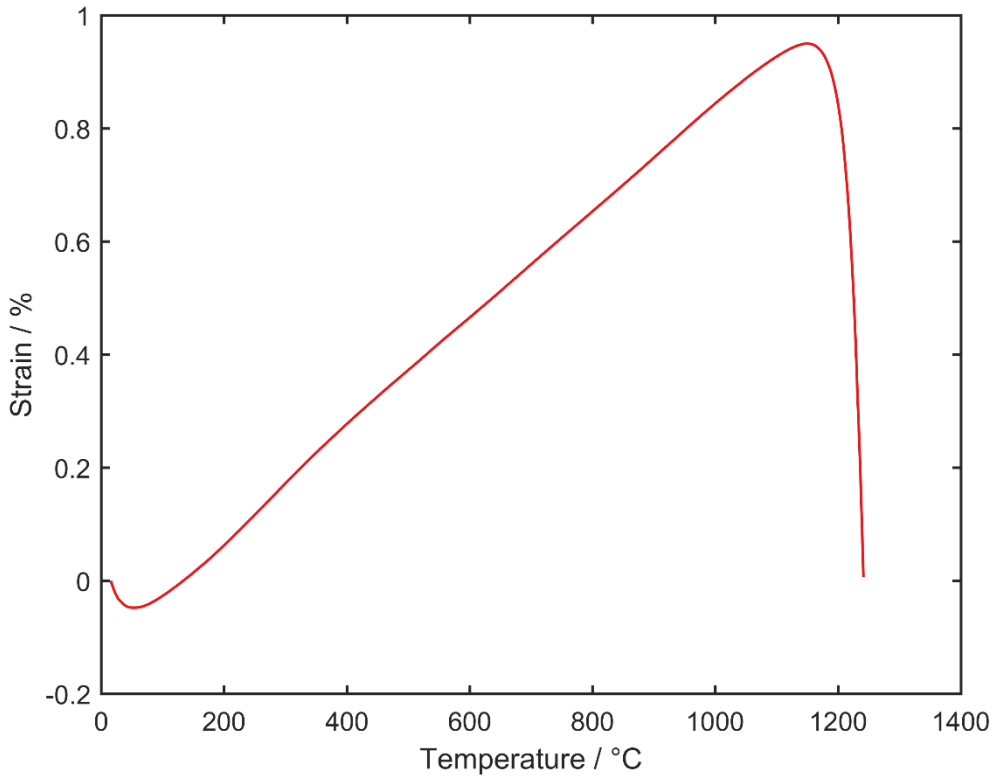

Figure 2.4: Dilatometer trace of linear expansion as a function of temperature. The peak is indicative of T_g since this defines the point where the material stops thermally expanding and begins contracting due to softening.

2.3.2. Particles

The alumina particles used were obtained by vibrating alumina powder within a stack of sieves for one hour, and then collecting the particles in the range 45–53 µm. The actual particle size was significantly smaller than expected, a likely reason for this being due to clumping, perhaps due to moisture within the powder. A particle size distribution was acquired using the Malvern Mastersizer/E and the results shown in Figure 2.5 indicate an average particle size of around 7 ± 3 µm, with no particles with a larger diameter, in the range 45–53 µm, as was expected. This was confirmed by measurements taken of particle diameters on SEM images. Nevertheless, the particles were deemed suitable for the first trials of manufacturing miniature DPF filters.

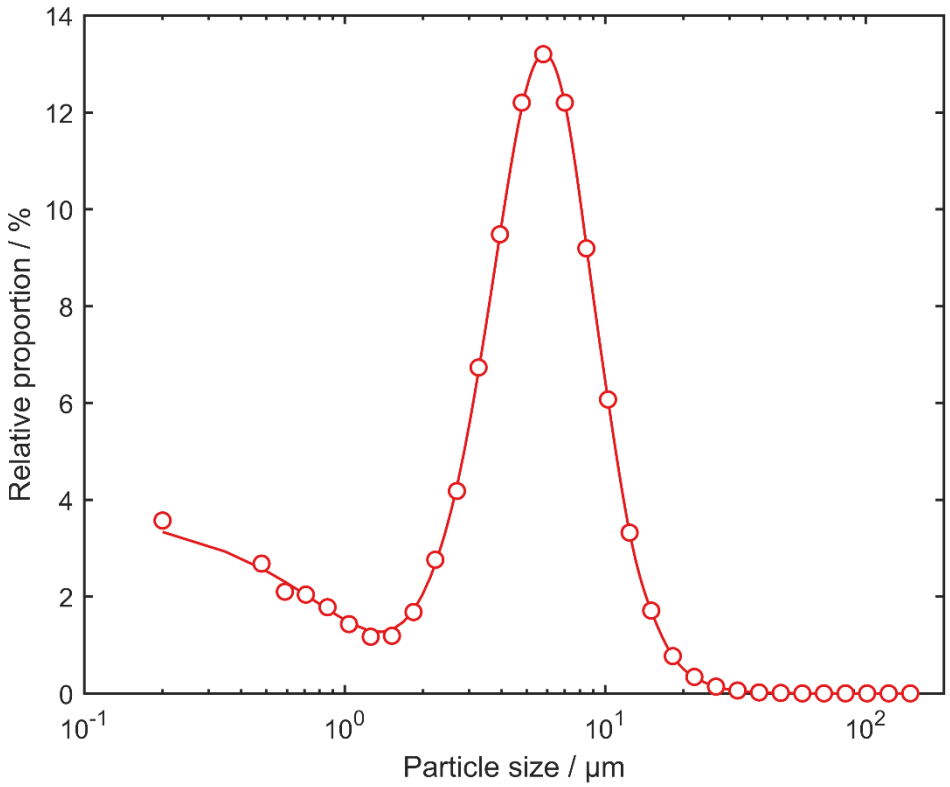

Figure 2.5: Particle size distribution of alumina powder used for the manufacture of miniature DPFs. The mean particle size is 7 µm.

To confirm the composition of the particles they were examined under a JEOL JSM-5500LV SEM and were verified by EDX to be composed (99%) of aluminium and oxygen; no other significant impurities were detected.

2.4. Second-generation materials

Whilst the first-generation of materials were used to obtain some preliminary results for particle-fibre composites, it was clear that these materials were far from optimal. The first problem was the difference in size between the fibres and particles. It was hoped that the fibres would be able to create some space between particles, whilst increasing the surface area for improved filtration. With particles of diameter 7 µm and fibres of diameters up to 15 µm, the particles ended up filling gaps between fibres instead. To achieve the desired effect, the particle size should be significantly larger than the fibre

diameter. Secondly, the amorphous nature of the fibres is not desirable. For a DPF application, temperatures can reach over 1000 °C during a drop-to-idle condition during regeneration. This would be close to the T_g value of the fibres, and therefore the fibres are not thermally stable. These major problems, as well as smaller problems such as a large range of fibre diameters, necessitated the use of a second-generation of materials.

2.4.1. Fibres

Fibres better suited to DPF usage were procured from Saffil®, supplied as a chopped fibre mat. During the production process, the shot is removed, and so this presented less of an issue than for the amorphous fibres. Analysis under the SEM showed that the fibres had a smaller and more uniform diameter, with a value of 3.7 ± 1.0 µm. These fibres are shown in Figure 2.6, after grinding, which is covered in more detail in Section 2.5.1.

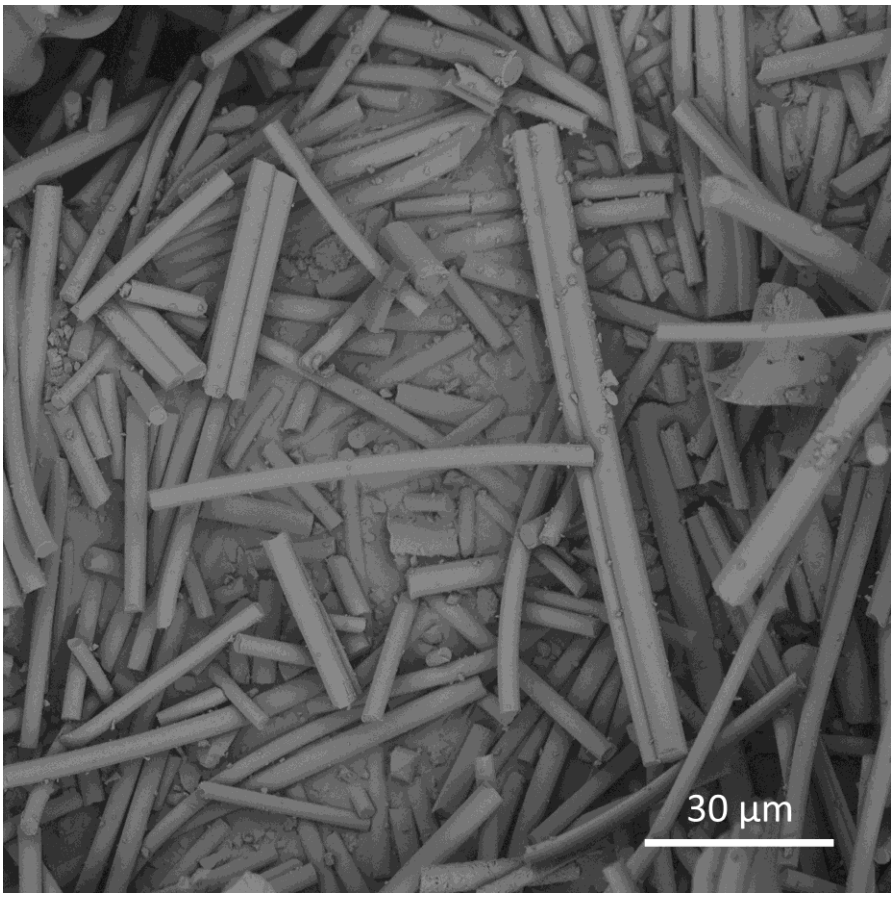

Figure 2.6: Secondary Electron image of the second-generation fibres. The fibre diameters were much more homogeneous and there were no shot particles.

A close-up of the end of a fibre can be seen in Figure 2.7. It is evident that an individual fibre consists of many grains fused together during manufacture in a solution extrusion technique.

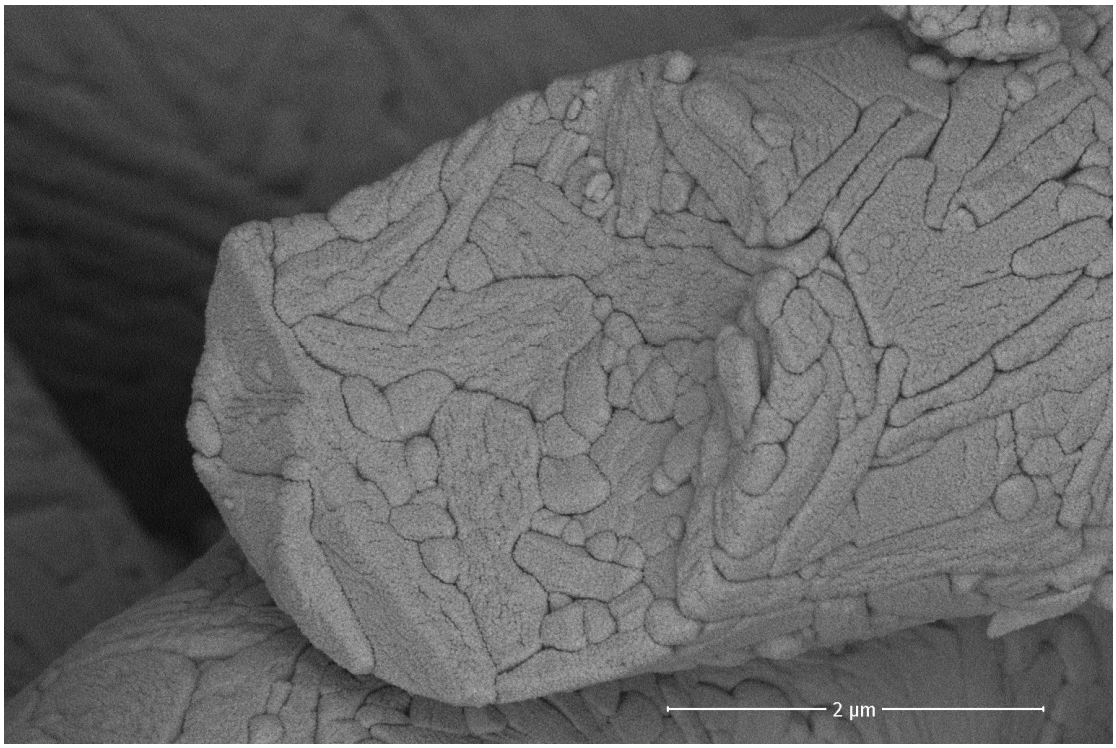

Figure 2.7: Close-up of a second-generation fibre captured by the back-scattered detector. Each individual fibre is formed from an assembly of fused Al_2O_3 grains.

These fibres have been studied in detail by Clyne *et al.* [145]. However, some basic properties were measured in the current work, to ensure that the material was identical to that investigated 30 years ago. XRD was used to determine the phases present in the material. For these fibres, sharp crystalline peaks were observed, indicating high crystallinity. When compared to the international crystallographic database, it was clear that the majority of the material was δ-Al_2O_3 [146] and α-Al_2O_3 [147], with any other phases being present at very low levels, as shown in Figure 2.8.

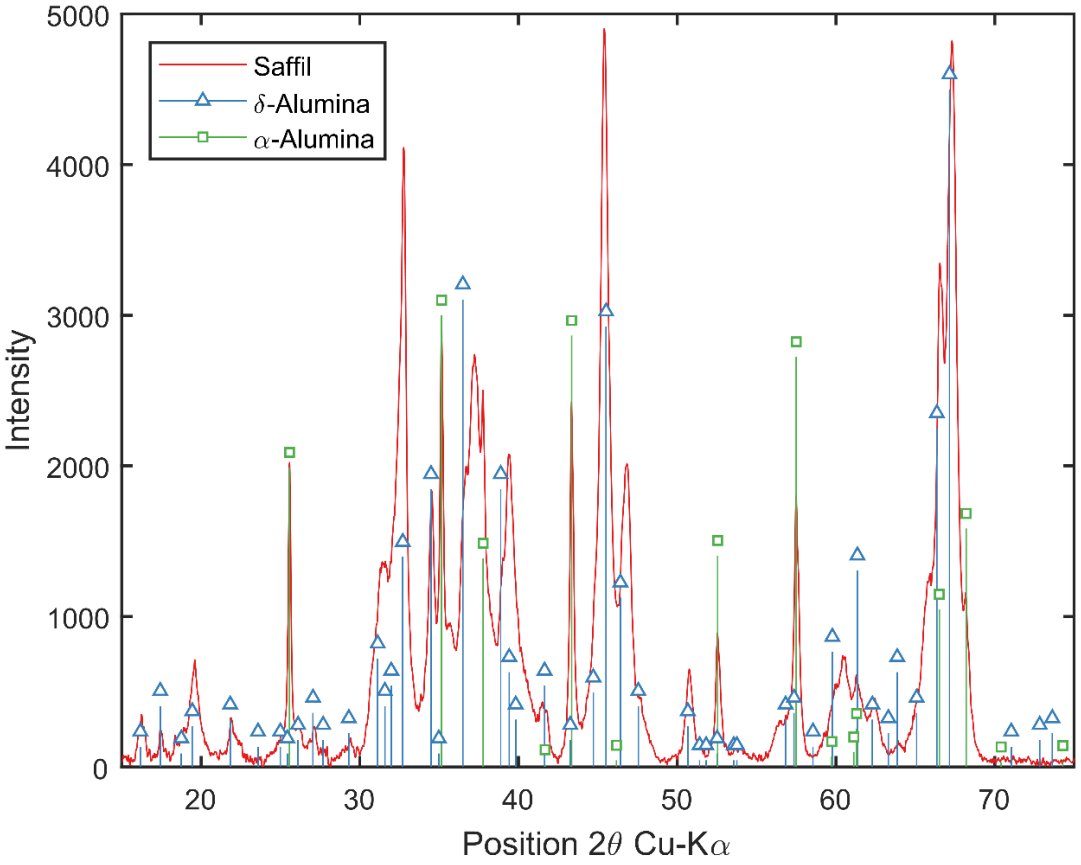

Figure 2.8: XRD trace of Saffil fibres, showing only crystalline peaks indicative of the δ-Al_2O_3 structure (blue lines) and α-Al_2O_3 structure (green lines).

This is in agreement with Clyne *et al.*, who found that the Saffil fibres were composed of a polycrystalline structure of predominantly δ-Al_2O_3. The addition of about 3–4% SiO_2, distributed throughout the δ-Al_2O_3 phase, stabilises the δ-Al_2O_3 crystal structure against transformation (at high temperature) to α-Al_2O_3 and also tends to inhibit coarsening of the fine (50 nm) grain size. The fibres are effectively free from porosity, and have excellent thermal stability up to 1200 °C [145].

2.4.2. Particles

In addition to the Saffil fibres, more suitably-sized alumina particles were required, such that the particle diameter was significantly greater that the diameter of the fibres (3 µm). Alumina powder of a larger diameter was sourced (Plasmalloy AI -1010 Spray

Powder) and a particle size distribution measurement confirmed a mean particle size of 30 µm. This is shown on Figure 2.9, plotted in addition to the original alumina particle size distribution for comparison. This alumina particle size offers considerable benefits over the previous size, although it is perhaps still slightly too small. However, these particles are considered large for conventional sintering, and so large pores will be retained.

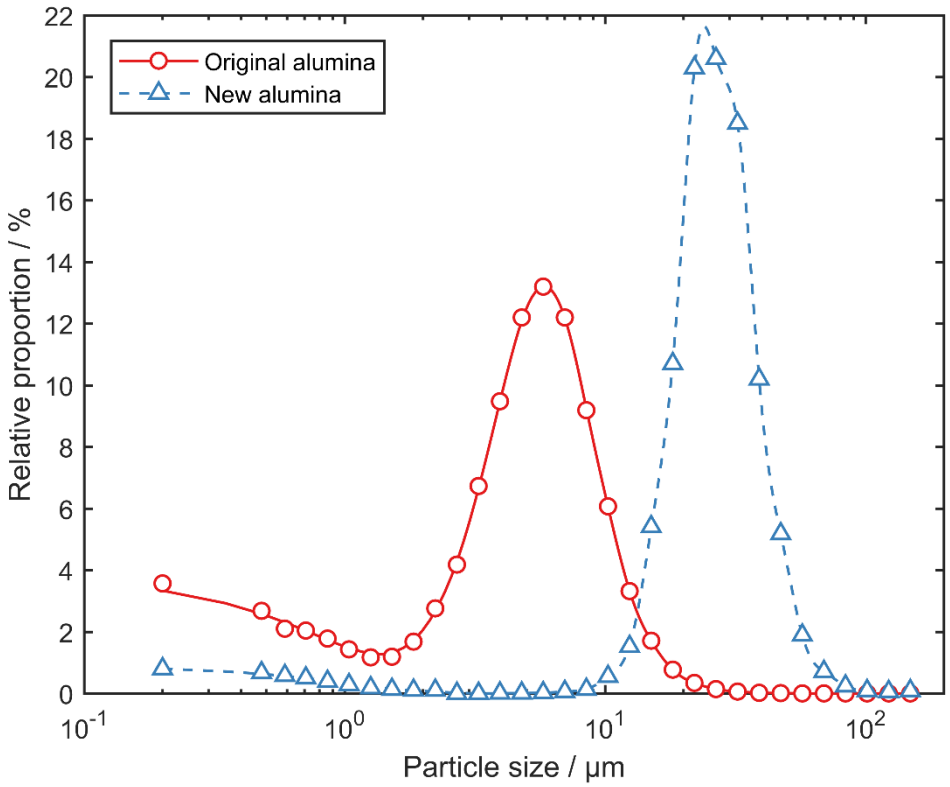

Figure 2.9: *The particle size distribution of the new alumina powder source (blue), and how it compares to the particle size of the original alumina (red). The new particle size is much more suitable, being much larger than the Saffil fibre diameter.*

This particle size distribution was verified by analysing the particle sizes in SEM images such as in Figure 2.10. The composition was confirmed to be alumina using EDX.

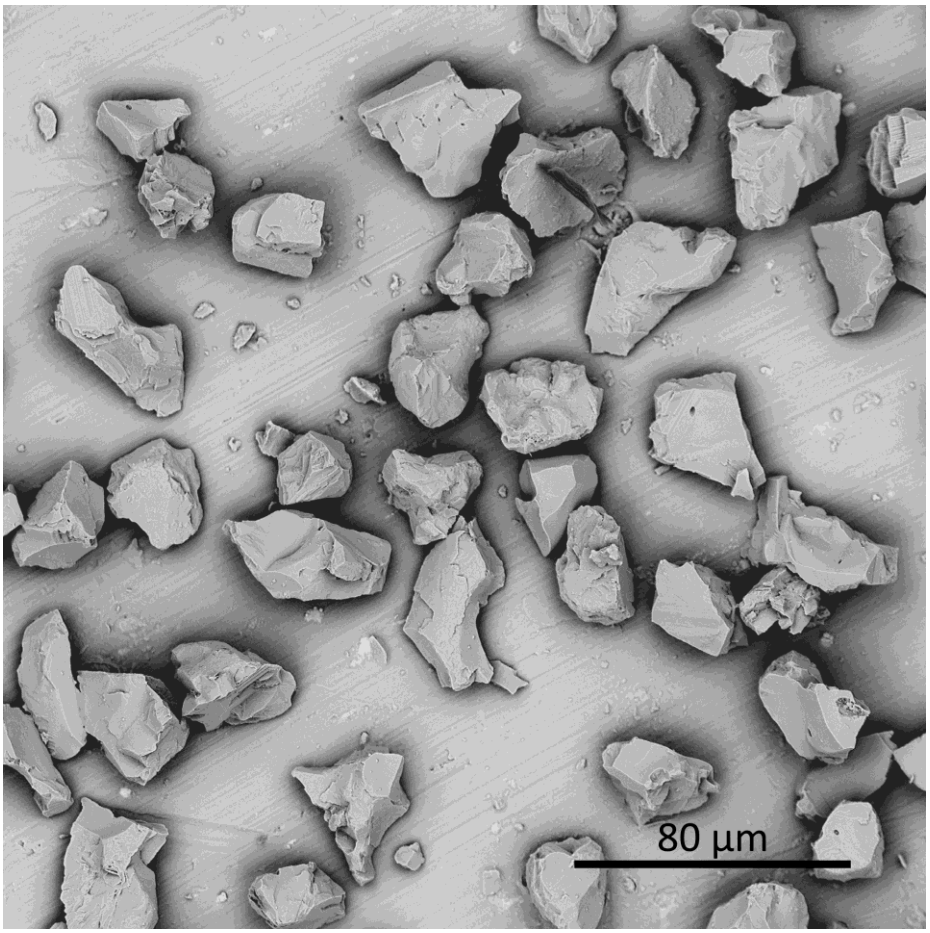

Figure 2.10: Backscattered detector image of the second-generation particles. The mean diameter was found to be 30 µm.

2.5. Preparation of samples

2.5.1. Grinding of fibres

The Saffil fibres used in the second-generation materials were received as a loose chopped fibre mat, with fibre aspect ratios (length /diameter) exceeding 1000. These fibres needed to be shortened since the long fibres would remain bundled together, rather than separating out the particles in a composite material. The easiest way of consistently reducing the fibre length was by ball-milling the fibres. A DECO All-Direction Planetary Ball Mill machine was used for this purpose. The milling time was an important consideration in producing fibres with the correct aspect ratio. Too little milling would

result in the fibres still being bundled tightly into a mat; too much milling would turn the fibres essentially into powder, rendering their inclusion as redundant.

The planetary milling speed was set constant at 300 rpm, and the number and diameter of the alumina balls added to the 1.5 L alumina container were also kept constant at 200 and 10.75 mm respectively. The fibres and balls were added in layers such that the balls were distributed throughout the container. There were five layers of balls, separated by four layers of fibres, with each layer of fibres containing 5 g of fibre mat, giving a total of 20 g of fibres per batch. Up to four containers could be loaded into the ball mill at once, allowing for a maximum of 80 g to be ground in one grinding session. The layering technique was found to improve the quality of the milling in early tests and so was applied to all runs. Preliminary tests also investigated the amount of fibres that could be ground in a single batch, with any more than 20 g producing poor results by not allowing the balls to move significantly in the container.

With everything else kept constant as detailed above, the grinding time was varied to observe the effect on fibre length. The ball mill was set to turn both clockwise and anti-clockwise, alternating direction every minute. The following grinding times were investigated: 3, 5, 10, 30 and 60 minutes. After grinding, the fibre lengths were investigated.

For the case of 3 minutes of grinding, the time was not sufficient to cause the fibre mat to break apart, instead the fibre mat was simply compressed. After 5 minutes, the fibres were broken up sufficiently such that the fibres were no longer in a solid mat but formed much smaller clumps. With increasing milling time these clumps became smaller, until after 60 minutes of grinding the material was indistinguishable from a powder. The fibres were observed under an electron microscope, and for each milling time a fibre length distribution was obtained by measuring the fibre lengths on many images. The distribution of fibre lengths is shown in Figure 2.11 and example SEM images are shown in Figure 2.12 for the various grinding times. Fibre lengths were not measured after 60 minutes of grinding as the fibres were ground to particles by this point.

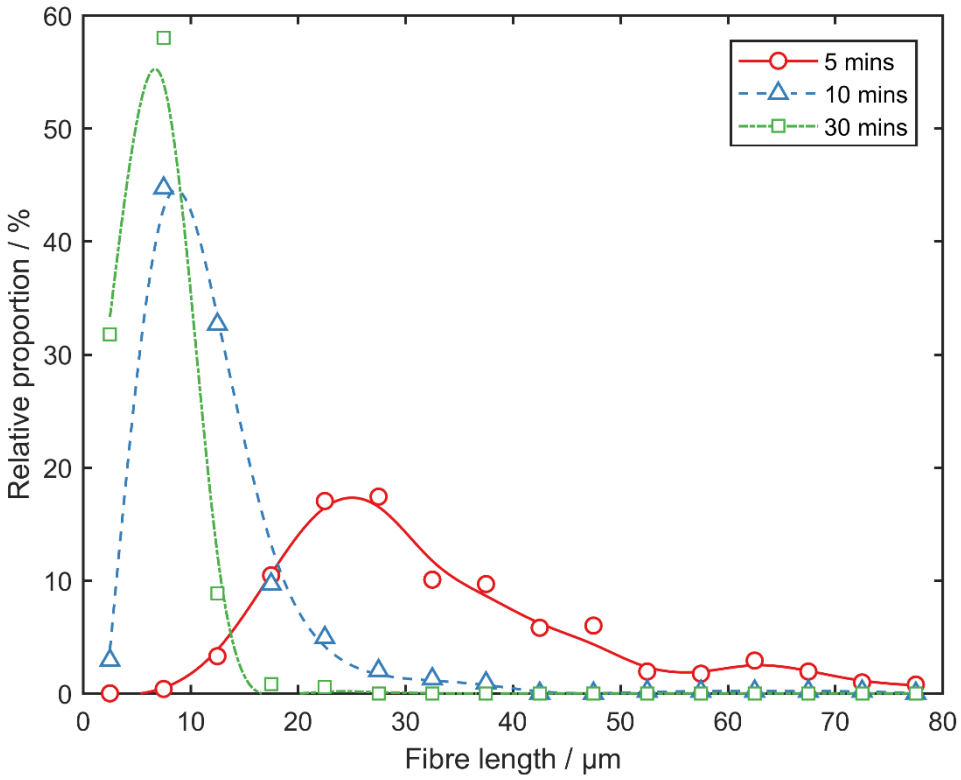

Figure 2.11: Variation in Saffil fibre length with ball milling time. A fibre length of approximately 30 µm is required, and so 5 minutes is an adequate milling time.

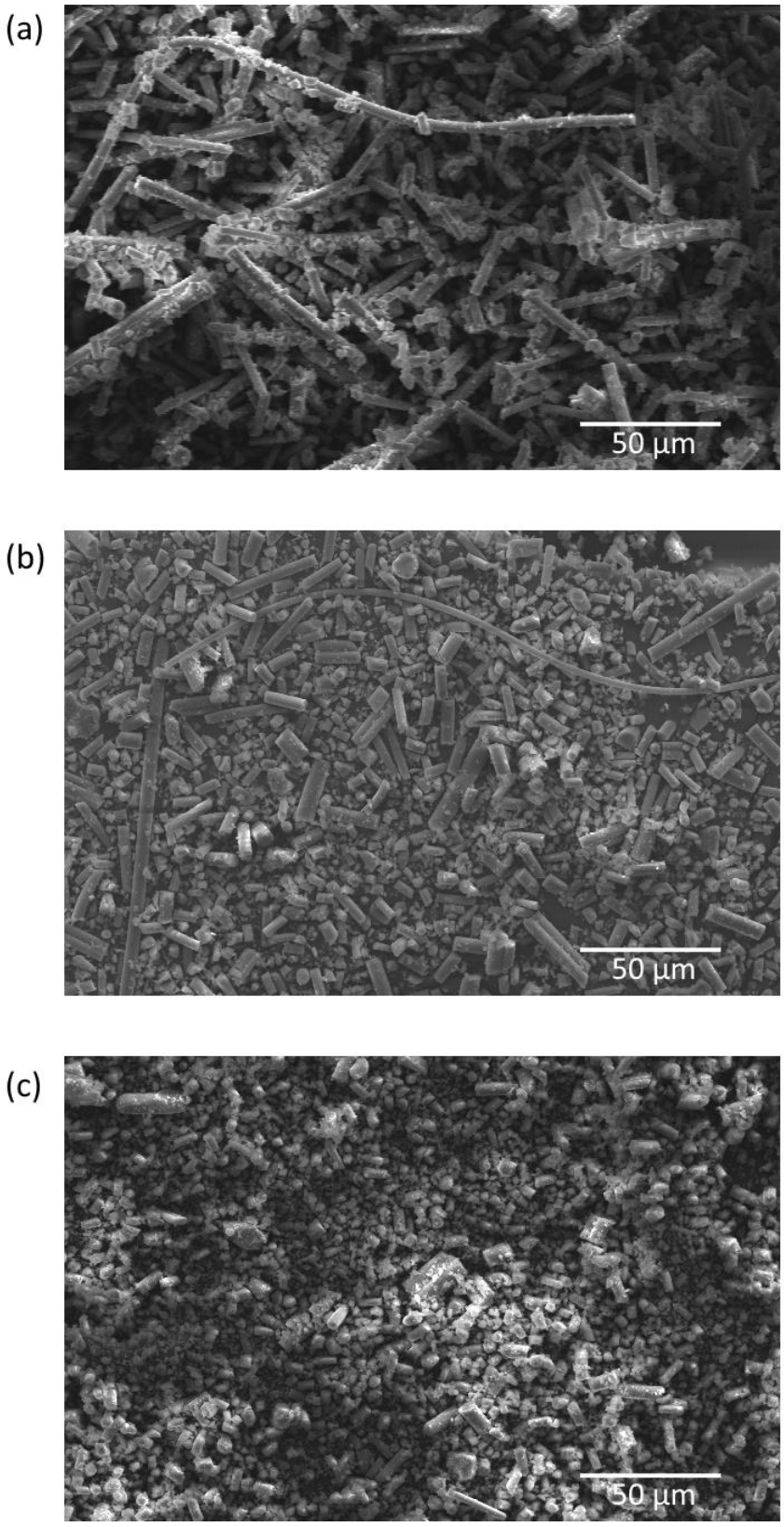

Figure 2.12: SEM images of Saffil at the same magnification for (a) 5, (b) 10, and (c) 30 minutes of milling. After 30 minutes, the fibres have become a powder.

It was predicted that to experience any benefit from adding fibres a suitable aspect ratio would be around 10 or higher, such that the fibres do not simply behave as smaller particles filling gaps between larger particles. As the Saffil fibres have a diameter of 3 μm, this means a fibre length of 30 μm is desirable. It is evident that after just 10 minutes the fibre lengths are much smaller than this, and so the ideal milling time was determined to be 5 minutes. This milling time is sufficient to break apart the fibre mat into much smaller bundles, but not so much that the aspect ratio is reduced too much. For all experiments using Saffil, 5 minutes of grinding was used.

2.5.2. Mixing of components

The ground fibres were then mixed with the alumina particles in varying proportions. The two phases were bound together using a 10 wt.% Poly(vinyl alcohol) (PVA) (molecular weight 89 000 – 98 000 g mol^{-1}) solution. This solution was mixed using a magnetic stirrer in a sealed container at 90 °C until the solution went from cloudy to transparent. Some preliminary experiments showed that the ideal PVA concentration to add was 2 wt.% (i.e. 20 wt.% of the solution). If too much of the solution (greater than 4 wt.%) was added, the green compacts formed were too wet; if there was too little, the green compacts would not hold together. This binder solution was added to the dry components (alumina fibres and particles), and the resulting mixture was stirred by hand. Often these mixtures were too dry, and so additional water was added until the mixture became a thick paste. The additional water required varied considerably with respect to the ratio of fibres to particles. As fibre content increased, much more additional water was required to form the same consistency of paste. The relationship was approximately linear and is shown below in Figure 2.13.

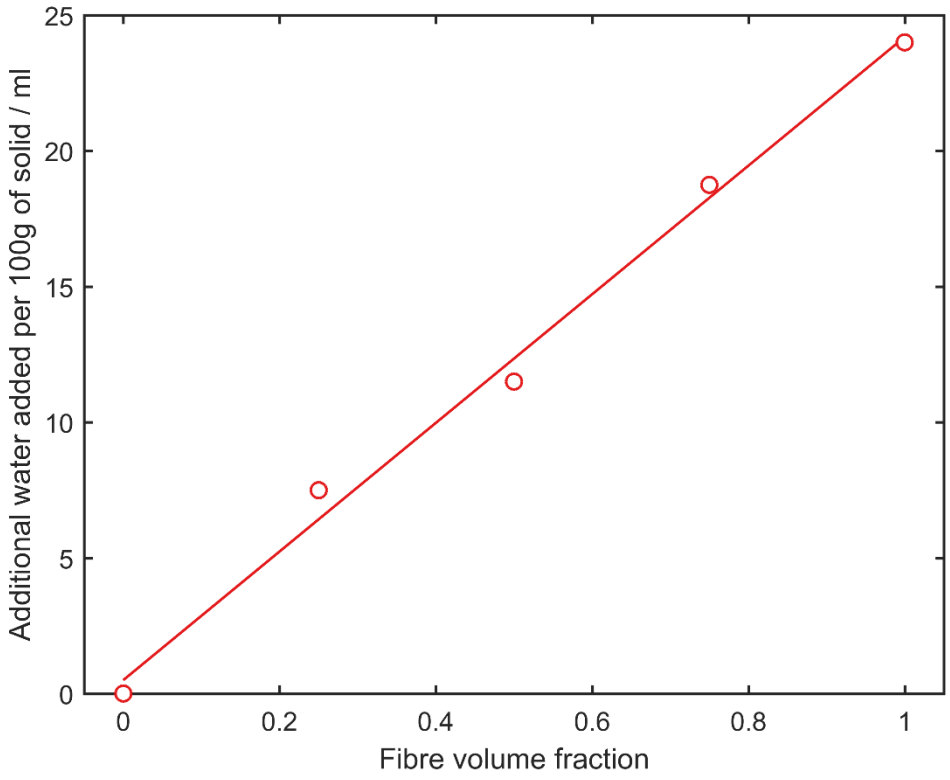

Figure 2.13: Variation of required additional water with increasing fibre volume fraction.

Once a paste was formed, it was distributed into silicon moulds of various shapes depending on the experiment. The two main geometries that were tested were cylinders (diameter: 36 mm, thickness: 15 mm) and cuboids (70 x 20 x 10 mm). The samples in their moulds were triple-bagged inside re-sealable plastic bags, ready for isostatic pressing.

2.5.3. Isostatic pressing

The samples were isostatically pressed in order to consolidate the paste into a green compact which could then be sintered. The press used was a Stansted Fluid Power press. Isostatic pressing was achieved by submerging the sealed sample in oil inside the press chamber and pressurising the oil. The press allowed for control of the pressure and time of pressurisation. These were varied in initial experiments on the first-generation materials, and the outcomes of this experimentation are presented in Section 4.5. For the

second-generation materials, a pressure of 1500 bar was applied for 5 minutes. After pressing, the samples were removed from the chamber and the plastic bags and were then ready for sintering.

2.5.4. Sintering

The green compacts were sintered in furnaces with a temperature range up to 1400 °C. The effect of sintering time and temperature was investigated for the first-generation materials, and the results are presented in Sections 4.3 and 4.4. For the crystalline alumina second-generation of materials, a temperature of 1540 °C would be considered ideal for efficient sintering. However, due to experimental limitations, a temperature of 1400 °C was used. 12 hours was found to be a suitable sintering time, providing adequate handling strength whilst maintaining a high porosity.

During the process of sintering, the PVA binder thermally decomposes, first by the elimination of water and acetic acid, then by the depolymerisation and oxidation of the vinyl chains [148]. At the elevated temperature, the first-generation materials were able to flow, since they were close to their T_g. During this process the softened fibres in contact with one another were able to bond with one another. For the second-generation materials, the binding mechanism was by conventional sintering. This process requires high temperatures, and at 1400 °C the DPFs are at a homologous temperature of 0.7 (the melting point of alumina is 2072 °C [149]). Sintering requires diffusion within the alumina fibres and particles, either by internal or by surface diffusion. The diffusion acts towards the contact points between the components and is driven by a reduction in surface area. During the process of sintering, small necks are formed between the components (and these necks will widen with increasing sintering time), and there is a small volume contraction and porosity reduction. After only 12 hours the necks were still very small, such that the porosity was maintained at a high level.

Figure 2.14 shows the microstructures of three second-generation samples with varying fibre content of (a) 0 vol.%, (b) 50 vol.% and (c) 100 vol.% fibres.

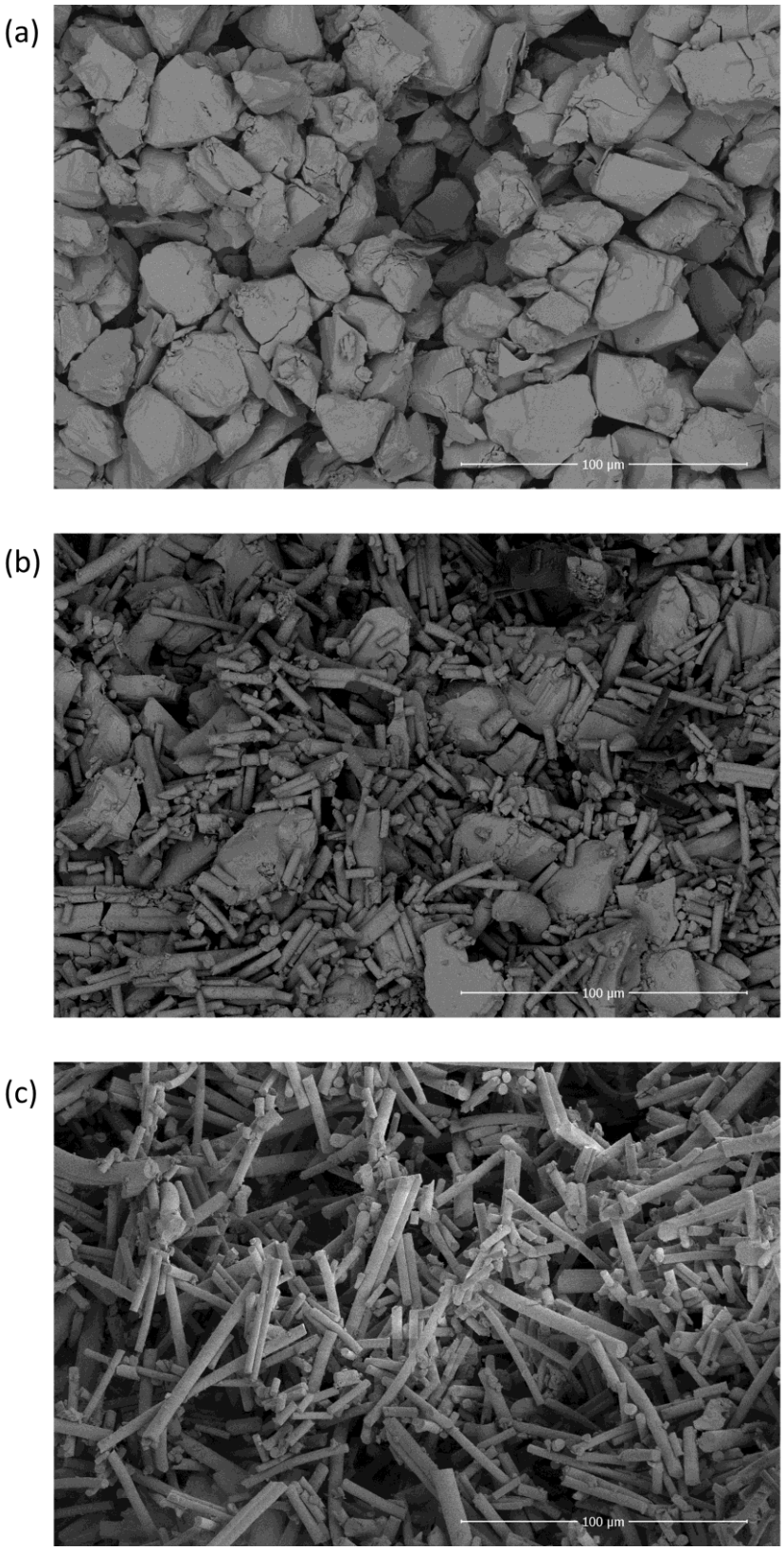

Figure 2.14: Microstructures of the fracture surface of three sintered composites containing (a) 0 wt.%, (b) 50 wt.% and (c) 100 wt.% fibres.

2.6. Note on fibre volume fraction

The filters created in this work can be considered to be three-part composites, containing fibres, particles and voids (porosity). The void content is considered in porosity experiments. For many other tests the ratio of fibres to particles is altered, and this is measured throughout the work as a "fibre volume fraction", as is standard for work on composite materials. However, this could become ambiguous, for example: a 50 vol.% fibre sample could be interpreted as half of the total volume being fibres, whereas actually it refers to a sample consisting of equal volume proportions of fibres and particles, regardless of porosity level. The fibre volume fraction is hence a measure of the proportion of solid phase that consists of fibres, and not as a proportion of the total volume (inclusive of pores). Since the particles and fibres have the same density, the volume fraction (as defined above) and weight fraction can be used interchangeably, but by using weight fraction in the discussion, any ambiguity is removed.

3. Experimental Techniques

3.1. Porosity

The porosity of the samples was tested using a simple hydrostatic weighing experiment by measuring the mass gain as the sample was submerged under water. The samples absorbed water into the open porosity, meaning that their effective density increased, as trapped air was replaced with water, reducing the effective volume of the sample. The initial mass of a sample with air-filled pores immediately upon submersion, m_0, was calculated theoretically by considering the dry mass, and the ratio of densities of water and the miniature filter:

$$m_0 = m_{dry}\left(1 - \frac{\rho_{water}}{\rho_{filter}}\right) \tag{3.1}$$

The density of the filter was calculated by measuring the dry mass and dimensions of each sample. The mass change was monitored with respect to time for approximately 72 hours, after which time the mass had settled to a constant value, m_{sub}. After this time, all the surface-connected porosity had been infiltrated with water. From the total mass change, it is possible to work out the volume fraction of connected porosity, ε:

$$\varepsilon = \frac{(m_{sub} - m_0)/\rho_{water}}{V_{filter}} \tag{3.2}$$

where the numerator in this equation is the volume of water that has penetrated into the sample, and V_{filter} is the total volume of the sample measured when dry. Once the measurements of porosity had been made, the samples were removed from the water and allowed to dry, before being tested for permeability.

3.2. Permeability

The permeability was measured by forcing nitrogen through the filter, such that a constant pressure gradient was developed across the filter. The sealing of the sample within the apparatus is shown in Figure 3.1. The lowest measurable pressure difference that could be obtained by this set-up was 100 mbar, which would be a high pressure difference in an actual DPF application, where regeneration would usually occur around this pressure. The steady state rate of gas flow through the filter was measured using the displacement of water from an upturned graduated cylinder, with a capacity of 100 ml. The time taken for the gas to displace 88 ml water was recorded (from the 10 ml mark to the 100 ml mark, reduced by 2 ml due to the pipe going up the cylinder).

Darcy's Law relates the flux Q ($m^3\ m^{-2}\ s^{-1}$) to the specific permeability κ (m^2), viscosity η (Pa s) and the pressure gradient $\Delta P/\Delta x$ (Pa m^{-1}):

$$Q = \frac{\kappa}{\eta}\frac{\Delta P}{\Delta x} \tag{3.3}$$

This can be manipulated to produce the following equation for permeability:

$$\kappa = \frac{V d \eta}{t A \Delta P} \tag{3.4}$$

where V is the volume of water displaced, d is the thickness of the filter, η is the dynamic viscosity of nitrogen (1.76 x10^{-5} Pa s [150]), t is the time taken to displace the water, A is the surface area of the filter and ΔP is the pressure difference.

The permeability is expected to relate to the porosity via the empirical Carman-Kozeny equation:

$$\kappa = \frac{\varepsilon^3}{\lambda S^2} \tag{3.5}$$

where S is the specific surface area ($m^2\ m^{-3}$), and λ is a dimensionless constant with a value of about 5 [48]. This is a simplified form of the equation, and its derivation is analysed later in this work in Section 6.3.

Of course, there is a problem that some of the nitrogen could come out of the sides of the cylinder, rather than passing straight through. This was solved by coating the outside of the samples with a quick setting two-part epoxy resin, covering the sample sides, and 1 mm in from the upper and lower faces. A thin cylindrical section of rubber was also stretched over this same area, and was found to help with the sealing. Difficulty also arose with sealing inside the sample holder (Figure 3.1). This was solved by using two soft silicone O-rings on either side of the sample, cushioning the sample from the hard O-rings. The sample holder was tightened until the hissing noise of nitrogen escaping from the sides of the sample became inaudible.

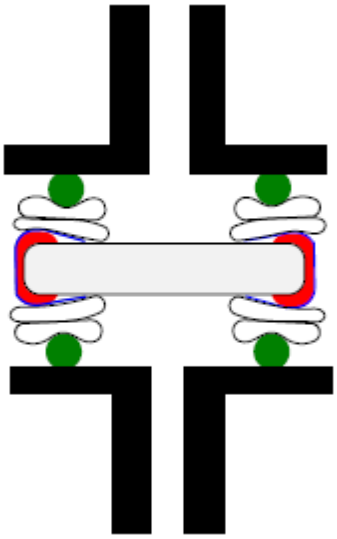

Figure 3.1: The set-up of the permeability experiment. The grey rectangle is the cross-section of the cylindrical filter, the edges of which were covered in a two-part epoxy (red), and then covered with a thin rubber sheath (blue). Four soft silicone O-rings (white) were used to protect the delicate specimens from the hard rubber O-rings (green). This was contained within the (black) frame of the permeability rig, the two sides of which were clamped together with screws. All of these measures ensured full sealing of the sample into the apparatus.

3.3. Extrusion

All of the previously mentioned tests of processing conditions were implemented on small standard DPF specimens – i.e. cylinders with a diameter of 30 mm and a height of

approximately 5 mm. These specimens were created using the method described fully in Section 2.5. However, it should be recognised that this method of manufacture is very different from that by which commercial DPFs are manufactured. Full-sized DPFs are manufactured using an extrusion process and, since the current work involves fibres that are likely to become aligned in the direction of extrusion, the effect of such a manufacturing route should be tested. For this process, a press with a 5 tonne hydraulic ram was modified into an extrusion rig by drilling a tapered hole through a base plate, as shown schematically in Figure 3.2.

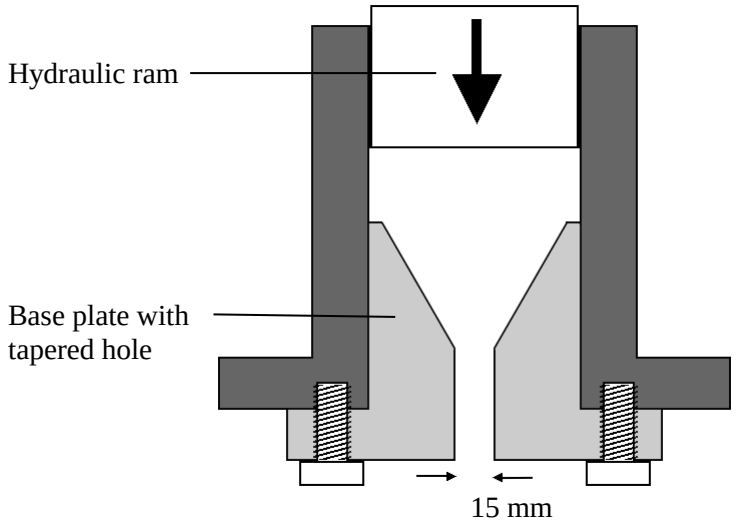

Figure 3.2: Schematic of the extrusion press.

Two compositions of material were prepared for extrusion, one with 67 wt.% fibres, and another with 20 wt.% fibres. A relatively large quantity of material was needed in each case, since the whole space within the extrusion die must be filled; the minimum volume required was 1.8 x10^5 mm^3. The two compositions were made with the minimum volume of additional water necessary to form a thick paste, and this was then extruded through the rig. The diameter of the exit hole of the die was 15 mm, and product lengths of around 70 mm were extruded. The process of extrusion tended to squeeze water out of the material, such that the extruded lengths had a much higher water content than the whole material, whereas material left in the die was considerably drier. This high water content made handling of the extruded cylinders difficult, since they would easily lose their shape. To solve this problem, the cylinders were extruded into plastic shells of

internal diameter equal to that of the die exit (15 mm). The plastic shells could then be cut open, and the extrudate left to dry. The extruded cylinders were then sintered at 1100 °C for 3 hours.

3.4. Tomography

Since it was difficult to experimentally measure a filtration efficiency without a full-size DPF filter being made, tomography was trialled as a potential technique to quantify the filtration efficiency by capturing a three-dimensional reconstruction of the internal pore structure.

The computerised tomography (CT) scanner that was used for this application was a SkyScan 1272, offering a resolution down to 0.5 µm. Since the fibres in the samples had a diameter of 3 µm, this necessitated that the highest resolution was used.

The CT scanner operates by passing X-rays through the sample. Where there is material in the path of the X-rays, the signal is attenuated, such that a detector on the far side of the sample would detect a darker region. Thus, a single image is formed showing the inside of a sample: where there is no material, it is bright; where there is most material it is dark. The exposure time for generating the image can be controlled such that the full range of greyscale values can be used, typically an exposure time of about 8 seconds was used for the DPF samples.

Of course, this is not enough information to determine the 3-dimensional internal structure of the material; there is no indication of depth of the material. To calculate exactly where the particles and fibres are in 3-dimensional space the sample must be rotated, and a new image taken. This must be done in small increments and for a full 180 ° around the sample. A typical rotation step was 0.08 °, requiring a total of 2250 images to be taken. For each of these images, frame averaging was used. This means that a number of images (often 4) were taken for each rotation step, and the images were averaged; this was essential for noise removal.

In order to get to the highest resolution, only a small sample could be scanned, since the full width of the sample must be visible in each picture for reliable reconstruction. Although it is possible to take double or even triple width panoramic images, the increase is scan time was too large and would not offer much more information. A single width scan therefore limited the size of the sample to around 1–2 mm in all dimensions. Binning of pixels is also a feature, but naturally for the highest resolution no such averaging effects were used.

The camera position automatically adjusts itself based on the magnification of the scan. For the highest magnification, the camera is in the far position, with a camera to source distance of 273 mm (the object to source distance was 13.7 mm). The voltage and current of the source could be manually changed, but the automatically selected values of 25 kV and 135 µA provided good contrast of the sample against the background. For more X-ray transparent samples, a filter could be introduced into the beam line, but this was not necessary for the DPF samples.

The output from the CT scanner was a series of 2250 images showing the rotational images about a vertical z-axis. For further analysis this needed to be converted to a stack of parallel images of the x-y plane. The software used was NRecon, provided by Bruker. In this software, the rotational images were converted and the greyscale was inverted, such that the material appeared bright against a dark background. Some artefacts from the scan could be removed at this stage, specifically ring artefacts and beam hardening. Ring artefacts are generated when there is dirt on the detector. This should mostly be accounted for during calibration, but any dust that lands on the detector will be detected in every rotational image, thus causing a ring when converted to an x-y image. The software can detect these rings and remove them by comparing them to surrounding pixels. Beam hardening appears as a shadowing effect of the material, often most obviously observed at sharp corners. Again, the software can account for these artefacts and diminish their presence. Figure 3.3 shows these artefacts before and after being treated by the software.

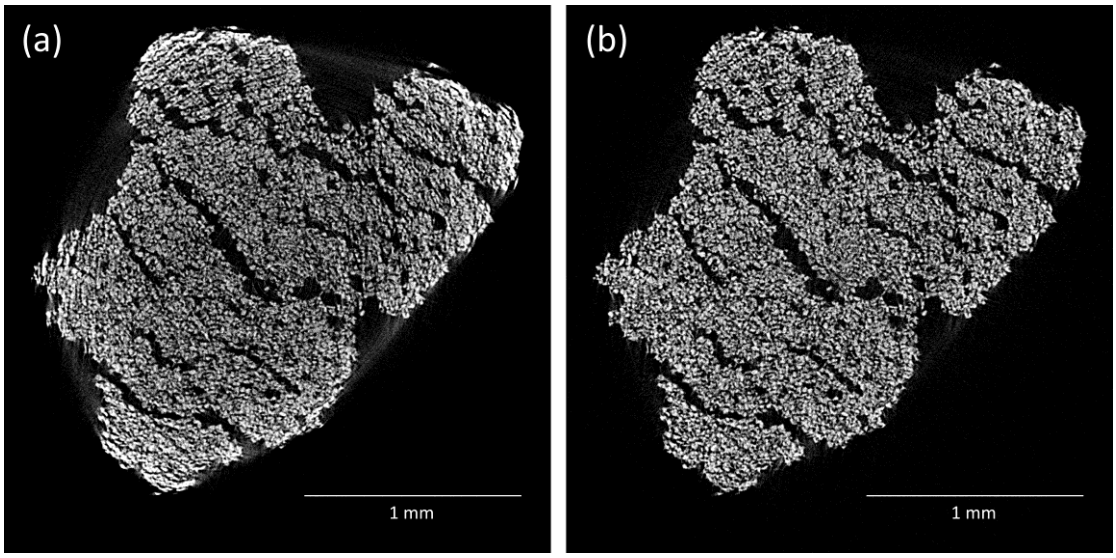

Figure 3.3: X-Y cross-section of 0 wt.% fibre sample, showing the sample (a) before and (b) after ring artefact reduction and beam hardening correction. The differences are most clear around the edges of the sample.

With the images now converted into parallel x-y plane slices, they can be imported into various other software. For quick visualisation of the whole structure, the program CTvox was used, and for more quantifiable results and mesh generation, ScanIP was used.

3.5. Fracture toughness

Fracture toughness was measured using an Charpy impact test. In preparation, samples of approximate dimensions 70 mm x 20 mm x 10 mm were scored at their half way mark to a depth of 2 mm as shown in Figure 3.4b below. The samples were subsequently mounted in a geometry as shown by the schematic in Figure 3.4a.

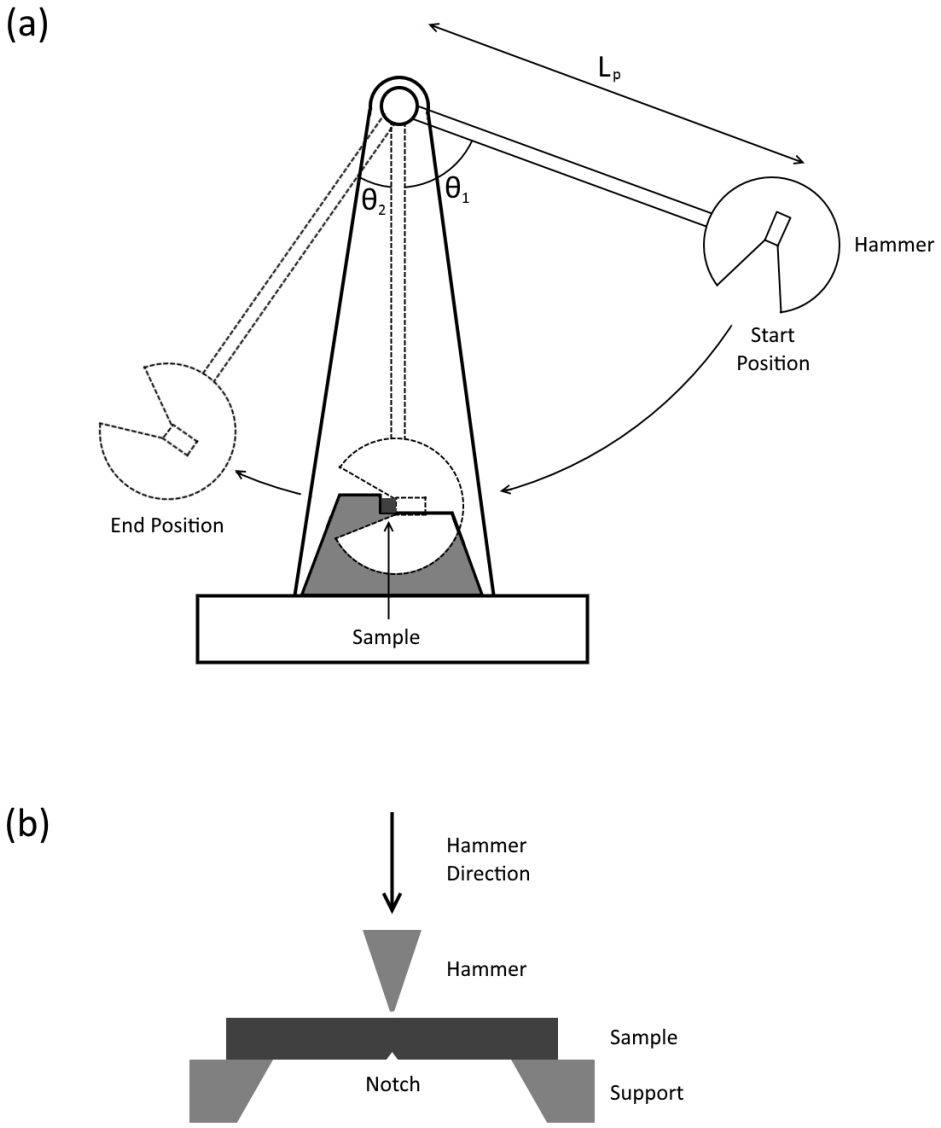

Figure 3.4: Schematic of the Charpy impact test, showing (a) side view, and (b) overhead view.

A pendulum arm with known length and mass is released from a known angle. The arm descends, hits the sample and fractures it into two equal parts. In all cases, the crack propagation was initiated at the scored mark, where tensile stresses would open the crack up in a mode I configuration. After cracking, the pendulum continues to swing upwards, unhindered by the fractured material and with minimal friction generated in the smooth bearings of the pivot. The pendulum then reaches a maximum at the far side, at a smaller

angle than the initial angle of release. These angles can be used to calculate the initial and final potential energy of the pendulum. The difference between these energies is that which has been lost by the pendulum, and thus used during crack propagation. The equation used to calculate the absorbed energy (per crack area) is given in Equation 3.6, which can be derived from the geometry of the schematic in Figure 3.4:

$$G_c = \frac{MgL_p(\cos\theta_2 - \cos\theta_1)}{A_{crack}} \tag{3.6}$$

where M is the mass of the pendulum (kg), g is the acceleration due to gravity (m s^{-2}), L_p is the length of the pendulum (m) (measured from the pivot to the centre of mass), A_{crack} is the crack area (m^2) and θ_1 and θ_2 are the initial and final angles of the pendulum, measured from vertical, respectively.

To improve the accuracy of the results, and to account for the friction of the equipment, test runs were carried out with no samples in place; the initial and final angles were the same and therefore any systematic errors due to the apparatus were deemed to be negligible. It was apparent that the smallest error in the energy would be at the position where the initial and final angles were as close to 0° or 180° as possible. At these points, a small difference in potential energy would lead to a considerable change of angle, larger than that which would be observed at 90°. Being porous ceramics, the samples were not tough, and so the measured energy changes were small. For this reason, a reasonably low release angle was chosen (40°), such that the pendulum still had ample potential energy to crack the samples, but the energy absorbed formed a considerable and easily measurable fraction of the total energy of the swinging pendulum.

It is important to note that the values of fracture energy obtained using this method may be higher than expected. Testing of such properties should normally be done under conditions of plane strain, requiring a large sample (so the crack is not close to the back surface). However, with small samples, the conditions are likely to be closer to plane stress, which can lead to substantially higher energy absorption [87].

Another consequence of these porous ceramics was a significant scatter in data due to varying amounts of micro-cracking already present in the sample before impact and the

distribution of pores within. To account for this, many samples (at least 15 per fibre content) were tested, such that an average could be determined. The fibre content of the samples was varied, and so data detailing how the fracture energy varied as a function of fibre content were obtained.

3.6. Stiffness

3.6.1. 4-point bend test

To predict how the thermal shock resistance might vary as a function of the fibre content, it was necessary to measure the variation of stiffness with respect to fibre content. The first method used to determine the stiffness of the samples was a 4-point bend test. This was done by manual loading (on the first-generation materials) and by tensometer loading (on the second-generation materials). Both experiments employed the set up as shown in Figure 3.5 below.

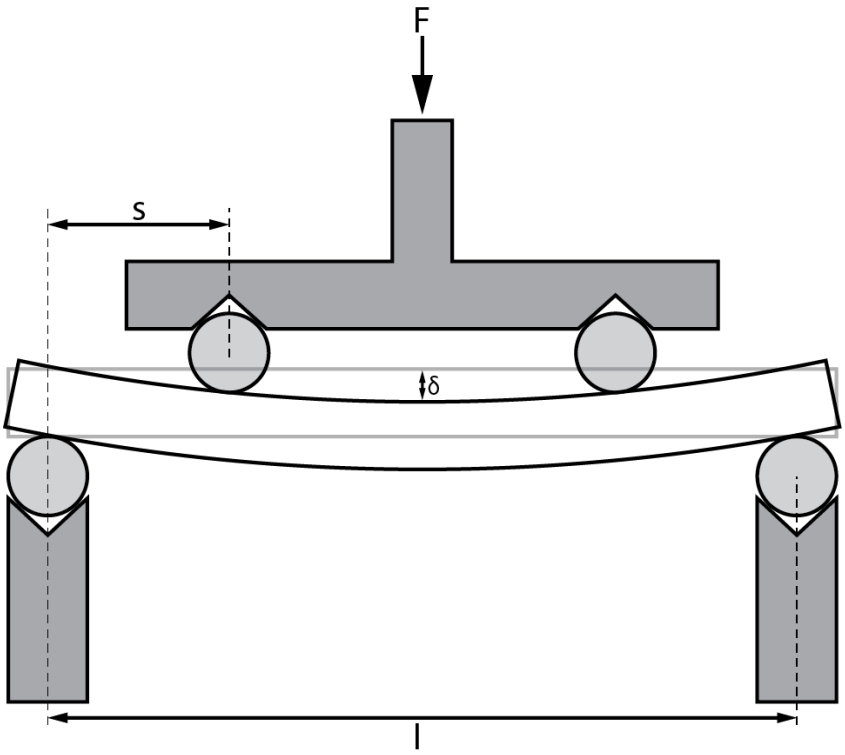

Figure 3.5: Schematic of four-point bend test rig.

Manual loading

The first-generation filters used in the permeability tests were cut using a scalpel blade, and ground on grinding paper, such that a rectangular sample of approximate dimensions 30 mm x 10 mm x 2 mm was formed. This could then be loaded into a four-point bend test rig to obtain a measurement of stiffness. A load-controlled system was used, adding a mass of 10 g every 120 seconds, up to a maximum mass of 50 g.

Once the filter had been fully loaded, all the masses were removed, and it was verified that the filter returned to the original zero deflection, confirming that any deformation was in the elastic regime.

The deflection of the filter was recorded using a laser micrometer, and the loading configuration is shown in Figure 3.5. The Young's modulus of the material, E, along the length of the rectangular beam can be obtained from the expression for the central deflection in this type of loading:

$$E = \frac{F}{\delta} \frac{s(3l^2 - 4s^2)}{4wh^3} \tag{3.7}$$

where s and l are defined in Figure 3.5, F is the applied load, and w and h are the width and height of the beam respectively. The height was made as uniform as possible and accurately measured (in view of the cube dependency of this value). By plotting a graph of deflection against load, the gradient can be used to obtain a value of F/δ.

Multiple readings were taken for each material, flipping the beam over such that the side that was in tension was in compression in the next test and vice versa, an average was then taken.

Tensometer loading

In this experiment, a Hounsfield 5 kN tensometer was used. The samples with approximate dimensions of 70 mm x 20 mm x 10 mm were used, and the experiment was set up as shown by the schematic in Figure 3.5.

The samples were loaded in displacement control, at a rate of 0.5 mm min^{-1}. The displacement of a linear variable differential transformer (LVDT) placed underneath the centre of the sample and the load applied by the machine (measured by the load cell) were recorded and plotted in real time. After the initial relaxing of the system, and once a reliable straight line had been obtained, the load was released, so as not to crack the brittle samples. The gradient of this force-displacement line could then be used to calculate the stiffness, again using Equation 3.7.

Performing such a test on brittle specimens necessitated care such that the maximum load applied did not exceed a low sample-dependent threshold where cracking would initiate. Consequently, as soon as a reasonable gradient could be seen the loading was stopped and released. Most samples were tested in the elastic regime, although several samples exhibited hysteretic behaviour on unloading, indicative of plastic work in the form of micro-cracking; the data collected from these samples were excluded from further analysis. Worse still, some samples cracked almost immediately upon loading, without any indication of a force-displacement gradient. It was found that this test was extremely sensitive to the top and bottom edges of the samples being as close to parallel as possible. Any deviation away from parallel resulted in regions of localised stresses which caused the macroscopic fracture of the samples. When fracture occurred, it was consistently found to be either directly underneath one of the two central cylinders, which can be assigned to the non-parallel surfaces, or in rarer cases, directly in the middle, in this case probably as a result of a statistically weaker sample.

3.6.2. Resonant frequency damping analysis

Whilst the 4-point bend test gave good data about the stiffness, it was decided to check the values using an alternative method. This second method of stiffness measurement was resonant frequency damping analysis (RFDA) which relies on measurement of a characteristic set of mechanical resonant frequencies, related to the object's mass, dimensions and elastic properties [151]. In this experiment, the sample, with dimensions of 70 mm x 20 mm x 10 mm, was supported on fine support threads at the nodes of its fundamental vibration, as shown in the schematic in Figure 3.6.

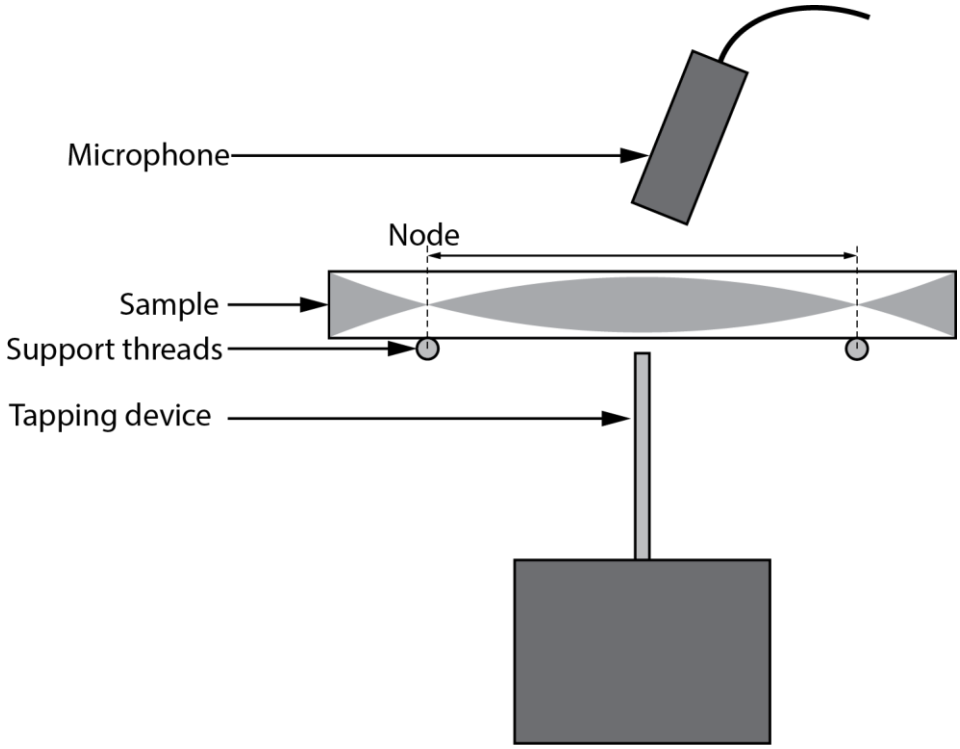

Figure 3.6: Schematic of RFDA testing set-up.

RFDA software was used to pneumatically control a light ceramic impulse device which displaced upwards by around 2 mm, tapping the sample. The sample oscillated, and the vibration was detected by a microphone clamped just above the surface. The microphone recorded the sound generated by the sample for a fixed interval (3 seconds) and then converted the signal to frequency analysis by taking a Fourier transform of the time-based data. This highlighted precise frequency peaks and so the fundamental mode of oscillation can be determined. From this frequency spectrum, the stiffness was calculated according to the ASTM E1786-15 standard [152], using Equation 3.8. This standard defines the impulse excitation technique for homogeneous, isotropic bars of constant cross-section; but success in the literature with two-phase materials [151] is a positive indication of this being a viable technique for the DPF composites.

$$E = 0.9465 \left(\frac{m\, {f_r}^2}{w}\right)\left(\frac{{L_s}^3}{d^3}\right) T_1 \qquad (3.8)$$

In this equation, m is the mass of the sample (g), f_r is the fundamental resonance frequency (Hz), and L_s, w and d are the length, width and thickness (mm) of the sample

respectively. T_1 is a correction factor for the fundamental flexural mode to account for the finite thickness of the sample and the Poisson's ratio. The full equation for T_1 can be found in the ASTM E1786-15 standard [152]. The value of this correction factor is significantly more dependent on the value of L_s/t than on the Poisson's ratio, and becomes important for small aspect ratios. Using values of 7 and 0.21 [153] for the aspect ratio and Poisson's ratio respectively, T_1 is calculated to be 1.131.

As well as being quicker to use, the RFDA offers a significant benefit over the 4-point bend test. Namely, it is a non-destructive test, which does not affect the properties of the DPF material during testing. Although great care was taken with the 4-point bend test to ensure the samples would not be damaged, often a small degree of micro-cracking was evident (noticeable as a decrease in stiffness upon re-measurement), and the number of samples that broke during testing, whilst small, hindered progress. The RFDA, on the other hand, gently taps the sample, which does very little damage at all to the DPF material, so the measurement can be repeated to give a precise and unchanging value of the stiffness.

3.7. Thermal expansivity

To measure the thermal expansivity, a Netzsch DIL 402 C dilatometer was used. This machine uses a small ram pushed lightly against the surface of the material, pinning it into position. The temperature is raised in a steady and controlled manner, and in doing so, the material expands. This expansion is registered by the ram, which maintains constant pressure against the surface of the material. A typical temperature profile is characterised in Figure 3.7, with a ramp rate of 3 °C min^{-1} and maximum temperature of 140 °C. The ramp rate was kept low because although the sample was small (approximately 10 mm x 2 mm x 2 mm), the material is known to have a low thermal conductivity, and so a low ramp rate ensures any local thermal strains are minimised. The experiments were undertaken in an argon environment.

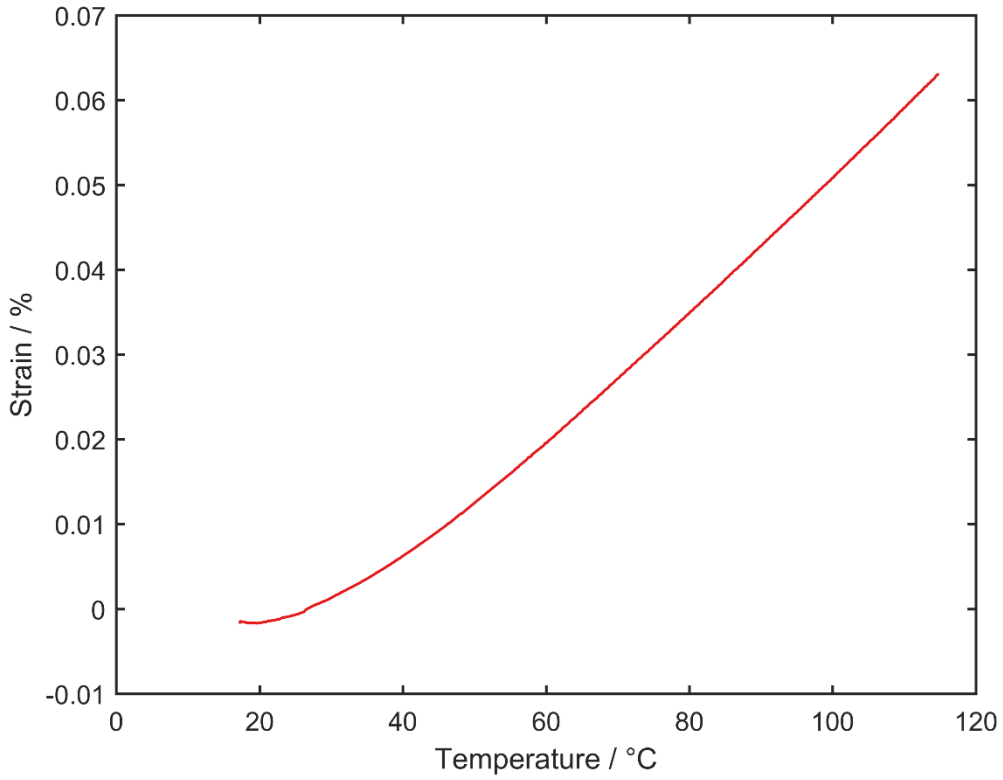

Figure 3.7: Data obtained for a sample of 50 wt.% fibres, as an example profile obtained from the dilatometer. The steady state linear portion of the graph (between 50 °C and 110 °C) was used for calculation of the thermal expansivity.

It is worth noting that the thermal conductivity is unlikely to vary significantly as fibres are added. Both the fibres and the particles are alumina and so there is no change of material, and structurally the only difference with increasing fibre content is an increasing porosity. However, it is a well-established observation that porous materials have the same expansivity as the corresponding fully-dense material, since the zero stiffness pores will not create any internal stresses or associated strains [87].

3.8. Thermal conductivity

Measuring the thermal conductivity was done by placing samples of varying fibre content into an experimental set-up as illustrated in Figure 3.8. Full details of this measurement technique are summarised by Tan *et al.* [154]. The samples, with dimensions

of around 16 mm x 16 mm x 8 mm, were placed between two flux meters, confirmed by EDX to be made of the titanium alloy Ti-6Al-4V (wt.%). This alloy has a desirably low thermal conductivity due to the titanium, which predominantly remains unaltered because of the retention of the α-phase in the matrix [155]. These flux meters were then in contact with two plates. The bottom plate was kept at a constant high temperature of 150 °C, using a resistive heater monitored by a PID controller. The top plate was maintained at a cooler temperature by pumping water through the block. Hence, a temperature gradient was formed, passing through both flux meters and the sample. This was ensured to be a unidimensional temperature gradient by surrounding the set-up with diatomaceous earth, a powder known for its excellent insulation properties (thermal conductivity of ~0.02 W m^{-1} K^{-1}, similar to air) [156]. It was therefore assumed that in the steady state heat flow, no heat would be transferred laterally through the diatomaceous earth.

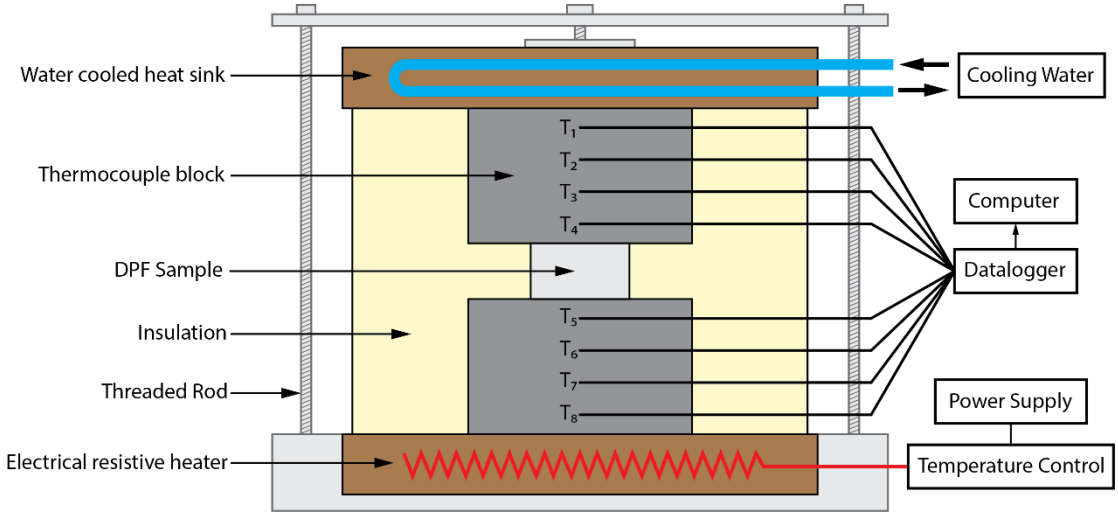

Figure 3.8: Set-up for thermal conductivity measurements.

The thermal conductivity is defined as

$$\frac{P}{A} = k\frac{dT}{dx} \tag{3.9}$$

where P/A is the heat flux (power per unit area), W m^{-2}, k is the thermal conductivity, W m^{-1} K^{-1}, and $\frac{dT}{dx}$ is the thermal gradient, K m^{-1}. The power going through the flux meters and the sample must be consistent and can be equated, assuming that their surface areas

are similar, as was the case in the current experiment. The final equation to calculate the thermal conductivity of the sample can therefore be given as:

$$k_{test}A_{test}\left(\frac{dT}{dx}\right)_{test} = k_f A_f \left(\frac{dT}{dx}\right)_f \quad (3.10)$$

where the subscripts $test$ and f refer to the sample to be tested and flux meters respectively.

To calculate k_{test}, in addition to the surface area of the flux meters and the sample and also the thermal conductivity of Ti-6Al-4V (k_f), which was found to be 7 W m^{-1} K^{-1} [155], the thermal gradients must be known. This can be calculated by measuring the temperature of the flux meters at intervals along the height of each flux meter using thermocouples. Once steady state has been reached, the thermal gradients of the flux meter should result in a linear heat change with respect to distance, giving a value for $\left(\frac{dT}{dx}\right)_f$ which can be averaged across the two flux meters. These thermal gradients can then be extrapolated towards the surfaces of the sample to give the temperature of the flux meter surfaces at each side of the sample. The interfacial thermal resistance is an important consideration, and can be quantified by using the (dimensionless) Biot number, Bi, as a ratio of the temperature drop at the interface to the thermal conductivity of the sample:

$$Bi = \frac{h_i\, d}{k_{test}} \quad (3.11)$$

where h_i is the interfacial heat transfer coefficient (W m^{-2} K^{-1}). The thickness of the samples (d) was approximately 10 mm, and the thermal conductivity was expected to be around 2 W m^{-1} K^{-1} (the thermal conductivity of bulk alumina is ~30 W m^{-1} K^{-1} [157], but this will decrease significantly with porosity [158]). The interfacial heat transfer coefficient was assumed to be reasonably good, since a force was applied to maintain good contact. A value of around 4 kW m^{-2} K^{-1} was assumed to be approximately representative based on work on similar materials [154]. Inserting these numbers into Equation 3.11 yields a Biot number of 20, this is a large value (>>1) and so the thermal resistance at the interfaces

can be assumed to be negligible. In fact, further calculation by considering the equation for the heat flux at the interface:

$$Q = h_i \, \Delta T_i \tag{3.12}$$

leads to the conclusion that the temperature drop at the interface, ΔT_i, is around 1 °C, and therefore can be considered negligible when compared to the temperature gradient across the sample (over 100 °C). In this calculation, the heat flux across the interface, Q, is assumed to be same as that passing through the flux meters.

If the interfacial thermal resistance was necessary, it could be calculated by repeating the experiment using samples of varying thickness. However, since the thermal interface resistance can be neglected, the temperature at each surface of the sample and the thickness of the sample is known, and so the thermal gradient, $\left(\frac{dT}{dx}\right)_{test}$, can easily be calculated. A thermal profile to aid visualisation of these variables is given in Figure 3.9.

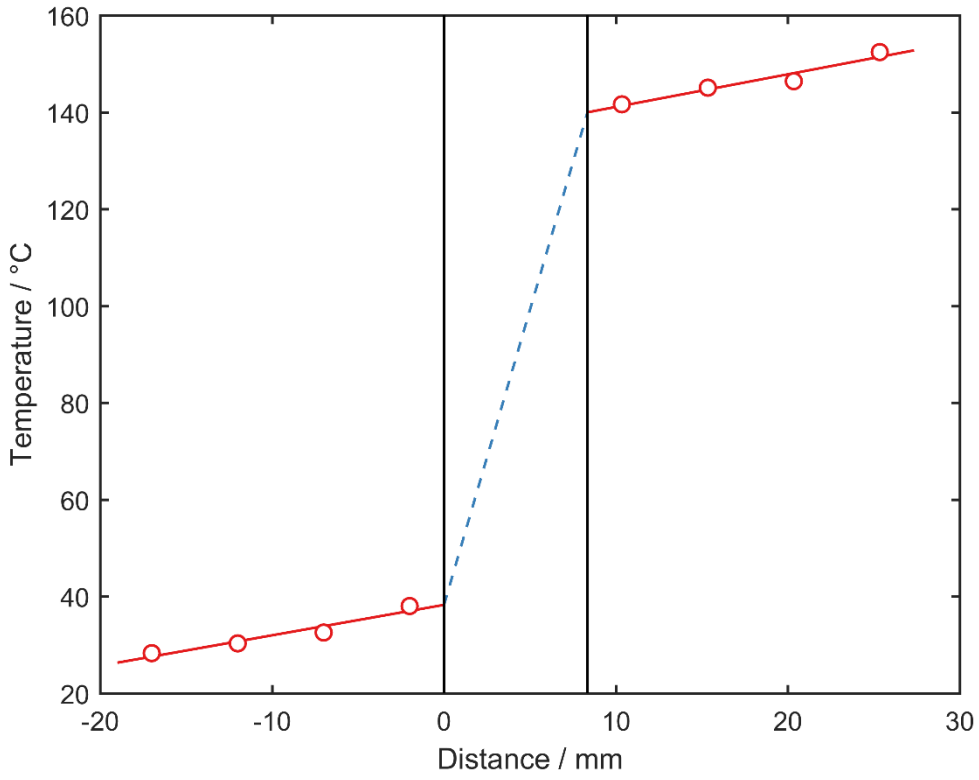

Figure 3.9: The thermal conductivity profile for a sample of 100 wt.% Saffil fibres. The red solid lines correspond to the thermal gradient within the flux meters which is measured using eight thermocouples. The blue dashed line is the predicted thermal gradient within the sample, considered by interpolating the red lines to the sample boundary and assuming negligible interfacial thermal resistance.

3.9. Vacuum plasma thermal shock

Thermal shock resistance was experimentally measured, requiring the samples to be exposed to an extremely demanding temperature gradient, such that damage due to thermal shock is induced. A Vacuum Plasma Sprayer (Plasma-Technik AG Switzerland) was used, not in its usual capacity as a method of coating a sample, but rather as an extreme heat source. In such a set-up, several DPF samples of dimensions 70 mm x 20 mm x 10 mm were clamped into position, as shown in the schematic in Figure 3.10. The rig was positioned such that it was 250 mm away from the tip of the plasma nozzle.

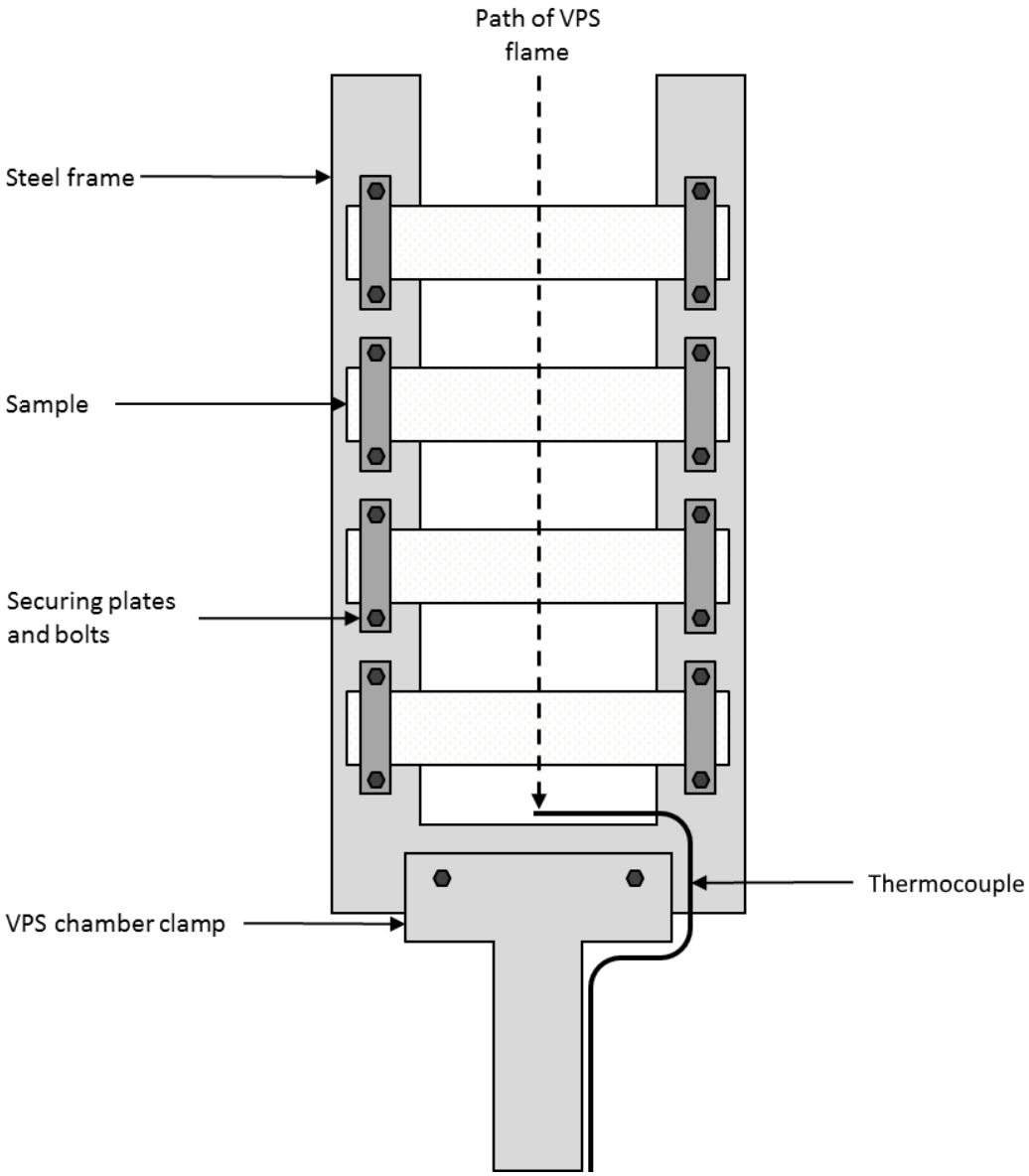

Figure 3.10: Schematic of mounting rig for samples in the VPS. The path of the VPS plume is also included. The direction of the plume is into the plane of the schematic.

This rig was placed into the large VPS chamber, and the seals cleaned and closed. The chamber was then pumped down to a rough vacuum, followed by re-pressurisation by argon to a pressure of 200 mbar. At this point, the plasma plume was initiated; a mixture of argon (50 normal litres per minute (NLPM)) and hydrogen (3 NLPM) were released from a nozzle and ignited by a spark. The arc current was 850 A and the voltage 40 V, so the plasma power was about 34 kW. The chamber pressure at this point was lowered to 120 mbar, allowing the plume to elongate. Once parameters were established

and the system was steady, the nozzle began on a path which passed the plume through the centre of the samples, moving at a rate of 10 mm s^{-1}, also shown on Figure 3.10. The plume rapidly heated up the samples and the temperature profile to which the samples were exposed is shown in Figure 3.11. Note that the thermal shock was at least a temperature difference of 1000 K and the peak rate of heating was 200 K s^{-1} at a minimum. The thermocouple used to measure this profile was K-type, which is not accurate above 1000 °C, and data logging was only possible at a rate of one reading per second. However, the heating cycle was captured well, although it is likely that the peak temperature was higher that 1400 °C.

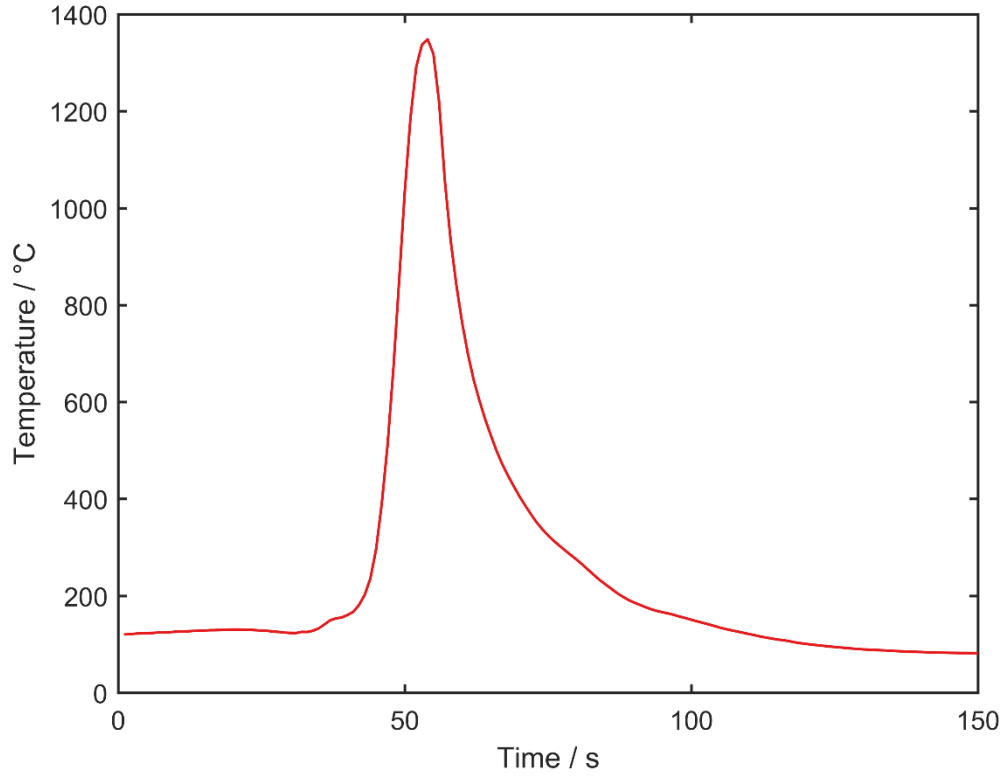

Figure 3.11: Typical heating cycle in VPS, 1000 K increase in just a few seconds.

Qualitative measurements of thermal shock were possible by observing the differences in visual appearance of the samples of varying fibre content, after an equal number of thermal shock cycles. Quantitative data were also obtained by measuring the stiffness of the samples before any thermal shock treatment, and at various intervals of a

certain number of passes of the plasma plume. In this way, a full profile of the degradation of the samples could be measured. RFDA was the chosen stiffness measurement technique because, in comparison to the 4-point bend test, the measurement process resulted in much less damage to the samples, and so almost all the damage to the samples could be attributed to micro-cracking arising from thermal shock, and not from the stiffness measurement technique itself.

4. Preliminary tests on first-generation materials

4.1. Introduction

The main purpose of testing the first-generation materials was to examine how various processing conditions affected the filters. There are a number of variables during processing that affect the production of the filters. The ones that were focussed on in this project were: fibre content, sintering time, sintering temperature, isostatic pressing time and isostatic pressing pressure. The effect of these variables on the generated filters were assessed by evaluating the porosity and permeability in each case.

Since the work presented here concentrates on the effect of adding fibres to the DPFs, the most critical of these dependencies was that of fibre content. In addition to porosity and permeability as indicators of filtration efficiency, the variation of stiffness was also analysed as an investigation into the mechanical properties, providing some preliminary results for study of the thermal shock resistance of the filters.

Extrusion was also examined as a method for producing samples, since this is a similar processing route to that used for the commercially manufactured DPFs.

4.2. Fibre content

Both porosity and permeability showed a strong dependence on the volume fraction of fibres in the sample. Figure 4.1 shows that the variation is approximately sigmoidal. In a DPF situation, a high porosity and permeability are desirable, such that a low EBP is maintained (although, of course, a very open structure would tend to also have a low

filtration efficiency). Even using fibres of a diameter comparable to that of the mixing powder, it is clear that it is beneficial in this respect to add fibres, with the highest porosity and permeability observed in the case where only fibres were present. This is expected, since fibres will provide a more open structure by opening up gaps between particles.

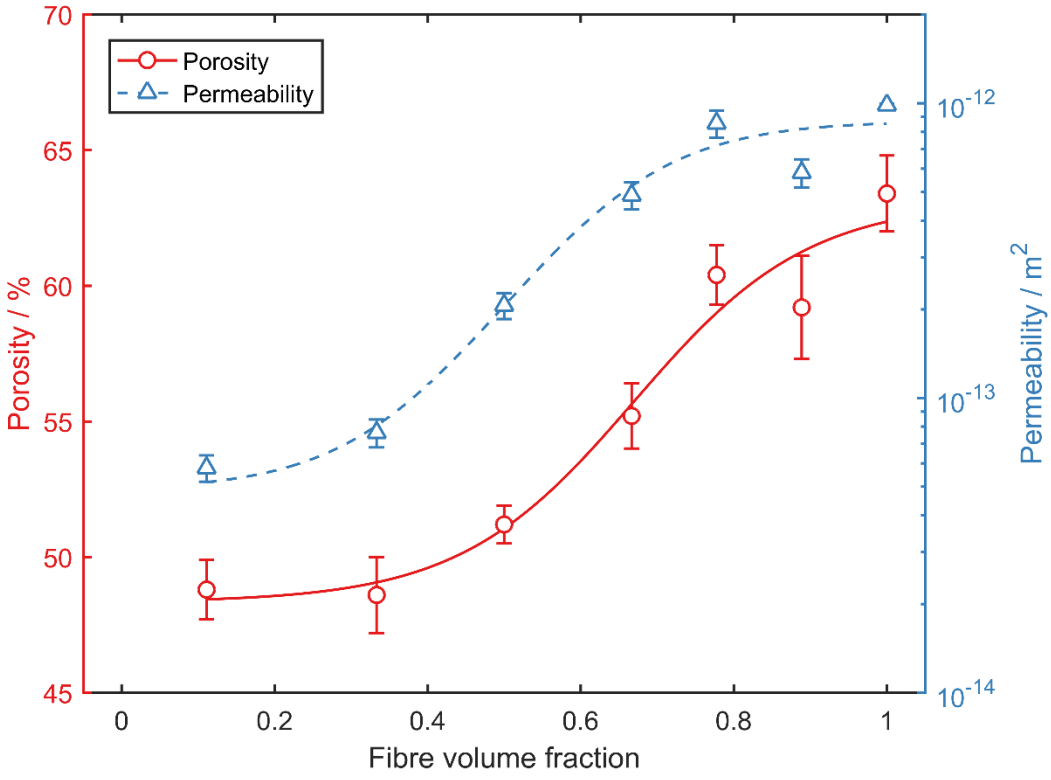

Figure 4.1: Variation of porosity and permeability with respect to the fibre volume fraction.

The fibre content also had a noticeable effect on the stiffness of the filters, as shown in Figure 4.2. The filters made with high powder concentrations (more than a 1:2 fibre:powder ratio) were very friable and impossible to make a four-point bent test sample without breaking the filter. Such materials did not have sufficient handling strength to be considered as a viable DPF material. Likewise, the sample made purely of fibres also lacked sufficient handling strength for a test sample to be produced, and so whilst this composition was optimal from the point of view of porosity and permeability, it is also not a candidate material for a DPF.

Stiffness, measured using the manual loading 4-point bend test, peaked with a fibre fraction of around 67 wt.% (i.e. a 2:1 fibre:powder ratio). Whilst it is desirable to keep the stiffness as low as possible, so as to improve the thermal shock resistance of the material, the observed values were all low (the maximum observed stiffness being only 2.6 GPa), despite considerable sintering of the material so close to the T_g value. Compared to the stiffness of bulk alumina (400 GPa [159]), this is certainly low, even at its peak. The decrease in stiffness by such a large extent is to be expected; Markaki and Clyne developed a model predicting that a fibre array, containing fibres with an aspect ratio of 10, would reduce the stiffness by a factor of 100 compared to the stiffness of a single fibre [92]. At high fibre contents the higher porosity will favour a low stiffness. However, at lower fibre contents the stiffness increases with increasing fibre content. Perhaps this increase is attributable to fibre pinning points being further apart at low fibre contents, and, as fibres are added, the average length of a segment between pinning points may decrease. This effect has been studied for purely fibrous arrays by Clyne and Markaki [91, 92, 94], although this model may not be applicable to these hybrid fibre and particle composites.

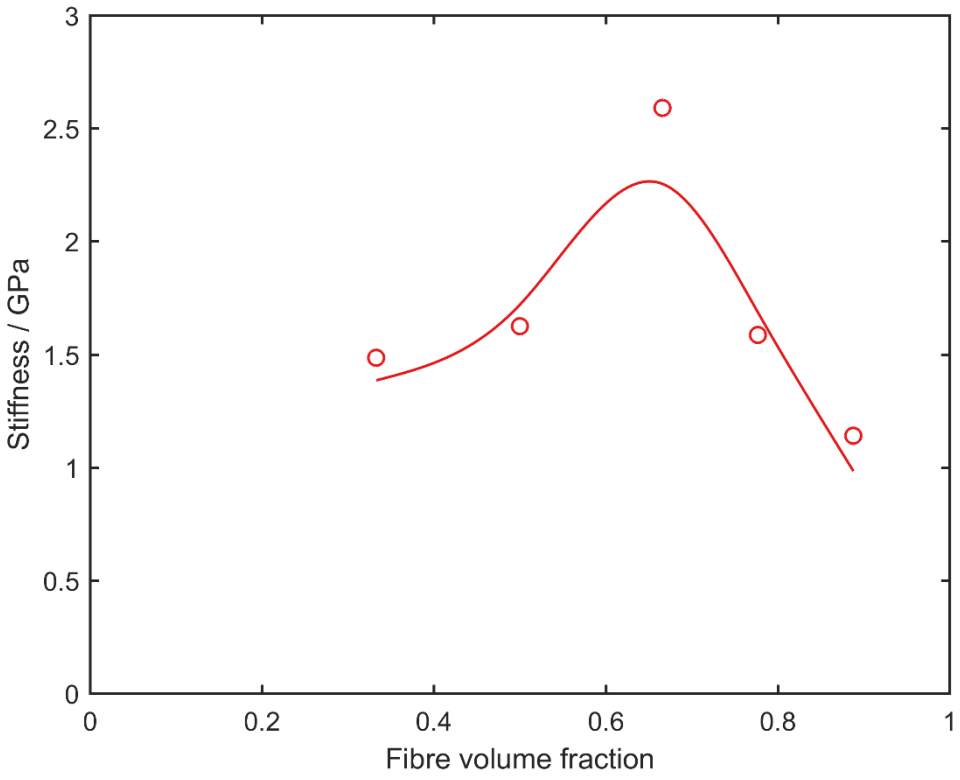

Figure 4.2: Variation of the filter stiffness with respect to the fibre volume fraction.

4.3. Sintering time

Figure 4.3 shows that there was very little variation observed in porosity and permeability with increased sintering time. It should be noted that, before sintering, the samples start with low values of porosity (36.5 %) and permeability (1.2 $x10^{-14}$ m^2), rising to constant values of approximately 49 % and 2.0 $x10^{-13}$ m^2 after only an hour of sintering at 1100 °C. These values were then approximately constant for all longer sintering times up to 12 hours.

This is to be expected, since when the filters are initially heated up to 1100 °C, the PVA binder is removed, as it decomposes rapidly above 200 °C. Once the PVA has decomposed after only a few minutes, additional sintering time results in strengthening interconnections between particles and fibres, but there is no further increase in porosity or permeability.

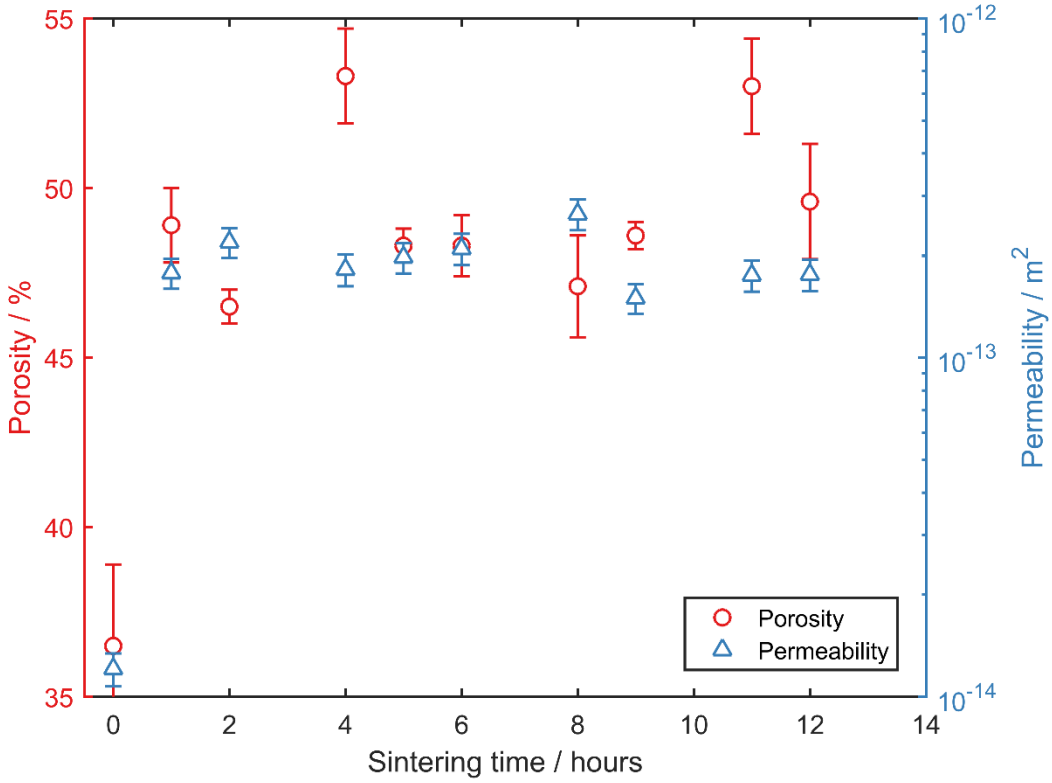

Figure 4.3: Variation of porosity and permeability with respect to the sintering time.

4.4. Sintering temperature

Three different sintering temperatures were investigated. All other tests were done at 1100 °C, since this was known to be just below the glass transition temperature of the fibres, and so this temperature was tested, as well as 900 °C and 1300 °C. The fibre content was constant at 50 wt.% fibres, cold isostatic pressing conditions were constant (120 s at 1500 bar), and the sintering time of 3 hours was the same in all cases.

There was very little variation between the porosity and permeability at 900 °C and 1100 °C, having values at both temperatures of around 47 % and 2 x10^{-12} m^2 respectively, as can be seen in Figure 4.4. However, when sintered at 1300 °C, the porosity and permeability both changed significantly. The porosity dropped to around 30 %, which can be explained by the fact that the sintering temperature is well above the glass transition temperature (T_g) of the amorphous fibres, and so the material will be able to flow, which

acts to close up pores in the filter. Permeability, on the other hand, changed in the opposite direction; when the sintering temperature was increased, the permeability also increased. This indicates that, whilst the porosity decreased, the flow of fluid through a sample actually increased, suggesting the possibility of large open channels being formed, contributing little to the porosity, but enhancing the permeability. These properties are certainly not desirable, since such a low porosity will not lead to good filtration efficiencies, and the fact that the fibres were sintered above their T_g implies that any benefit offered by a fibrous microstructure will be lost. This abnormal behaviour, attributed to a widening of the pore-channel diameters, has also been observed in the literature in porous mullite [69], alumina [160], and zirconia [161].

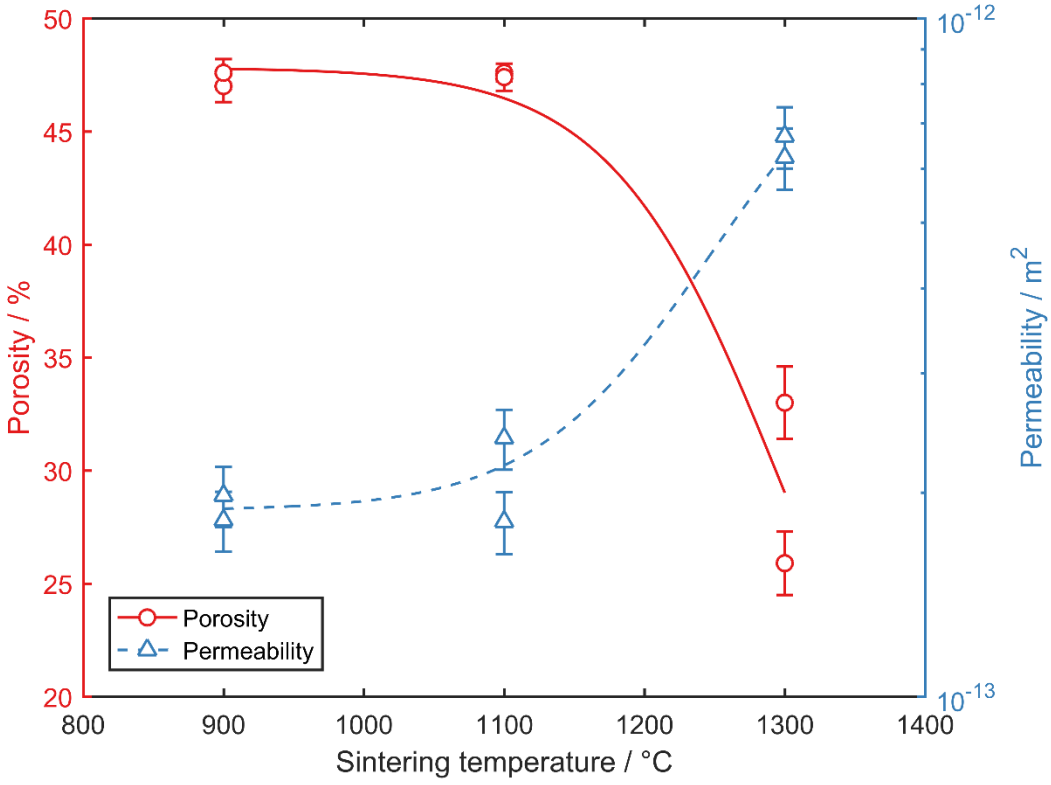

Figure 4.4: Variation of porosity and permeability with respect to sintering temperature.

By sintering at 1300 °C, a much higher handling strength and stiffness was achieved. For the porosity experiments, a uniform cylinder is required which means that samples are ground on SiC grinding paper after sintering. All samples produced at sintering

temperatures below 1300 °C could easily be ground into shape due to the friable nature of the filters. However, for the samples sintered at 1300 °C, grinding was not possible, since the material produced was not friable and the Al_2O_3 was too hard. Instead, the filter had to be cut into shape using a Struers Accutom-5 circular saw. The stiffness was tested by four point bend testing, and was found to be 13.2 GPa. Whilst this is still much lower than that of bulk alumina (400 GPa [159]), it is significantly greater than all other samples that were produced at lower sintering temperatures. The comparable stiffness of a filter produced under all the same conditions apart from being sintered at 1100 °C was 1.6 GPa, almost an order of magnitude lower. The filter material was noticeably less fragile in feel compared to other filters. This decrease in porosity and increase in handling strength is to be expected since there is strong dependence of the fracture strength on the porosity [162]. The higher strength can be attributed to necks formed between the alumina particles. Whilst improved handling strength may be beneficial, the low porosity, high stiffness and low specific surface area are all undesirable.

4.5. Isostatic pressing time and pressure

The cold isostatic pressing time and pressure were also varied, to see whether there was any effect on the porosity and permeability. In all cases the fibre:powder ratio was kept constant at 50 wt.% fibres, as were the sintering conditions (3 hours at 1100 °C).

A range of times between 1 s and 1800 s were investigated, and pressures of 500, 1500 and 1700 bar (the maximum pressure possible on the specific press) were tested, as well as a sample that was not put in the press at all. The results are shown in Figure 4.5.

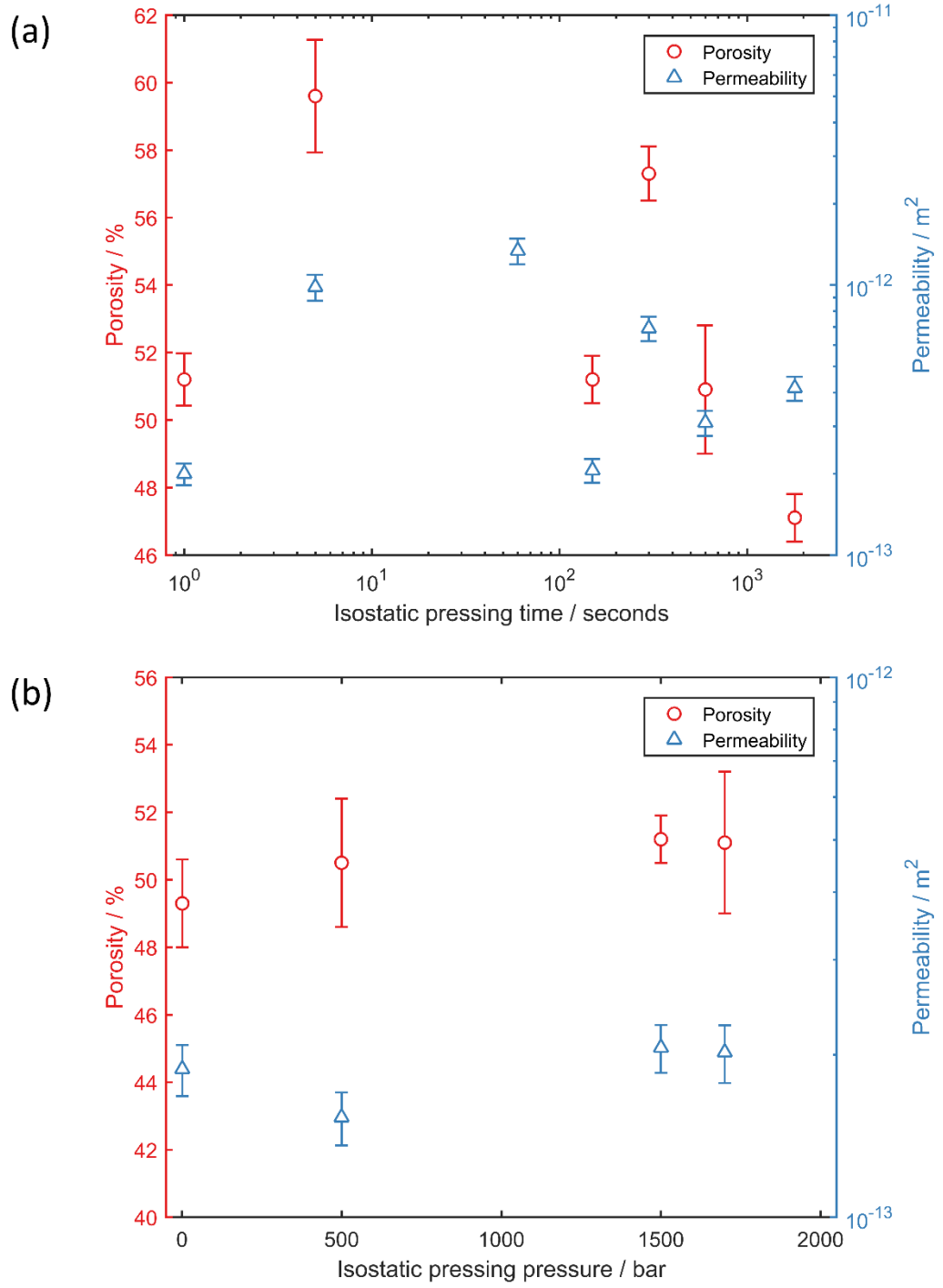

Figure 4.5: Variation of porosity and permeability with respect to (a) isostatic pressing time, and (b) isostatic pressing pressure.

Both porosity and permeability after sintering seemed to be approximately independent of both the pressing time and pressure. Porosity remained constant over the

whole range, with an average value of around 51 %, this is unaffected by the pressing procedure because the PVA and water are still present. Permeability was also consistent across most of the range, at around 1.8 x10^{-13} m^2.

It is useful that the cold isostatic pressing time and pressure have no effect on the porosity or permeability, since a time can be chosen after which the material seems to have consolidated into a green compact, without worrying about having any effect on the filtration properties. Likewise, there is freedom to choose any pressure to create the green compact, in the knowledge that the filtration properties will be unaffected.

4.6. Extrusion

The purpose of the simple extrusion rig was to observe any effects of fibre alignment that might occur during the process. In order to analyse this, the extruded cylinders were examined via SEM, producing images such as in Figure 4.6.

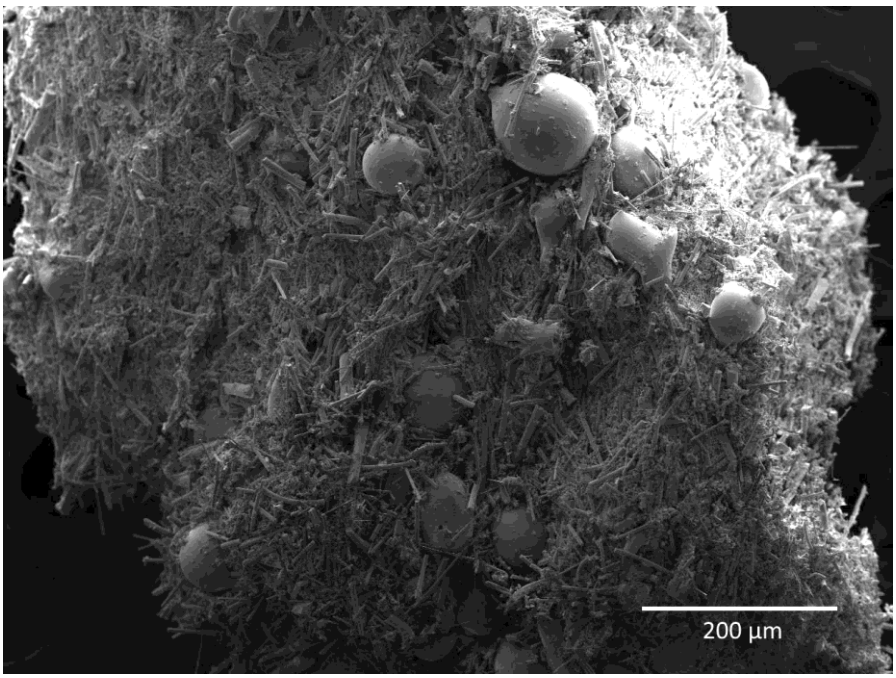

Figure 4.6: SEM image of the fractured surface of the middle of an extruded sample. Large shot particles, one of the problems with the first-generation materials, are also visible.

Using image processing software (ImageJ), the alignment of the fibres was calculated by recording the angle of all fibres in an SEM image in two-dimensions. Figure 4.7 plots this alignment, by considering the orientation of the fibres as an angle from the direction of extrusion, from 0 to 90 °. The results that are plotted in Figure 4.7 are therefore symmetric about the X and Y axes.

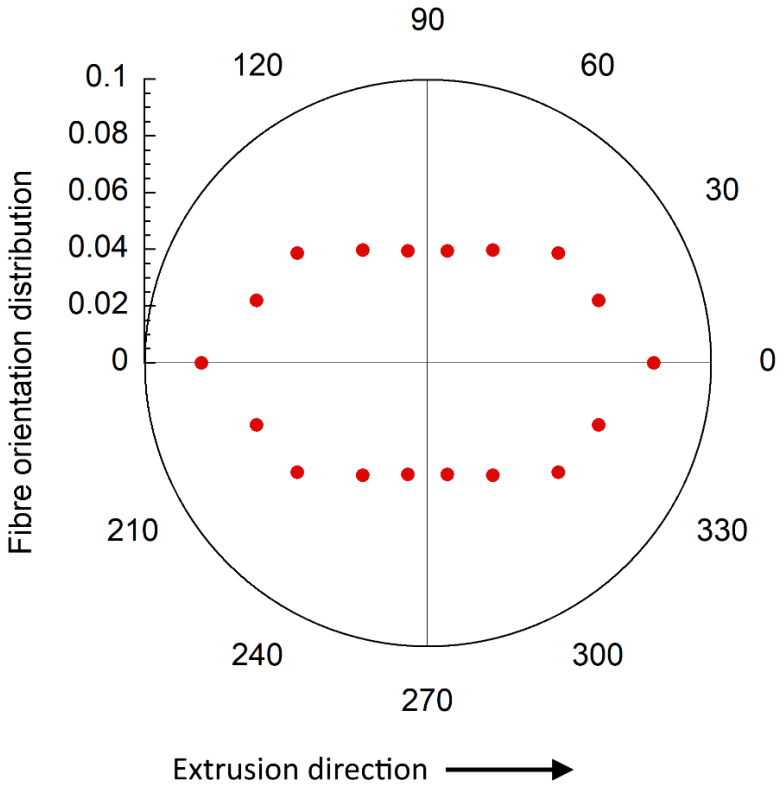

Figure 4.7: Distribution of fibre orientations in extruded sample.

The results indicate that the fibres are aligned by extrusion, with twice as many found aligned parallel to the extrusion direction compared to perpendicular. This alignment was found to be similar at the edge and the centre of the extrudate. This result hints that some of the macroscopic properties may be anisotropic. For example, Markaki *et al.* have shown that both the thermal conductivity [163] and stiffness [93] are dependent on fibre orientation in porous fibre arrays.

4.7. Conclusion

Although far from being perfect DPF materials, the first-generation materials offered valuable information for the future work involving the second-generation materials, although it is important to consider that the effects could differ when the particles and fibres are changed. The important results are the effects of processing conditions on the mini DPF samples. It was encouraging to observe that the sintering time and temperature, the isostatic pressing time and pressure and extrusion all had little effect on the porosity and permeability (at least until the glass transition temperature, which is not a concern in crystalline ceramics). In this way it can be seen that the porosity and permeability are independent of the processing conditions, and therefore any variation can be attributed to the fibre volume fraction. As expected, as fibres were added, the composites became more open, with an increasing porosity and increasing permeability. This will offer a lower back-pressure but could lead to a potential decrease in the initial filtration efficiency.

Whilst not being of importance for the porosity and permeability, the processing conditions could be of importance for the mechanical properties. The samples appeared to have higher handling strength at higher sintering temperatures, and at longer sintering times. The stiffness peaked at 67 wt.% fibres, suggesting that, as fibres are added, the stiffness initially increases, perhaps due to an increase in the number of connections during sintering, but eventually drops off at higher fibre fractions, since the number of particles in a fibre-rich composite is being reduced and so there is less pinning of the fibres, and the flexural fibre compliance can be utilised.

The following work in this thesis now concerns only the second-generation of materials.

5. Filtration Efficiency

5.1. Introduction

Filtration efficiency can be defined as either the number of diesel particulates that are trapped, or the mass that is collected, as a percentage of the total particulate introduced. To experimentally measure either of these properties a source of diesel particulate is required (i.e. a diesel engine or a source carbon black). Since neither were available within this project, the filtration efficiency had to be estimated by other means.

Two properties that are linked to one another, and also can act as predictors of filtration efficiency, are the porosity and the permeability of the structures. Permeability tends to increase with increasing porosity, as seen in the first-generation materials (Section 4.2) and predicted by the Carman-Kozeny equation. However, the Carman-Kozeny equation also includes a term for the specific surface area, and if the surface area increases significantly (as might be expected for the introduction of fine fibres), then it is possible for permeability to decrease even with increasing porosity.

For a high filtration efficiency, the permeability should be lowered. This will allow more particulate matter to be mechanically filtered as it passes through the DPF, but this will also lead to an unfavourable increase in back-pressure.

An increase in specific surface area could also be beneficial to filtration efficiency, since a higher surface area will result in a larger area on which soot can accumulate. As mentioned in Section 1.3.3, the clean filtration efficiency of commercial DPFs is initially low until the soot cake forms. At this point, the soot itself improves the efficiency of the filter greatly. With a larger surface area, it is possible that this soot cake initiation could

occur sooner. A larger surface area also offers more space for the soot to accumulate and therefore the filter could potentially hold more soot before the back-pressure increases too much and regeneration is required. A longer time between regenerations means fewer regenerations for a given distance of driving, an extended lifetime of the DPF, and less wastage of fuel.

In this chapter, the porosity and permeability of the second-generation materials are investigated and these are used to predict the specific surface area using the Carman-Kozeny equation. Tomography is also explored as a possibility for measuring a filtration efficiency from simulations, in addition to an analysis of pore characteristics.

5.2. Porosity

The values of porosity measured for the first-generation of materials gave a preliminary feel for how the porosity varied as a function of fibre volume fraction. The same experiment was repeated with the second-generation of material (3 μm diameter fibres, 30 μm diameter spherical particles), with a more appropriate ratio between the particle and fibre size. Also, the crystalline nature of the second-generation material led to more successful partial sintering than the amorphous fibres of the first-generation material which softened upon exceeding the glass transition temperature. The results for the second-generation of material are shown in Figure 5.1.

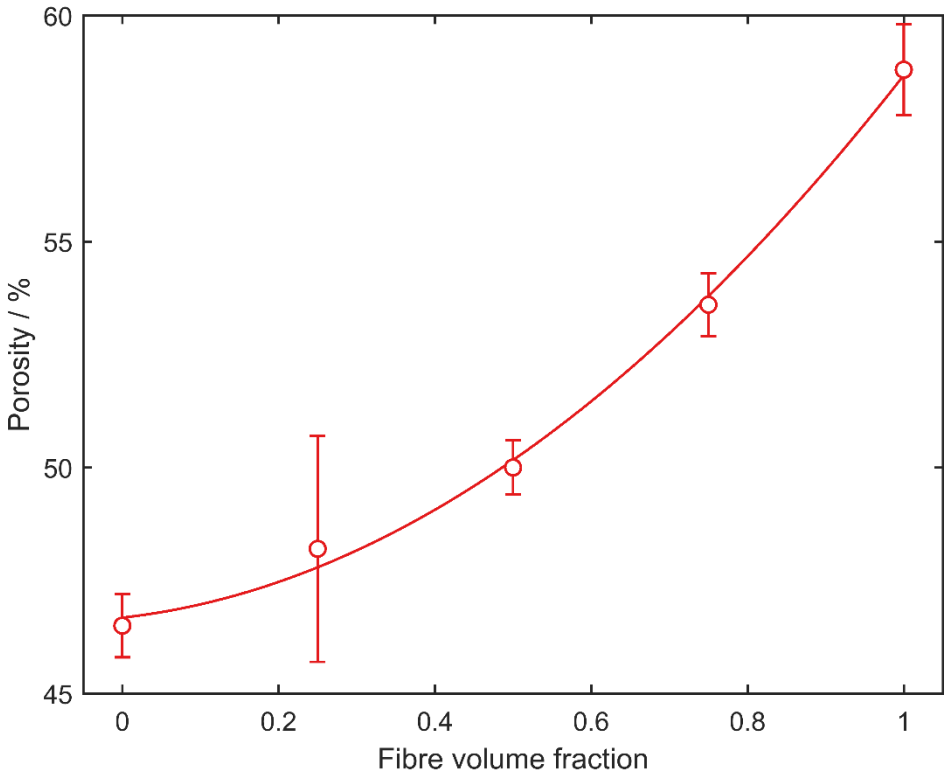

Figure 5.1: Variation of porosity with respect to fibre volume fraction. The line of best fit is a second order polynomial.

Similar to the first-generation materials, the second-generation materials also showed a clear trend of increasing porosity as the fibre volume fraction was increased. This trend is to be expected because the addition of fibres acts to space out the particles in the structure

5.3. Permeability

The permeability was also measured again for the second-generation of materials. Figure 5.2 shows the data for the new materials.

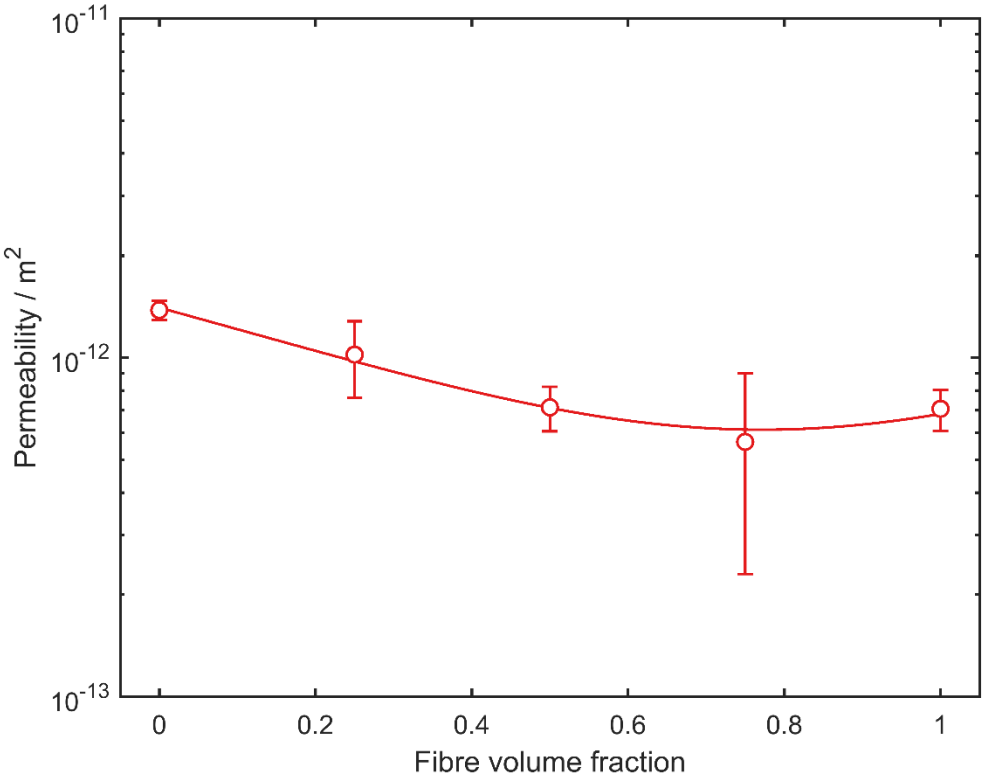

Figure 5.2: Variation of permeability with respect to fibre volume fraction. The line of best fit is a second order polynomial.

It is interesting to note that whilst the porosity of the two generations of material were fairly consistent with one another, the permeability takes on very different forms. As a reminder from Section 3.3.1 for the case of the first-generation materials, there appears to be an increase in the permeability as the fibre volume fraction was increased. This is an expected result, since in general a higher porosity is expected to also yield a higher permeability, as can be predicted using the Carman-Kozeny equation (Equation 3.5). It can be seen that the two are linked together by a third variable, which is the specific surface area of the pores. If this value is assumed to be constant, then the result of an increasing permeability with porosity, as observed in the first-generation of materials, is unsurprising.

However, in the case of the second-generation of materials, rather than the permeability increasing with increasing porosity, the permeability actually remained close to constant, and even appeared to decrease slightly, within experimental error. By

comparing this with the Carman-Kozeny equation, it can be concluded that the specific surface area of the pores must increase with increasing fibre volume fraction. This result is discussed further in the following section (Section 5.4).

In both cases, the magnitude of the permeability was comparable to the values obtained in commercial DPFs, which often have quoted values of around 10^{-12} m^2 for wall flow filters [35]. The value of permeability gives a direct indication of the magnitude of the back-pressure that will build up across the DPF. Too low a permeability will raise the back-pressure and impair the efficiency of the engine; too high is likely to be associated with a reduced filtration efficiency.

5.4. Specific surface area

Since the porosity and permeability have both been experimentally measured, the specific surface area, S (m^2 m^{-3}), of the structure can be predicted by using the Carman-Kozeny equation (Equation 3.5). Taking the best fit lines of both the porosity and permeability values, the derived specific surface area as a function of fibre volume fraction can be plotted. This plot is shown in Figure 5.3.

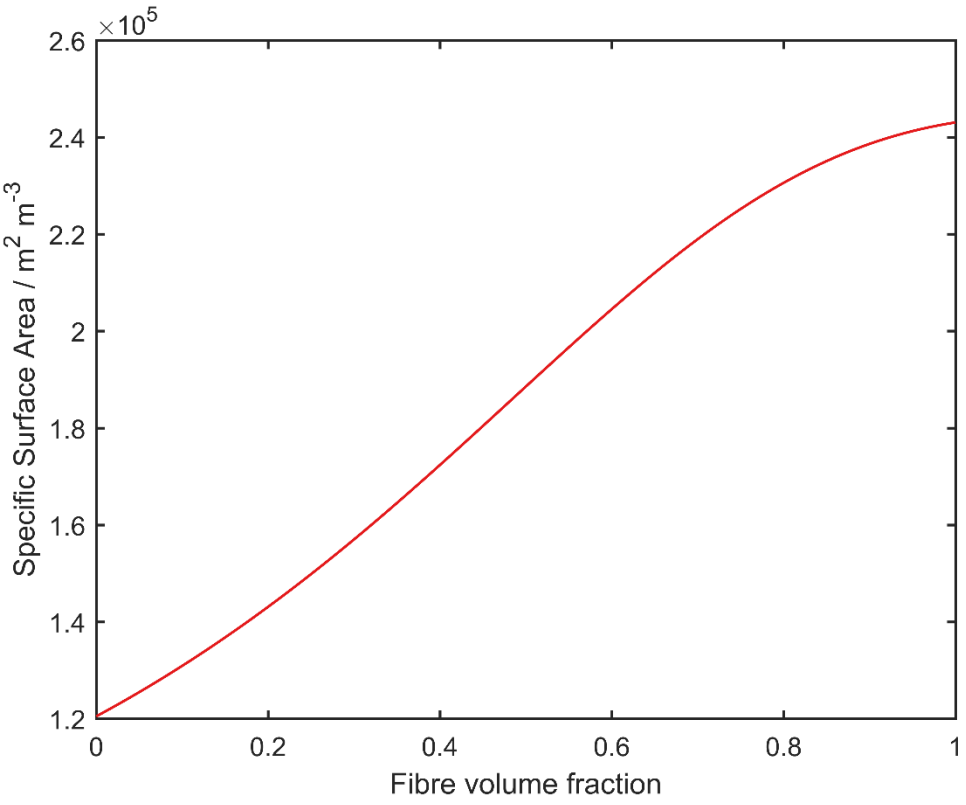

Figure 5.3: Variation of specific surface area with respect to fibre volume fraction, calculated using the Carman-Kozeny equation and experimental measured values of porosity and permeability.

There is a significant increase in the specific surface area as the fibre volume fraction is increased. For a given volume, the surface area for a purely fibrous array is twice that of an arrangement of particles. A larger surface area suggests that there is a larger area on which soot could be trapped, and so the initial soot trapping could be improved. In addition to the higher porosity, this result indicates that a higher total mass of soot could be supported before regeneration is required.

5.5. Tomography

5.5.1. Observation

The internal structure of the DPF filters was captured using a CT scanner as described in Section 4.2.2. Visualisation of the whole structure was made possible using software called CTvox, provided by Bruker. By importing the stack of x-y plane images into the software, the luminosity and transparency of varying greyscale values could be smoothly varied so as to get a clear three-dimensional representation of the structure in each case. The volumes that were studied, with fibre volume fractions of 0, 25, 50 and 75 wt.%, are shown in Figure 5.4.

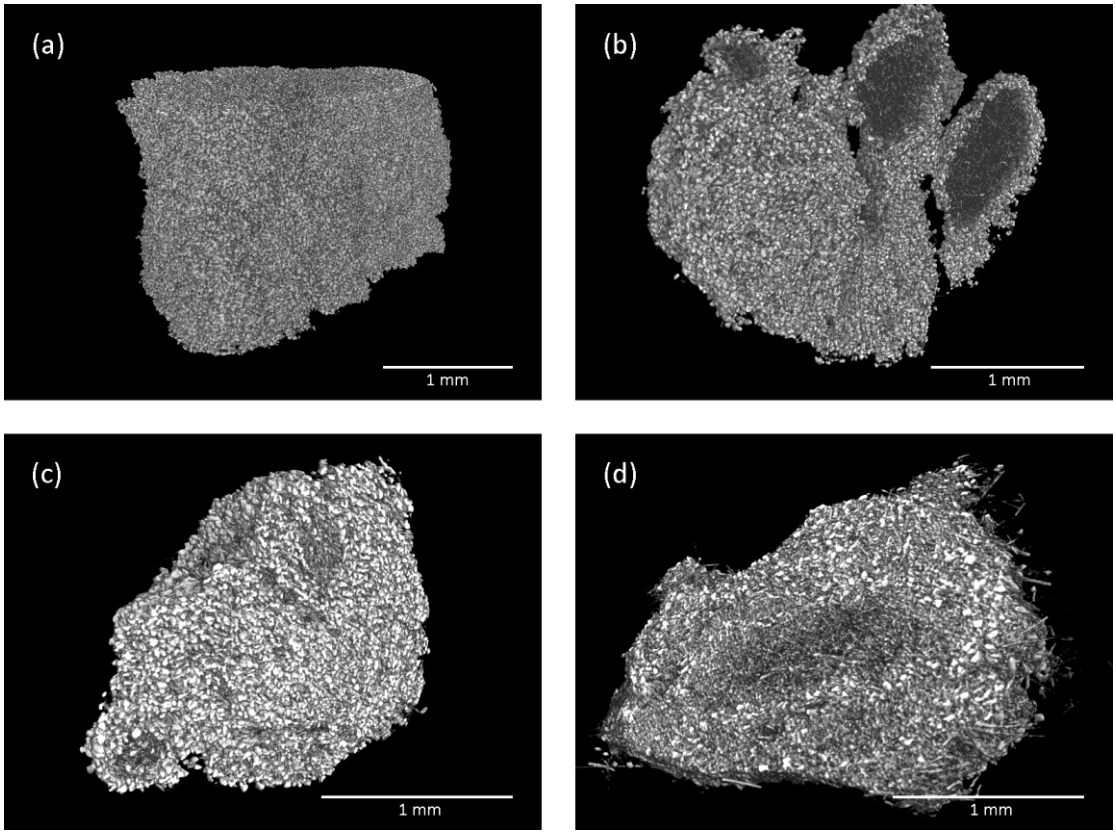

Figure 5.4: Images of the tomographic volumes viewed on CTvox (Bruker) software. Contrast is provided by artificial illumination within the software. The volumes contain (a) 0 wt.%, (b) 25 wt.%, (c) 50 wt.%, and (d) 75 wt.% fibres.

In each case the particles can be clearly identified as bright regions, approximately spherical with a diameter around 30 µm, as expected. The fibres are more difficult to see but are most obvious in the centre and at the edge of the 75 wt.% sample.

One immediate observation is that the structures containing both fibres and particles are inhomogeneous; this is most apparent for the 25 wt.% image. In this case there are darker regions within the volume where it seems that fibres have clustered together, surrounded by particles. This formation is a result of the ball milling procedure during production. The ball milling was limited to 5 minutes, since any further milling would have decreased the aspect ratio of the fibres too much. However, after only 5 minutes the fibres still remained in small clumps, less than 1 mm across. During the blending process with the particles a paste was formed, and by this point the fibres and particles were considered mixed. It can be observed in the CT images that these fibre clumps remain, surrounded by the particles. They tend to occur at the centre of the analysed volumes, since the volumes were obtained by fracturing a small crumb off a larger sample. The fact that the particles often form the outside of these crumbs, with fibre clumps in the centre, suggests that the fracture energy to separate the particles is lower than the fracture energy to break the clumps apart. By optimising the processing on the second-generation materials, this effect of inhomogeneity could have been reduced.

Even with this inhomogeneity present, the volumes were analysed by selecting random volumes from within the total volume, and averaging results.

5.5.2. Pore characterisation

These volumes were too large to import the entire structure into analysis software. For each scan, six 100 µm cubes were extracted, using a random number generator to select coordinates to avoid any bias, and imported into ScanIP. Each one of these cubes had a range of greyscale values which needed to be categorised as either material or air. The volume of interest is the air, and so a greyscale threshold was chosen such that any greyscale values darker than the selected threshold would be included in a mask.

This thresholding process is not perfect and has to be estimated by eye. Within a given sample, the threshold was kept constant across all volumes, but as an indication of the difficulty of choosing this value, Figure 5.5 shows a cross-section through a volume with three different possible thresholds. Any one of these could be chosen, and there is a large variation in the porosity based on which threshold is chosen. The threshold level could not be chosen to be consistent with measured porosity levels because of the inhomogeneity in the scanned volumes. The best solution is to aim to be as consistent as possible between samples. This thresholding issue should not lead to much bias in the results, since it is the structure of the materials, rather than the absolute porosity, which is of interest.

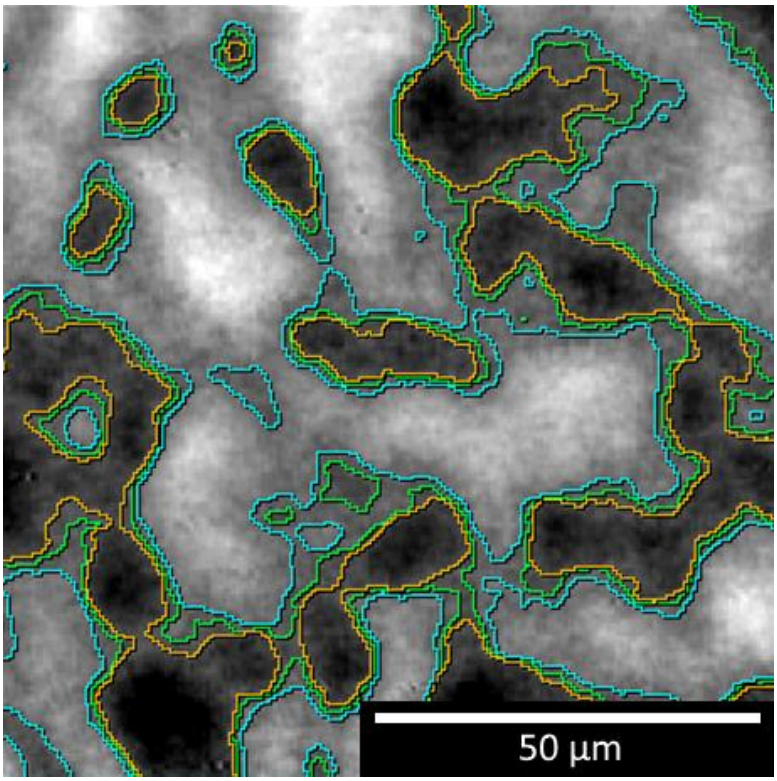

Figure 5.5: Various possible thresholds that could be used when constructing a mesh for a volume of 25 wt.%. This choice of threshold can greatly affect the porosity and so consistency in selection is key.

The mask that was generated at this stage would be very angular and granular. To improve the quality of the mesh, it was first dilated such that every voxel in the mesh was assigned a sphere of diameter 1 µm centred on that voxel. A Gaussian smoothing

operation was then applied, which eroded the mask back to its original size, but the surfaces were now smooth rather than pixelated. The porosity after these two operations was unchanged and so the two together can be assumed to be a volume-conserving smoothing filter.

Finally, there would be a number of "islands" in the mask. These would signify disconnected porosity. These are unlikely to exist in any significant proportion in the case of partially sintered fibres and particles, so they were assumed to be artefacts, where a single voxel had appeared darker than expected due to noise in the scan. These islands were removed such that the mask was formed of only one contiguous volume. Small voids were also filled in within the mask, caused by the opposite problem above, where a single voxel would appear lighter than expected due to noise.

With this mask generated, it can be analysed to see how the pores vary between samples. The centreline editor tool in ScanIP draws a line down the centre of a pore channel. If the pore splits into multiple directions, then a node is formed. In this way, the pore structure can be converted into a network. This network can be analysed by considering the total length of all the lines in the volume, the mean curvature of the lines, and also the mean cross-sectional area around the lines. Figure 5.6 shows this network for (a) a 0 wt.% sample and (b) a 75 wt.% sample.

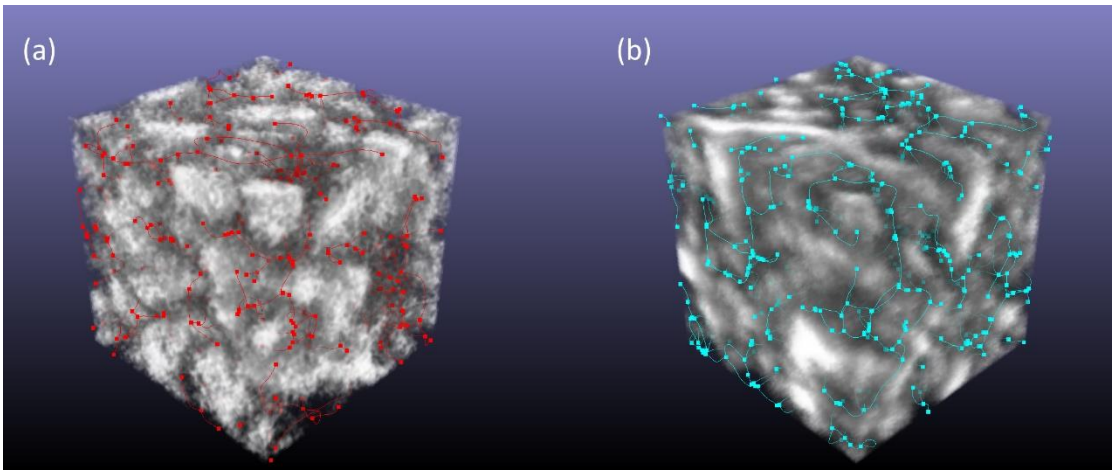

Figure 5.6: 100 µm cubes taken from (a) a 0 wt.% fibre sample and (b) a 75 wt.% fibre sample. In each case, a centreline network has been applied to a mask (not pictured), which contains just the air sections of the volume.

The variations of total length, mean curvature and mean cross-sectional area are shown in Figure 5.7.

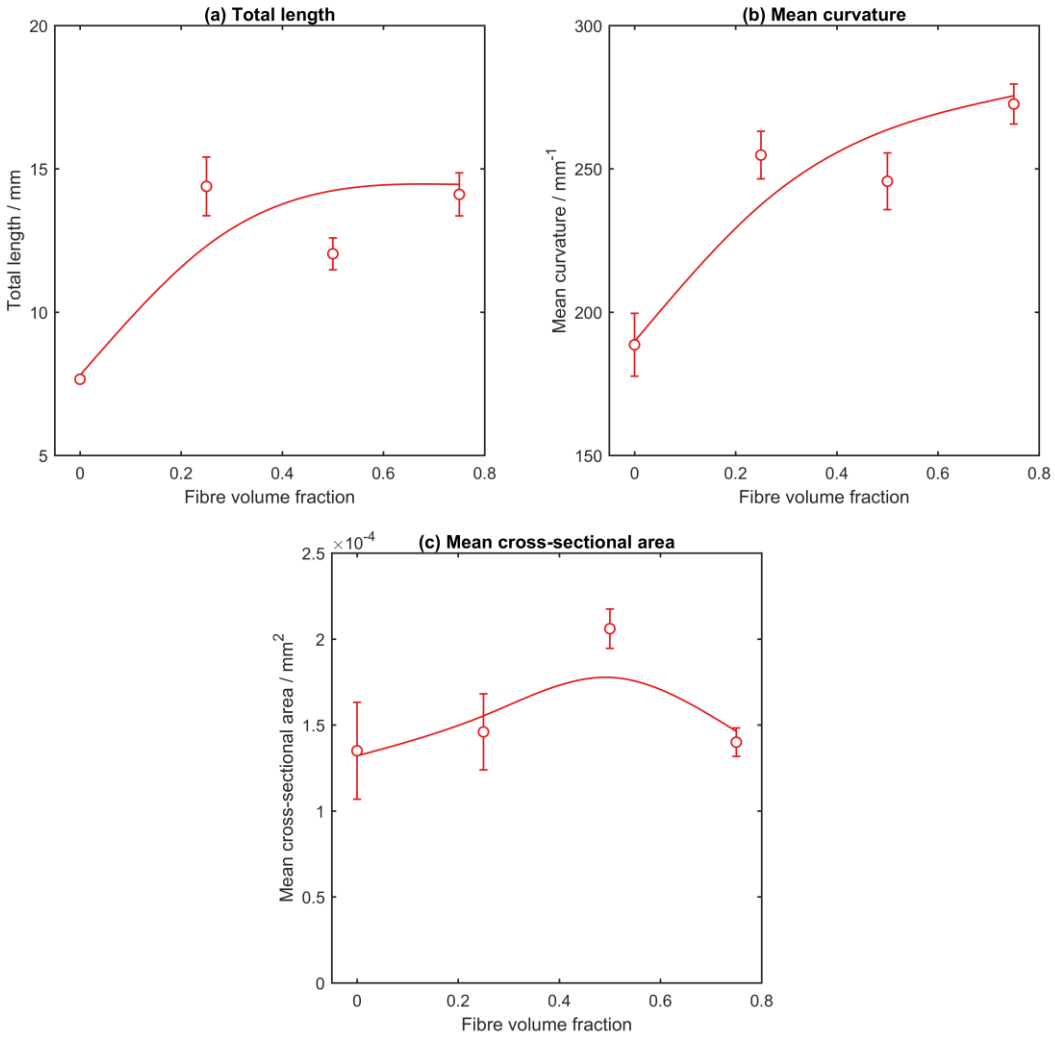

Figure 5.7: The variation of (a) total length, (b) mean curvature and (c) mean cross-sectional area with respect to fibre volume fraction for centreline networks generated from tomographic volumes.

The plots in Figure 5.7 have error bars defined as the standard error in the mean across the six samples that were tested at each fibre volume fraction. The fit lines passing through the points are simple smooth spline fits.

Beginning with Figure 5.7a, there is a possible trend for the total length of pores within the 100 µm cubes to increase with increasing fibre volume fraction. This is what

would be expected, since a volume of fibres will have more routes through the structure than that of particles, in the case where the particles are much larger than the fibre diameter. A large increase would be expected initially as the first few fibres are added, since bridging fibres will divide pore channels between particles. The effect would expect to plateau at higher fibre fractions since when the composite is fibre-rich there are already many channels between fibres, and additional fibres will have relatively little effect. The point at 25 wt.% seems to be larger than expected, perhaps due to the inhomogeneity that was mentioned earlier, resulting in regions of high fibre content to be analysed at the expense of areas of high particle concentration.

Figure 5.7b shows the mean curvature of the pores, measured in mm^{-1}, as the inverse of the radius of curvature. Again, an increasing trend is observed, suggesting that as the fibre content is increased, the fluid flow through the structure becomes more tortuous; this is expected, since the fibres will disrupt flow around the particles. The value at 25 wt.% is again higher than would be expected, but this will be due to the same reason as for Figure 5.7a, and it is unsurprising to see that the mean curvature follows the same trend as the total length of the network. Both results imply a more tortuous structure as the fibre volume fraction is increased.

Figure 5.7c shows the cross-sectional areas of the lines that are used to construct the pore network. The mean cross-sectional area would be expected to follow a decreasing trend with fibre volume fraction since fibres may fill in gaps between particles, especially if they have a small aspect ratio, which would lead to a decrease in the cross-sectional area. On the contrary, as the fibre volume fraction is increased, the fibres will act to separate the particles, and so potentially increase the mean cross-sectional area. The results show that neither of these competing effects seems dominant, and the cross-sectional area appears approximately constant.

5.5.3. Fluid flow simulation

The masks analysed in the previous section were also used to generate meshes that could be exported into computational fluid dynamics (CFD) modelling software, COMSOL. A steady state laminar flow CFD model was implemented such that one face

was assigned to be the inlet, with a mass flow-rate of air of 1 x10^{-11} kg s^{-1} across the entire surface, and the opposite face was the outlet, which was assigned a pressure of 0 Pa (as a reference pressure). At all other walls, including the internal structure wall, a no-slip boundary condition was applied.

The laminar flow was modelled on the Navier-Stokes equations. These are conservation equations that govern fluid dynamics in the form of coupled non-linear partial differential equations:

$$\rho \frac{du}{dt} = -\nabla p + \eta \nabla^2 \underline{u} + \underline{F} \tag{5.1}$$

$$\nabla . \underline{u} = 0 \tag{5.2}$$

where ρ is the density of the fluid, u is the velocity of the fluid, η is the coefficient of viscosity, p is the pressure acting on the fluid, and $\underline{F}$ represents the contributions of internal and external forces. An example volume for each fibre volume fraction is shown in Figure 5.8.

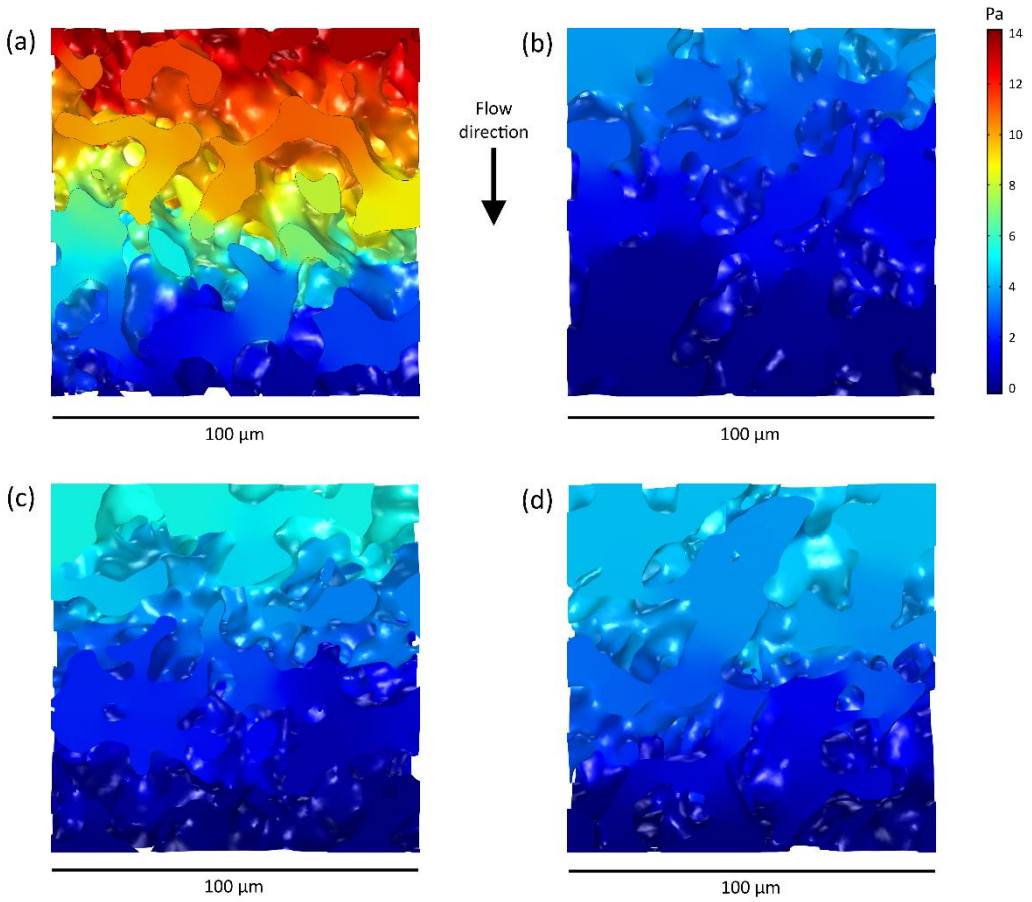

Figure 5.8: Pressure simulation across volumes with fibre volume fractions of (a) 0 wt.%, (b) 25 wt.%, (c) 50 wt.%, and (d) 75 wt.%.

Each volume has a similar pressure drop of around 5 Pa except for the 0 wt.% sample, which developed a significantly higher back-pressure of 14 Pa; this is considered further in Figure 5.11.

A value for the permeability could be measured in two different ways. The first assumes that Darcy's Law (Equation 3.3) is applicable in this situation, so that by using the pressure gradient, the viscosity of the air, and the average velocity throughout the volume, all of which are calculated by COMSOL, a permeability can be estimated. The second method uses the Carman-Kozeny equation (Equation 3.5). This requires the porosity and specific surface area, both of which can be measured precisely either in ScanIP or COMSOL, and an estimate for the dimensionless tortuosity constant, λ, which

was assumed to have a value of 5. Note that this second calculation, unlike the first, does not require solving of the fluid flow model. The permeabilities calculated by these two methods, in addition to the values measured experimentally are shown in Figure 5.9.

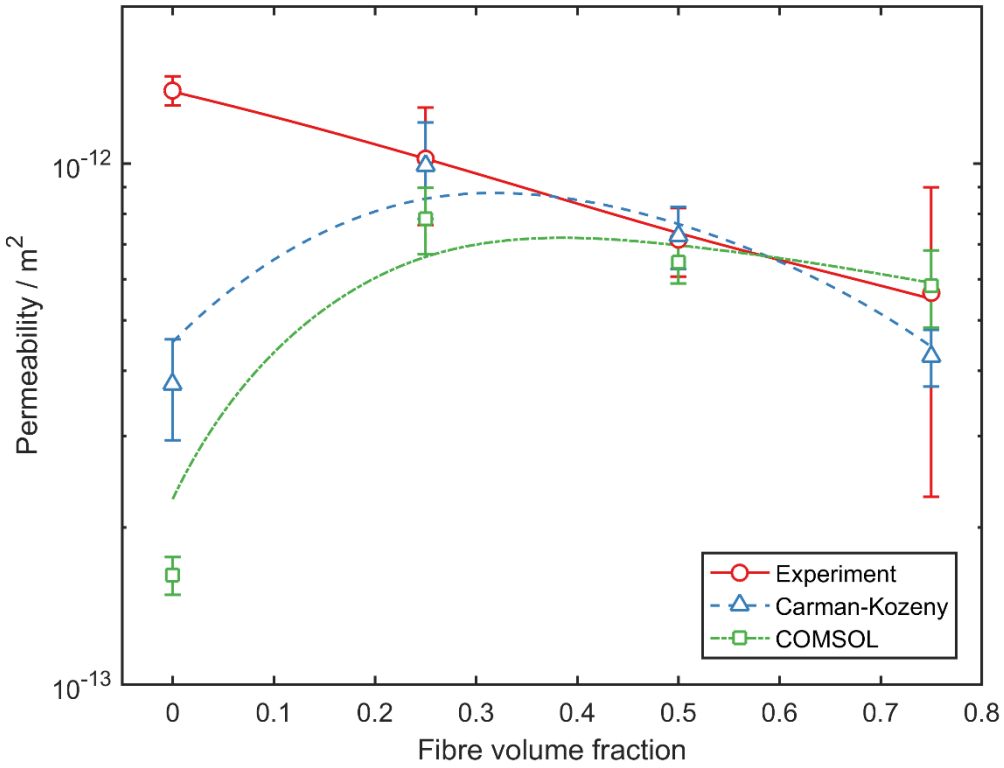

Figure 5.9: Variation of permeability with respect to fibre volume fraction as measured by experiment, predicted by Carman-Kozeny and calculated from COMSOL CFD simulations using Darcy's Law.

The permeability results agree within experimental error for fibre volume fractions of 25 wt.% and above. However, there is a large discrepancy in the results at 0 wt.%. At higher volume fractions, all seem to predict a decreasing permeability with increasing fibre content, which is to be expected due to the large increase in specific surface area achieved by higher fibre volume fraction samples. The deviation at 0 wt.% is difficult to explain. There are no small fibres and so, of all the structures, this structure should have been captured most accurately by the tomography scanner. The porosities of the tomographic volumes were lower than the experimentally measured porosities (36.9 % compared to 46.5 %), but the porosity was systematically measured to be 10 % lower for

every fibre volume fraction. It is possible that the discrepancy is due to the thresholding (recalling the issue highlighted in Figure 5.5), but this would seem to affect volumes of all fibre volume fractions.

The reason for the discrepancy might come down to the inhomogeneity of the structures. As mentioned previously, the fibres tend to be segregated into clumps surrounded by particles. Although samples were picked randomly from within the volumes (using coordinates generated from a random number generator), the volume was rejected if the volume included any empty space from outside the sample. However, due to the fibre clumps, the centres of the volumes tended to contain more fibres than the edges, and so for volumes selected from 25, 50 and 75 wt.% samples there may have been a bias towards fibre-rich volumes. This bias does not exist within the 0 wt.% sample, as there is no inhomogeneity (as the sample contains only particles).

Another possible explanation could be due to the size of the volumes having more of an effect for the coarser microstructure of the 0 wt.% sample. The selected volumes were only 100 µm cubes, which may be too small when considering 30 µm particles but becomes more reliable when analysing fibres with diameter of 3 µm.

From the fluid flow simulations, it was possible to measure a back-pressure by considering the average pressure on the inlet surface, since the outlet was set to have a reference pressure of 0 Pa, the back-pressure is shown in Figure 5.11.

These fluid flow simulations were then coupled with a particle tracing interface. A one-way coupling was used so that the flow rate affected the particles, but the particles did not affect the flow rate. Ideally, this coupling would have been in both directions, such that the accumulation of soot particles also affected the fluid flow, and the effect of soot cake formation could be observed. However, due to a lack of computational power, only a steady state fluid flow could be modelled.

Single spherical particles with a diameter of 0.015 µm (corresponding to the average size of a nucleation mode particulate from a diesel engine exhaust, see Figure 1.2), were "injected" at the inlet at uniform time intervals with random spatial placement with a velocity of 0.1 m s^{-1} at an initial temperature of 500 K. A drag force was assumed to be

acting on them, modelled by a Stokes velocity, and gravity was ignored. Examples of the resulting particle traces are shown in Figure 5.10.

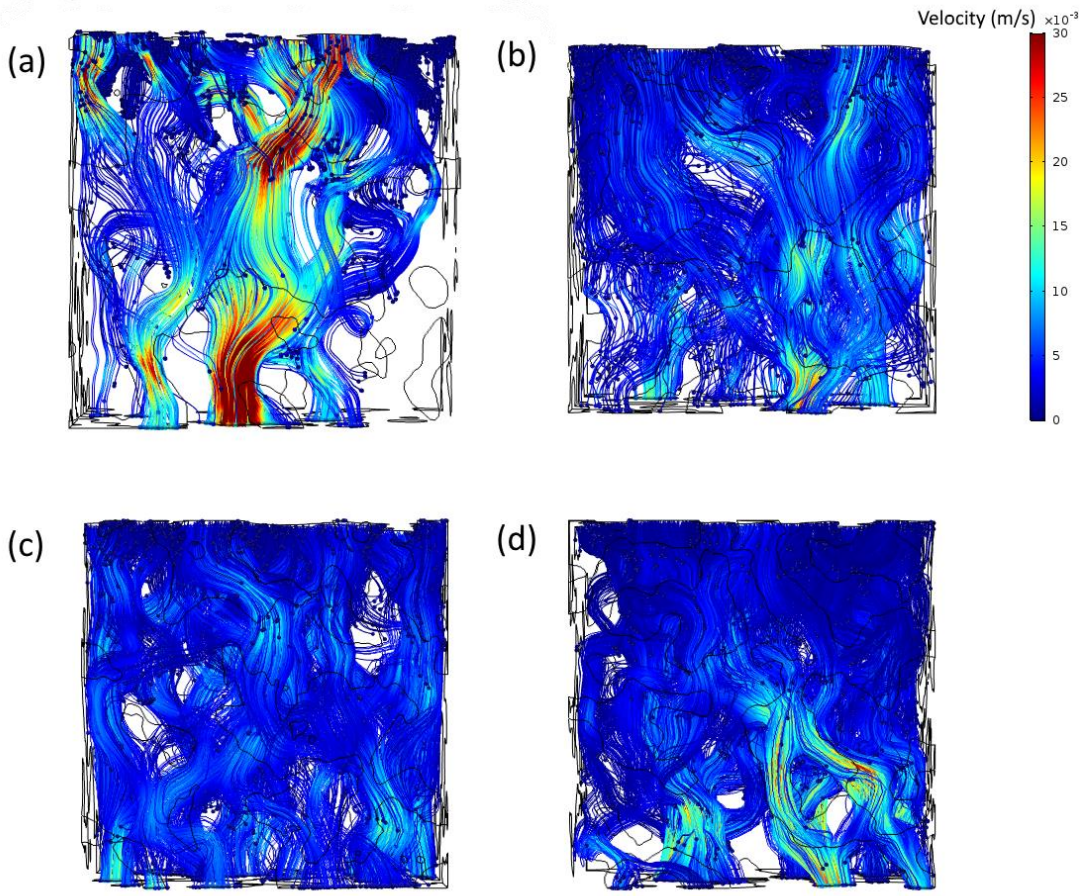

Figure 5.10: Particle trajectories for four volumes with fibre contents of (a) 0 wt.%, (b) 25 wt.%, (c) 50 wt.%, and (d) 75 wt.%.

The particle traces certainly look quite different for different fibre volume fractions. Most obviously, the 0 wt.% volume looks very different from the other three (and this was true for all volumes). In this case, there seems to be fewer possible paths for the particles to take, and consequently the speed of the particles passing through the filter was much greater than in the fibrous composites. Upon adding fibres (25 wt.%) there appear to be many more paths through the structure and as such the speed of the particles reduces. This effect can be explained by considering that the fibres will space out the particles. This trend continues to 50 wt.%, but when the fibre content is increased to 75 wt.% the

paths become more defined again and the particle speed increases. This could be evidence of the fibres now filling too much of the gaps between the particles. The composite has changed from fibres within a particle matrix to particles within a fibre matrix.

It was then possible to monitor the number of particles that made it to the outlet and the number of particles that hit the inside walls, where it was assumed that 100 % of particles were stopped on hitting the walls of the filter, probably a valid assumption due to the highly adhesive nature of the particles [164]. This ratio was used to approximate the filter efficiency, although all results are semi-quantitative at best. The results are plotted on Figure 5.11, alongside the back-pressure measurements.

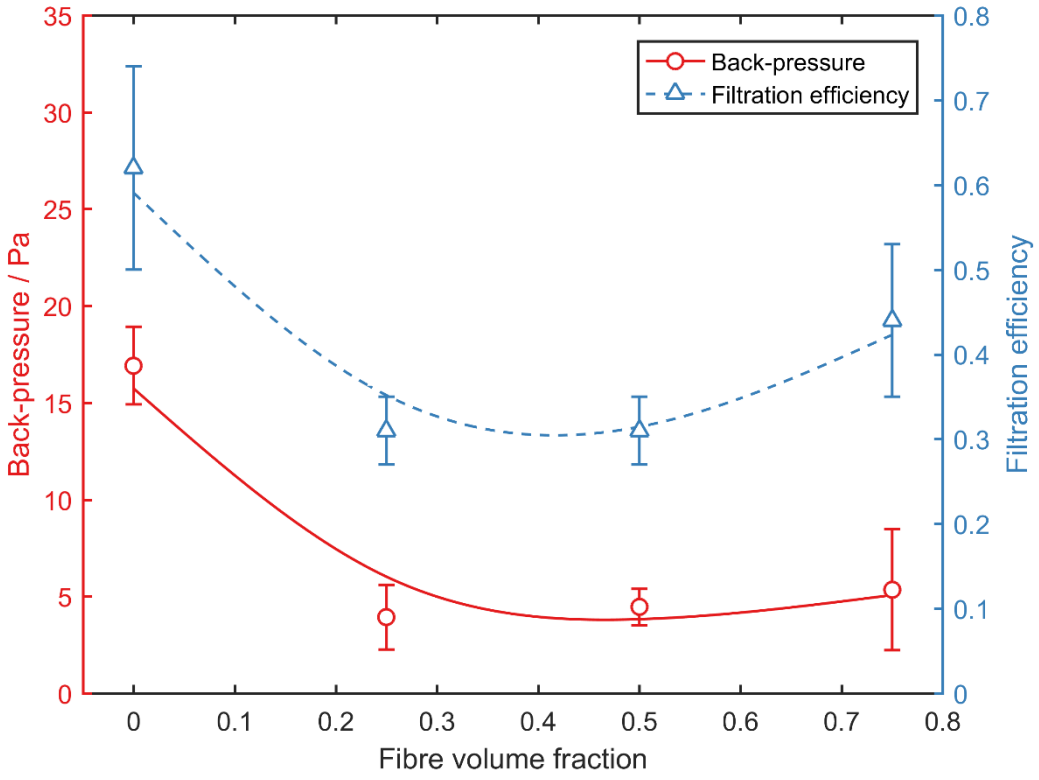

Figure 5.11: Variation of both back-pressure and filtration efficiency as measured by COMSOL CFD simulations.

The modelled "filtration efficiency", defined as the ratio of particles that impacted on the internal structure of the 100 µm cube to the sum of the number that made it through plus the number that were stopped (which is not the same as the total number of particles

introduced, since any particles that left via the side walls were discounted from the calculation), resulted in low numbers for the filtration efficiency (30–60 %). This is not surprising for two reasons. Firstly, the particles followed a steady-state laminar flow, allowing for little movement perpendicular to the fluid flow. If the flow had been turbulent, much more deposition could be expected, but with a large increase in back-pressure. Secondly, and fundamentally for all DPFs, the filtration efficiency of a clean filter is low. It is not until a significant soot cake layer has formed that the filtration efficiency increases (see Figure 1.9). The filtration efficiency of a new commercial filter can be as low as 40 % [42], similar to the measured values above.

With the exception of the 0 wt.% samples, the back-pressure was observed to remain approximately constant with respect to fibre volume fraction. Within experimental error, the same could be said about the filtration efficiency, but there does appear to be a slight upwards curve to the data. These results should be taken as being a basic analysis of filtration efficiency, especially as the small diameter of the fibres means that the tomography will not have properly captured the structure entirely. However, it is certainly encouraging to see that the inclusion of more fibres appears to increase filtration efficiency, whilst not affecting the back-pressure significantly.

Once again, the results at 0 wt.% seem higher than expected, and this could be due to the same reasons as noted in the case of the permeability; a problem either with inhomogeneity or volume size. However, by looking at the particle traces in Figure 5.10, it is unsurprising to see that the back-pressure and filtration efficiency might be higher for the 0 wt.% samples. The particles are confined to a lower porosity, and there are fewer possible routes through the structure. Back-pressure would then be expected to decrease as the particles are separated by the fibres, but then increase again as there are enough fibres to fill the gaps between the particles.

It is also worth noting that, whilst several volumes were taken from within the scanned sample, the sample itself was always the same, and the small crumbs that were analysed may not have been representative of the overall structures. This is, of course, true for all the samples.

5.6. Conclusion

Whilst it was impractical to measure a filtration efficiency experimentally, other properties were evaluated to indicate how the filtration might be affected. Porosity and permeability were both measured and, as with the first-generation materials, the porosity was observed to increase with increasing fibre content, from 48 % at 0 wt.% fibres to 59 % at 100 wt.% fibres. This exactly matched the results of Liu *et al.* who reported the same values for a commercial particle-based cordierite filter and a fibrous cross-linked cordierite matrix [83]. However, the permeability showed a different trend: decreasing as fibre content increased, although all measured permeabilities were on the order of 10^{-12} m^2, comparable to commercial filters [35]. This difference from the results from the first-generation of materials can be attributed to the larger difference in size between the particle and fibre diameters which will result in a more significant increase in the specific surface area.

A lower permeability would directly lead to an increase in back-pressure, which is not good, but also would indicate that a higher filtration efficiency might be attained.

Tomographic evidence actually predicted a decrease in back-pressure upon the addition of fibres. However, there was little change of back-pressure once any fibres were present and, with increasing fibre content, the particle tracing analysis suggested that the filtration efficiency of a clean filter could improve with more fibres, although it might not reach the efficiency of a filter with no fibres. The tomography also predicted an increase in pore channel length and curvature with increasing fibre content implying a more tortuous microstructure, which is also beneficial for an increased filtration efficiency.

The experimentally obtained values of porosity and permeability are the most reliable results presented in this chapter. Whilst tomography is a viable technique for such analysis, the small fibre diameter (3 µm) compared to the resolution of the CT scanner (0.5 µm) meant that complete capture of the structure was not possible. In addition, the inhomogeneity of the samples require that many more volumes should be analysed, both within a single crumb and ideally from several crumbs per fibre volume fraction.

6. Simulation of flow within a sphere and cylinder model

6.1. Introduction

Since the resolution of the tomography work made reliable capture of the pore architecture rather marginal, a new method was considered: rather than attempting to capture the structure, the structure was generated artificially by modelling the particles and fibres as simple spheres and cylinders.

There have been several attempts to simulate the permeability of the wall of a DPF [118-121]. Usually this assumes that partially sintered particles form the matrix, although some studies, outside the field of DPFs, have considered a fully fibrous structure [125-128]. However, there was no evidence in the literature of combining particles and fibres in the same model. This work therefore concentrates on this hybrid regime, allowing a range of porosities and fibre contents to be investigated by varying the number of particles and fibres within a volume. By altering the size of the particles and fibres, the effect on the permeability can also be observed.

Fluid flow in this chapter is simulated by solving the Navier-Stokes equations, as introduced in the previous chapter when considering tomography (Equations 5.1 and 5.2). The use of the Navier-Stokes equations can be compared to the Lattice Boltzmann Methods which were discussed in Section 1.5.3 and are commonly used in the literature for solving fluid flow through DPFs. There is no definite answer as to which approach is better; in general, LBM offers more, especially if non-Newtonian or multiphase flow (e.g. liquid and gas) is required, but for the case of homogeneous flow through a porous

structure, the Navier-Stokes equations will offer equivalent results with comparable computational speed [165].

6.2. Generating structures

MATLAB was used to generate random distributions of particles and fibres. For importing into COMSOL, each particle is specified by the three coordinates of its centre and a radius, which was taken to be the same for all particles so as to minimise the number of parameters. Each fibre required six parameters to specify its position, three to place the coordinate of one end of the fibre, and a further three to specify the orientation from that position, expressed as a vector in cartesian space. Again, in order to minimise the number of parameters needed to be imported into COMSOL, all the fibres were taken to have the same length and radius. In future work, and using more powerful computing, this could be extended to have a size distribution of both particles and fibres. Since the generated structures were created with simple spheres and cylinders, there was also no inclusion of any surface roughness, or curvature to the fibres. When compared to SEM images of experimental samples, e.g. in Figure 6.1 below, the former is certainly a large assumption, but the latter seems to be a good approximation. Fibre curvature is not expected to be a problem, since Nabovati *et al.* showed that the effect of fibre curvature on the overall permeability of a fibrous medium can be considered negligible [125].

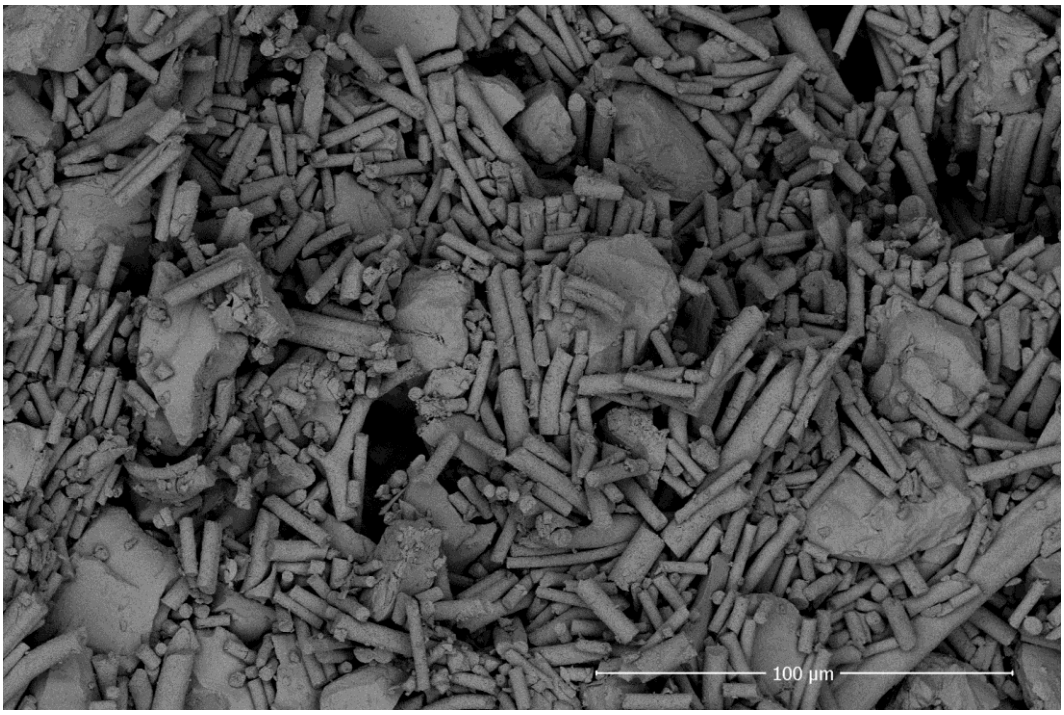

Figure 6.1: Back-scatter detector image of experimental sample with fibre volume fraction of 50 %. Fibres can be seen to be approximately straight, and particles are approximately spherical.

The MATLAB script used for generation of the structures worked by calculating the number of spheres and cylinders which were required to make a best approximation of a specified fibre volume fraction and porosity within a predetermined cubic volume. The particles were placed into the volume first. Each one was inserted individually by taking a random set of coordinates and calculating the distance between that new sphere's coordinates and any existing spheres in the system already. If the minimum distance between its coordinates and any other sphere's coordinates was greater than the sphere diameter minus an allowed overlap (taken to be 2 µm for the 30 µm diameter spheres, as a model of sintering, see Figure 6.2a for a schematic representation) then the position of the new sphere was accepted. If the minimum distance was less than this, there was assumed to be too much overlap between the particles and the sphere was rejected and the next randomly positioned sphere was trialled. This process was repeated until the desired number of particles were included within the volume.

Periodic boundary conditions in all three directions were also included during this stage, so that any accepted sphere led to 26 further spheres being added into equivalent positions in the 26 cubes surrounding the central volume of interest.

Once the particles had been inserted, the fibres were added. This process was similar, but slightly more complicated. Again, the cylinders were trialled one at a time, with randomly-decided positions and orientations. However, the acceptance criterion this time was that the new cylinder must touch at least one sphere and/or an already accepted cylinder. By using this method, it ensured that after only a few fibres were added, all the particles and fibres were connected into one structure, realistic of the real-world situation. Again, the overlap was controlled, fibres were only allowed to overlap into other fibres or particles by 2 μm, representative of a certain degree of sintering. If the minimum distance of any part of the fibre to any other part of another fibre or particle resulted in more overlap than this, or if there was no overlap at all, the fibre was rejected, and a new random fibre tested. Again, periodic boundary conditions were maintained by copying every accepted fibre into the 26 surrounding volumes.

Once all the fibres had been added, the number of particles and fibres was cropped down to a small volume, containing all fibres and particles which have any influence on the central volume. It was difficult to do this with full confidence without including some unnecessary fibres and particles, but simply including any particles with centres contained within the desired volume with a margin of one particle radius on each side was sufficient for the particles. For the fibres, if any part of the cylinders fell inside a sphere with radius equal to half the face diagonal of the cube plus one fibre radius, they were included in the cut. These two methods ensure all necessary particles and fibres were included, albeit with a few that were unnecessary.

In addition to the above acceptance criteria, another further requirement was that there was a minimum tolerance as to how close to a volume boundary a fibre or particle could be. COMSOL struggles when there is a very thin wall and so a minimum tolerance was also defined, such that if two objects were within this minimum tolerance, either of each other or of the walls of the volume, they were also rejected. In all models, this minimum tolerance was set to be 1 μm, the consequence of which is that no two non-touching

objects will be within 1 µm of each other, nor the volume walls, as shown schematically in Figure 6.2b.

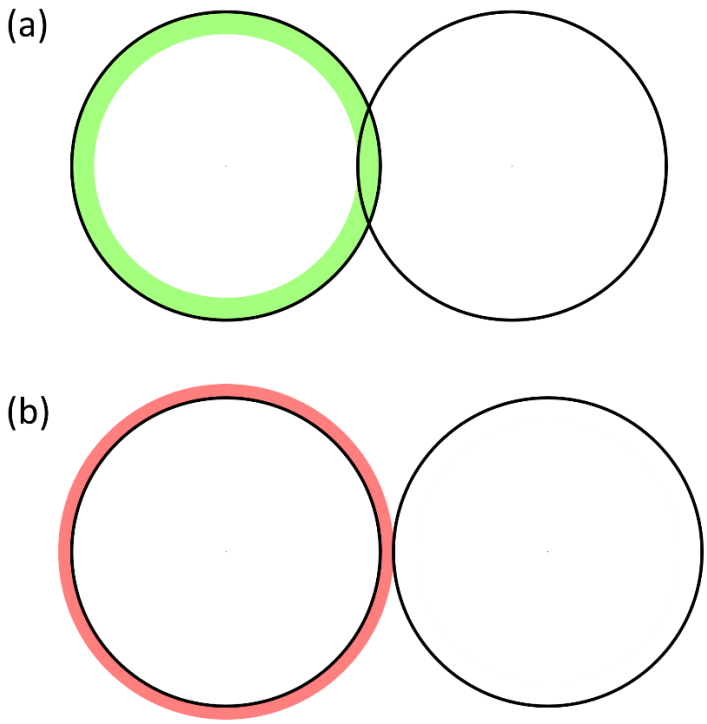

Figure 6.2: *(a) Two-dimensional interpretation of the allowed overlap of two particles, taken to be 2 µm, which can also be extended to fibres. The two circles show the maximum allowed overlap; anywhere within the green shaded region is acceptable, but if the circles were any closer, then the new circle would be rejected, and a new particle trialled. (b) A minimum tolerance was defined such that non-touching particles, fibres and volume boundaries would not be within 1 µm of each other. The circles above define the minimum distance between two non-touching circles, and if they were any closer whilst still being non-touching (the red shaded area), the new particle or fibre would be rejected.*

Once the positions of all these spheres and cylinders were determined, they were exported as an Excel file, with all the parameters listed: the number of spheres, the number of cylinders, the radius of all spheres, the radius of all cylinders, the length of all cylinders, and then the coordinates and orientations of each cylinder and sphere to be imported.

Determined by the porosity, fibre fraction and size of the cubic volume, spheres and cylinders, the number of imported parameters varied between 23 and over 10 000.

A summary table was also created, since in total more than 2 000 volumes were generated this way. The summary table kept a record of the cube volume, the size of the cylinders and spheres, the actual porosity and fibre fraction, which could differ quite significantly from the input, the numbers of fibres and particles in the volume and the number of parameters in the Excel file. The number of fibres and particles in a given volume were always integer, since the periodic boundary conditions meant that any fibre or particle which overlapped with the box boundary was accounted for by the rest of the volume on the other side of the cube.

By analysing the summary table, some key samples were chosen, since it was simply not possible in any reasonable timescale to analyse all the data using COMSOL. The first difficulty arose when trying to import large numbers of parameters into COMSOL. Through trial and error, it appeared that there is a limit to the number of parameters COMSOL can import, and this limit is due to the memory storage on the computer. Using an 8 GB RAM computer, this limit was found to be at 1859 parameters. Since it takes six parameters to specify each fibre, and because the fibres in this model had a smaller volume than the particles, this meant that higher fibre fractions and lower porosities were impossible to measure on this computer. This limited the range of fibre fractions to an upper limit of 0.5 (50 %). It's also interesting to note that the porosities and fibre fraction values were not at all independent. Figure 6.3 shows the full range of data sets for the case where particles had a diameter of 30 µm, and fibres had length and diameter of 30 µm and 3 µm respectively.

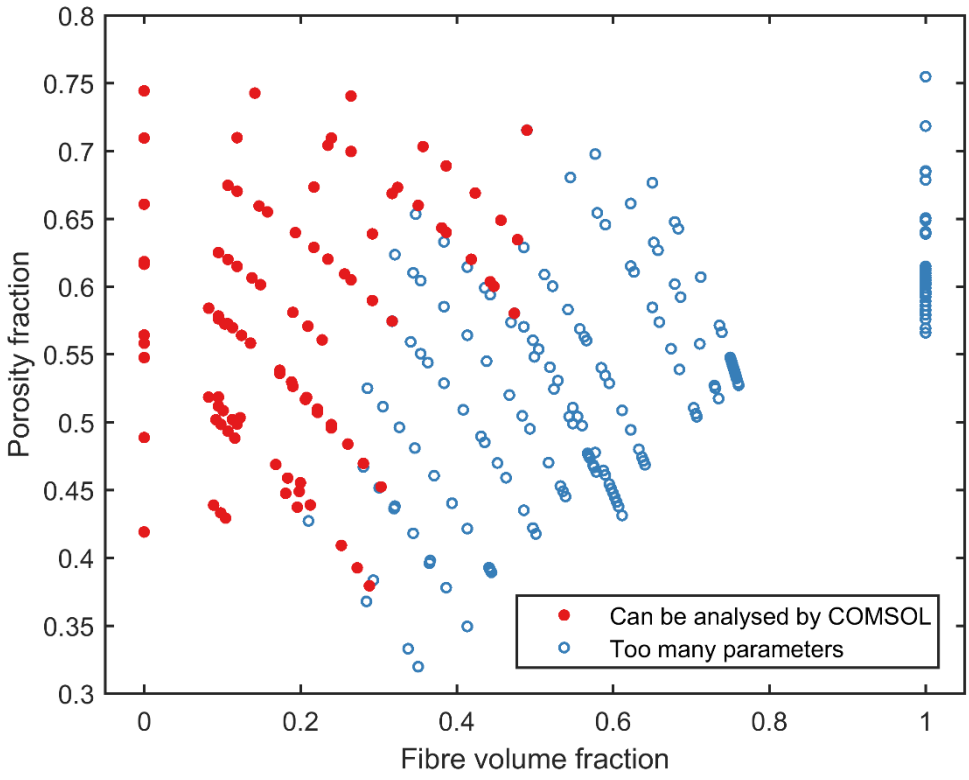

Figure 6.3: *The full range of volumes generated for the case where the particle diameter, fibre length and fibre diameter were 30, 30 and 3 µm respectively. The red data points are the only ones that could be analysed using an 8 GB RAM. A more powerful computer would be able to analyse higher fibre volume fractions.*

There are obvious paths that these points form through the space of porosity and fibre fraction, due to the integer nature of the objects in the volume. Each line represents an integer number of spheres; as fibres are added, the porosity decreases, and the fibre fraction increases, and so the lines curve down towards high fibre fractions and low porosities. It is also apparent that, due to the integer requirement for spheres in a given volume, it is difficult to enter the region between fibre fractions of around 0.8 to 1.0 due to the jump from a single sphere to no spheres. To enter this region, larger volumes would need to be analysed, but this would require more parameters than COMSOL can handle on a computer with 8 GB RAM.

For selected volumes, the coordinates of all the spheres and cylinders were imported into COMSOL using the application builder feature. By recording the method to add

single spheres and cylinders it was possible to enter the java script within the application builder to insert some simple "for-loops", such that all the cylinders and spheres could be imported within seconds. At this point, the imported sample would look like Figure 6.4: a unit cell of a generated structure designed to mimic the experimental materials, e.g. Figure 6.1.

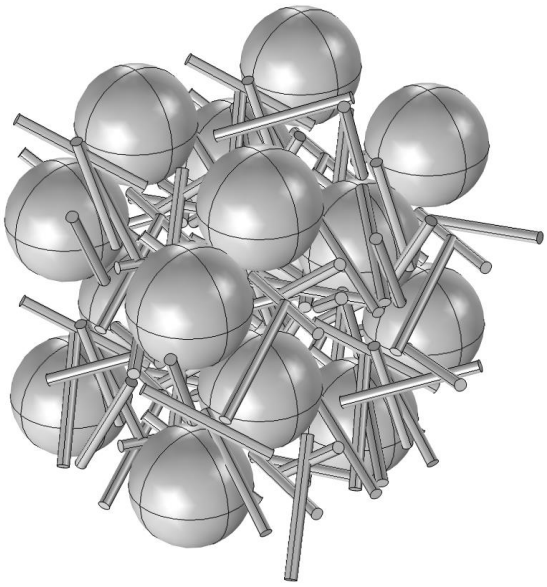

Figure 6.4: Imported structure of spheres and particles. This particular volume has the periodic repetition of a 50 µm cube and contains 30 µm diameter spheres and fibres of length and diameter of 35 and 3 µm respectively. Its porosity is 62.6 % and fibre volume fraction is 0.10.

The periodicity introduced into the structure by the imposed boundary conditions could lead to some artificial channelling effects in the fluid flow. However, some preliminary two-dimensional tests showed that this did not significantly affect the permeability results.

The region of interest is, of course, not the fibres and particles themselves, but rather the space between them. Therefore, it was necessary to convert to the negative of this structure. A block of the same dimensions of the cube of interest was added to the

geometry, and the spheres and cylinders were subtracted from this volume using the difference function. A mesh could then be generated automatically. Wherever possible, boundary layers were included to improve the fluid flow calculations around the surfaces of the objects in the volume. However, in the majority of cases, it was difficult to include these boundary layers, due to objects being too close together. This could perhaps be corrected in the future by including a larger minimum tolerance than 1 µm mentioned above, although increasing this value risks influencing the packing of objects within the structure. For those volumes where boundary conditions were possible, the values calculated were identical whether boundary layers were included or not. Many simulations of DPF pore structures in the literature use Lattice Boltzmann Methods (LBM), which do not use boundary layers. Therefore, the lack of boundary layers was not considered an issue in the other samples. Figure 6.5 shows the final meshed volume created from the cylinders and spheres in Figure 6.4, including a close-up of the mesh to show the boundary layers in this example. Periodic boundary conditions can also be observed.

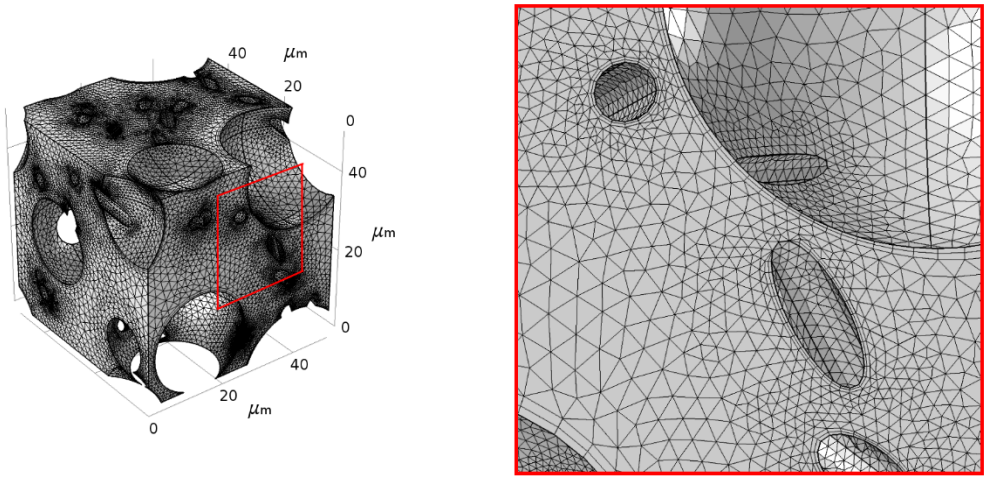

Figure 6.5: Finalised mesh of air volume surrounding the assembly of particles and fibres in Figure 6.4. The volume has periodic boundary conditions and in this case boundary layers were present.

There were often problems associated with the meshing procedure, occurring mostly when COMSOL struggled to deal with two just-overlapping objects. Rather than cutting away the overlapping region, as should be done in the subtraction step of structure generation, the two overlapping surfaces were kept. When COMSOL then attempts to mesh the structure, it encounters overlapping boundary elements, an example of which is shown in blue in Figure 6.6.

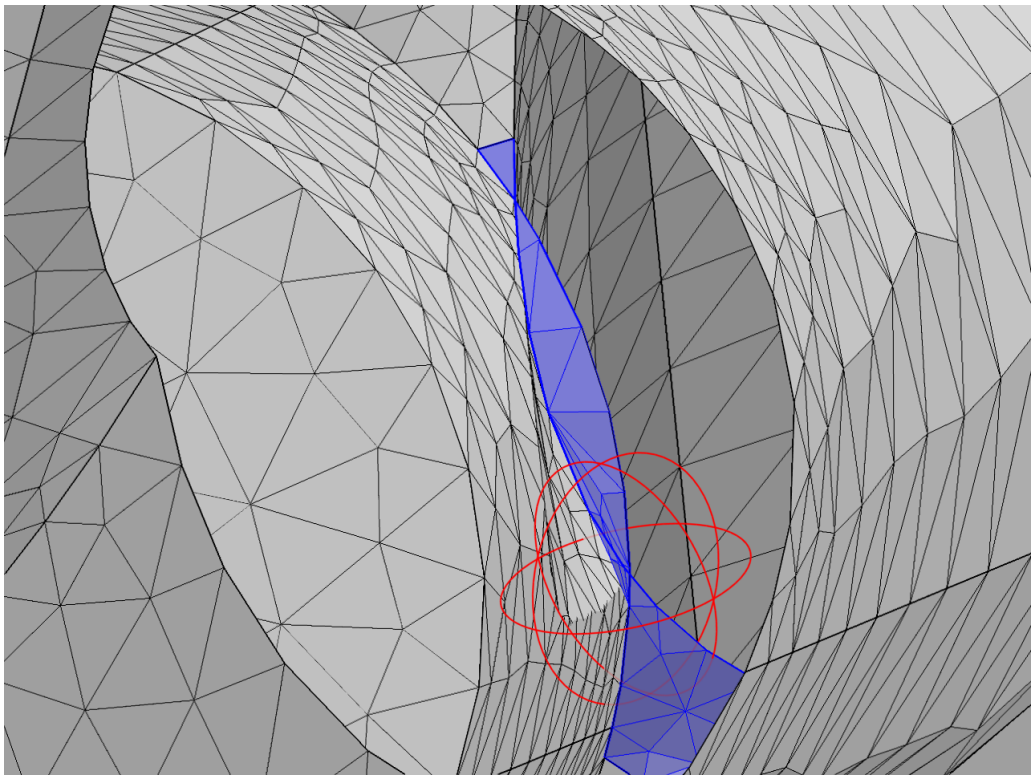

Figure 6.6: Problems with mesh generation were caused by overlapping mesh elements

This overlapping region can be fixed manually by finding the coordinates of the problem, which are recorded in an error message by COMSOL, and placing a small sphere (radius < 1 μm) at those coordinates and subtracting the sphere from the volume. This small removal refreshes the structure in this region, and removes the whole problem, even if the sphere only intersects with a small region of the problem, e.g. a sphere contained within the red lines would solve the whole problem in Figure 6.6. This will inevitably have a small impact on the volume and surface area estimates of the structure but, as the introduced spheres are so small, it can be considered negligible. It was common for volumes to have at least one problem like this, but rarely as many as five or more.

With the mesh generated, a time-independent laminar flow study was investigated. The fluid was set to have the properties of air, which are pre-defined within COMSOL. Laminar flow is a safe assumption for these models, since analysis by Dwivedi and Upadhyay [166] showed that for flow through a packed bed, the dimensionless Reynolds number is given by:

$$Re = \frac{\rho \, v_s \, D_p}{\eta} \tag{6.1}$$

where ρ is the density of the fluid (kg m^{-3}), v_s is the superficial velocity (m s^{-1}), i.e. the inlet velocity, D_p is the diameter of the particles of which the packed bed is composed (m), and η is the dynamic viscosity of the fluid (Pa s).

If the air is assumed to be at around 500 K (approximately exhaust temperature under normal operating conditions), the density and viscosity have values of around 0.7 kg m^{-3} and 27 µPa s [167] respectively. Assuming an inlet gas velocity of 0.1 m s^{-1} (again, approximately normal exhaust conditions), and a particle diameter of 30 µm, the Reynolds number is around 0.08, safely below the lower bound cut off for the laminar to turbulent transition of around 10 [168].

For each volume, the initial conditions were set up such that on one side of the cube there was a constant inlet velocity of 0.1 m s^{-1}. The outlet on the other side of the cube was set to have 0 Pa pressure, such that the average pressure on the inlet face would be a direct measure of the back-pressure across the volume. The periodic boundary conditions were set up such that fluid was free to flow between the two other sets of parallel faces of the cube. Unfortunately, periodic boundary conditions in the inlet/outlet faces was not possible due to computation limitations, but in future work it could be useful to consider that the inlet velocity is dependent on the outlet velocity, therefore getting a more accurate bulk response from the material.

Each volume was tested across at least three directions (flowing from positive X, Y and Z to negative X, Y and Z respectively), and in some cases all six directions were tested (the three opposite directions in addition to those above). An example of the velocity and pressure results are given in Figure 6.7. In each case, a permeability was

measured by using Darcy's Law (Equation 3.3) evaluated at the inlet surface as this gives a value of the pressure gradient, the viscosity of the air, which is a constant across the volume, and the average velocity throughout the volume, which in steady state is the same as the inlet velocity, 0.1 m s^{-1}. Also at this inlet surface, the average pressure was recorded. In addition to these solutions to the fluid dynamics simulations, the volume of the structure (i.e. a precise measure of its porosity) and surface area were computed.

From the precise values of porosity and surface area, a predicted permeability using the Carman-Kozeny equation could be determined, in addition to the permeability calculated by COMSOL.

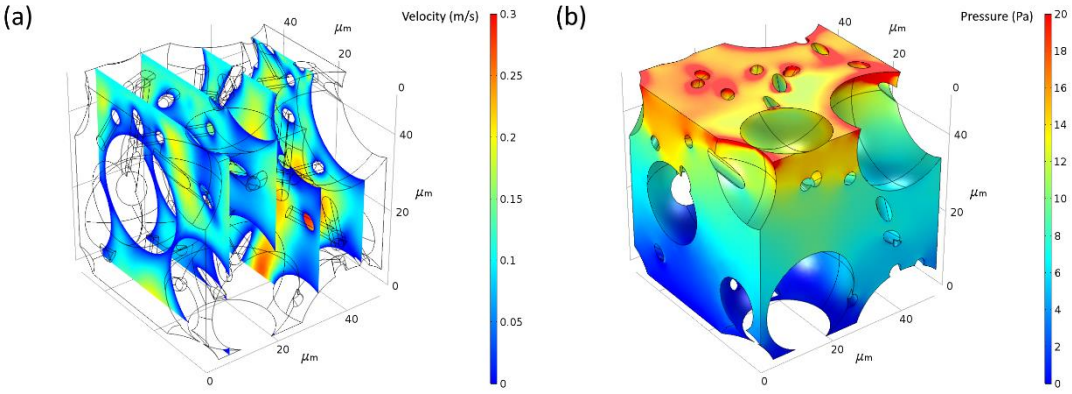

Figure 6.7: (a) Velocity slices and (b) Pressure surface from mesh created in Figure 6.5.

6.3. Simplification and adaptation of the Carman-Kozeny equation

The Carman-Kozeny equation is used for predicting the flow through a packed bed of particles. It is often written in a form similar to that found in the Unit Operations of Chemical Engineering by McCabe *et al.* [169]:

$$\frac{\Delta P}{d} = \frac{150\, v_s\, \eta}{\Phi_s^2 D_p^2} \frac{(1-\varepsilon)^2}{\varepsilon^3} \qquad (6.2)$$

where $\Delta P/d$ is the pressure gradient (Pa m^{-1}), v_s is the superficial velocity (m s^{-1}), η is the dynamic viscosity (Pa s), ε is the porosity, Φ_s is the sphericity of the particles forming

the packed bed and D_p is the sphere equivalent diameter of the particles (m). This is a useful form of the equation because all the inputs are easily measurable by experiment. However, it can be simplified in this case because the internal specific surface area ($m^2\ m^{-3}$) is known as an output from COMSOL. In this case it is possible to remove the factors of the sphericity and sphere-equivalent diameter (although these can be calculated for the cylinders in the COMSOL model).

The derivation of the Carman-Kozeny equation starts by assuming that the cavities through which fluid will flow can be modelled as simple pipes with surface area and volume equal in the two cases, as shown in Figure 6.8.

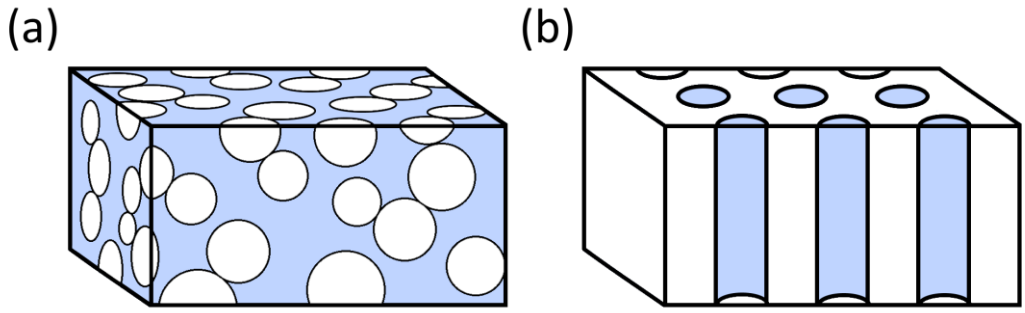

Figure 6.8: (a) Actual shape of void in a packed bed. (b) Modelling the same volume as equivalent pipes; the shaded areas have the same surface area and volume.

To find the flow through a pipe, using the Hagen-Poiseuille equation, an expression for the diameter of these pipes, and the velocity through them is required. The diameter can be calculated by considering that the two structures should have the same surface area and volume, leading respectively to the following two equations:

$$n\,\pi\,D_{eq}\,d = S\,A\,d \tag{6.3}$$

$$\frac{1}{4}\,n\,\pi\,{D_{eq}}^2\,d = A\,d\,\varepsilon \tag{6.4}$$

where n is the number of parallel channels, D_{eq} is the diameter of the channels (m), d is the thickness of the packed bed (m), S is the surface area per unit volume ($m^2\ m^{-3}$), A is

the surface area of the top surface of the packed bed (m^2) and ε is the porosity. This results in an expression for D_{eq}:

$$D_{eq} = \frac{4\,\varepsilon}{S} \tag{6.5}$$

The average velocity in the channels, $\bar{v}$, is proportional to v_s/ε, the superficial velocity (i.e. the inlet velocity) divided by the porosity. Inserting these values into the Hagen-Poiseuille equation gives:

$$\frac{\Delta P}{d} = \frac{32\,\bar{v}\,\eta}{{D_{eq}}^2} = \frac{\lambda\,S^2\,v_s\,\eta}{\varepsilon^3} \tag{6.6}$$

where λ has been inserted as a constant tortuosity correction factor, also incorporating a factor of 2. The literature shows that this value lies around 4 or 5 [48, 169], although the value will be examined in the results of this work.

Finally, by combining with Darcy's law (Equation 3.3), a very simple relationship between the permeability, κ, and porosity, ε, is found:

$$\kappa = \frac{\varepsilon^3}{\lambda\,S^2} \tag{6.7}$$

This is the form of the equation which was used in the experimental analysis in the previous chapters. Compared to the version of Carman-Kozeny above, this simplified version seems to be missing a factor of $(1-\varepsilon)^2$ on it's denominator. However, it can be seen below that this factor is actually contained within the value of S.

To try to find a more meaningful value of the surface area in this specific sphere and cylinder model without using sphericity, the actual surface area can be predicted. If no overlap between any of the spheres and cylinders is assumed, the specific surface area will be:

$$S = \frac{n_s\,A_s + n_c\,A_c}{V_T} \tag{6.8}$$

where V_T is the total volume of the cube, n_s and n_c are the number of spheres and cylinders contained within the volume respectively, and A_s and A_c are the surface areas of a single sphere or cylinder respectively. Recalling that n_s and n_c must be integers in this model due to the periodic boundaries, the two values can be expressed in terms of the fibre volume fraction, f, and the porosity, ε:

$$f = \frac{n_c V_c}{n_s V_s + n_c V_c} \tag{6.9}$$

$$1 - \varepsilon = \frac{n_s V_s + n_c V_c}{V_T} \tag{6.10}$$

Therefore n_s and n_c can be written as:

$$n_s = (1 - f)(1 - \varepsilon)\frac{V_T}{V_s} \tag{6.11}$$

and,

$$n_c = f(1 - \varepsilon)\frac{V_T}{V_c} \tag{6.12}$$

Substituting these expressions into the equation for S above, and by writing the areas and volumes of the spheres and cylinders in terms of their linear dimensions, the sphere diameter, D_s, cylinder diameter, D_c, and cylinder length, L, the equation for S, ignoring any overlap, becomes:

$$S = (1 - \varepsilon)\left[\frac{6(1 - f)}{D_s} + \frac{4f}{D_c} + \frac{2f}{L}\right] \tag{6.13}$$

This expression can then be substituted back into the simplified Carman-Kozeny equation (Equation 6.7) to get a predicted relationship between the permeability, porosity, and fibre content of a composite, dependent on the size parameters of the sphere and cylinder components, D_s, D_c and L. Rearranging the equation to get a linear relationship describing how porosity and permeability should vary as fibre content increased leads to:

$$\sqrt{\frac{\varepsilon^3}{\lambda\,\kappa\,(1-\varepsilon)^2}} = f\left(\frac{4}{D_c} + \frac{2}{L} - \frac{6}{D_s}\right) + \frac{6}{D_s} \qquad (6.14)$$

So, by plotting $\sqrt{\varepsilon^3/\lambda\,\kappa\,(1-\varepsilon)^2}$ against f, a straight line would be expected.

6.4. Permeability, back-pressure and lambda

Focusing on just the set of results where the spheres and cylinders were closely matched to experimental values, i.e. sphere-equivalent particle diameter of 30 µm, fibre diameter of 3 µm and fibre length of 30 µm, then it is possible to plot the variation of permeability, back-pressure and lambda as a function of both porosity and fibre fraction. The first two properties were those which were simulated by COMSOL, the value of lambda was obtained by using the simplified Carman-Kozeny equation, with the simulated COMSOL permeability, and the exact values of the specific surface area and porosity, measured on COMSOL.

The influence of porosity on both the permeability and back-pressure is clear, it is expected that as the porosity increases, then the permeability will also increase, and the back-pressure will decrease. However, it is not so clear what will happen as the fibre volume fraction is increased, whilst maintaining a constant porosity. The specific surface area will increase, and therefore a decrease in permeability and an increase in back-pressure might be expected.

The 3D surface plots of the variability of permeability, back-pressure and lambda are shown in Figure 6.9, Figure 6.10 and Figure 6.12 respectively.

Permeability

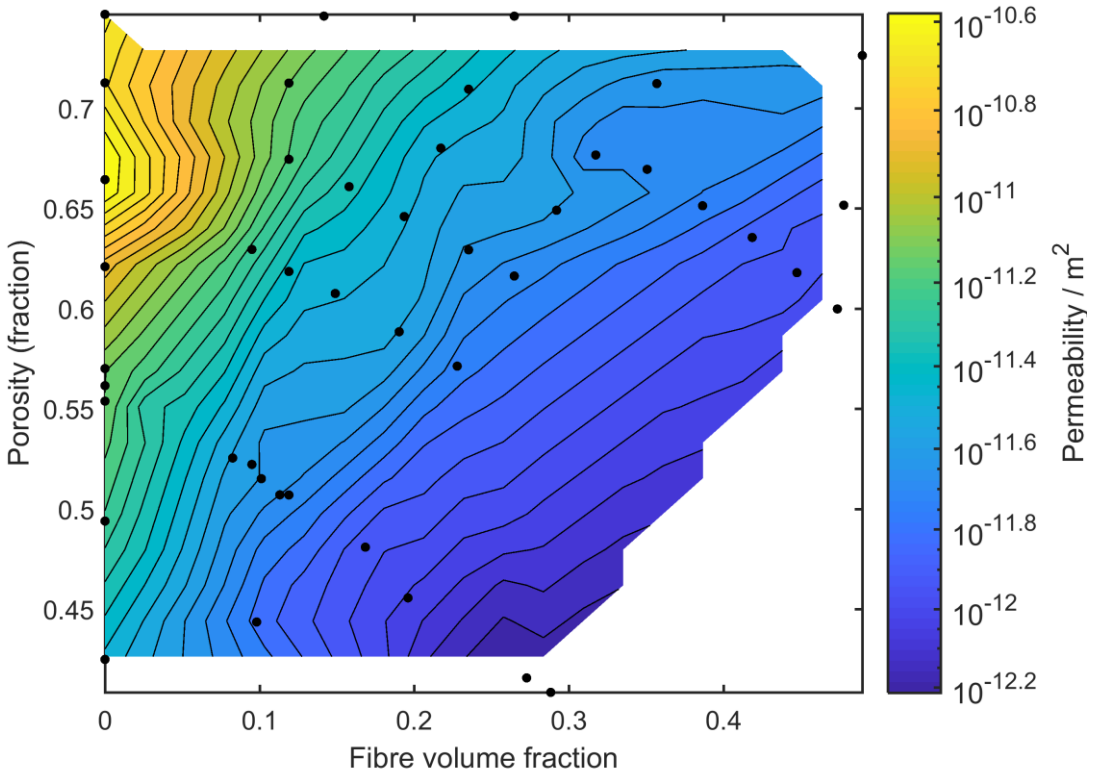

Figure 6.9: Variation of permeability, plotted as filled contour lines against porosity and fibre volume fraction. The black markers represent the volumes that were analysed.

In Figure 6.9, permeability is observed to vary significantly with both porosity and fibre volume fraction. It is important to note that the permeability scale in this case is logarithmic, and so the full range of data spans almost two orders of magnitude. As predicted, at high porosities, the permeability is also large. This is expected as a consequence of the Carman-Kozeny equation. In addition, the permeability is significantly affected by the fibre volume fraction. As the fibre fraction is increased, the permeability decreases, this is most significant as the first few fibres are added but remains true at higher fibre fractions also. The permeability values in all cases are comparable to experimental values, since both commercial DPFs [35] and experimental samples produced in this study (Figure 5.2) have permeability values of around 10^{-12} m^2 .

Back-pressure

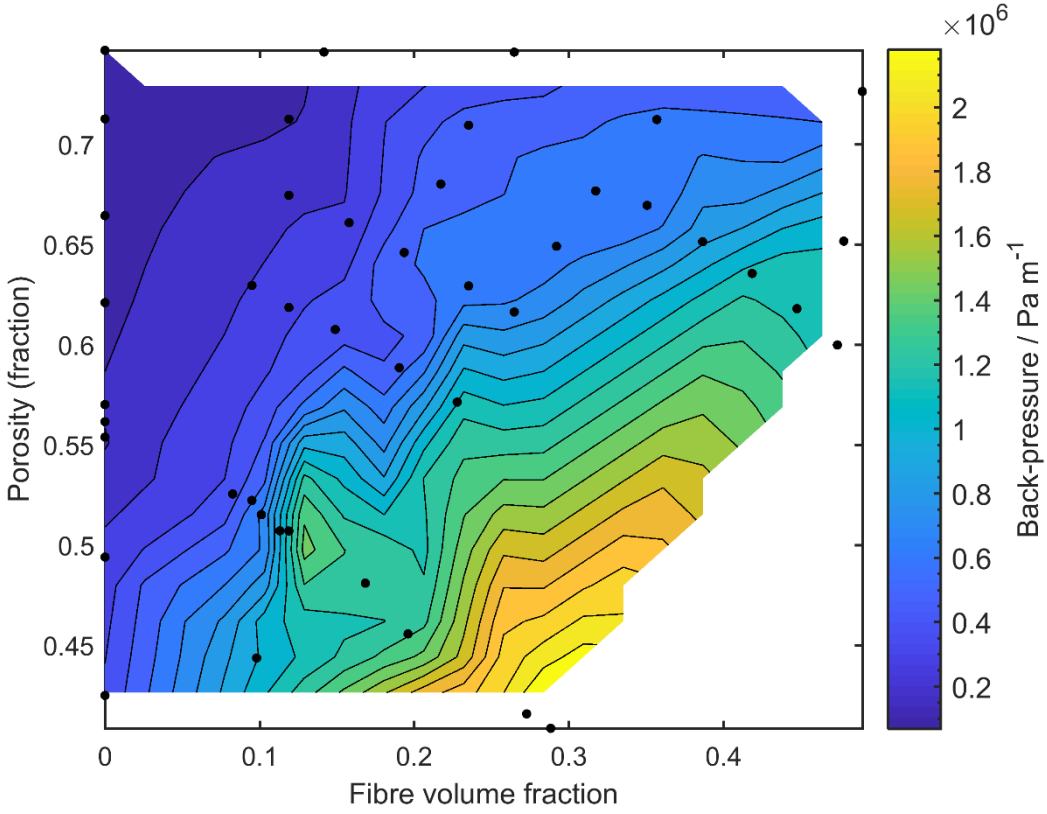

Figure 6.10: Variation of back-pressure, plotted as filled contour lines against porosity and fibre volume fraction. The black markers represent the volumes that were analysed.

Figure 6.10 shows how back-pressure varies as a function of both porosity and fibre volume fraction. This value of back-pressure was measured on COMSOL by considering the average pressure at the inlet, in reference to the outlet, which was set to have 0 Pa pressure. This pressure was then normalised as a pressure gradient, measured in Pa m^{-1}, since the volumes analysed ranged in size. A value of back-pressure was measured for every value of permeability, and so each one of the black markers in Figure 6.10 represents an individual volume, for which a back-pressure was measured in three (and sometimes six) directions. The contours were derived by taking the average value for each volume.

The contours are less regular than the permeability contours in Figure 6.9, due to a higher dependency of the pressure measurement on the exact arrangement of spheres and

cylinders. This is due to the conditions imposed during the fluid flow simulation in COMSOL; a constant inlet velocity was imposed everywhere over the inlet surface. With this restriction, if there happened to be a region on the inlet surface where the inlet immediately became a narrow pinch-point or a dead-end, then the gas would struggle to flow into the structure; this leads to more gas being forced into the region than can easily escape and a resultant region of high porosity. This effect, shown in a particularly bad case in Figure 6.11, would not be observed experimentally.

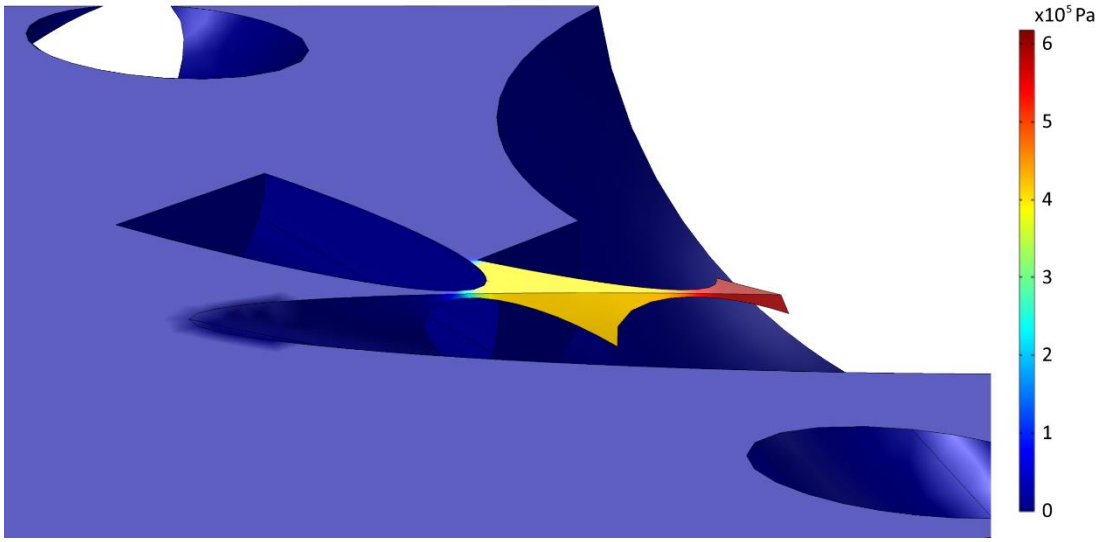

Figure 6.11: An example of a particularly bad case of narrow pinch points at the inlet surface of a model. The flat surface is the inlet, with air being introduced at a constant rate of 0.1 m s^{-1}. This results in some extremely high pressures being generated as the gas struggles to escape these regions. The colour bar indicates pressures as high as 6 x10^5 Pa, four orders of magnitude higher than elsewhere on the inlet surface.

These features rarely led to extremely high pressures, like those observed in Figure 6.11, but it was observed that this effect was present, and so the variation in back-pressure results was much greater than the variation of the permeability results. It is the back-pressure that is of interest when considering filtration, and so this is what was investigated, but perhaps more precise results would be obtained by setting the inlet condition to a constant pressure and monitoring the inlet velocity. In this case, any structural features would not increase the pressure to extreme levels, instead, very little gas would be supplied into these regions.

Analysis of the data in Figure 6.10 unsurprisingly results in the opposite trend to that found in Figure 6.9. i.e. where there is high permeability there is low back-pressure, and vice-versa. Specifically, this means that at high porosities the back-pressure is low, and also at low fibre volume fractions. The region of highest back-pressure is that where both the porosity is low and the fibre volume fraction is high. The contour scalebar this time is linear, but the change is still significant. For example, at a constant porosity of 50 %, by increasing from 0 wt.% fibres to 30 wt.% the back-pressure increases by one order of magnitude. The back-pressure values are similar to those found in a DPF; assuming a wall thickness of 300 µm, a pressure gradient of 1 x10^6 Pa m^{-1} corresponds to a pressure difference of 300 Pa (3 mbar), which agrees with values in the literature for the back-pressure of a clean filter, e.g. Figure 1.8b [43].

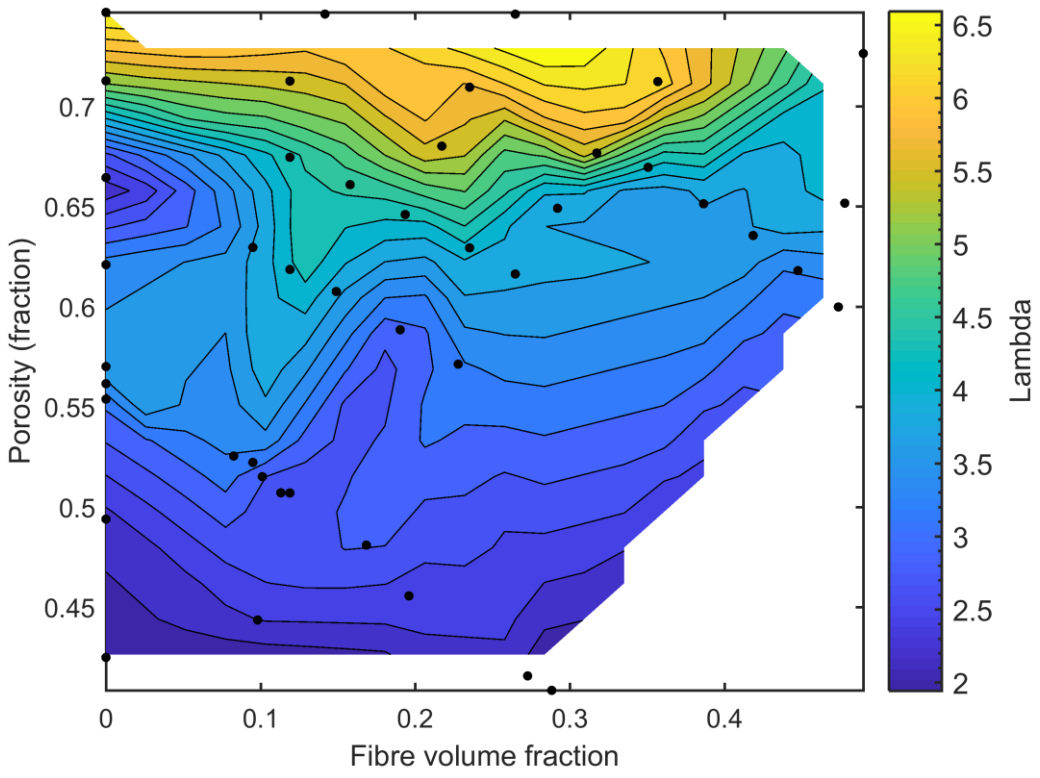

Figure 6.12: Variation of lambda, plotted as filled contour lines against porosity and fibre volume fraction. The black markers represent the volumes that were analysed.

It is interesting to note that in Figure 6.12, there is a clear trend in the variation of lambda. Lambda is a dimensionless measure of the tortuosity of the structure, and it is generally accepted to be a constant with a value of around 5 [48, 169]. Therefore, the expected variation of lambda would be random noise across the porosity-fibre volume fraction space. However, this is not observed, rather there is a strong trend for the value of lambda to decrease as the porosity decreases. The implication of this result is that the fluid experiences a more tortuous path through the structure as porosity increases. This seems counter-intuitive, because with a higher porosity there are surely more paths passing straight through the structure, therefore not requiring much deviation from the straight through route. Whereas with lower porosity, perhaps the gas may be forced around a more tortuous route.

The disagreement from this expected behaviour could be justified by considering that in a more open structure there are more potential paths that the fluid could take, and perhaps there is more interaction between various streams passing through the volume. In a lower porosity volume, the path may be better defined, and although tortuous, the gas may be able to flow through easily, with limited interactions with other gas streams. It may be possible to test this idea experimentally in future work by observing gas flow through the filters using coloured smoke.

Figure 6.13 shows two different volumes, with velocity streamlines passing through the structures, with gas flowing from the top surface to the bottom. These volumes had the same fibre volume fraction (= 0.12, two spheres and 18 cylinders in both volumes). However, the cell parameters of the two structures were different: 48 µm and 40 µm. This difference necessitates that the porosity decreased for the smaller volume, and the porosities were 0.71 and 0.51 for the two structures. The difference in lambda was significant, with the higher porosity value being twice that of the lower porosity value (5.56 compared to 2.77).

The streamlines in the higher porosity case seem to pass straight through the structure with little deviation. In the lower porosity case, the streamlines twist around more, avoiding the higher concentration of obstacles, indicating a higher tortuosity as would be expected. The reason for the higher lambda value is perhaps not in the tortuosity of the

structure, but the ease with which gas can pass through the structure. On average, the velocity of the streamlines passing through the lower porosity volume is higher, and so, although the gas streams follow a more tortuous route, they do so quickly, with most streams finding the easiest path through the structure.

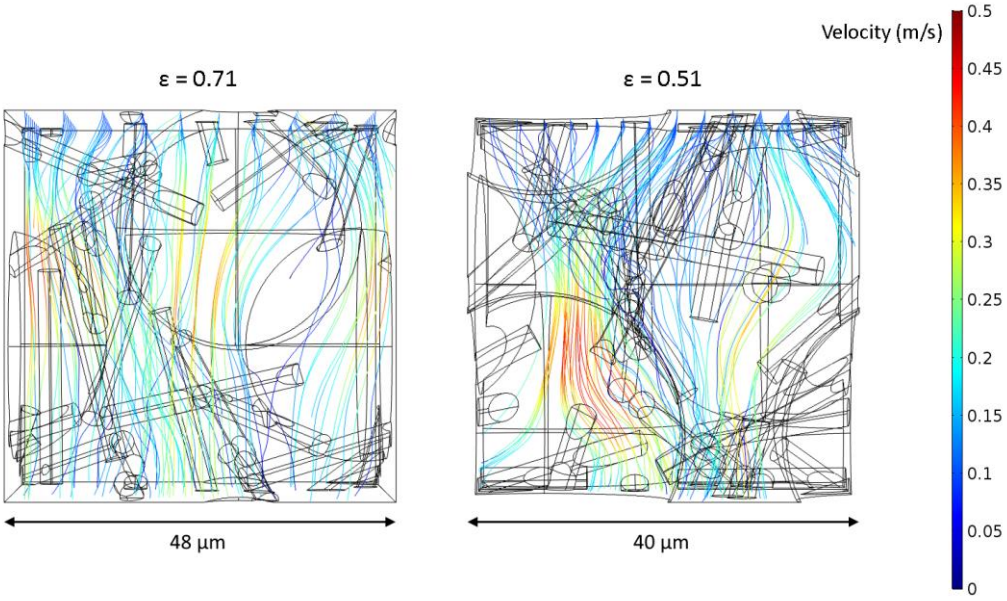

Figure 6.13: Velocity streamlines passing through two volumes. Both volumes have the same number of particles and fibres (and therefore identical fibre volume fractions), but the different cell parameters result in a significant porosity difference.

6.5. Lambda correction

The outcome of this result is that the assumption that lambda remains constant for all structures is not valid, with values at porosities of 70 % being over twice the values of those at 45 % porosity. The variation with fibre fraction does not highlight anything conclusive, and can be assumed to be constant for a given porosity. Analysing all of the lambda data, it is possible to predict how the line of best fit which relates lambda to porosity would look like, by assuming that lambda is in fact a linear function of porosity, i.e. of the form $\lambda = m_\lambda \varepsilon + c_\lambda$, where m_λ and c_λ are the gradient and intercept respectively. Figure 6.14 plots all the values of lambda against porosity using the same data from Figure 6.12.

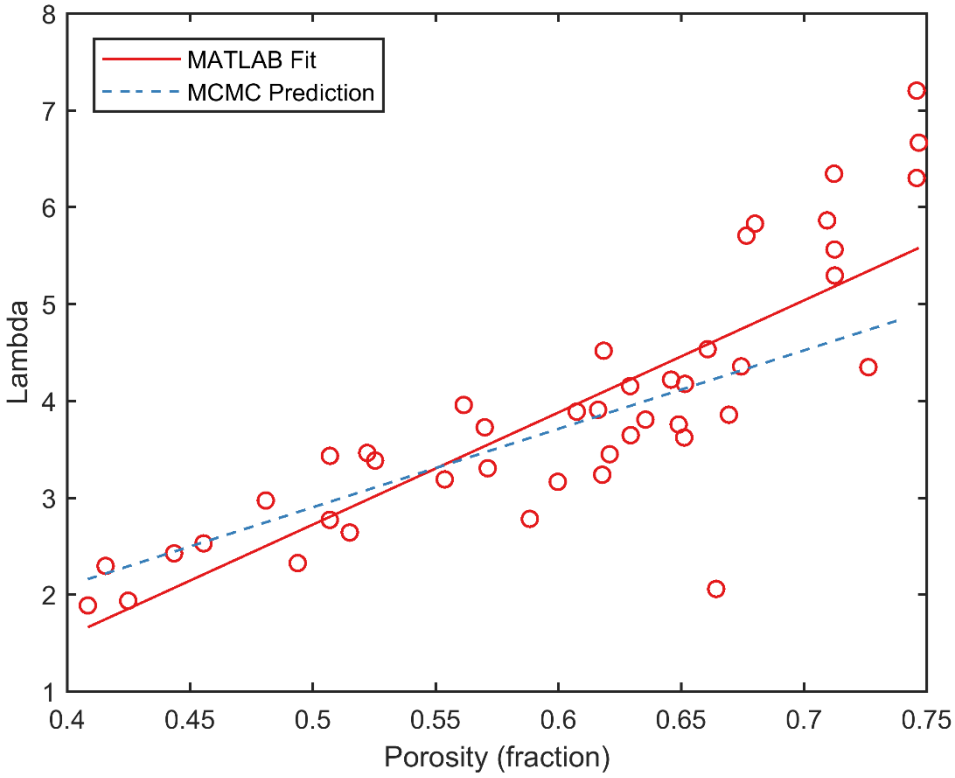

Figure 6.14: The variation of lambda with porosity, from samples with constant particle and fibre sizes, but varying fibre fraction. Also included are best fit lines predicted by MATLAB and by the Markov Chain Monte Carlo method which finds the best fit over multiple datasets.

For a single set of data, it would be possible to find a line of best fit easily by just fitting a straight line through the data using graph plotting software, in this case MATLAB. However, a more detailed approach can be used here, due to the fact that data have been gathered for various different fibre lengths, fibre diameters and particle diameters. The combinations of these parameters that were analysed are shown in Table 6.1.

Table 6.1: Combinations of fibre diameter, fibre length and particle diameters that were studied.

Fibre diameter / μm	Fibre length / μm	Particle diameter / μm
3	30	30
4	30	30
5	30	30
3	15	30
3	35	30
3	30	20
3	30	10

All these data can be used to find the best fit for a straight line in one optimisation step, rather than analysing each data set individually and attempting to find a common solution between them. Using a more statistical approach also allows for clear visualisation of whether the additional porosity dependence is justifiable to include, or whether a simple constant value of lambda is sufficient, and anything more would be adding unnecessary complication into the model.

To find the line of best fit, a Markov chain Monte Carlo (MCMC) method was used. By starting with uniform priors for both m_λ and c_λ, the distributions of both parameters were calculated by random sampling in a probabilistic space. In such a method, random values of m_λ and c_λ, are chosen, and for two pairs of parameter values, the best pair is added to the chain of parameter values with a certain probability, determined by how much better it is (i.e. a Markov chain). The goodness of a pair of parameters was evaluated by Gaussian likelihood to obtain the best value of lambda to predict the permeability. The permeabilities calculated by COMSOL can be assumed to be distributed normally about a plane in porosity-fibre volume fraction-permeability space. This distribution will be defined by a mean predicted permeability, κ_{pred}, and a standard deviation, σ_κ, such that, for a given permeability calculated by COMSOL, κ_{meas}, the Gaussian likelihood can be determined by:

$$\frac{1}{\sqrt{2\pi{\sigma_\kappa}^2}}\, e^{\frac{-\left(\kappa_{meas}-\kappa_{pred}\right)^2}{2\sigma_\kappa}} \tag{6.15}$$

By taking the product of the Gaussian likelihood for all measured permeabilities, the largest value is taken to be the better solution.

In this case, σ_κ has a physical interpretation, as it is a measure of the deviation from the correct value, but this will be determined by the different arrangements of particles and fibres in a certain volume. So σ_κ gives an indication on the effect of the arrangement of the structure on the permeability.

After iterating the process a number of times, a steady state distribution is found, and can be plotted using a corner plot to find the region which best described the line of best fit, shown in Figure 6.15.

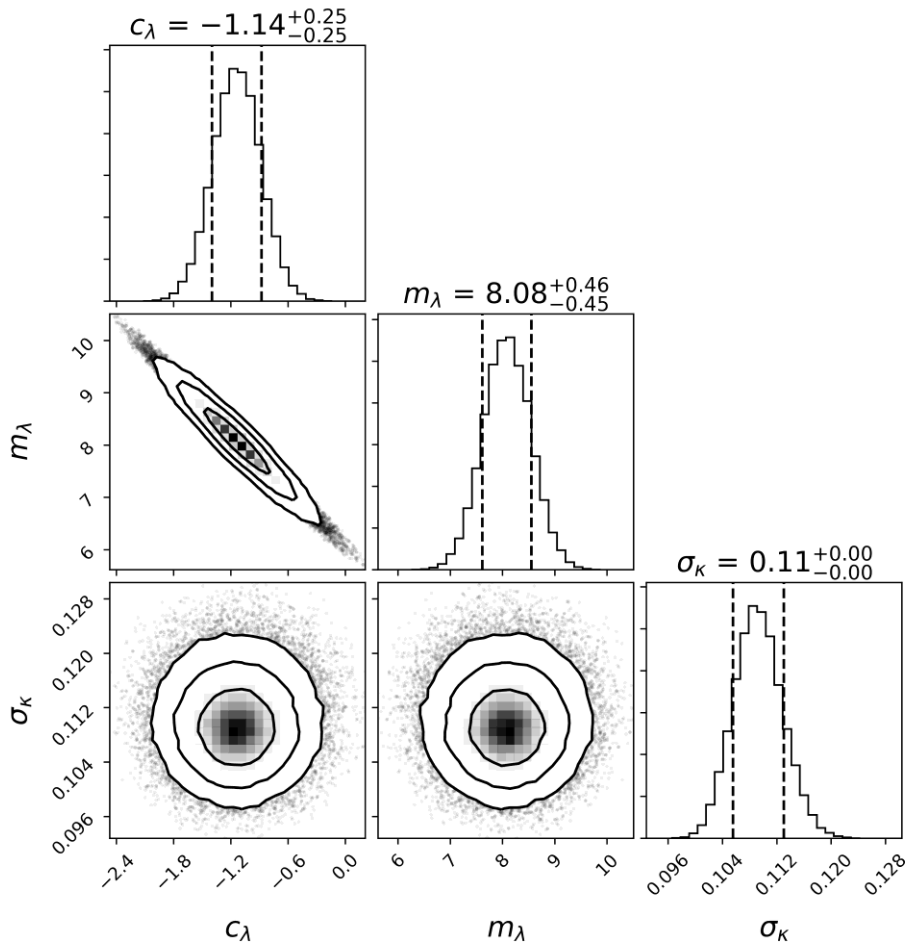

Figure 6.15: Corner plot figure showing the probability distributions for the variables m_λ, c_λ and σ_κ and the interactions between them. The two-dimensional histograms have been smoothed by a Gaussian with width of 1 bin.

This corner plot shows the interactions between m_λ and c_λ and also σ_κ, the standard deviation of the measured permeability values to the predicted permeability surface. Firstly, the three probability distributions down the diagonal show evidence of normally distributed data, with their mean value and positive and negative errors quoted above each plot. The three remaining plots show how the parameters interact with each other. These plots show contours which represent standard deviations of the MCMC generated solutions. i.e. 68 % of trials lie within the first contour, 95 % within the second and 99.7 % within the final contour. Outside of the third contour, the remaining 0.3 % of trials are shown as individual points. In the centre of the contours, a histogram is also used to bin the data.

The scatter plot on the second row is of particular interest, showing the relationship between m_λ and c_λ. It is of no surprise that there is some degeneracy between these two values. For a set of data, it is natural for there to be a range of best fit lines, and by reducing the gradient, the y-intercept is expected to rise, and so a negative trend is observed between the two values. In Figure 6.15, this negative trend is observable. If it assumed that there is no dependence of the porosity on lambda, then there should be a reasonable expectation that m_λ could equal zero, thus predicting zero gradient, and lambda would be a constant value of c_λ. The evidence in Figure 6.15 shows that m_λ is so far from zero that it is extremely unlikely that there is no dependence on porosity, and it can be safely assumed that the inclusion of a porosity dependence is necessary.

Looking at the data in Figure 6.14, the specific case where the particle diameter is 30 μm, fibre diameter is 3 μm and fibre length is 30 μm, it might be tempting to try fitting another dependency, perhaps a quadratic or exponential term to account for those values at high porosities which appear to be consistently under-predicted by the MCMC prediction. Whilst this would probably improve the fit, it is important to not overcomplicate the model, and the data seem appropriately described by the straight line, especially in the region of porosities between 45 % and 65 %, where most experimental samples are found. It is also possible to look at Figure 6.14 and assume that the MCMC model predicts a worse line of best fit than that simply calculated by MATLAB. This is

true for this particular dataset, but when all datasets of all different fibre and particle sizes are included, this simple relationship describes the best fit of lambda to all datasets.

The two scatter plots on the bottom row of Figure 6.15 show the relation between c_λ and σ_κ, and m_λ and σ_κ. In both cases, the distribution formed is a symmetric function, showing no skew. This is a positive result, showing that the predicted mean value of σ_λ has no dependence on m_λ or c_λ. No skew means that there is enough data, and that the parameters are well constrained by the data.

Thus, the ideal solution for lambda appears to be:

$$\lambda = 8.1\,\varepsilon - 1.14 \tag{6.16}$$

This solution does lead to the non-sensical result of negative values of λ when the porosity is very low (below 0.14). This is because there are no data from such low porosities and, if there were, then this result would not be predicted. Although permeating pathways exist for fluid flow for porosities as low as 0.08 [125], this porosity level is well below what would be achieved by random packing of spheres and cylinders, either in a simulation or in an experiment, without a significant degree of sintering, and so it does not lead to a cause for concern.

6.6. Comparing predicted trends to COMSOL data

As mentioned in Section 6.3, the specific surface area of a particle and fibre composite can be written in terms of the linear dimensions of the spheres and particles. By substituting the new expression for S into the simplified Carman-Kozeny equation, the following result is reached:

$$\sqrt{\frac{\varepsilon^3}{\lambda\,\kappa\,(1-\varepsilon)^2}} = f\left(\frac{4}{D_c} + \frac{2}{L} - \frac{6}{D_s}\right) + \frac{6}{D_s} \tag{6.17}$$

which suggests that if $\sqrt{\varepsilon^3/\lambda\,\kappa\,(1-\varepsilon)^2}$ were plotted against f a straight line should be obtained. The gradient of the line will be dependent on all three linear dimensions of the

spheres and cylinders, namely the sphere diameter, D_s, the fibre diameter, D_c, and the fibre length, L. The y-intercept should only have dependence on the particle diameter.

In the standard case, trying to maintain similarity with experiments, the values of D_s, D_c, L were taken to be 30 µm, 3 µm and 30 µm respectively. Permeability values from both COMSOL simulations and Carman-Kozeny predictions (using a precisely measured value for S, measured using COMSOL) were plotted, with lambda taken to be the porosity dependent value derived in the previous section, and the results can be seen in Figure 6.16.

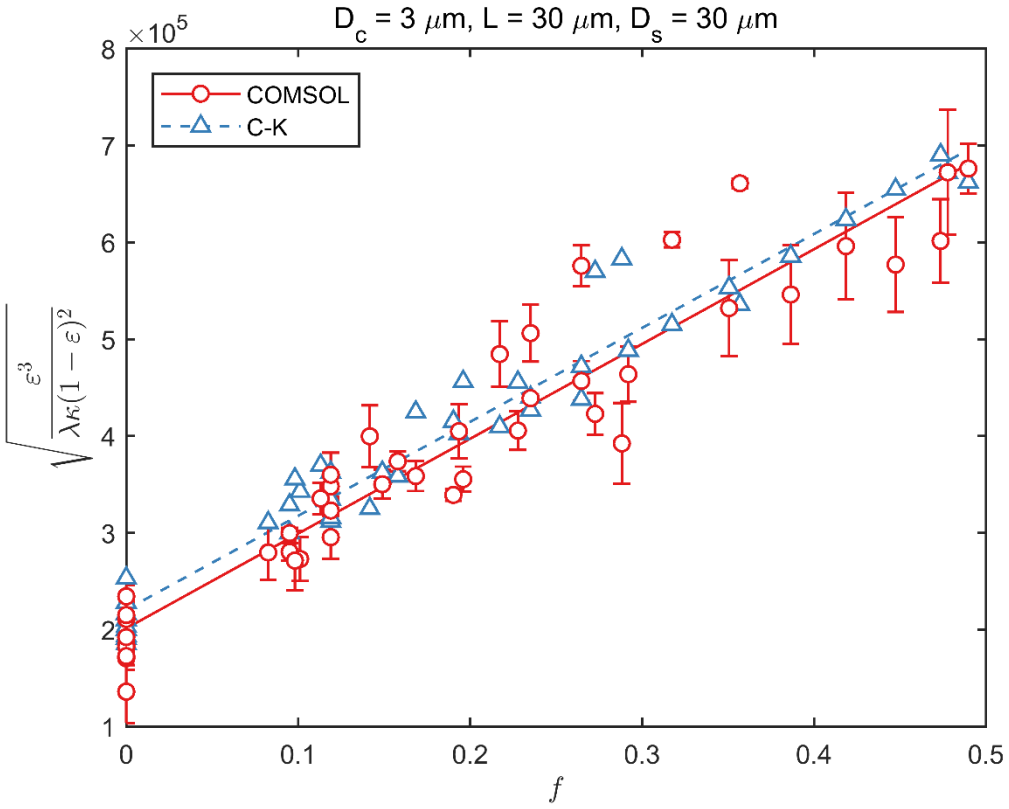

Figure 6.16: $\sqrt{\varepsilon^3/\lambda\,\kappa\,(1-\varepsilon)^2}$ *plotted against* f *for the case where* D_c *= 3 µm,* L *= 30 µm and* D_s *= 30 µm.*

Both the simulated values and those predicted by Carman-Kozeny show a linear relationship, and excellent agreement between each other. The Carman-Kozeny points have comparatively less deviation from the linear line, which is to be expected because the original equation being tested was derived from the Carman-Kozeny equation. The

values for the permeability show greater variation. This is also expected, because the volumes that were trialled were relatively small, all lying somewhere in the region of 40 to 50 µm cubes, limited by the number of parameters that COMSOL could handle. Considering that these cubes contained particles of 30 µm diameter, it becomes clear that this volume might not be large enough to be considered representative. Each cube was tested in at least three directions, and for some of them in six directions, to find an average permeability for the structure, and this average value is what is plotted above, with the error bars assumed to be the value of the error in the mean. These error bars are not a true indication of the error in a given value, but rather provide an indication of the variation of the permeability computed in three or six directions for a given sample. The true error would consider the differences between volumes with the exact same fibre volume fraction and porosity and would indicate how the specific packing arrangement of spheres and cylinders contributed to differences in computed permeability.

From Equation 6.17, there is also a theoretical line that can be drawn, based on the size of the particles and fibres. By calculating the expected gradient and y-intercept, this line can be plotted and compared to the data in Figure 6.16. This line is shown plotted in Figure 6.17.

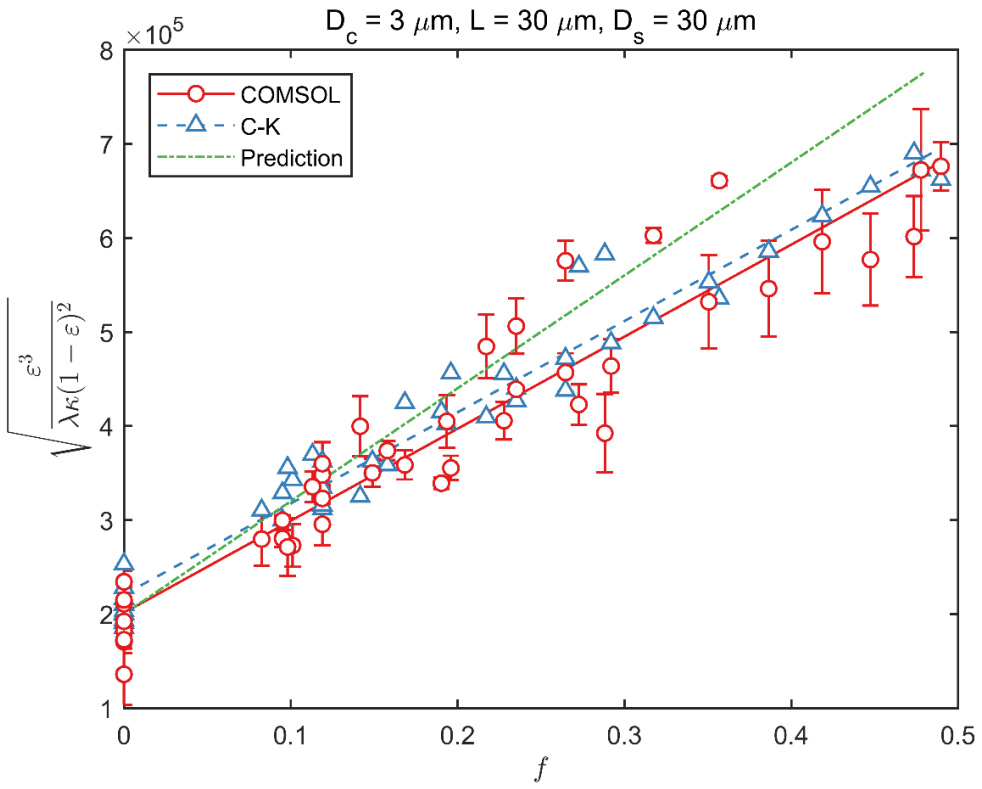

Figure 6.17: Predicted line added onto Figure 6.16

The y-intercept of the line looks to be approximately correct, but the gradient is too large. However, the equation of the line was derived by assuming that there was no overlap between any of the spheres and cylinders, and therefore the specific surface area that has been calculated is significantly higher than in the actual situation, where a degree of overlap is allowed (as a representation of the effect of sintering). At each point of overlap, there is a loss of surface area, and also an increase in the porosity. The change in porosity is not an issue, since it is assumed that the porosity is an input into the calculation. It is the surface area that is unknown in an experimental system. A lower surface area would explain why this gradient is too large, and an overlap factor could be applied.

Before the addition of this correction factor, it would be useful to see if the line tends to approximate the simulation data for other configurations of spheres and cylinders. Looking at the predicted gradient of the line,

$$\left(\frac{4}{D_c}+\frac{2}{L}-\frac{6}{D_s}\right) \tag{6.18}$$

and remembering that the values of D_s, D_c, L were 30 µm, 3 µm and 30 µm respectively, the largest change in the gradient for an absolute change in one of these values will be to change the value of D_c. For example, by changing the value of D_c from 3 µm to 5 µm, the gradient is reduced by 45 %. For an equivalent reduction in gradient by changing D_s, the particle diameter would have to be decreased from 30 µm to 8 µm, a much more significant change. Hence, for an easily observable change, without having too much effect on the number of COMSOL parameters, D_c was varied. Figure 6.18 shows the permeabilities predicted by COMSOL and Carman-Kozeny, as well as the predicted line, assuming no overlap, for fibres of (a) 4 and (b) 5 µm diameter.

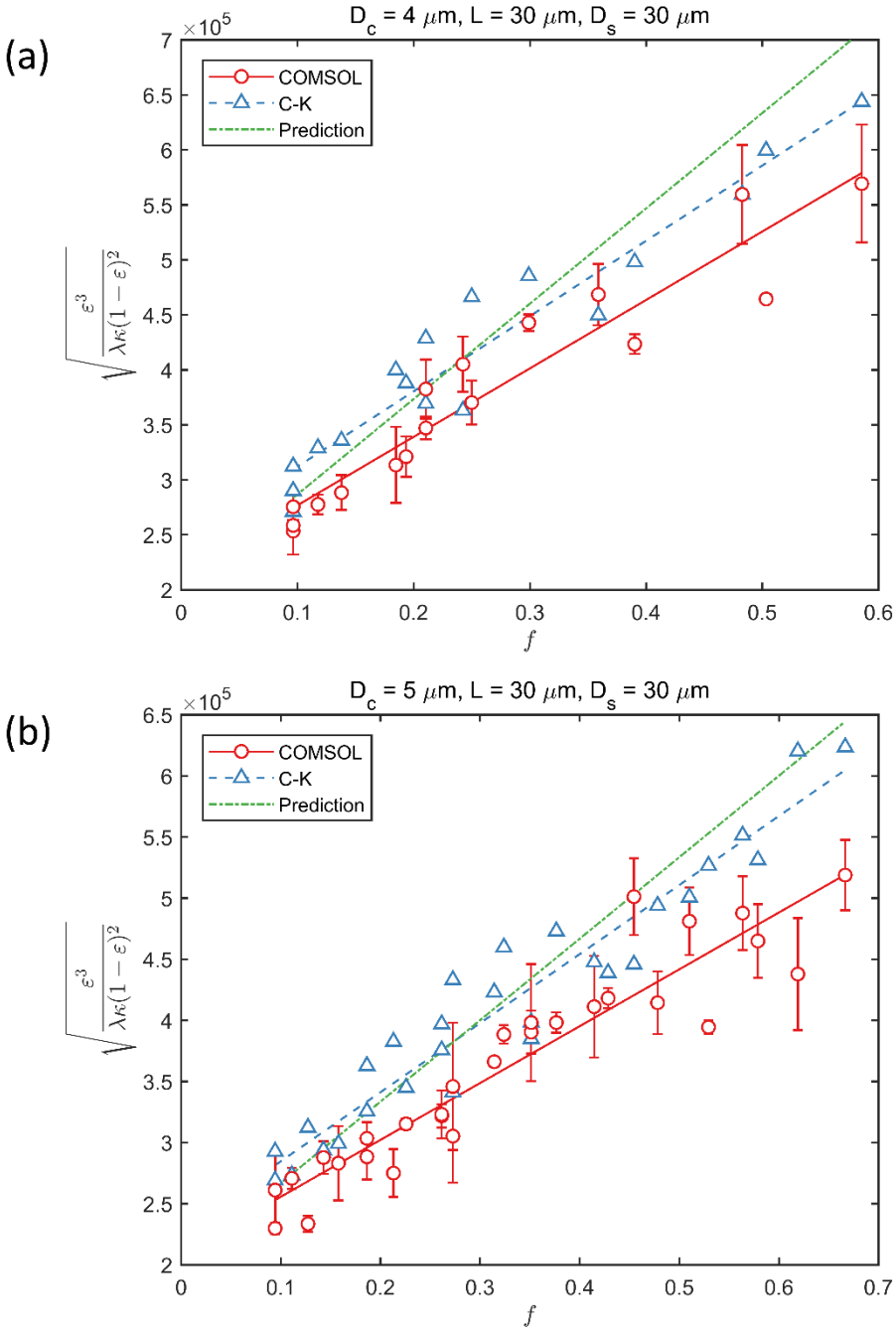

Figure 6.18: $\sqrt{\varepsilon^3/\lambda\,\kappa\,(1-\varepsilon)^2}$ *plotted against* f *for the case where (a)* D_c *= 4 µm and (b)* D_c *= 5 µm. Fibre length and particle diameter remained constant with values of L = 30 µm and* D_s *= 30 µm.*

These plots look very similar to the case with 3 µm diameter fibres. The simulated COMSOL permeabilities and the predicted Carman-Kozeny permeabilities are similar,

with both exhibiting a linear relationship. The predicted line is also in a similar location, again with a gradient that is too large (due to the neglect of a surface area correction term). It seems that the relationship between the size of the fibres and particles and their effect on the permeability is correct, but needs to be rescaled by an overlap factor. If the results from all three fibre diameters are plotted on a single graph, plotting just the line of best fit of the simulated COMSOL data and the prediction line in each case for clarity, Figure 6.19 is produced.

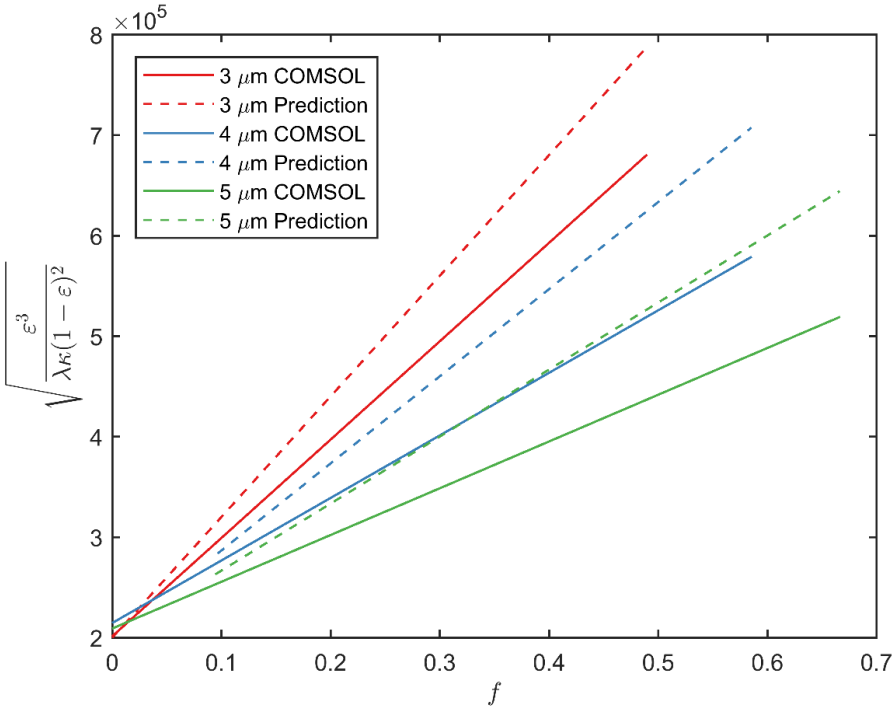

Figure 6.19: Comparison of COMSOL results and predicted trends, assuming no overlap, for fibre diameters of 3, 4 and 5 µm.

According to the model, all three data sets should have the same y-intercept because this is only dependent on the particle size and is not affected by the size of the fibres at all. This is true within the errors in the system, and so it would appear that the correction factor should just be a correction to the fibre overlap, and not affect the particle diameter term.

To check if the intercept is a function of the sphere diameter, the sphere diameter can be changed, with everything else remaining constant (the fibre diameter returned to

3 µm), to see if this affects the intercept as well as the gradient. Figure 6.20 shows the same graphs again, but this time with the sphere diameter changed from 30 µm to (a) 20 µm and (b) 10 µm.

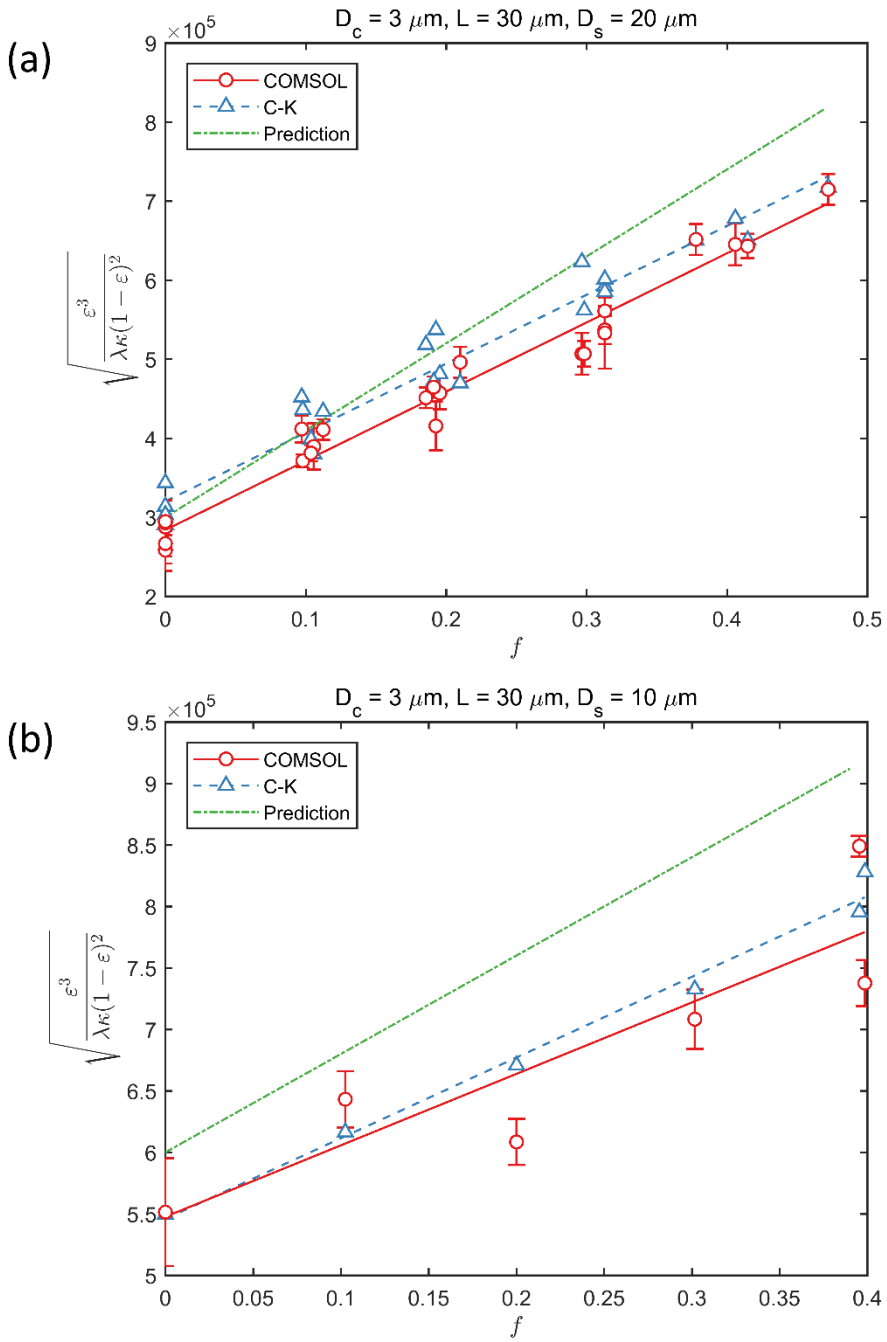

Figure 6.20: $\sqrt{\varepsilon^3/\lambda\,\kappa\,(1-\varepsilon)^2}$ *plotted against* f *for the case where (a)* D_s *= 20 µm and (b)* D_s *= 10 µm. Fibre length and diameter remained constant with values of* L *= 30 µm and* D_c *= 3 µm.*

As before, straight lines are produced in both cases. Comparatively few volumes were analysed when the particle diameter was reduced to 10 µm, because COMSOL struggled to mesh a volume consisting of lots of small, just-overlapping spheres. With larger spheres, very few corrections of the type shown in Figure 6.6 were required, but, when the particle size was reduced, there were many problems with intersecting face elements. Consequently, each volume was time-consuming to analyse, and required so much correction to the mesh that it is possible that there was a non-negligible effect on the permeability values.

When plotted on the same axes, and only including the COMSOL best fit line and the prediction line, the result is seen in Figure 6.21:

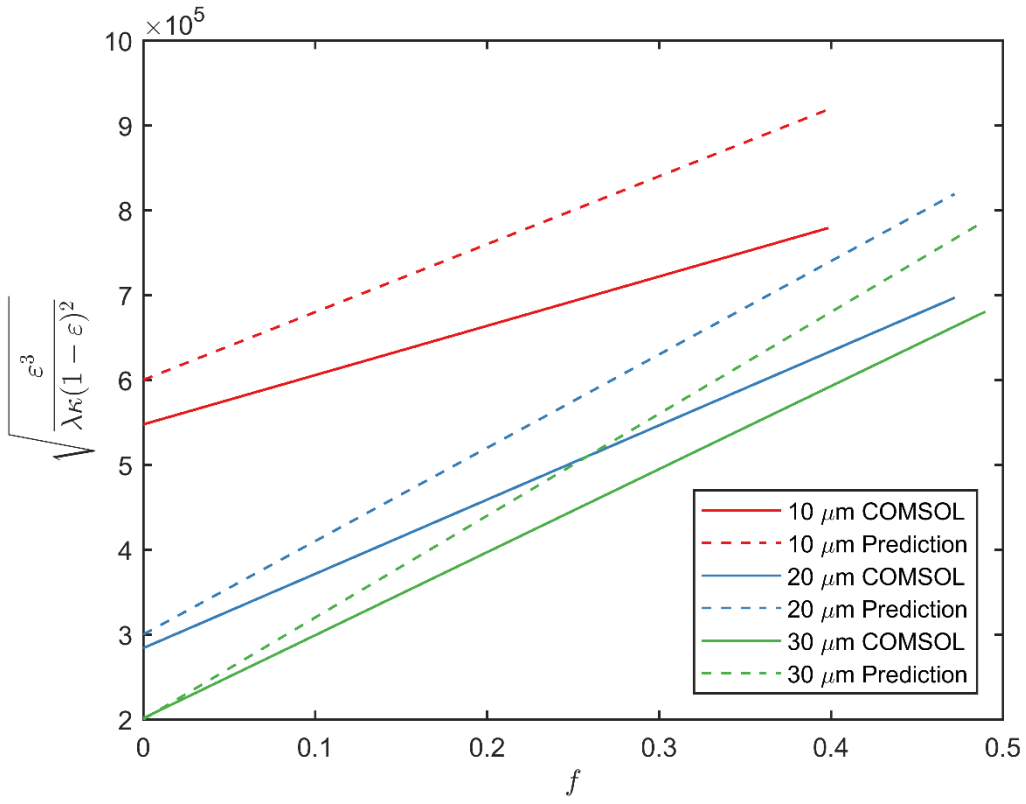

Figure 6.21: Comparison of COMSOL results and predicted trends, assuming no overlap, for particle diameters of 10, 20 and 30 µm.

These graphs provide suitable evidence that the form of the equation above is correct, but in all cases the result is off by a certain amount due to unaccounted overlap. However, this overlap factor is something that can be calculated for each analysed volume.

6.7. Effect of overlap

Each volume has an integer number of spheres and cylinders contained within it, and each of these cylinders and spheres have an easily calculable surface area. Therefore, it is easy to find a value of the surface area within the volume, if no overlap is assumed. Also, as an output of COMSOL, the actual surface area within the structure can be obtained, with overlap taken into account. For each volume it is therefore possible to calculate the difference between these values, as a fraction of the original surface area, i.e. the fraction of surface area that has been lost due to the overlap. Figure 6.22 plots this overlap as a 3-dimensional surface as a function of both porosity and fibre fraction.

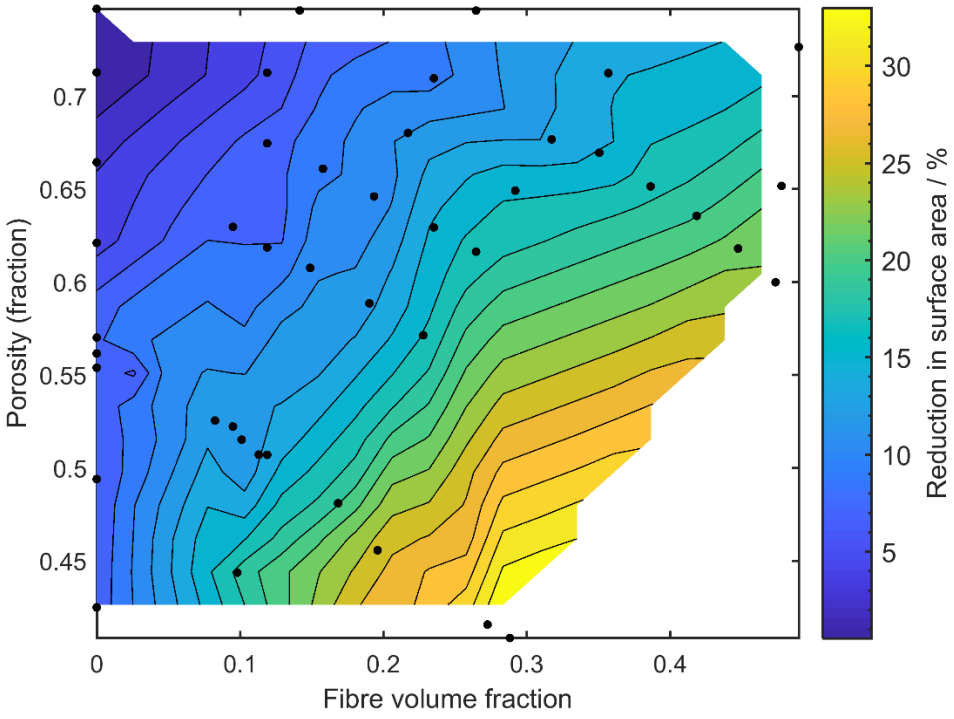

Figure 6.22: Reduction in surface area due to overlap, plotted as filled contour lines against porosity and fibre volume fraction. The black markers represent the volumes that were analysed.

If the surface in Figure 6.22 had been approximately flat, this would indicate that a simple scaling factor could be introduced into the equation above. However, this is not the case, and it appears that the surface is a function of both fibre fraction and porosity. This overlap can also be seen to have a considerable effect when predicting the permeability. At low fibre volume fractions and high porosities, the effect is not too large and will not have a large effect on the predicted permeability. However, when the porosity decreases and the fibre volume fraction increases, the reduction in surface area is significant, increasing to as high as 30 %.

The amount by which this overlap affects the surface area will, of course, be a function of how much overlap is allowed within the model. In the initial model set-up, an allowed overlap of 2 µm was defined. If this overlap was reduced, then a lower reduction in surface area would be observed and vice-versa. 2 µm was decided upon since it was small enough that the structure of fibres and particles was clear, but also large enough that the structure generation would not take too much time, due to the method of randomly placing spheres and cylinders requiring more attempts for a smaller defined overlap. In the experimentally produced samples, the overlap was significantly smaller than 2 µm, but the actual value will be a measure of how much sintering a sample has undergone.

This dependency on the magnitude of the allowed overlap means that the following analysis of the effect of overlap will hold just for this specific case. However, the methods used could be applied to further work and serve as a basis for making a more generalised model, by applying the same analysis to volumes with varying allowed overlaps.

The specific surface area in the model is given by Equation 6.13, repeated below:

$$S = (1-\varepsilon)\left[\frac{6\,(1-f)}{D_s} + \frac{4\,f}{D_c} + \frac{2\,f}{L}\right] \qquad (6.19)$$

Since it has been shown in Figure 6.22 that the surface area reduction is a function of both porosity and fibre volume fraction, the initial idea was, for each of the three terms, to include three additional parameters: a constant offset term, a term for a linear dependence on porosity, and a term for a linear dependence on fibre fraction. This leads to an additional nine degrees of freedom, plus a standard deviation term, defining the

variation in the actual measured values of S compared to the predicted value. Equation 6.19 now looks like the following:

$$S = (1-\varepsilon)\left[\frac{(1-f)\left(6 + c_{D_s} + m_{f,D_s}f + m_{\varepsilon,D_s}\varepsilon\right)}{D_s} + \frac{f\left(4 + c_{D_c} + m_{f,D_c}f + m_{\varepsilon,D_c}\varepsilon\right)}{D_c} + \frac{f\left(2 + c_L + m_{f,L}f + m_{\varepsilon,L}\varepsilon\right)}{L}\right] + \sigma_S \quad (6.20)$$

This is a lot of additional parameters, and it was hoped that some of these would be unnecessary. To evaluate how these parameters affected the model, a Markov chain Monte Carlo method, similar to that described for the determination of lambda earlier, was used. On this occasion, all nine parameters and the deviation of the predicted and measured values of S were assumed to have uniform prior values and were allowed to vary. The optimal solution was found for this case. Naturally, with so many additional degrees of freedom, the fit between the COMSOL and predicted specific surface area was very good.

Ideally, the number of additional parameters should be reduced as much as possible, whilst still providing an accurate fit to the experimentally measured values. One way to quantify this is to use a Bayesian model comparison, which aims to quantify the experimental support for one model over another, regardless of whether they are correct. An advantage of this technique is that it inherently incorporates a penalty for including too much model structure, and therefore simpler solutions can be favoured even if the fit is slightly worse, offering protection against overfitting. At this stage, no plausibility factors, a user-determined favouring of one model over another, were introduced (i.e. $Pr(Model)$ in Equation 6.21 was assumed to be 1).

The parameters were systematically removed in various combinations as detailed in Table 6.2. There is a natural progression in these combinations. At first, similar parameters were removed together to find a good starting point. From there, individual parameters were removed and the effect on the evidence was observed. For each combination of parameters, a value of the evidence, Z, is calculated. Z is a measure of the likelihood of the model in view of the data ($Pr(Model|Data)$), and so a larger value of

Z represents a more suitable model. These values are recorded in Table 6.2 as $\ln(Z)$ to aid their interpretation.

$$Z = Pr(Model|Data)\ Pr(Model) \tag{6.21}$$

To compare models, the Bayes factor, K, can be introduced. K is defined as the evidence of one model divided by the evidence of another model. A commonly used metric for the acceptance of one model over another is the value of $2\ln(K)$. Since the values in Table 6.2 are $\ln(Z)$, this is equivalent to taking the difference between two models and multiplying by 2. Kass and Raftery [170] suggest that a value of $2\ln(K) > 10$ can be considered "very strong evidence" to choose one model over another. This corresponds to a difference of 5 between the values of $\ln(Z)$ in Table 6.2. Therefore, any of these models offers a significant improvement over the non-modified equation for specific surface area, but there is also a desire to maximise this value whilst not over-complicating the expression.

Table 6.2: Variation of evidence for different combinations of additional degrees of freedom.

Trial	c_{D_s}	m_{ε,D_s}	m_{f,D_s}	c_{D_c}	m_{ε,D_c}	m_{f,D_c}	c_L	$m_{\varepsilon,L}$	$m_{f,L}$	$\ln(Z)$	Notes
1										652.73	No terms
2	✓	✓	✓	✓	✓	✓	✓	✓	✓	1400.87	All terms
3	✓			✓			✓			1164.33	Only constant terms
4	✓	✓		✓	✓		✓	✓		1376.37	Constant and porosity dependent terms
5	✓		✓	✓		✓	✓		✓	1153.54	Constant and fibre content dependent terms
6		✓	✓		✓	✓		✓	✓	1091.28	Fibre content and porosity dependent terms
7	✓			✓	✓		✓	✓		1380.74	Trial 4 is best of 4,5 and 6. Removing m_{ε,D_s} improves it further
8	✓	✓		✓			✓	✓		1347.18	Removing m_{ε,D_c} reduces evidence of trail 4 significantly
9	✓	✓		✓	✓		✓			1377.78	Removing $m_{\varepsilon,L}$ improves trial 4 slightly
10	✓			✓	✓		✓			1383.13	Trial 7 and 9 suggest removing both m_{ε,D_s} and $m_{\varepsilon,L}$
11				✓	✓		✓			1366.39	Removing c_{D_s} from trial 10 - reduces evidence
12	✓				✓		✓			1078.39	Removing c_{D_c} from trial 10 - significantly decreases evidence
13	✓			✓	✓					1388.36	Removing c_L from trial 10 - increases evidence
14				✓	✓					1370.85	Removing c_{D_s} from trial 13 - all terms are related only to D_c
15					✓					1007.17	Removing c_{D_c} from trial 14 - significantly decreases evidence
16				✓						1148.91	Removing m_{ε,D_c} from trial 14- significantly decreases evidence

By following the progression of trials in Table 6.2, it is clear that trial 14 is the most natural solution. It does not offer the highest evidence, but a drop of only 30 in the value of $\ln(Z)$ whilst removing seven out of nine of the original parameters is a very good result. Of course, a difference of 30 is significantly greater than 5, which suggests at first that there is very strong evidence to pick the solution with all nine parameters included (trial 2). However, at this stage the plausibility factors can be introduced and, since a model with only two additional degrees of freedom offers a significant improvement in usability over nine, trial 14 can be assumed to offer a better solution, especially when compared with the other evidences that were calculated.

Trial 14 could not be simplified any further, as shown by trials 15 and 16. In fact another good result was found in trial 13; this trial had the second highest evidence with only 3 additional parameters, second only to the case of all the parameters. However, trial 14 was chosen to be a better solution because the two additional degrees of freedom only acted on a single term in Equation 6.20, namely the cylinder diameter term. The gain in simplicity, and thus interpretability, was considered to be much more significant than the relatively small decrease in evidence.

With the important parameters chosen to be c_{D_c} and m_{ε,D_c}, and all others assumed to be zero, Equation 6.20 was tested via the Markov chain Monte Carlo method to find the optimal solutions to these two new parameters. As the specific surface area is a physical parameter, the optimisation was chosen such as to minimise σ_S, the standard deviation of measured values of specific surface area to the value predicted by the model. This was also optimised alongside the value for lambda and the whole expression was run so as to minimise σ_κ, the standard deviation between the values of permeability measured on COMSOL to the permeability values calculated by the new model. As before, a corner plot can be produced to see how all of these parameters and standard deviations depend on one another, and this is plotted in Figure 6.23.

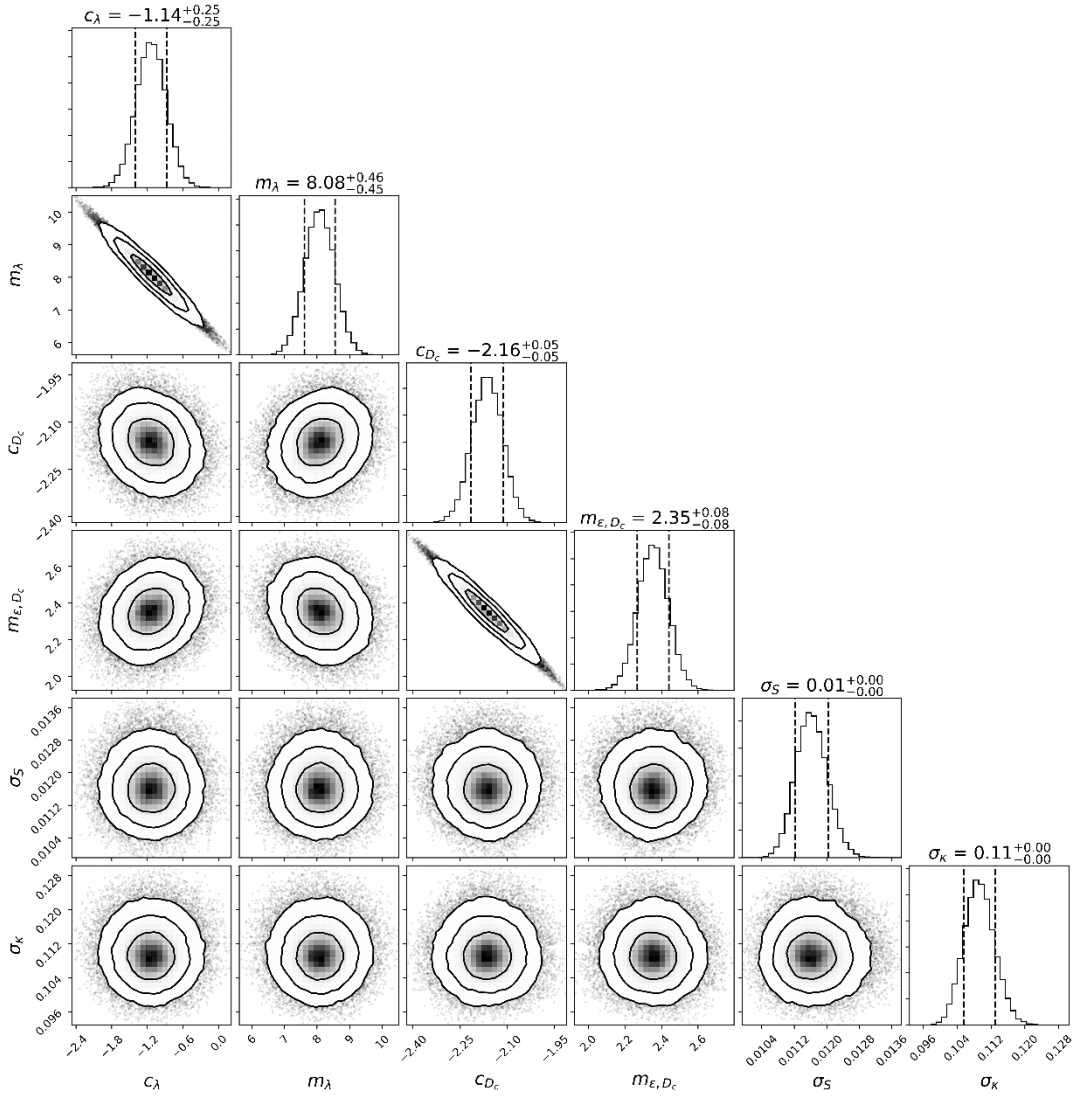

Figure 6.23: Corner plot figure showing the probability distributions for the variables c_λ, m_λ, c_{D_c}, m_{ε,D_c}, σ_S and σ_κ and the interactions between them.

This corner plot can be interpreted in the same way as the one shown in Figure 6.15. Along the diagonal, the error in the value of any of the six parameters seem to be normally distributed. The mean value and the positive and negative errors are provided above the histograms in each case. The top two rows are identical to those found in Figure 6.15. The following two rows show the dependency of the two new parameters, c_{D_c} and m_{ε,D_c}, on the lambda parameters and on each other. The first two columns in those rows show that there is no dependency on the values of the new parameters on the lambda parameters. The remaining scatter plot is of interest because it shows that there is a dependency of c_{D_c}

and m_{ε,D_c} on each other. This is a consequence of the fact that the two values are the intercept and gradient of a line and, as before, if the gradient decreases it is expected that the y-intercept will increase, manifesting as a negative relationship between the two values. Nevertheless, although the two are dependent on one another, the error of both is small.

The scatter plots on the bottom two rows of Figure 6.15 show the relation between the four additional parameters that have been included and the standard deviation of the values of specific surface area and permeability. In all cases, the distribution formed is a symmetric function, showing no skew. These are positive results, showing that the predicted mean values of the four new parameters correlate to the mean value of the standard deviation of the measured permeabilities about predicted planes of both specific surface area and permeability.

Hence, the values for c_{D_c} and m_{ε,D_c} were found to be -2.17 and 2.36 respectively. Relating back to the original equation for the specific surface area (Equation 6.20), this means that the correction factor takes the form of:

$$(1-\varepsilon)f\frac{2.35\varepsilon-2.16}{D_c} \tag{6.22}$$

With the correction factor obtained, the full equation for the link between porosity, permeability and fibre volume fraction can be written as the following:

$$\kappa=\frac{\varepsilon^3}{(8.1\,\varepsilon-1.14)(1-\varepsilon)^2\left[\frac{6(1-f)}{D_s}+\frac{(1.84+2.35\,\varepsilon)f}{D_c}+\frac{2\,f}{L}\right]^2} \tag{6.23}$$

As a check for how well it matches the simulated permeabilities, Figure 6.19 and Figure 6.21 can be replotted, this time plotted against $\sqrt{\varepsilon^3/\lambda\,\kappa\,(1-\varepsilon)^2}-\,2.35\varepsilon f/D_c$, to include the COMSOL data and the predictions including the overlap function. These new plots are shown in Figure 6.24 below.

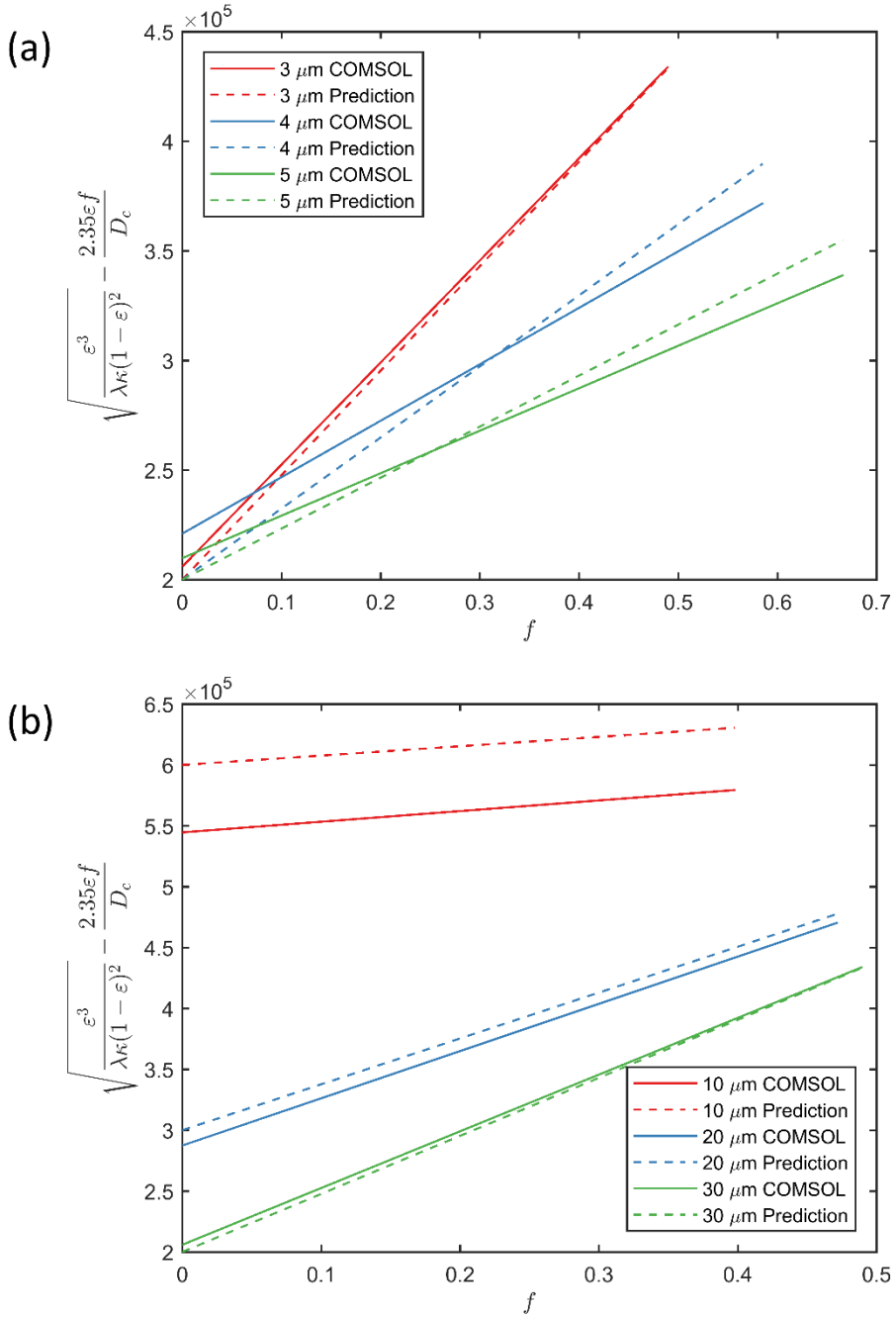

Figure 6.24: Comparison of COMSOL results and predicted trends, including an overlap term, for (a) varying fibre diameter of 3, 4 and 5 µm (with constant particle diameter of 30 µm) and (b) varying particle diameter of 10, 20 and 30 µm (with constant fibre diameter of 3 µm). In all cases the fibre length remained at 30 µm.

When compared to the original plots (Figure 6.19 and Figure 6.21), it is clear that the prediction lines are now much closer to the data collected via COMSOL. The only

discrepancy seems to come at small particle sizes, as shown by the red line on Figure 6.24b. The gradient seems to have been predicted correctly, but the intercept is incorrect. As the intercept is only dependent upon the particle diameter term, this intercept could be fixed by adding a correction factor on the particle diameter. In fact, this would be exactly what would be suggested if trial 13 had been selected rather than trial 14 (Table 6.2). However, as explained previously, the linear correction term to the particle diameter was omitted for the reason of maintaining simplicity in the correction factor by only allowing it to affect one term, the fibre diameter.

As well as the effect of particle diameter and fibre diameter, the fibre length was also varied. However, the inclusion of the fibre length into the original equation (Equation 6.13) is only due to the surface area of the ends of the fibres. This will have some impact, as there will be fewer fibre ends per unit volume as the fibres become longer but, compared to the effect on the curved cylinder surface area when the fibre diameter is changed or the particle surface area when the particle size is altered, the effect is negligible. As such, even when the fibre length is more than doubled from 15 µm to 35 µm, the permeability remains close to constant. This observation was also made by Nabovati *et al.* [125] who found that aspect ratios greater than 6 (fibre lengths longer than 18 µm in the current study) resulted in permeability values independent of aspect ratio. However, at lower aspect ratios, the permeability increased with fibre length. Figure 6.25 is included to show the correction factor applied to varying fibre lengths, but the measurements are close enough to assume that, if it is possible to maintain a constant porosity and fibre fraction, the fibre length is actually not too significant when creating a fibre/particle composite.

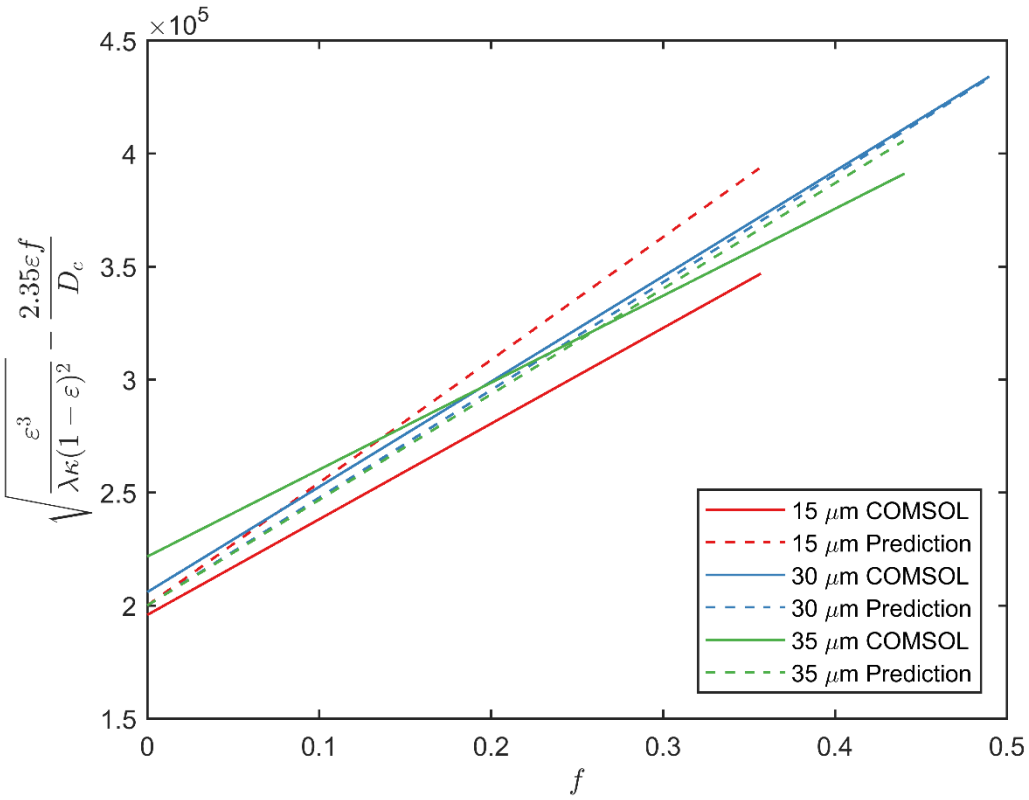

Figure 6.25: Comparison of COMSOL results and predicted trends, including an overlap term, for fibre lengths of 15, 30 and 35 µm.

Whilst these graphs are useful to show that the model is well fitted to the data, the axes are not particularly informative. The results become clearer by plotting the variation of permeability with both porosity and fibre volume fraction, as shown in Figure 6.26.

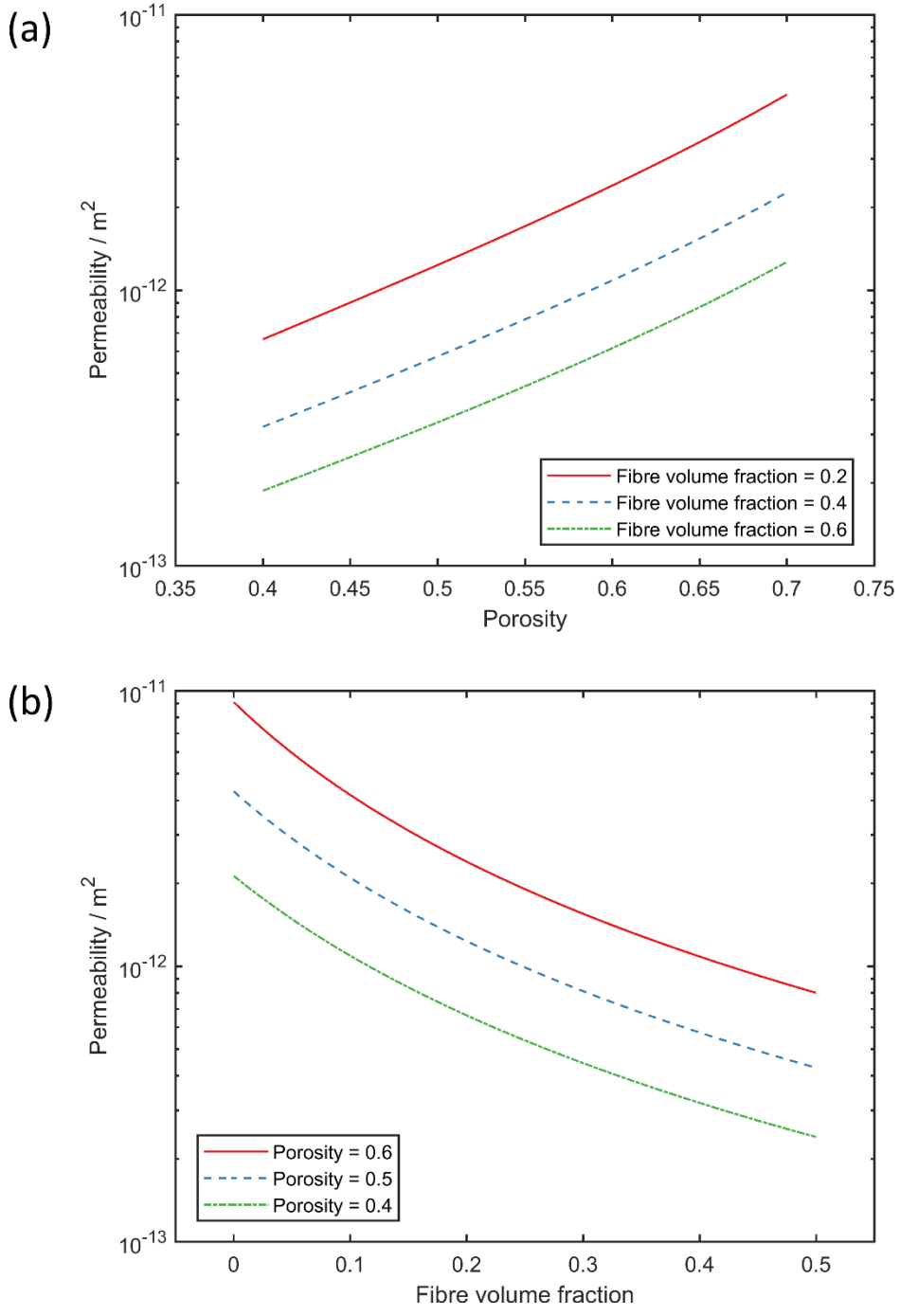

Figure 6.26: Simulated variation of permeability with (a) porosity and (b) fibre volume fraction for the case where D_c = 3 µm, L = 30 µm and D_s = 30 µm.

The results plotted here show very clear trends. As the porosity is increased, the permeability increases, as would be expected from the Carman-Kozeny equation.

However, the dependence of permeability on fibre content, for a constant porosity, is also very significant, with permeability decreasing by an order of magnitude as the fibre content is increased from 0 to 50 wt.% fibres.

6.8. Comparison with experiments

In real-world situations, the entirety of porosity-fibre volume fraction space is not available, but rather is confined along certain paths through this space, dependent on processing conditions. For example, compacting the samples at a higher pressure will likely lead to a lower porosity, as will sintering for longer times, or using smaller fibre lengths. The effect of these various factors on the porosity and permeability of samples was covered in detail in the first-generation materials section. However, as the simulation has been based on fibre and particle sizes found in the second-generation materials, this is the data which will be compared.

As a reminder, for these samples both a porosity and a permeability were measured. These results can be found summarised in Figure 5.1 and Figure 5.2.

It would be useful to see whether the spheres and cylinders model provides a good comparison to the experimental data. One way to do this would be to use the permeability surface graph to predict the permeability of a sample by tracing along the porosity line found experimentally.

Figure 6.27 shows the line of best fit from experimentally collected porosity data as a function of fibre volume fraction overlaid onto the predicted permeability surface.

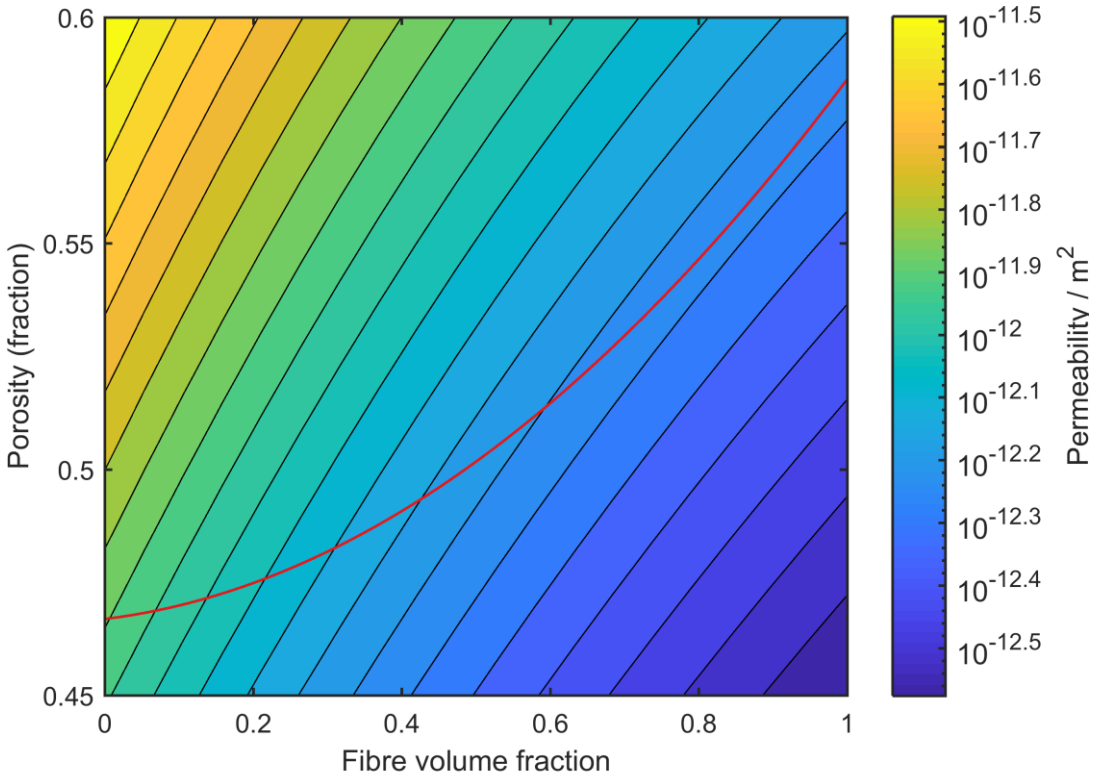

Figure 6.27: The smooth permeability surface generated by using Equation 6.23. Overlaid on the surface is the best fit line of the experimentally measured porosity data, taken from Figure 5.1.

One disadvantage of the spheres and cylinders model is in the assumption that there is no distribution in fibre or particles sizes. A constant value must be chosen for each of the particle diameter, fibre diameter and fibre length. The values of these parameters were found experimentally to be 28 ± 12 µm, 3.7 ± 1.0 µm and 37 ± 10 µm respectively, where the errors given are the standard deviation of these distributions.

Following this path through porosity-fibre volume fraction space, and viewing the permeability profile along the line, Figure 6.28 is produced, plotted against the fibre volume fraction rather than as distance along the line to enable comparison with the experimentally measured permeabilities. Also included in Figure 6.28 are the measured permeabilities, which tend to lie approximately along the predicted line, showing reasonable correlation between the spheres and cylinders model and experimentally observed values. The predicted value using the mean values for the sizes of the particles

and fibres gives the solid line prediction. By using the standard deviations for the particle and fibre sizes listed above, an uncertainty in these values can be given. This is shown by the shaded area between dashed lines. The upper boundary curve is produced by considering the largest values of particle and fibre diameters, the lower boundary is derived assuming the smallest values for the particle and fibre diameters. The fibre length has little effect on the shape or position of the curves.

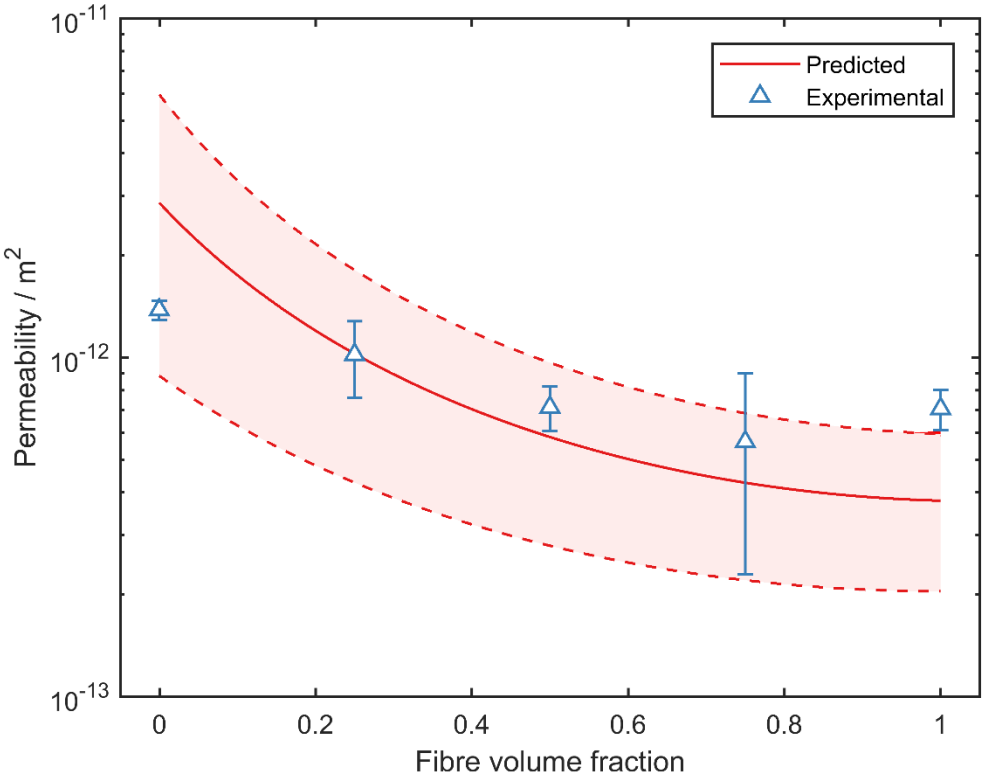

Figure 6.28: Using mean values for the sizes of the particles and fibres, the solid line is predicted from the model. This is close to fitting the experimental data (blue points), but discrepancies could come from the distributions of particle and fibre sizes which is not accounted for in the model. Considering the standard deviation of these distributions leads to the dashed boundary lines.

Figure 6.28 shows that the form of the results predicted by the sphere and cylinder model seem to be correct, and by choosing certain values within one standard deviation of the particle and fibre sizes, the line can be fitted to pass through the experimental points. An example of this fitting is shown in Figure 6.29 where the values of 20, 30, and

4.7 µm have been assumed for the particle diameter, fibre length and fibre diameter respectively.

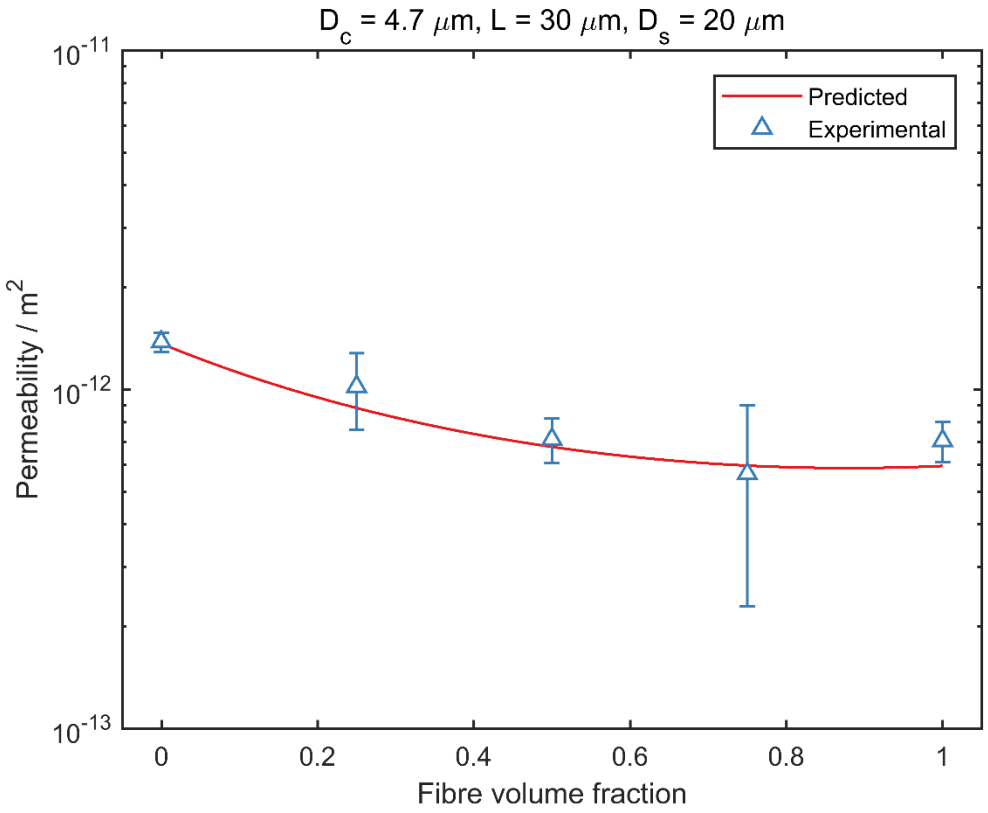

Figure 6.29: By selecting different values of the fibre diameter, fibre length and particle diameter within one standard deviation of their mean measured values, an accurate trendline can be produced for the data, showing promise that the sphere and cylinder model is capable of predicting real-world permeabilities from porosity and fibre fraction alone.

Figure 6.29 therefore shows that whilst the exact values of permeability are difficult to predict, the sphere and cylinder model can be fitted to the shape of a trend line that passes through the experimental data.

6.9. Comparison with tomography

In addition to comparing the experimental results to the model, an intermediate step worth considering is tomography. Using tomography allows the internal structure of real

experimental samples to be captured, and by using thresholding and smoothing techniques in ScanIP software, as explained in Section 5.5.2, a mesh that can be imported into COMSOL can be obtained.

Randomly selected volumes from inside three samples were imported into COMSOL. These samples had fibre volume fractions of 0 wt.%, 25 wt.% and 50 wt.%, and the mesh volumes which were taken from inside these structures were cubes with side length of either 135 μm or 140 μm, depending on the exact resolution of the scan. For each sample, five cubes were examined. The distribution of pores, particles and fibres were not uniform within the samples, and so a random number generator was used to pick coordinates of the cubes, to avoid any bias in the selection.

Each volume required thresholding of the greyscale image into regions which were considered to be material or void. This thresholding process is not perfect and has to be estimated by eye, see Figure 5.5 for a reminder of this issue. After thresholding, the masks were smoothed by dilating the mask and then applying a Gaussian smoothing filter. Finally, a single contiguous region was selected (since the pore structure is highly connected this only removed a small number of islands), and any small voids within the pores were filled in, as this was considered to be noise introduced by the CT scanner.

Meshes were generated from these masks, and these meshes were imported into COMSOL in order to conduct a similar fluid flow analysis to the sphere and cylinder model. The difference in this case is that the edges of the cubes were not periodic. However, it would not be correct to assume them to be solid walls either. The best situation seemed to be to add symmetric boundaries on all the cube edges that were not the inlet or outlet. This effectively meant that each cube edge was a reflection of itself, rather than a translation as is the case with periodic boundary conditions. The other difference, which is also motivated by the lack of periodic boundaries, is that there were many more artificial “dead-ends” in the structure due to the edges of the cube. This is difficult to avoid, and also generates unrealistic results when the inlet condition is set to be a constant inlet velocity, as was the case in the sphere and cylinder model, since the gas cannot flow anywhere but more gas is being added, leading to the development of extremely high and unrealistic pressures, similar to the effect illustrated in Figure 6.11.

However, an easy fix to this problem is to set the inlet condition to be a constant pressure, of 100 Pa, rather than a constant velocity. In this case, even if the gas was being forced into a dead-end pore the gas would not build up a large back-pressure, since once the pressure reached the specified pressure, no more gas would be added. The consequence of such inlet conditions is that the back-pressure cannot be measured and compared to the sphere and cylinder model, but the permeabilities can be assumed to be close to the actual values, despite the non-periodic boundaries.

For each volume, the permeability was calculated in all six directions, with the inlet being each face of the cube, and the outlet always the opposite face in each case. As with the sphere and cylinder model, in addition to permeabilities calculated by COMSOL the permeabilities can also be predicted by using the simplified Carman-Kozeny equation (Equation 6.7), in this case lambda was taken to be 5, a standard accepted value from the literature [48], and the specific surface area, S ($m^2\ m^{-3}$), was measured precisely on COMSOL, as was the porosity, ε. An example of a meshed tomographic structure, and the steady state fluid flow simulation is shown in Figure 6.30.

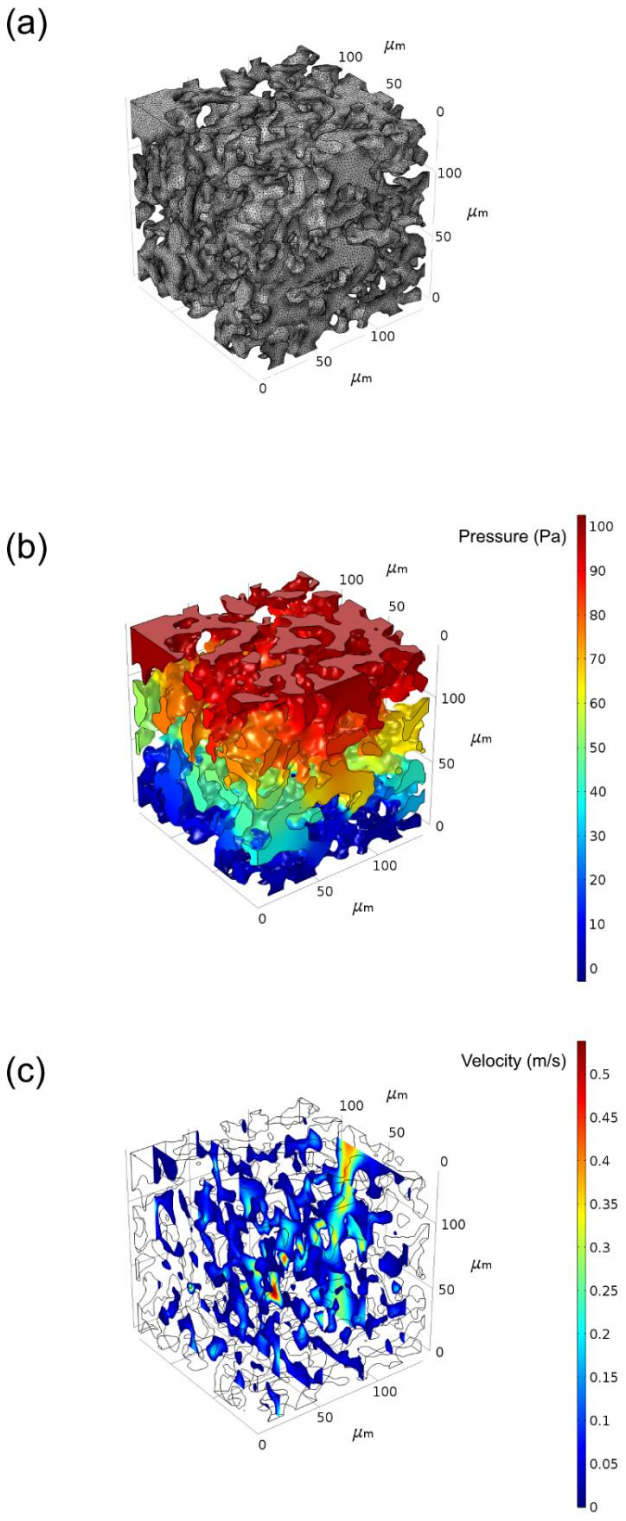

Figure 6.30: (a) the mesh generated by ScanIP. (b) the variation in pressure through the structure and (c) four slices through the structure, showing the variation in velocity. All images are of the same 0 wt.% sample.

For each fibre volume fraction, 0, 25 and 50 wt.%, it is therefore possible to plot a graph of permeability against porosity to compare the permeability predictions of the sphere and cylinder simulation to the tomography values, for both values calculated by COMSOL and calculated by the Carman-Kozeny equation. Also plotted on these graphs is a single point, derived from experiments. The three graphs are shown in Figure 6.31.

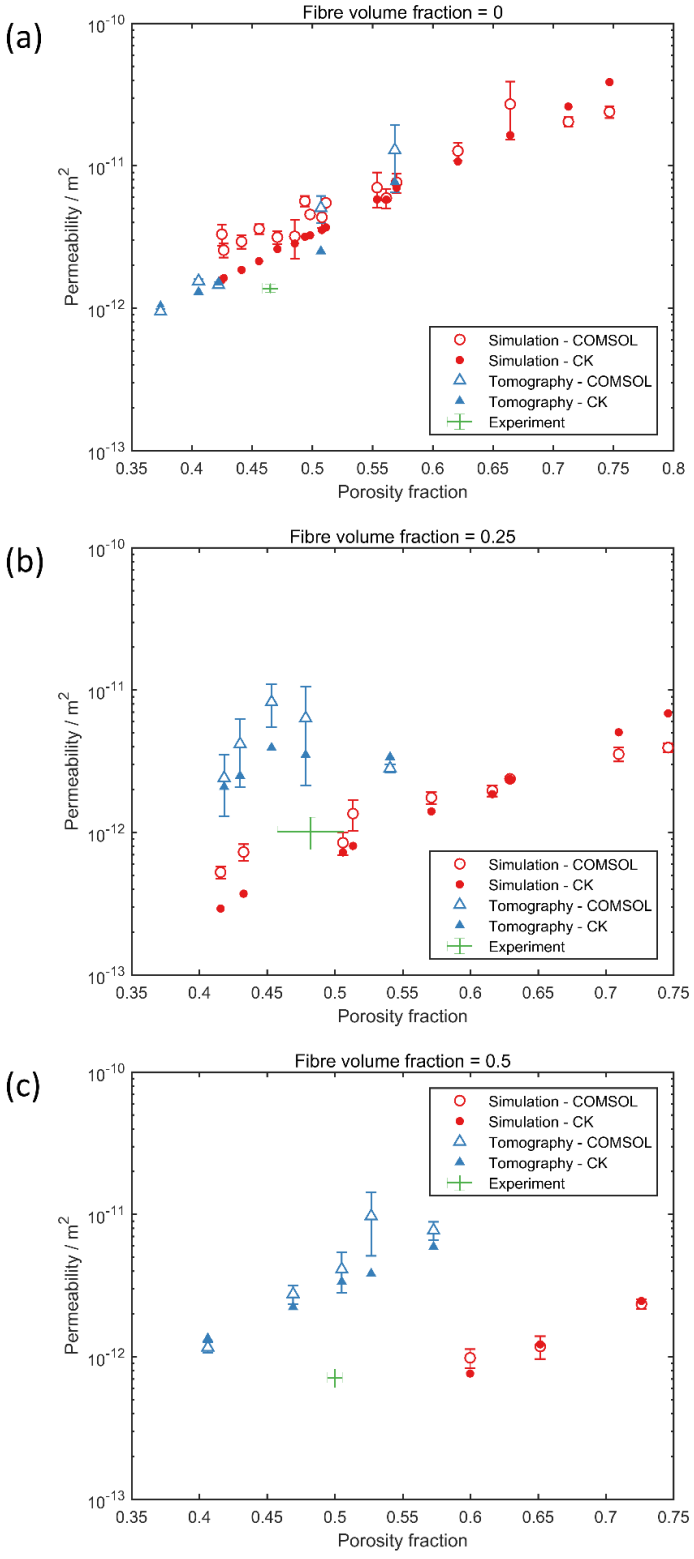

Figure 6.31: Comparison of simulation results (COMSOL and CK) and tomography results (COMSOL and CK) with experimental results for fibre volume fractions of (a) 0 wt.%, (b) 25 wt.%, and (c) 50 wt.%.

It is worth noting that permeability is plotted on a logarithmic axis, and the lines appear to be approximately linear. This is just a coincidence since rather than there being an exponential dependence on porosity the actual dependence, as predicted by Carman-Kozeny, is that permeability is proportional to $\varepsilon^3/(1-\varepsilon)^2$. In this central region of porosity (between 35 % and 75 %) this dependence appears approximately linear on a half-logarithmic plot. The experimental results form just a single point on the graph, with all porosity and permeability behaviour localised in a small area (the error bars on the graph are determined by the error in the mean for a number of samples in each case).

For the case of a fibre volume fraction of 0 wt.% (Figure 6.31a), the tomography results agree well with the sphere and cylinder simulation. The best fit lines have been omitted to maintain clarity, but all four are close to one another. The results tend to over-predict the permeability when compared to the experimental data, but the result is close.

As the fibre volume fraction is increased to 25 wt.% (Figure 6.31b), both the simulated data and the experimental data decrease in permeability, whereas the tomography data remains largely unchanged. The sphere and cylinder model still appears to be a good fit for the experimental data, with best fit lines passing within experimental error. However, the tomography still seems to over-predict the permeability.

Finally, at a fibre volume fraction of 50 wt.% (Figure 6.31c), the simulated data and experimental data were observed to decrease further in permeability, but the tomography values remained high. At 50 wt.% there were only three available volumes that could be analysed via the simulation technique with an 8GB RAM computer (see Figure 6.3 for a reminder of the possible volumes). Naturally, these three volumes had a high porosity and so the goodness of fit to the experimental data in this case must be done by extrapolation. The extrapolation suggests that the permeability might be under-predicted by the model, but it would be useful to test this further with volumes of a comparable porosity. The results for the tomography once again resulted in over-predicting the permeability. This over-prediction has been getting worse with increasing fibre content such that by 50 wt.% fibres the permeability predicted by tomography is almost an order of magnitude higher than that measured experimentally.

Although higher fibre volume fractions could be analysed by tomography and were measured experimentally, further graphs with higher volume fractions could not be produced due to the limitations on the number of parameters needed by COMSOL for higher volume fraction sphere and cylinder models.

Another way to view this data is to consider all three volume fractions plotted on a single graph to compare (a) simulation to experiment, and (b) tomography to experiment. These graphs are presented in Figure 6.32, with only the Carman-Kozeny data plotted for clarity (omitting the COMSOL calculated permeabilities).

In Figure 6.32a, the simulations follow the correct trend, i.e. for a given porosity, as the fibre volume fraction increases, the permeability decreases. This corresponds to an increase in specific surface area, which is expected for the fibres compared to particles. The same trend is seen in the experimental data, but the discrepancy between the simulations and the experiment is in the magnitude of this effect. The simulations appear to predict that the permeability will drop by an order of magnitude when going from 0 to 50 wt.% fibres, whereas the effect in the experimental results is much more moderate. This leads to the simulation over-predicting the permeability at low fibre volume fractions but under-predicting the values at higher volume fractions.

Figure 6.32b shows the same graph but considering the tomography permeabilities rather than those predicted by simulation. Whereas the experimental data increases in porosity and decreases in permeability with increasing fibre volume fraction, the tomography shows no change. For all three fibre volume fractions, the relationship between porosity and permeability follows the same path, implying a constant value for the specific surface area. In all cases, the predicted permeability is higher than the experimentally measured value, and this gets worse at higher fibre volume fractions as the experimental values decrease in permeability.

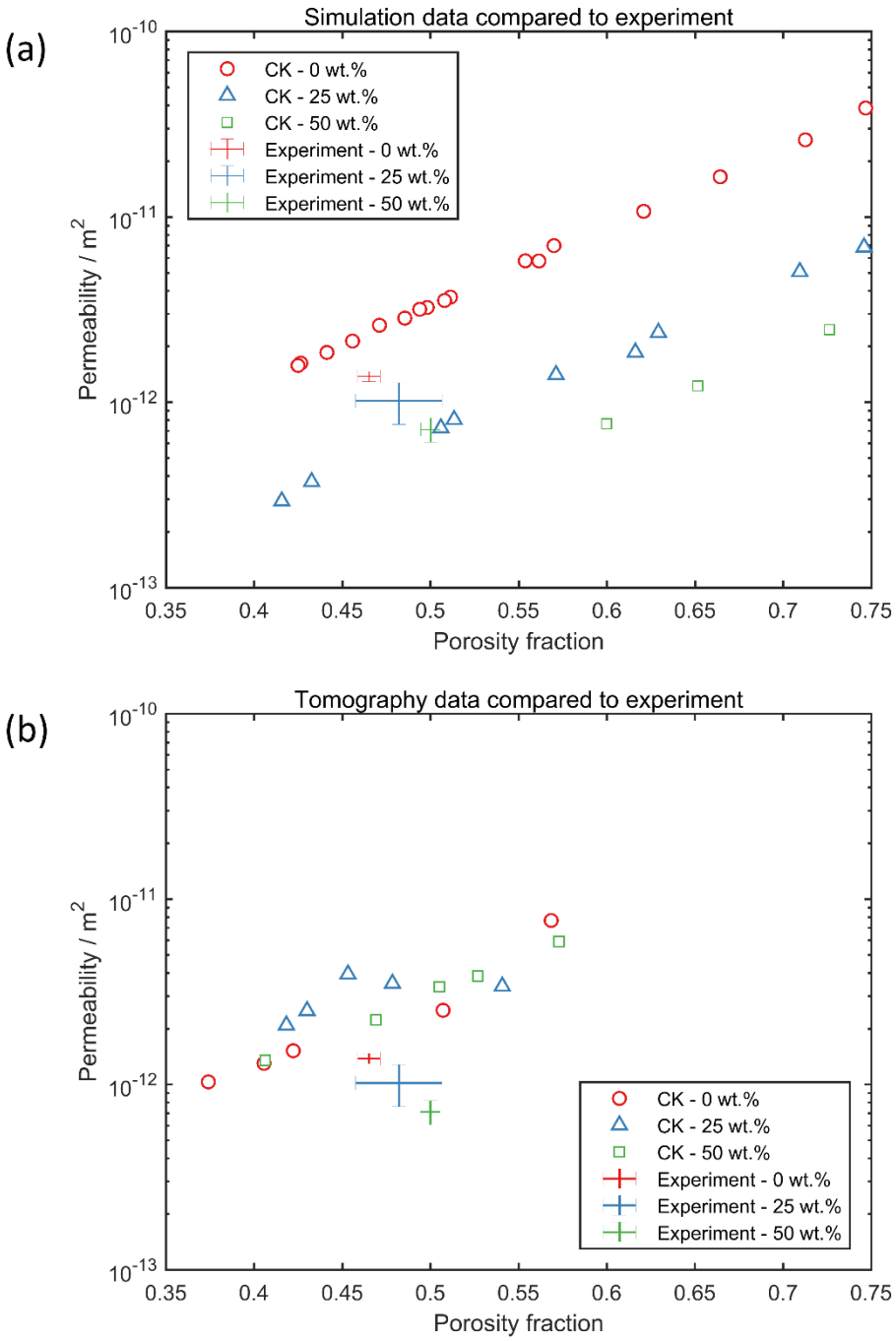

Figure 6.32: Comparing (a) CK simulation data and (b) CK tomography data to experimental data for 0, 25 and 50 wt.% fibres.

The results of the tomography are spread out over a much larger porosity range than the experimental error bars. This is because there is a range of scales of structure within the samples, and the tomography volumes are not large enough to be considered

representative of the overall sample. However, it would be impossible to fully capture the overall structure in a single volume, and so the random sampling average is necessary. Within the samples there are regions of very large pores, around 100 µm across, there is also segregation of the fibres and particles, such that some areas are almost all fibres and vice versa in other areas. A large scale tomographic slice of a 50 wt.% fibre volume is shown in Figure 6.33. This volume has dimensions of 8.4 x 11.0 x 18.0 mm and analysing the full volume would be impossible.

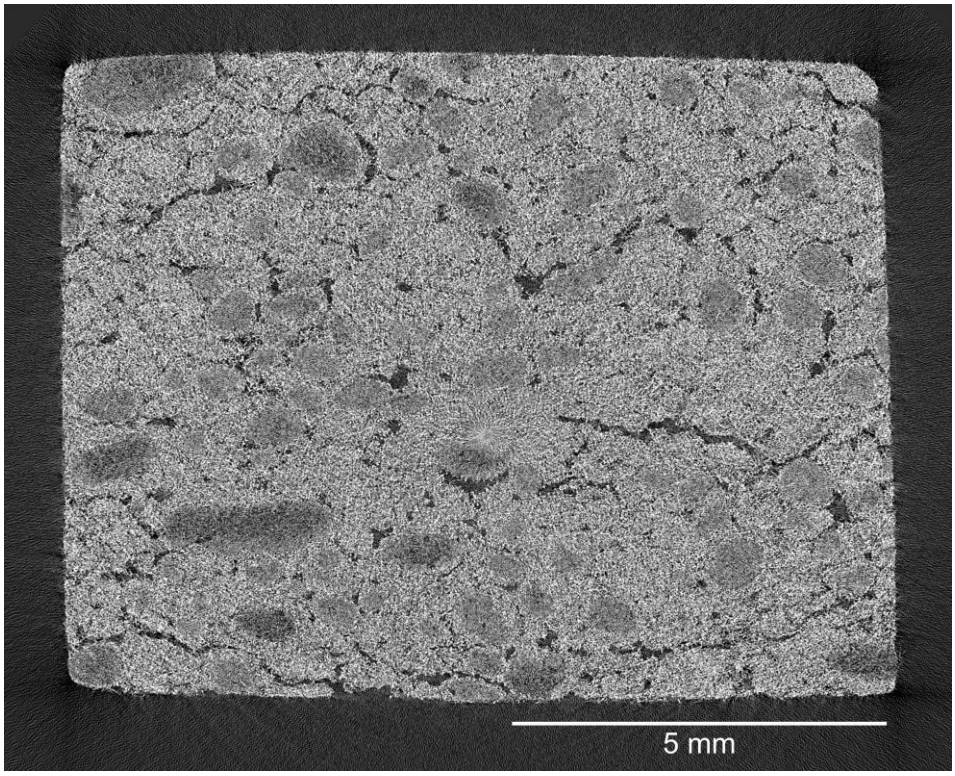

Figure 6.33: Cross-section of a bulk sample of 50 wt.% fibres. Macroscopic porosity in the form of cracks can be observed, and there appears to be regions of high fibre content, appearing as slightly darker (and more porous) regions. The microstructure is not homogeneous.

This section aimed to compare the predictive ability of the spheres and cylinder model and tomography. The trends observed in experiment are better described by the simulation work, but the data in both cases is collected on small volumes, neither of which can be considered to be representative of the overall structure.

The tomography results showed no change in the porosity/permeability relationship as the fibre volume fraction increased, which implies the specific surface area is roughly constant. The specific surface area is expected to increase as the fibre volume fraction increases. This is known by simply considering the geometry, by analysing the experimental data (Figure 5.3) and is predicted by the sphere and cylinder model. The fact that the specific surface area remains constant in the tomography work implies that detail about the structure is being lost in the scan.

This is not too surprising, as the fibres have a diameter of only 3 μm. Even though the CT scanner was used at its highest resolution, producing images with a pixel size of 0.5 μm, it was still difficult to see the fibres. The images did not appear as black and white, void and material, but rather as various shades of grey which made thresholding difficult (as shown in Figure 5.5). In this noise, the fibres were lost, especially during any smoothing processes when generating the mesh, and so the surface area remained similar for all samples. The technique would work well for thicker fibres or a higher resolution scanner, but for this purpose the true structure of the filters could not be captured.

Of course, this inability to successfully capture the fibres does not impact on the case of 0 wt.% fibres. In this case, the structure is comprised only of 30 μm particles, which are sufficiently large to be captured by the CT scanner. The thresholding on these samples was easier due to a higher contrast between void and material, and the result is that the tomography predicts a permeability and porosity similar to that seen in experiment and predicted by the model. This agreement is best illustrated in Figure 6.31a. This is further evidence that although the tomography was not successful at capturing the fibres in this case, it is a valid and useful technique when considering coarser microstructures.

6.10. Conclusion

In this chapter a new modelling technique for fibre and particle composites was introduced. The sphere and cylinder model offers an improvement over tomographic analysis especially for fine microstructures where the CT scanner fails to resolve the fine details. The main limitation of the technique is in the surface area correction factor. This is necessary, but must be empirically fitted to existing data. The values obtained for the

correction factor will be different depending on the amount of overlap allowed in the system. As the overlap tends towards zero, the inclusion of the correction factor will become less important, and actually in the experimental results there was very little overlap.

In addition to overlap it would be beneficial to test the model over a wider range of sizes of the particles and fibres. Most of this modelling was for fibres and particles of a similar size to the experimental filters, but it would be interesting to see how the model changes with more radical changes in fibre and particle dimensions; this would require a much more powerful computer. Since the size distributions of the fibres and particles are known, it would also be of interest to vary the sizes of the components within the model according to these distributions. Assigning each individual particle and fibre its own unique dimensions would significantly increase the number of parameters that would need to be imported into COMSOL, and so again, a more powerful computer would be necessary.

Even with its limitations, it does show promise for being able to predict trends in permeability for samples with a known porosity and fibre volume fraction. With the knowledge that the model offers a good comparison to the experimental results this could be used to predict filtration efficiencies by simulating the flow of particles through these idealised structures. However, this technique will still suffer from the same problems as the tomography case, which is that it takes a lot of computational power to have a time dependent fluid flow and particle tracing simulation interacting together, such that the particle accumulation on surfaces will affect the fluid flow through the structure. It is this build-up of a soot cake which is the most important factor controlling filtration efficiency, and so future work should concentrate on soot cake formation, and subsequent filtration, to assess the relative effectiveness of these composite filters.

7. Thermal Shock Resistance

7.1. Introduction

DPFs in service will be exposed to high temperatures, sometimes as high as 1000 °C during uncontrolled regeneration. In drop-to-idle conditions, this can lead to local hotspots forming in the DPF, which can raise the temperature at high temperature gradients. These temperature gradients can lead to cracking of the DPF in a mechanism known as thermal shock. In this process, a large localised temperature gradient leads to expansion of the material. This material is constrained and so the stress increases until it reaches a critical value, at which point pre-existing cracks in the material enlarge to accommodate the strain. Repeated thermal shock cycles will lead to the premature failure of the component.

To theoretically predict the effect of fibre inclusion on thermal shock it is beneficial to derive a merit index, linking the thermal shock resistance to more readily measurable properties. Such figures of merit do exist in the literature [171], but these use a strength-based approach which is not well-defined for brittle materials. Therefore, a fracture mechanics (energy-based) approach is used here. Figure 7.1 shows the effect of thermal shock on a constrained sample (in this case the analysis is for quenching, but the same result will be applicable to rapid heating situations). This effect will happen in all directions transverse to the heat flow axis, so that the ratio of stress to strain in all such directions is the biaxial modulus ($E/(1-\nu)$).

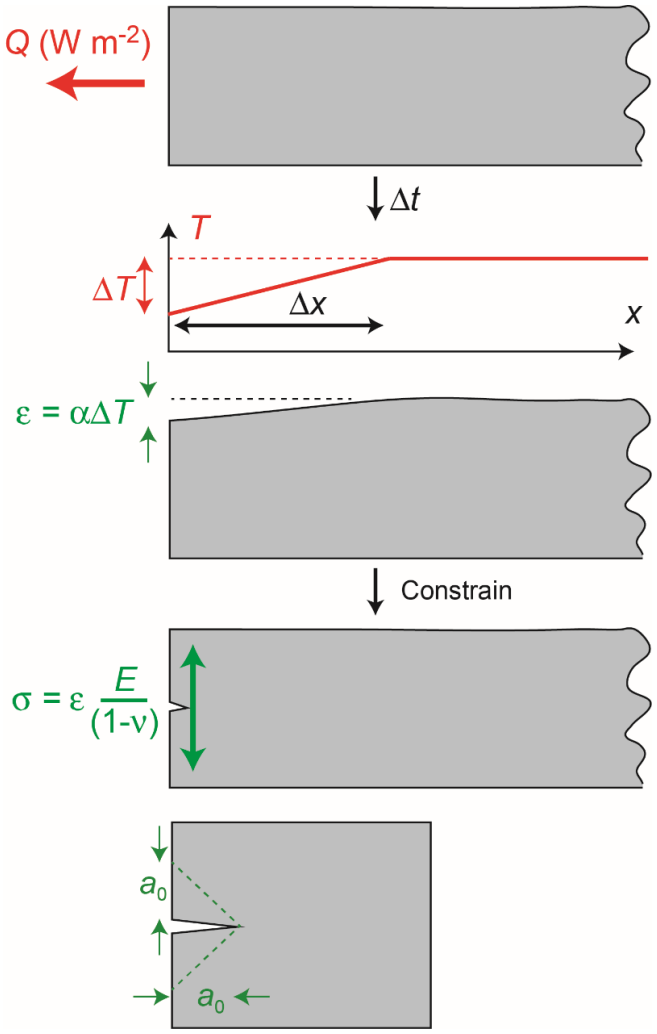

Figure 7.1: Schematic representation of how thermal shock (quenching of the free surface of a hot sample in this case) creates stresses that may lead to fracture.

Taking the thermal gradient to be linear (despite the transient nature of the process), the quantity of heat extracted (per unit area normal to the heat flow direction), during the time interval concerned, can be written:

$$Q_h \, \Delta t = \frac{1}{2} c \, \Delta T \, \Delta x \qquad (7.1)$$

where c is the volumetric heat capacity of the material (J K^{-1} m^{-3}). Recalling from Equation 3.9, the heat flux, Q_h, can also be written as:

$$Q_h = k \frac{dT}{dx} \qquad (7.2)$$

where k is the thermal conductivity (W m^{-1} K^{-1}). The temperature drop at the surface can then be expressed as:

$$\Delta T = Q_h \sqrt{\frac{2\,\Delta t}{c}} \tag{7.3}$$

Looking at Figure 7.1, an expression for the critical strain energy release rate, G_c, for a crack of length a_0, taking the volume in which strain is released to be the simple triangular regions shown, may be written:

$$G_c = \frac{1}{2}\sigma_r \varepsilon_r \frac{2\sqrt{2}\, a_0 z\, \Delta a_0}{2\, z\, \Delta a_0} = \frac{\sqrt{2}}{2}\sigma_r \varepsilon_r\, a_0 = \frac{\sqrt{2}}{2}{\varepsilon_r}^2 \frac{E}{(1-\nu)}\, a_0 \tag{7.4}$$

where $\sigma_r \varepsilon_r / 2$ is the strain energy released per unit volume (J m^{-3}), z is the thickness into the page (m) and Δa_0 is the small increase in crack length being considered (m). Taking the thermal expansivity to be $\alpha = \varepsilon_r / \Delta T$, and by combining Equations 7.3 and 7.4, an expression is obtained for the critical heat flux to cause fracture:

$$Q_{crit} = \frac{1}{\alpha}\sqrt{\frac{G_c(1-\nu)kc}{\sqrt{2}\, E a_0 \Delta t}} \tag{7.5}$$

A figure of merit, M_{TS}, dependent only on material properties, can be obtained by simply removing a_0 and Δt from this expression:

$$M_{TS} = \frac{1}{\alpha}\sqrt{\frac{G_c(1-\nu)kc}{E}} \tag{7.6}$$

This is suitable for ranking purposes, although it does have the drawback of not representing a well-defined physical characteristic. However, if a physically meaningful number were required, then it would be possible to use Equation 7.5, substituting plausible values for a_0 (a flaw size) and Δt (a quenching period) so as to give an actual heat flux (in W m^{-2}) likely to cause fracture.

These dependencies are unsurprising; a higher fracture energy results in a material being able to withstand higher stresses before fracture, a lower Poisson's ratio will result in lower strains, a higher heat capacity allows the material to store more internal energy for a given temperature change, a higher thermal conductivity allows for faster heat conduction, meaning that the high temperatures formed in a local hotspot can be more effectively dispersed, a lower stiffness means that a thermally induced strain will result in a lower stress and a lower thermal expansivity means that, for a given temperature, the generated strains will be lower.

7.2. Fracture toughness

Fracture toughness exhibited a trend of an increasing fracture toughness with increasing fibre volume fraction. The results are plotted in Figure 7.2.

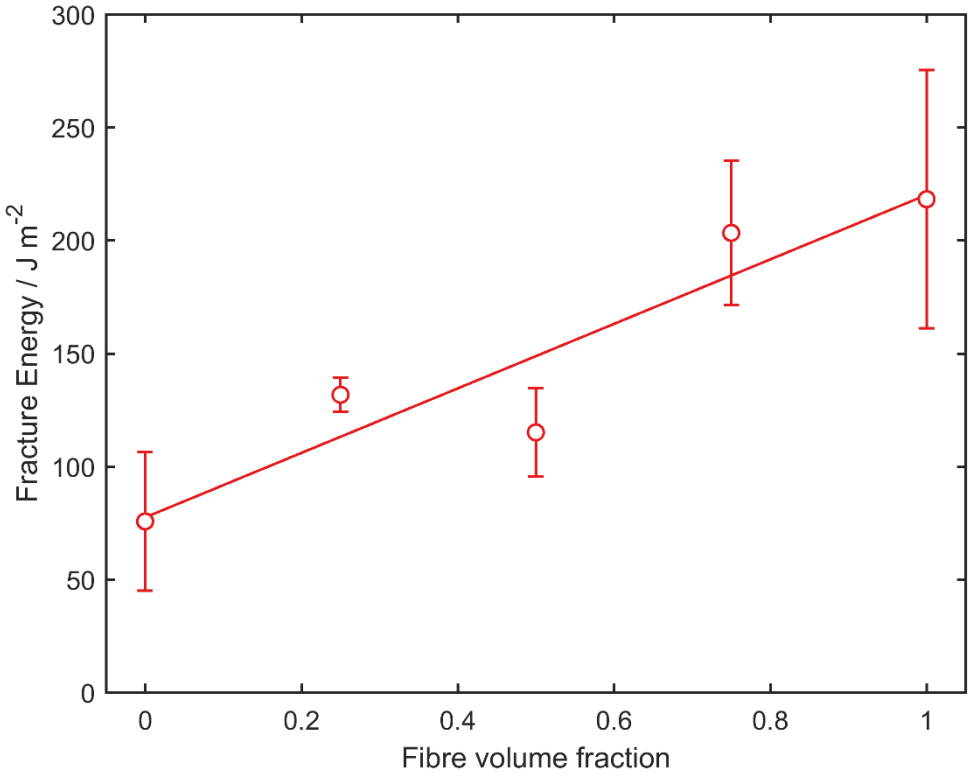

Figure 7.2: Variation of fracture energy as a function of fibre volume fraction

Since the samples were brittle porous ceramics, there was a large variation in fracture energy at each fibre content, determined by the connectivity of the pore structure and any micro-cracks which may have arisen during manufacture, sintering or handling. To overcome such difficulties, the fracture toughness was measured on many samples (~15) per fibre volume fraction. A mean was taken, and the error bars were evaluated by taking the error in the mean. The resulting graph shows that there is certainly an increase in fracture energy as fibre volume fraction increases, with the value at 100 % fibres being double that of 0 % fibres. With large error bars it is difficult to say anything precise about the nature of the relationship, but a straight line provides an acceptable fit.

The values themselves are within the expected range. They are certainly fairly low, but agree with values in the literature for similar materials [172].

Even in porous systems, the trend of an increasing fracture toughness with addition of fibres can be explained by the mechanism of fibre pull-out. This mechanism is well understood by those in the field of composite materials [87] and is a leading reason as to why fibres are used in such situations. In the process of fibre pull out, as a crack penetrates through a material, fibres brace the gap which opens, and resist further crack opening. In order for the crack to progress, the fibres must be broken, therefore acting as a method of energy absorption. Due to the ceramic nature of the fibres in these composites, the break of the fibre might not even occur in the cracked region but rather at a weak part of the fibre buried within the material. In such a scenario, not only is energy absorbed by the process of a fibre breaking, but also in the friction of its removal from the rest of the material. These two energy absorbing mechanisms are crucial in understanding how fibres strengthen materials, and their impact can be clearly seen in the results presented above.

A higher fracture toughness is beneficial as it appears as a numerator in the thermal shock resistance merit index presented in Section 7.1. This is understandable since obviously if cracking of the filters under thermal stresses is to be avoided, a higher resistance to crack propagation is essential. Considering such results, it would be clear to suggest that adding fibres would be a very beneficial addition to a DPF due to the significant increase in fracture toughness that results.

7.3. Stiffness

Stiffness was measured many times with respect to fibre content using both tensometer 4-point bend tests and Resonant Frequency Damping Analysis (RFDA) techniques. The summary of all these techniques is presented in Figure 7.3.

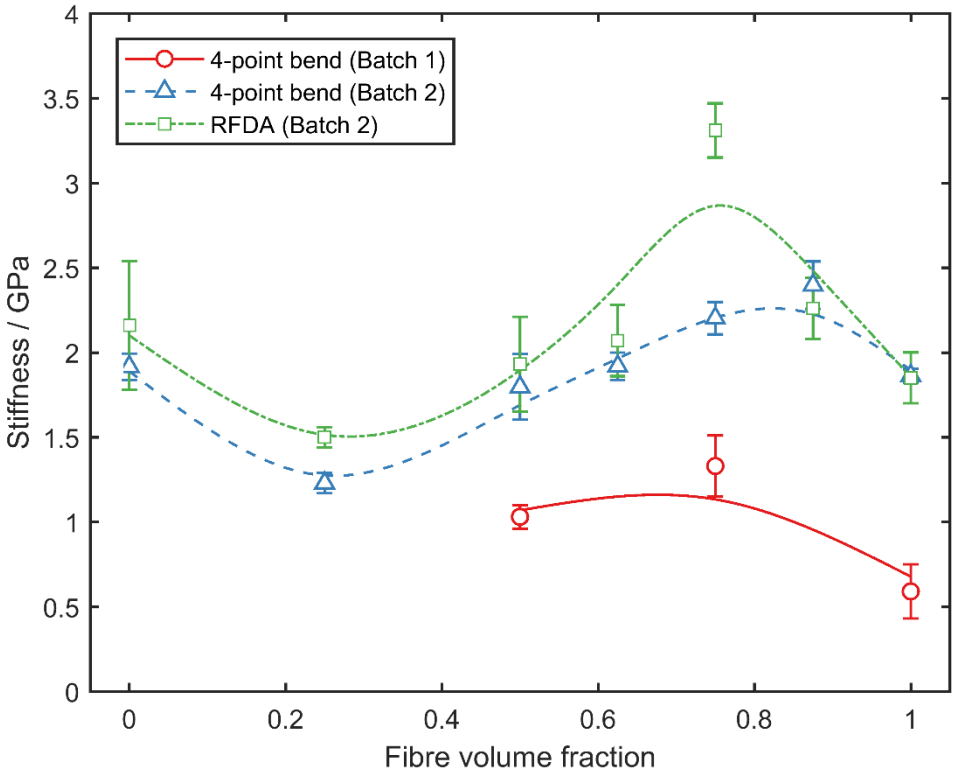

Figure 7.3: Variation of stiffness with fibre volume fraction measured on two batches of samples. The first was measured only by a 4-point bend test, whereas the second was measured using 4-point bending and RFDA.

The most important result is that the stiffness values themselves are desirably low. In a DPF application, where thermal shock is to be avoided, a lower stiffness allows accommodation of a larger strain before failure of the material. For comparison, current cordierite DPFs have a slightly larger Young's modulus of 4.7 GPa [173].

The stiffnesses of two batches of samples were measured. For each fibre volume fraction in a given batch, at least four samples were tested. For the first batch, only the

four-point bend test was used. Stiffnesses were all low, and seemed to peak at 75 wt.% fibres. The second batch of samples measured the stiffness across the entire range of fibre ratios, by four-point bend test and also by RFDA. There was good agreement between the two testing methods. The only point of discrepancy is at a fibre fraction of 75 wt.%, which is difficult to explain, but can be treated as an anomaly.

Whilst the shape of the batch 1 results seems to reflect the same trend as the two batch 2 datasets, the absolute figures are significantly lower. These results were obtained on samples with a higher water content than the other samples, highlighting the need for consistent water content of samples during production.

All three curves show evidence of a peak stiffness around 75 wt.%. This is also in agreement with the results found on the first generation of materials, where a similar stiffness peak was observed (Figure 4.2). Having gathered evidence from three different experimental batches, and using manual and automated four-point bending in addition to RFDA, this peak in stiffness seems to be a true representation of the variation in stiffness of these hybrid particle and fibre composites. The decrease in stiffness with fibre addition at low and high fibre contents can be rationalised as being due to the increase in porosity [158]. In the intermediate fibre content levels, where there are approximately equal volumes of particles and fibres, the stiffness appears to increase with increasing fibre content. This increase could be explained by a greater number of fibre contact points leading to shorter fibre segments [91], and perhaps this factor dominates in the intermediate regime. It is clear from these results that the hybrid particle and fibre composites are complex systems where the stiffness cannot be explained as simply as in the case of purely particle arrangements or arrays of fibres.

7.4. Thermal expansivity

Thermal expansivity was measured as a function of fibre volume fraction using a dilatometer. The results are shown in Figure 7.4.

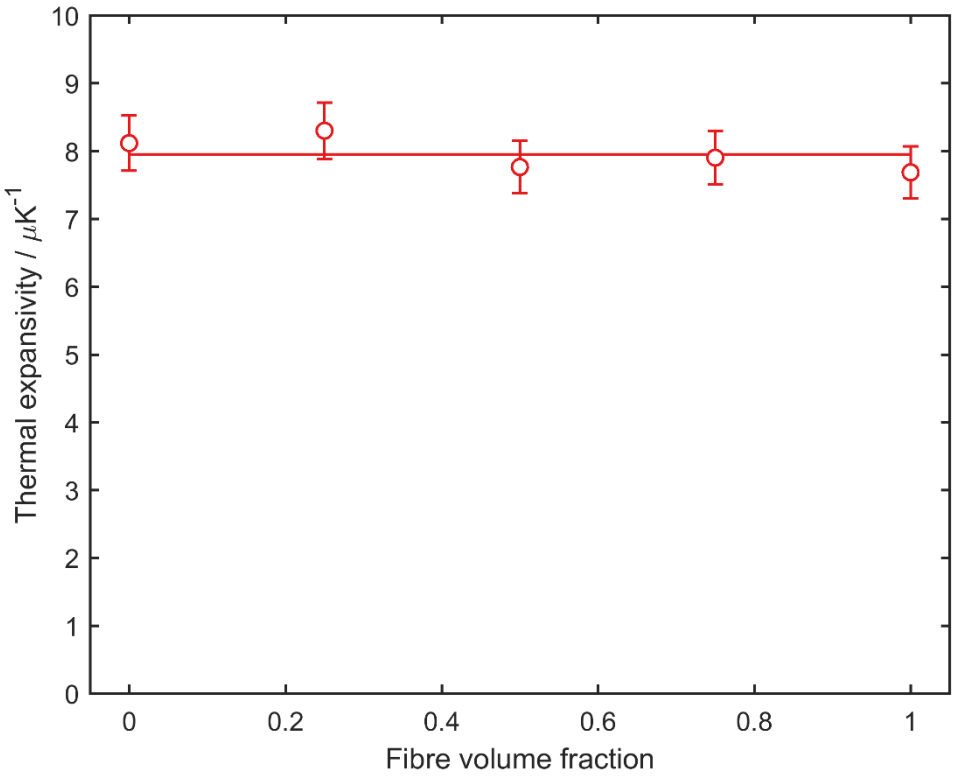

Figure 7.4: Variation of thermal expansivity with respect to fibre volume fraction

The thermal expansivity essentially remained constant with respect to fibre volume fraction. Certainly, the thermal expansivity does not vary much, and fluctuations of less than 0.5 μK^{-1} are small enough that they can simply be attributed to being due to experimental error. In fact, the error bars on the points, determined by errors accumulated in the dilatometer, extend over a similar range.

Although there is no dependency on fibre content, the absolute value itself is worthy of note. The thermal expansivities of the samples were measured to be 8 μK^{-1}. Thermal expansivity appears as a denominator in the thermal shock resistance merit index, as such the thermal expansivity must be minimised. This is easily understood by considering the effect of a thermal expansion within a DPF: During regeneration, the exhaust temperature is raised to around 650 °C. Locally, it is possible to observe temperature spikes of over 1000 °C within the material. This is a significant temperature increase which will induce expansion of the material. A DPF is constrained within the exhaust system, and, locally,

by the surrounding material. As a consequence, a sharp heating spike can cause large thermal stresses in the material, which can lead to the premature failure of a DPF. By selecting a material with a low thermal expansivity, the thermal stresses will be reduced, and thus the likelihood of failure is reduced.

The value of 8 μK^{-1} is the same as that for bulk alumina [167], which is expected due to the widely-acknowledged independence of porosity on thermal expansivity [87]. Whilst this work is focussed on the feasibility of adding fibres to a DPF filter material, rather than the material itself, it is worth discussing how alumina, the material used throughout this project, compares with commonly used materials in commercial DPFs. The most commonly used materials are cordierite and silicon carbide. Cordierite has a very low thermal expansivity (1.4 μK^{-1} [174]) and it is in fact one of the reasons why it was first selected as a DPF material. Its very low thermal expansivity means that a DPF can be made of a single cordierite piece and the induced thermal stresses will be low enough that fracture is uncommon. SiC on the other hand has a relatively high thermal expansivity (4.9 μK^{-1} [175]). It outperforms cordierite in many other aspects, but the thermal expansivity of SiC is one of its weaknesses. Its higher value means that expansion in a DPF-sized unit of SiC wold be detrimental, with thermal stresses able to fracture the material in a single regeneration cycle. However, there is a simple solution to this problem which is used in all SiC-based DPFs, which is to divide the DPF up into regions, separated by a low modulus grout. This grout is made of short silica fibres dispersed in a fine grain cementitious matrix and is substantially more porous than the filtering material [82, 176]. The thermal stresses within the smaller sub-units never build up to a catastrophic level, and so crack propagation is avoided, and the sub-units are free to expand into the low modulus grout.

It is apparent that the thermal expansivity of alumina does not make it a favourable material for a DPF. Although, if any of its other properties put it at a clear advantage against the currently used materials, there is the possibility of dividing up the DPF into sub-units to overcome this problem.

7.5. Thermal conductivity

Measurements of thermal conductivity, using the experimental method outlined in Section 3.8, yielded the results observed in Figure 7.5.

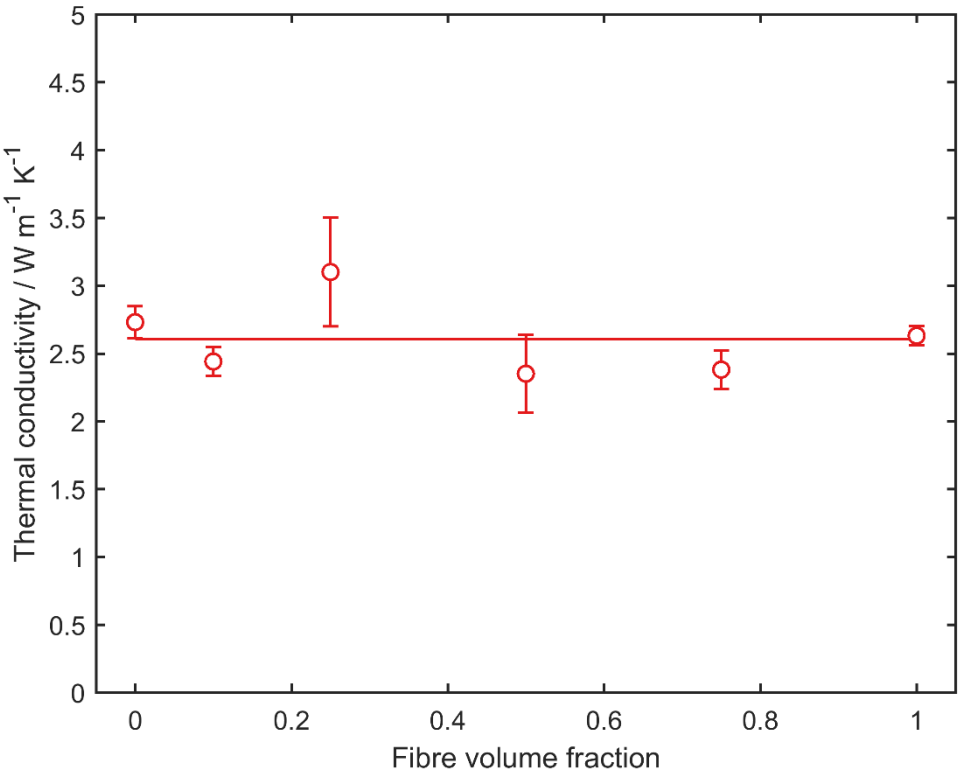

Figure 7.5: Variation of thermal conductivity with respect to fibre volume fraction

It is apparent that across the fibre volume fraction range there seems to be little variation in the thermal conductivity when tested at temperatures up to 150 °C. Naturally, due to the low thermal conductivity of air it might be expected that as porosity increases with increasing volume fraction (Section 4.3.1), the thermal conductivity of the material might decrease, though no such trend was observed.

By looking at the merit index for thermal shock resistance it is clear that the thermal conductivity must be maximised. The reason for maximising the thermal conductivity is to allow for any thermal hotspots in the DPF filter to dissipate the heat effectively to

surrounding regions, thus reducing the risk of cracking due to highly localised thermal stresses.

Returning to Figure 7.5, it is clear to see that as the porosity has increased, which is favourable for reducing the back pressure, it has had no effect on the thermal conductivity. In fact, although thermal conductivity has been shown to be highly dependent on porosity for porosity levels <20 %, at higher porosities (40–60 %) the dependence has also been shown to be much weaker in the case of cubic packed grains in a continuous pore phase [158]. This is reassuring since if the thermal conductivity had decreased as might be expected it would imply that adding fibres might negatively affect the thermal shock resistance. A possible explanation for this is that there is some competing factor in the structure which maintains the thermal conductivity at a constant level. This competing factor is likely due to the nature of the structure itself: fibres lead to a more connected structure between particles, and with more connections, a higher thermal conductivity may be achieved. Markaki *et al.* [163] showed that the thermal conductivity in fibrous arrays is dependent on the angle between the fibre axes and the heat flow direction (with the conductivity decreasing with increasing angle). Whilst the fibres in the current samples are expected to be isotropically arranged, it is evident that fine adjustments in microstructure can lead to noticeable variation in thermal conductivity.

It appears that the trend of thermal conductivity with fibres offers no benefit of adding fibres. However, it is interesting to compare the absolute value. The thermal conductivity was measured to be around 2.5 W m^{-1} K^{-1}. This is a low thermal conductivity, even for a ceramic, with fully dense SiC and alumina having values of 90 W m^{-1} K^{-1} [177] and 33 W m^{-1} K^{-1} [178] respectively. Clearly this property makes SiC a strong candidate material for a DPF application. The value obtained above in Figure 7.5 was much lower than the fully dense alumina value, and that is due to the partially sintered porous nature of the filters. These results are actually better than the values of cordierite which is a commonly used DPF material; fully dense cordierite has a thermal conductivity of just 1–3 W m^{-1} K^{-1} [35], with its porous value falling well below the 2.5 W m^{-1} K^{-1} measured for porous alumina above. Whilst this report is not aiming to propose alumina as a new DPF material, this is an area in which it performs better than DPFs currently on the market.

7.6. Thermal shock

The Vacuum Plasma Sprayer (VPS) was a method chosen to experimentally determine the thermal shock resistance, rather than relying on a merit index. In this experiment, the clamped samples are exposed to a high temperature in a specific area of the sample. The localised heating leads to micro-cracking as the stress in the constrained sample increases as the localised region attempts to thermally expand.

The effect of thermal shock resistance was quantified by measuring the stiffness before and after such a treatment. RFDA stiffness measurements were favoured due to the non-destructive nature of the test. The entirety of the results is presented in Figure 7.6.

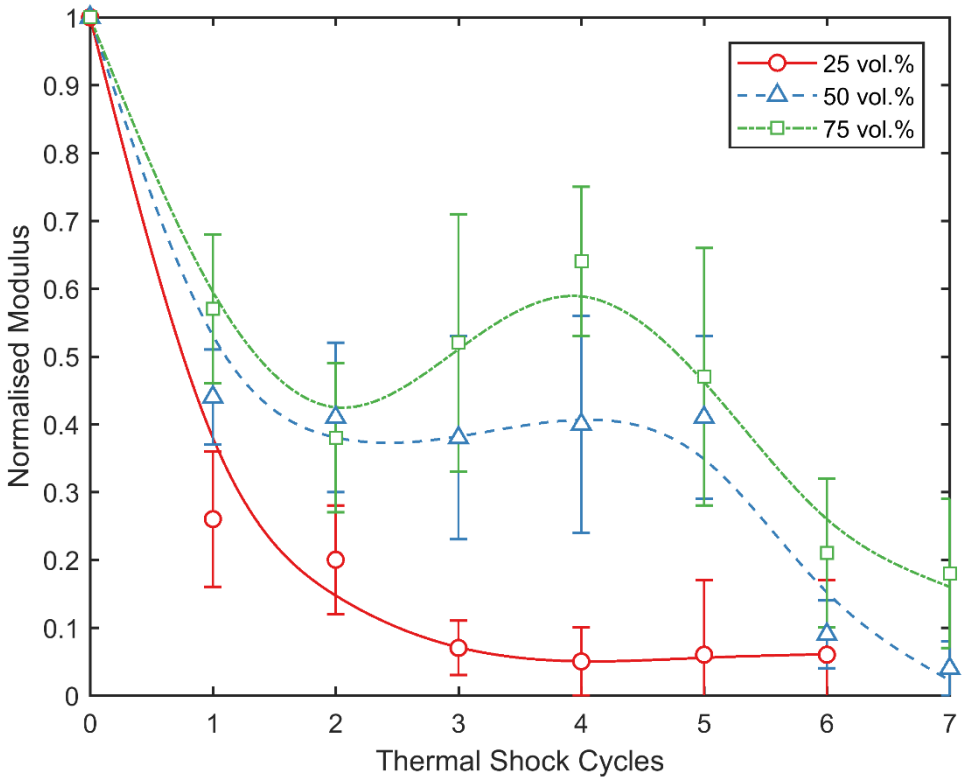

Figure 7.6: All data from the VPS thermal shock experiment.

As can be seen there is a huge amount of variability in the results, a consequence of working with highly porous ceramics. Also, these values represent averages of all samples that have undergone certain conditions, whereas some of them are not entirely identical.

For example, the 50 wt.% marker at 3 thermal shock cycles is an average of three samples: the first had its stiffness tested once, after all 3 thermal shocks, the second had its stiffness tested after one thermal shock and then again after a further two, and the third was tested after each thermal shock. Although these are the same number of thermal cycles, there is an unavoidable degree of micro-cracking which can occur when loading and unloading the samples into the testing rig, and even the act of testing the stiffness which, whilst described as non-destructive, does still impact on the sample and can lead to a reduction in stiffness. With all of the above considered, samples were very carefully handled, and no more stiffness measurements than were necessary (two consistent readings) were taken. These precautions will minimise the errors mentioned, but they should still be noted as problems, and can lead to significant variability in the results.

From Figure 7.6 it is clear that there is an overall trend for the stiffness to decrease with increasing numbers of thermal shock cycles. This is expected, and the peaks at around 4 thermal shock cycles for both the 50 and 75 wt.% samples are due to averaging of samples having undergone different numbers of stiffness measurements. Of course, there is no mechanism by which the stiffness can increase having undergone an additional shock cycle; for an individual sample, the stiffness was always observed to decrease upon further thermal shock. There is also an indication that as fibre volume fraction is increased the effect of thermal shock resistance is reduced. It is difficult to separate the results of the 50 wt.% samples and the 75 wt.% samples, due to the size of the error bars, but both seem to be significantly better than the 25 wt.% samples.

Focusing in on the detail of Figure 7.6, the effect of just a single thermal shock cycle can be seen, and is plotted on a separate graph, Figure 7.7.

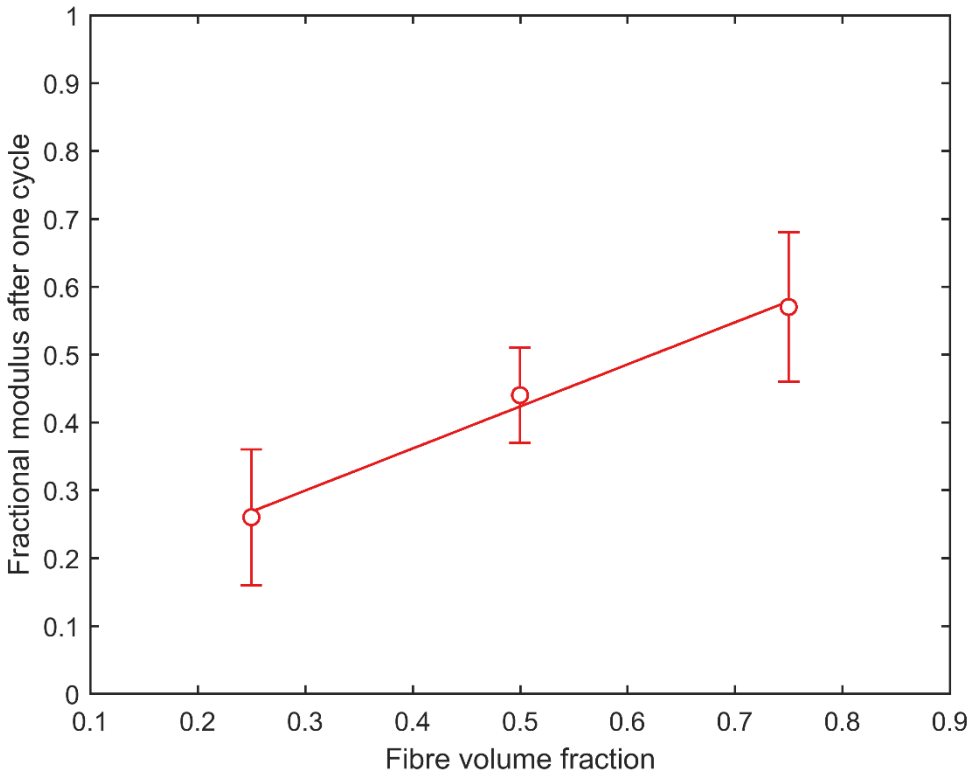

Figure 7.7: The stiffness after one cycle as a fraction of the original stiffness of the untested sample plotted against fibre volume fraction.

This will be some of the most reliable data from the initial plot, since all samples will have been treated exactly the same: stiffness measurement, put into the rig, one thermal cycle, second stiffness measurement. In terms of the mean result there is a very clear trend that as fibre volume fraction is increased from 25 wt.% up to 75 wt.% the thermal shock resistance seems to also increase, i.e. the initial drop in stiffness is considerably less for higher volume fractions.

Another detail to note is how many cycles are required until failure. These results are presented in Figure 7.8.

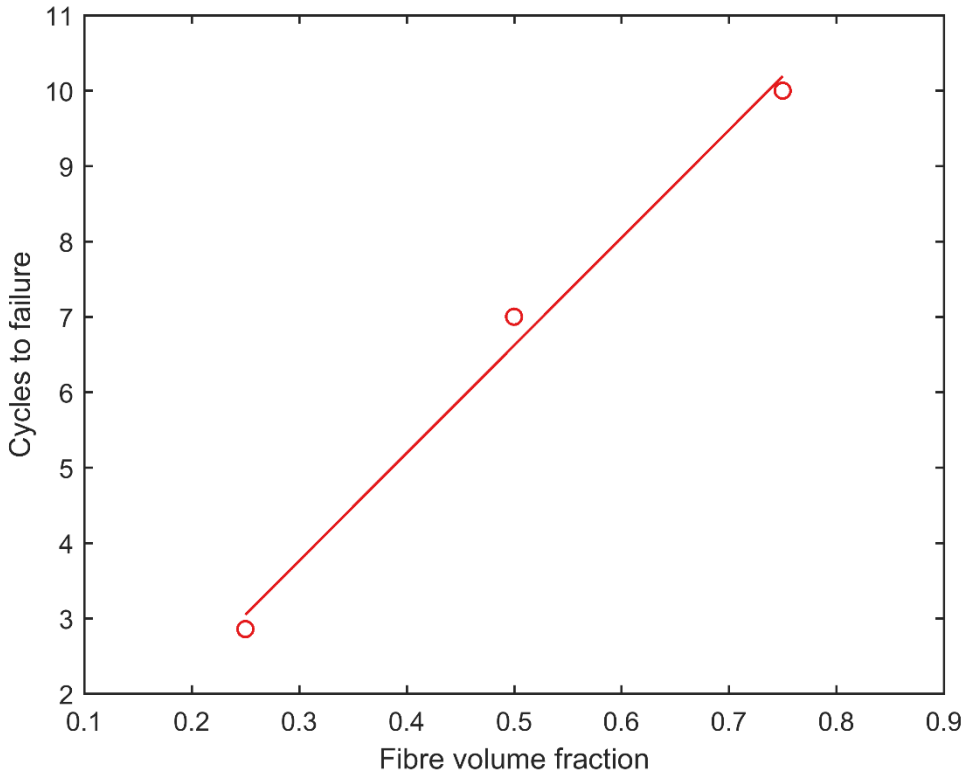

Figure 7.8: The average number of cycles required to crack a sample due to thermal shock plotted as a function of fibre volume fraction.

It can be seen that the lifetime of samples with higher fibre volume fractions was longer than those with a lower fibre content. Visibly this was also observed; samples subjected to the same conditions looked significantly more damaged at lower fibre contents but looked largely unaffected by the heat treatment as fibre content was increased. This will be linked to the more friable nature of the low fibre content samples.

7.7. Thermal shock resistance merit index

By substituting these parameter values into the thermal shock merit index (Equation 7.6), the variation of thermal shock resistance can be semi-quantitatively calculated. The Poisson's ratio is assumed to remain unchanged as fibre content is varied. Although models predict a slight decrease in Poisson's ratio with increasing porosity [153, 179], experiments performed on porous alumina show that the value remains essentially

constant within experimental error [179]. The Poisson's ratio was assumed to be 0.21 [153]. The volumetric heat capacity was also assumed to be constant, at 3 MJ m^{-3} K^{-1} [180], since it is a property analysed per volume of solid material, and thus unaffected by porosity. The thermal expansivity remained constant, and, slightly surprisingly, the thermal conductivity also remained constant. The merit index therefore was only dependent on the ratio of the fracture energy to the stiffness.

The merit index values obtained by using values found in Sections 7.2–5 are plotted below in Figure 7.9.

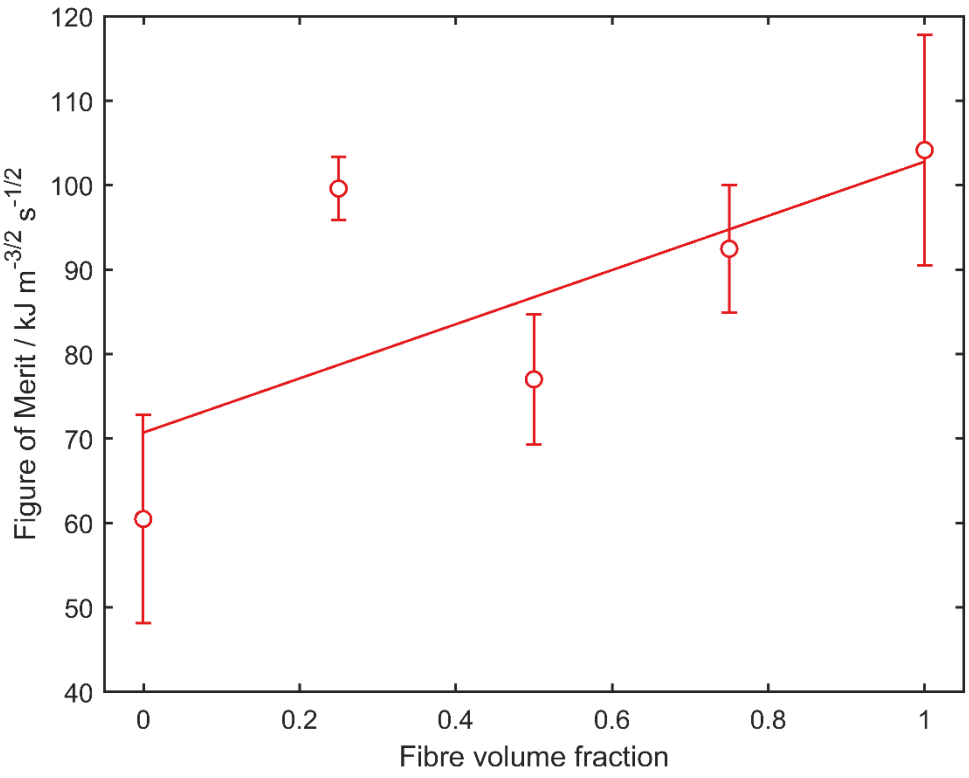

Figure 7.9: Figure of Merit of thermal shock resistance (J $m^{-3/2}$ $s^{-1/2}$) as a function of fibre volume fraction.

The data show that there could be an increase in the thermal shock resistance as fibre content is increased. A clear exception to the simple linear fit that has been applied to the data is the result at 25 wt.% fibres. It is clear where this high value has come from: the fracture toughness was slightly higher than might have been expected, but the main reason

will be due to the low stiffness (Figure 7.3). The complexity of the hybrid particle and fibre system, with its many competing factors, will likely lead to a non-linear relationship of merit index and fibre content. In fact, it can be reasoned that there would be significant benefits to adding just a few fibres to a predominantly particle matrix (fracture energy was shown to increase and stiffness decreases), but this initial advantage could be overcome as the fibre content approaches an even mixture of particles and fibres, due to increased interlinking of fibres, and thus shorter fibre segments, leading to an increased stiffness. At high fibre contents, the composites may be thought of as a small number of particles in a fibrous matrix and, by replacing the few remaining particles with fibres, the fracture toughness increases and stiffness decreases leading to a second peak in the thermal shock resistance.

However, disagreement arises when comparing this analysis with the results from the VPS thermal shock experiment. In this experiment, the thermal shock was observed to be significantly worse for the 25 wt.% samples compared to the 50 and 75 wt.% fibre samples. In fact, the results from the VPS would suggest an improving thermal shock resistance with increasing fibre inclusion, with no secondary peak around 25 wt.%. Of course, in either the VPS tests or the derivation of the merit index, analysis is being performed on very few different fibre volume fractions, and large uncertainties hinder any definite conclusions being drawn.

7.8. Conclusion

This chapter aimed to quantify the effect of adding fibres into a porous particle-based filter on the thermal shock resistance. With the aid of a merit index, various properties were measured to examine how thermal shock resistance varied. The merit index was found to be solely dependent on the variations of fracture energy and stiffness, since thermal expansivity and thermal conductivity were measured to be constant across the range of fibre contents (the former is unsurprising, but the latter is an interesting result).

The results indicate that the thermal shock resistance does appear to increase with increasing fibre content. However, the dependency is likely to be more complicated than a simple linear relationship, and a high value at 25 wt.% indicates there may be a benefit

of a small number of fibres within a predominantly particle-based composite over an even mixture of particles and fibres.

An attempt was also made to measure the thermal shock resistance experimentally using a vacuum plasma sprayer. The results had a high degree of uncertainty but hinted at an improved thermal shock resistance with increasing fibre content, in terms of both severity and lifetime.

Overall Conclusions

In this study, the effect of fibre inclusion in porous particle-based materials has been considered, in the context of Diesel Particulate Filters. The following conclusions can be drawn:

- A novel type of highly porous, hybrid ceramic composite has been produced, incorporating a range of proportions of coarse, equiaxed alumina particles and fine alumina fibres having aspect ratios on the order of 10–20.

- Processing conditions (isostatic pressing time and pressure, sintering time and temperature) have no effect on the porosity or permeability of the filters. This is due to the presence of water and PVA during pressing and limited levels of sintering.

- These materials are highly porous, with higher porosities observed for the materials containing greater proportions of fibres; increasing from 46 % to 59 % for 0 and 100 wt.% fibres respectively (Figure 5.1). Permeability, on the other hand, was shown to decrease over the range of fibre volume fraction (Figure 5.2), although not by a significant amount (from 1.03×10^{-12} m^2 at 0 wt.% to 0.7×10^{-12} m^2 at 100 wt.% fibres). The implication of these two trends is that the specific surface area of the filters increases greatly with fibre content.

- Tomography was used in an attempt to predict filtration efficiency. Whilst some basic properties could be determined, it proved ineffectual for porous structures on the scale of these miniature DPFs. Difficulties in resolution prompted the generation of an idealised model consisting of spheres and cylinders packed into

periodically repeating cubes. This model, in combination with the Carman-Kozeny equation, allowed for an empirical equation (Equation 6.23) to be generated to predict the permeability of a fibre-particle-void composite given the porosity, fibre content, and particle and fibre dimensions. Agreement was observed when comparing the predictions with experimental values, and therefore the model can be considered a suitable interpretation of the actual composites.

- Measurements of fracture energy showed a positive correlation of increasing toughness with increasing fibre content, with those consisting solely of fibres displaying energy absorption over twice that of the particle-based composites (Figure 7.2).

- Stiffness showed a complex relationship with respect to fibre content. This was first observed in the preliminary tests on first-generation materials, but the same trend was observed for the second-generation materials (Figure 7.3). All stiffness values were desirably low, although a peak stiffness was observed at around 75 wt.% fibres.

- A figure of merit derived for the thermal shock resistance was shown to increase with increasing fibre content (Figure 7.9). This is expected to be much more complex than a simple linear relationship, and fibre contents of ~25 wt.% are worth possible further investigation. Thermal shock was also measured experimentally, and the lifetime and severity of the thermal shock were observed to improve with increasing fibre content.

Overall, there is a strong argument for the addition of fibres into the DPF filter material. The increased porosity, whilst also significantly increasing the specific surface area, suggests the filter could offer a higher soot loading capacity, thus lengthening the time between regenerations. Permeability is not significantly affected, and the inclusion of small diameter fibres (compared to the particle diameter) increases the Stokes number, thus it is predicted that the period of initially low filtration efficiency of a clean filter could be shortened. Fibres also offer significant advantages for the thermal shock

resistance. Fibres are well-known for their toughening ability and this remains true for these hybrid particle and fibre composites.

Further Work

This study has shown that there are significant benefits to adding fibres to porous particle-based filters. A natural progression to this work would be to test the fibre-based composites in a real DPF scenario. It would be worthwhile to produce a full-size DPF made of these fibrous hybrid composites, which could then be tested using industrial equipment. One of the main focusses of this study, the filtration efficiency, was only possible to predict using porosity and permeability.

Most of the filtration in a DPF actually occurs by passing the exhaust gases through the soot cake. This soot cake formation was not considered in this study, but rather the fluid flow through a perfectly clean DPF was investigated. Whilst it has been theorised that fibres will result in quicker soot cake formation (due to their finer scale) and perhaps higher soot loading capacity, allowing for a smaller back-pressure for a given quantity of soot (due to the increased porosity and specific surface area) it would be beneficial to quantify these claims experimentally.

The work on simulation of fluid flow through arrays of spheres and cylinders is an area which has not been considered in the literature. There are plenty of examples of fluid flow past spheres, or fibres, but the hybrid regime has been overlooked. The analysis in this work is applicable to a wide range of applications beyond diesel particulate filters and it would be beneficial to develop the ideas introduced in this work further. By studying a wider range of fibre and particle sizes, a clearer picture of the variation of permeability with respect to fibre content, porosity and fibre and particle sizes can be obtained. Ideally, this could be confirmed by experiments.

One of the issues that arose during modelling was that of computing power. Analysis of data was limited by computer memory, and perhaps using more powerful hardware would allow for study of higher fibre content materials, an area which was studied experimentally, but proved impossible to simulate on the available computer resources. This limitation was not actually due to the simulation of fluid flow through the structure, but simply due to importing the structure into the software. Perhaps other modelling software other than COMSOL might be more suitable. COMSOL solves the fluid dynamics problem by solving the Navier-Stokes equations for fluid flow; whilst this leads to accurate results, similar values may be found using less computationally taxing methods, e.g. the commonly-used lattice Boltzmann (LB) methods which are favoured by the literature for analysing fluid flow through DPFs. LB methods are not available on COMSOL, but other software may be able to simplify the fluid flow problem, and the simpler approach may lead to the possibility of predicting accumulation of PM particles within the structure. In this way, the soot cake layer could be analysed, providing important predictions for the effect of fibre content on the soot cake layer.

References

1. Schmidt, C.W., *Beyond a One-Time Scandal: Europe's Onging Diesel Pollution Problem.* Environmental Health Perspectives, 2016. **124**(1): p. A19.
2. The International Council on Clean Transportation, *European Vehicle Market Statistics Pocketbook*. 2014.
3. Heywood, J.B., *Internal combustion engine fundamentals*. Vol. 930. 1988: Mcgraw-hill New York.
4. Kittelson, D.B., *Engines and nanoparticles: a review*. Journal of aerosol science, 1998. **29**(5): p. 575-588.
5. United States Environmental Protection Agency. *Frequent Questions about Volkswagen Violations* [cited 2019 16/01/2019]; Available from: www.epa.gov/vw/frequent-questions-about-volkswagen-violations.
6. Prasad, R. and V.R. Bella, *A review on diesel soot emission, its effect and control.* Bulletin of Chemical Reaction Engineering & Catalysis, 2011. **5**(2): p. 69-86.
7. Sehlstedt, M., et al., *The Role of Particle Size and Chemical Composition for Health Risks of Exposure to Traffic-Related Aerosols—A Review of the Current Literature.* Final Report, 2007. **71212**.
8. United States Environmental Protection Agency, *Expanding and Updating the Master List of Compounds Emitted by Mobile Sources - Phase III*, 2006.
9. Hall-Roberts, V., et al., *The origin of soot in flames: Is the nucleus an ion?* Combustion and flame, 2000. **120**(4): p. 578-584.

10. Maricq, M.M., *Chemical characterization of particulate emissions from diesel engines: A review.* Journal of Aerosol Science, 2007. **38**(11): p. 1079-1118.

11. Ristovski, Z.D., et al., *Respiratory Health Effects of Diesel Particulate Matter.* Respirology, 2012. **17**: p. 201-212.

12. Robinson, A.L., et al., *Updating the conceptual model for fine particle mass emissions from combustion systems Allen L. Robinson.* Journal of the Air & Waste Management Association, 2010. **60**(10): p. 1204-1222.

13. Department of Economic and Social Affairs, *World Urbanization Prospects: The 2014 Revision, Highlights*, 2014, United Nations.

14. Pope III, C.A. and D.W. Dockery, *Health effects of fine particulate air pollution: lines that connect.* Journal of the air & waste management association, 2006. **56**(6): p. 709-742.

15. Wichmann, H.-E., et al., *Daily mortality and fine and ultrafine particles in Erfurt, Germany part I: role of particle number and particle mass.* Research report (Health Effects Institute), 2000(98): p. 5-86; discussion 87-94.

16. Brown, D.M., et al., *Size-dependent proinflammatory effects of ultrafine polystyrene particles: a role for surface area and oxidative stress in the enhanced activity of ultrafines.* Toxicology and applied pharmacology, 2001. **175**(3): p. 191-199.

17. Guan, B., et al., *Review of the state-of-the-art of exhaust particulate filter technology in internal combustion engines.* Journal of environmental management, 2015. **154**: p. 225-258.

18. Jantzen, K., et al., *Oxidative damage to DNA by diesel exhaust particle exposure in co-cultures of human lung epithelial cells and macrophages.* Mutagenesis, 2012.

19. Pope III, C.A., et al., *Lung cancer, cardiopulmonary mortality, and long-term exposure to fine particulate air pollution.* Jama, 2002. **287**(9): p. 1132-1141.

20. World Health Organisation and International Agency for Research on Cancer, *IARC: Diesel Engine Exhaust Carcinogenic, Press release number 213*, 2012: Lyon, France.

21. Attfield, M.D., et al., *The diesel exhaust in miners study: a cohort mortality study with emphasis on lung cancer*. Journal of the National Cancer Institute, 2012. **104**(11): p. 869-883.

22. Silverman, D.T., et al., *The diesel exhaust in miners study: a nested case–control study of lung cancer and diesel exhaust.* Journal of the National Cancer Institute, 2012.

23. Committee on the Medical Effects of Air Pollutants, *The Mortality Effects of Long-Term Exposure to Particulate Air Pollution in the United Kingdom*, 2010.

24. Harrison, R., et al., *Airborne particulate matter in the United Kingdom.* Third Report of the Quality of Urban Air Review Group, 1996.

25. Jacobson, M.Z., *Strong radiative heating due to the mixing state of black carbon in atmospheric aerosols.* Nature, 2001. **409**(6821): p. 695-697.

26. Hansen, J., et al., *Climate change and trace gases*. Philosophical Transactions of the Royal Society of London A: Mathematical, Physical and Engineering Sciences, 2007. **365**(1856): p. 1925-1954.

27. Penner, J., C. Chuang, and K. Grant, *Climate forcing by carbonaceous and sulfate aerosols.* Climate Dynamics, 1998. **14**(12): p. 839-851.

28. Brimblecombe, P., *Air composition and chemistry*. 1996: Cambridge University Press.

29. Adler, J. and U. Petasch, *Diesel Particulate Filters*, in *Handbook of advanced ceramics: materials, applications, processing, and properties*, S. Somiya, Editor. 2013, Academic Press.

30. The Automotive Association. *Euro car emission standards*. 2017 [cited 2019 16th January]; www.theaa.com/motoring_advice/fuels-and-environment/euro-emissions-standards.html.

31. Vouitsis, E., et al., *An investigation on the physical, chemical and ecotoxicological characteristics of particulate matter emitted from light-duty vehicles.* Environmental Pollution, 2009. **157**(8-9): p. 2320-2327.

32. Department for Environment Food & Rural Affairs, *Clean Air Strategy 2019*, 2019.

33. Weiss, M., et al., *On-road emissions of light-duty vehicles in Europe.* Environmental science & technology, 2011. **45**(19): p. 8575-8581.

34. European Commission, *Commission welcomes Member States' agreement on robust testing of air pollution emissions by cars (press release)*, 2015: Brussels, Belgium.

35. Adler, J., *Ceramic diesel particulate filters.* International Journal of Applied Ceramic Technology, 2005. **2**(6): p. 429-439.

36. Su, V.M.T. and T.W. Clyne, *Hybrid Filtration Membranes incorporating Nanoporous Silica within a Nanoscale Alumina Fibre Scaffold.* Adv. Eng. Materials, 2015. **18**(1): p. 96-104.

37. Olson, R.A. and L.C. Martins, *Cellular ceramics in metal filtration.* Advanced Engineering Materials, 2005. **7**(4): p. 187-192.

38. Primus, R., et al., *An appraisal of advanced engine concepts using second law analysis techniques*, 1984, SAE Technical Paper.

39. Hield, P., *The Effect of Back Pressure on the Operation of a Diesel Engine*, 2011, Defense Science and Technology Organization Victoria (Australia) Maritime Platforms Division.

40. Aravelli, K. and A. Heibel, *Improved lifetime pressure drop management for robust cordierite (RC) filters with asymmetric cell technology (ACT).* SAE Technical Paper, 2007. **2**: p. 007-01.

41. Konstandopoulos, A.G., E. Skaperdas, and M. Masoudi, *Microstructural properties of soot deposits in diesel particulate traps*, 2002, SAE Technical Paper.

42. Wirojsakunchai, E., et al., *Detailed diesel exhaust particulate characterization and real-time DPF filtration efficiency measurements during PM filling process*, 2007, SAE Technical Paper.

43. Swanson, J., et al., *Filtration Efficiency and Pressure Drop of Miniature Diesel Particulate Filters.* Aerosol Sci. and Techn., 2013. **47**: p. 452-461.

44. Choi, S., K.-C. Oh, and C.-B. Lee, *The effects of filter porosity and flow conditions on soot deposition/oxidation and pressure drop in particulate filters.* Energy, 2014. **77**: p. 327-337.

45. Peckham, M.S., *Personal communication of Cambustion data*, 2015.

46. Konstandopoulos, A.G., et al., *Fundamental studies of diesel particulate filters: transient loading, regeneration and aging*, 2000, SAE Technical Paper.

47. Vafai, K., *Handbook of porous media*. 2015: Crc Press.

48. Valdes-Parada, F.J., J.A. Ochoa-Tapia, and J. Alvarez-Ramirez, *Validity of the permeability Carman -Kozeny equation: A volume averaging approach.* Physica A: Statis. Mechan. & its Applns., 2009. **388**: p. 789 -798.

49. Merkel, G.A. and T. Tao, *Narrow pore size distribution cordierite filters with reduced pressure drop*, 2007, Google Patents.

50. Ichikawa, Y., S.-i. Yamada, and T. Yamada, *Development of wall-flow type diesel particulate filter system with efficient reverse pulse air regeneration*, 1995, SAE Technical Paper.

51. Williams, A.M., et al., *Low Power Autoselective Regeneration of Monolithic Wall Flow Diesel Particulate Filters*, 2009, SAE Technical Paper.

52. Mason, A., et al., *Non-Thermal Particulate Filter Regeneration Using Rapid Pulse Electric Discharges*, 2013, SAE Technical Paper.

53. Graupner, K., et al., *Pulsed Discharge Regeneration of Diesel Particulate Filters.* Plasma Chemistry and Plasma Processing, 2013. **33**(2): p. 467-477.

54. Chen, K. and D. Luss, *Temperature rise during stationary and dynamic regeneration of a diesel particulate filter.* Reviews in Chem. Eng., 2010. **26**(5-6): p. 133-147.

55. Rocher, L., et al., *New generation fuel borne catalyst for reliable DPF operation in globally diverse fuels,* 2011, SAE Technical Paper.

56. Sappok, A. and V. Wong, *Ash effects on diesel particulate filter pressure drop sensitivity to soot and implications for regeneration frequency and DPF control.* SAE International Journal of Fuels and Lubricants, 2010. **3**(1): p. 380-396.

57. Lance, M., et al., *Evaluation of fuel-borne sodium effects on a DOC-DPF-SCR heavy-duty engine emission control system: simulation of full-useful life.* SAE International Journal of Fuels and Lubricants, 2016. **9**(3): p. 683-694.

58. Konstandopoulos, A.G., et al., *Simulation of triangular-cell-shaped, fibrous wall-flow filters,* 2003, SAE Technical Paper.

59. Liu, Z.G. and R.K. Miller, *Flow Distributions and Pressure Drops of Wall-Flow Diesel Particulate Filters*, 2002, SAE Technical Paper.

60. Tsuneyoshi, K. and K. Yamamoto, *Experimental study of hexagonal and square diesel particulate filters under controlled and uncontrolled catalyzed regeneration.* Energy, 2013. **60**: p. 325-332.

61. Nakamura, M., et al., *Flow analysis during soot trapping on aluminum titanate ceramics filter with hexagonal cell geometry*. International Journal of Automotive Engineering, 2015. **6**(1): p. 31-37.

62. Shibuta, T., et al., *Characterization of advanced aluminum titanate ceramic filter having hexagonal cell geometry.* International Journal of Automotive Engineering, 2014. **5**(3): p. 109-113.

63. Howitt, J.S. and M.R. Montierth, *Cellular ceramic diesel particulate filter.* SAE Transactions, 1981: p. 493-501.

64. Ogyu, K., et al., *Ash storage capacity enhancement of diesel particulate filter*, 2004, SAE Technical Paper.

65. Young, D.M., et al., *Ash storage concept for diesel particulate filters*, 2004, SAE Technical Paper.

66. Bouteiller, B., et al., *One dimensional backpressure model for asymmetrical cells DPF*, 2007, SAE Technical Paper.

67. Bardon, S., et al., *Asymmetrical channels to increase DPF lifetime*, 2004, SAE Technical Paper.

68. Barea, R., et al., *Fabrication of highly porous mullite materials.* Journal of the American Ceramic Society, 2005. **88**(3): p. 777-779.

69. She, J. and T. Ohji, *Fabrication and characterization of highly porous mullite ceramics.* Materials Chemistry and Physics, 2003. **80**(3): p. 610-614.

70. Abe, H., et al., *Preparation of bimodal porous mullite ceramics.* Journal of Materials Science, 1994. **29**(5): p. 1222-1226.

71. Atisivan, R., S. Bose, and A. Bandyopadhyay, *Porous mullite preforms via fused deposition.* Journal of the American Ceramic Society, 2001. **84**(1): p. 221-223.

72. Liu, Y.-F., et al., *Porous mullite ceramics from national clay produced by gelcasting.* Ceramics International, 2001. **27**(1): p. 1-7.

73. Yang, F., et al., *Effects of sintering temperature on properties of porous mullite/corundum ceramics.* Materials Letters, 2012. **73**: p. 36-39.

74. Binner, J., S. Hughes, and R.M. Sambrook. *Gel cast foam diesel particulate filters*. in *Key Engineering Materials*. 2004. Trans Tech Publ.

75. Ding, S., Y.P. Zeng, and D. Jiang, *Fabrication of mullite ceramics with ultrahigh porosity by gel freeze drying.* Journal of the American Ceramic Society, 2007. **90**(7): p. 2276-2279.

76. Samborski, S. and T. Sadowski, *Dynamic fracture toughness of porous ceramics.* Journal of the American Ceramic Society, 2010. **93**(11): p. 3607-3609.

77. Roberts, A.P. and E.J. Garboczi, *Elastic properties of model porous ceramics.* Journal of the American Ceramic Society, 2000. **83**(12): p. 3041-3048.

78. Shyam, A., et al., *The Thermal Expansion, Elastic and Fracture Properties of Porous Cordierite at Elevated Temperatures.* J. Amer. Ceram. Soc., 2012. **95**(5): p. 1682–1691.

79. Howitt, J.S., *Thin wall ceramics as monolithic catalyst supports*, 1980, SAE Technical Paper.

80. Bachiorrini, A., *New hypotheses on the mechanism of the deterioration of cordierite diesel filters in the presence of metal oxides.* Ceramics international, 1996. **22**(1): p. 73-77.

81. Montanaro, L. and A. Bachiorrini, *Influence of some pollutants on the durability of cordierite filters for diesel cars.* Ceramics international, 1994. **20**(3): p. 169-174.

82. Ohno, K., K. Shimato, and M. Tsuji, *Honeycomb filter and ceramic filter assembly*, 2003, Google Patents.

83. Liu, J.J., et al. *Use of Ceramic Microfibers to Generate a High Porosity Cross-Linked Microstructure in Extruded Honeycombs*. in *Ceramic Engineering and Science Proceedings*. 2009.

84. Ingram-Ogunwumi, R., et al., *Performance evaluations of aluminum titanate diesel particulate filters*, 2007, SAE Technical Paper.

85. Kim, I.J., *Thermal Stability of Al2TiO5 Ceramics for New Diesel Particulate Filter Applications- A Literature Review.* Journal of Ceramic Processing Research, 2010. **11**(4): p. 411-418.

86. Su, V.M.T., M. Terehov, and T.W. Clyne, *Filtration Performance of Membranes Produced Using Nanoscale Alumina Fibres (NAF).* Adv. Eng. Mats., 2012. **14**(12): p. 1088-1096.

87. Hull, D. and T.W. Clyne, *An Introduction to Composite Materials*. Cambridge Solid State Science Series, ed. D.R. Clarke, S. Suresh, and I.M. Ward. 1996, Cambridge: Cambridge University Press.

88. Gordon, T., A. Shyam, and E. Lara-Curzio, *The Relationship between Microstructure and Fracture Toughness for Fibrous Materials for Diesel Particulate Filters.* J. Amer. Ceram. Soc., 2010. **93**(4): p. 1120-1126.

89. Clyne, T.W., et al., *Porous Materials for Thermal Management under Extreme Conditions.* Phil. Trans. Roy. Soc. A - Math., Phys. & Eng. Sci., 2006. **364**(1838): p. 125-146.

90. Gibson, L.J. and M.F. Ashby, *Cellular Solids: Structure and Properties*. 2nd ed. 1997, Cambridge: Cambridge University Press. 357.

91. Markaki, A.E. and T.W. Clyne, *Magneto-Mechanical Stimulation of Bone Growth in a Bonded Array of Ferromagnetic Fibres.* Biomaterials, 2004. **25**(19): p. 4805-4815.

92. Markaki, A.E. and T.W. Clyne, *Magneto-Mechanical Actuation of Bonded Ferromagnetic Fibre Arrays.* Acta Materialia, 2005. **53**(3): p. 877-889.

93. Clyne, T.W., A.E. Markaki, and J. Dean, *4.6 Mechanical Properties of Metallic Fiber Network Materials*, in *Comprehensive Composite Materials II*. 2018, Elsevier: Oxford. p. 173-187.

94. Clyne, T.W., A.E. Markaki, and J.C. Tan, *Mechanical and magnetic properties of metal fibre networks, with and without a polymeric matrix.* Composites Science and Technology, 2005. **65**(15–16): p. 2492-2499.

95. Ke, X., *High-Performance Ceramic Membranes with a Separation Layer of Metal Oxide Nanofibers.* Advanced Materials, 2007. **19**: p. 785-790.

96. Ke, X., et al., *Metal Oxide Nanofibres Membranes Assembled by Spin-coating Method.* Desalination, 2009. **236**: p. 1-7.

97. Peri, J., *A Model for the Surface of γ–Alumina.* The Journal of Physical Chemistry, 1965. **69**(1): p. 220-230.

98. Silvestroni, L., et al., *Toughened ZrB2-based ceramics through SiC whisker or SiC chopped fiber additions.* Journal of the European Ceramic Society, 2010. **30**(11): p. 2155-2164.

99. Kavecký, Š. and P. Šebo, *Short aluminosilicate fibre reinforced aluminium.* Journal of materials science, 1996. **31**(3): p. 757-764.

100. Davies, I., et al., *Effect of sintering conditions on mechanical and physical properties of MgO ceramic reinforced with chopped Si–C–O fibre.* Materials Letters, 2000. **43**(4): p. 203-207.

101. Demir, A., *Effect of Nicalon SiC fibre heat treatment on short fibre reinforced β-sialon ceramics.* Journal of the European Ceramic Society, 2012. **32**(7): p. 1405-1411.

102. Yang, S., et al., *Diesel particulate filter design simulation: A review.* Advances in Mechanical Engineering, 2016. **8**(3): p. 1-14.

103. Konstandopoulos, A.G., et al., *Progress in diesel particulate filter simulation*, 2005, SAE Technical Paper.

104. Galindo, J., et al., *Heat transfer modelling in honeycomb wall-flow diesel particulate filters.* Energy, 2012. **43**(1): p. 201-213.

105. Haralampous, O.C., G.C. Koltsakis, and Z.C. Samaras, *Partial regenerations in diesel particulate filters*, 2003, SAE Technical paper.

106. Yi, Y., *Simulating the soot loading in wall-flow DPF using a three-dimensional macroscopic model*, 2006, SAE Technical Paper.

107. Kostoglou, M., P. Housiada, and A.G. Konstandopoulos, *Multi-channel simulation of regeneration in honeycomb monolithic diesel particulate filters.* Chemical Engineering Science, 2003. **58**(14): p. 3273-3283.

108. Konstandopoulos, A.G., M. Kostoglou, and P. Housiada, *Spatial non-uniformities in diesel particulate trap regeneration*, 2001, SAE Technical Paper.

109. Hinterberger, C., M. Olesen, and R. Kaiser, *3D simulation of soot loading and regeneration of diesel particulate filter systems*, 2007, SAE Technical Paper.

110. Bissett, E.J., *Mathematical model of the thermal regeneration of a wall-flow monolith diesel particulate filter.* Chemical Engineering Science, 1984. **39**(7-8): p. 1233-1244.

111. Konstandopoulos, A.G., et al., *Optimized filter design and selection criteria for continuously regenerating diesel particulate traps*, 1999, SAE Technical Paper.

112. Konstandopoulos, A.G. and M. Kostoglou, *Periodically reversed flow regeneration of diesel particulate traps*, 1999, SAE Technical Paper.

113. Konstandopoulos, A.G. and M. Kostoglou, *Reciprocating flow regeneration of soot filters.* Combustion and flame, 2000. **121**(3): p. 488-500.

114. Haralampous, O. and G.C. Koltsakis, *Intra-layer temperature gradients during regeneration of diesel particulate filters.* Chemical Engineering Science, 2002. **57**(13): p. 2345-2355.

115. Guo, Z. and Z. Zhang, *A one-dimensional numerical model for diesel particulate trap performance study during loading and regeneration.* International Journal of Engine Research, 2005. **6**(3): p. 247-262.

116. Depcik, C. and D. Assanis, *Simulating area conservation and the gas-wall interface for one-dimensional based diesel particulate filter models.* Journal of Engineering for Gas Turbines and Power, 2008. **130**(6): p. 062807.

117. Muntean, G.G., et al., *Lattice-Boltzmann diesel particulate filter sub-grid modeling-a progress report*, 2003, SAE Technical Paper.

118. Yamamoto, K., N. Takada, and M. Misawa, *Combustion simulation with Lattice Boltzmann method in a three-dimensional porous structure.* Proceedings of the Combustion Institute, 2005. **30**(1): p. 1509-1515.

119. Yamamoto, K., et al., *Simulation on soot deposition and combustion in diesel particulate filter.* Proceedings of the Combustion Institute, 2009. **32**(2): p. 1965-1972.

120. Yamamoto, K. and K. Yamauchi, *Numerical simulation of continuously regenerating diesel particulate filter.* Proceedings of the Combustion Institute, 2013. **34**: p. 3083-3090.

121. Kong, H. and K. Yamamoto, *Simulation on soot deposition in in-wall and on-wall catalyzed diesel particulate filters.* Catalysis Today, 2018.

122. Tsushima, S., et al., *Lattice Boltzmann simulation on particle transport and captured behaviors in a 3D-reconstructed micro porous DPF*, 2010, SAE Technical Paper.

123. Hasimoto, H., *On the periodic fundamental solutions of the Stokes equations and their application to viscous flow past a cubic array of spheres.* Journal of Fluid Mechanics, 1959. **5**(2): p. 317-328.

124. Sousa, A. and A. Nabovati, *LBM mesoscale modelling of porous media.* WIT Transactions on Engineering Sciences, 2008. **61**: p. 59-68.

125. Nabovati, A., E.W. Llewellin, and A.C. Sousa, *A general model for the permeability of fibrous porous media based on fluid flow simulations using the lattice Boltzmann method.* Composites Part A: Applied Science and Manufacturing, 2009. **40**(6-7): p. 860-869.

126. Koponen, A., et al., *Permeability of three-dimensional random fiber webs.* Physical Review Letters, 1998. **80**(4): p. 716.

127. Gebart, B.R., *Permeability of unidirectional reinforcements for RTM.* Journal of composite materials, 1992. **26**(8): p. 1100-1133.

128. Clague, D., et al., *Hydraulic permeability of (un) bounded fibrous media using the lattice Boltzmann method.* Physical Review E, 2000. **61**(1): p. 616.

129. Chen, S., et al., *Lattice gas automata for flow through porous media.* Physica D: Nonlinear Phenomena, 1991. **47**(1-2): p. 72-84.

130. Rothman, D.H., *Cellular-automaton fluids: A model for flow in porous media.* Geophysics, 1988. **53**(4): p. 509-518.

131. Frisch, U., et al., *Lattice gas hydrodynamics in two and three dimensions*, 1986, Los Alamos National Lab., NM (USA); Observatoire de Nice, 06 (France); Ecole ….

132. Wolfram, S., *Cellular automaton fluids 1: Basic theory.* Journal of statistical physics, 1986. **45**(3-4): p. 471-526.

133. Frisch, U., B. Hasslacher, and Y. Pomeau, *Lattice-gas automata for the Navier-Stokes equation.* Physical review letters, 1986. **56**(14): p. 1505.

134. d'Humieres, D., P. Lallemand, and U. Frisch, *Lattice gas models for 3D hydrodynamics*. EPL (Europhysics Letters), 1986. **2**(4): p. 291.

135. Higuera, F.J. and J. Jiménez, *Boltzmann approach to lattice gas simulations.* EPL (Europhysics Letters), 1989. **9**(7): p. 663.

136. Chen, S. and G.D. Doolen, *Lattice Boltzmann method for fluid flows.* Annual review of fluid mechanics, 1998. **30**(1): p. 329-364.

137. Kong, X., et al., *Simulating the Flow and Soot Loading in Wall-Flow DPF Using a Two-Dimensional Mesoscopic Model*, 2018, SAE Technical Paper.

138. Dupuis, A. and B. Chopard, *Theory and applications of an alternative lattice Boltzmann grid refinement algorithm.* Physical Review E, 2003. **67**(6): p. 066707.

139. Lagrava, D., et al., *Advances in multi-domain lattice Boltzmann grid refinement.* Journal of Computational Physics, 2012. **231**(14): p. 4808-4822.

140. Alexander, F.J., et al., *Lattice Boltzmann model for compressible fluids.* Physical Review A, 1992. **46**(4): p. 1967.

141. Narsilio, G.A., et al., *Upscaling of Navier–Stokes equations in porous media: Theoretical, numerical and experimental approach.* Computers and Geotechnics, 2009. **36**(7): p. 1200-1206.

142. Fourie, W., et al. *The simulation of pore scale fluid flow with real world geometries obtained from X-ray computed tomography*. in *Proceedings of the Boston COMSOL Conference*. 2007.

143. LS Instruments. *Small angle light scattering.* [cited 2019 09/01/2019]; Available from: https://lsinstruments.ch/en/technology/small-angle-light-scattering-sals.

144. Heuer, M. and K. Leschonski, *Results obtained with a new instrument for the measurement of particle size distributions from diffraction patterns.* Particle & Particle Systems Characterization, 1985. **2**(1-4): p. 7-13.

145. Clyne, T.W., et al., *The use of a δ–Alumina Fibre for Metal Matrix Composites.* J. Mat. Sci., 1985. **20**: p. 85-96.

146. Tsybulya, S.V. and G.N. Kryukova, *New X-ray powder diffraction data on δ-Al 2 O 3.* Powder Diffraction, 2003. **18**(4): p. 309-311.

147. Többens, D., et al. *E9: the new high-resolution neutron powder diffractometer at the Berlin neutron scattering center*. in *Materials Science Forum*. 2001. Trans Tech Publ.

148. Baklouti, S., et al., *Binder burnout and evolution of the mechanical strength of dry-pressed ceramics containing poly(vinyl alcohol).* J. Europ. Ceram. Soc., 2001. **21**(8): p. 1087-1092.

149. Patnaik, P., *Handbook of inorganic chemicals*. Vol. 529. 2003: McGraw-Hill New York.

150. Lemmon, E.W. and R. Jacobsen, *Viscosity and thermal conductivity equations for nitrogen, oxygen, argon, and air.* International journal of thermophysics, 2004. **25**(1): p. 21-69.

151. Roebben, G., et al., *Impulse excitation apparatus to measure resonant frequencies, elastic moduli, and internal friction at room and high temperature.* Rev. Sci. Instr., 1997. **68**(12): p. 4511-4515.

152. ASTM International, *E1876-15 Standard Test Method for Dynamic Young's Modulus, Shear Modulus, and Poisson's Ratio by Impulse Excitation of Vibration*, 2015: Philadelphia.

153. Asmani, M., et al., *Influence of porosity on Young's modulus and Poisson's ratio in alumina ceramics.* Journal of the European Ceramic Society, 2001. **21**: p. 1081-1086.

154. Tan, J.C., et al., *A Steady-State Bi-Substrate Technique for Measurement of the Thermal Conductivity of Ceramic Coatings.* Surf. Coat. Techn., 2006. **201**(3-4): p. 1414-1420.

155. Zhang, W., B. Reddy, and S. Deevi, *Physical properties of TiAl-base alloys.* Scripta Materialia, 2001. **45**(6): p. 645-651.

156. Presley, M.A. and P.R. Christensen, *Thermal conductivity measurements of particulate materials: 5. Effect of bulk density and particle shape.* Journal of Geophysical Research: Planets, 2010. **115**(E7).

157. Auerkari, P., *Mechanical and physical properties of engineering alumina ceramics*. 1996: Technical Research Centre of Finland Espoo.

158. Coble, R.L. and W.D. Kingery, *Effect of Porosity on Physical Properties of Sintered Alumina.* J. Am. Ceram. Soc., 1956. **39**(11): p. 377-385.

159. Knudsen, F., *Effect of porosity on Young's modulus of alumina.* Journal of the American Ceramic Society, 1962. **45**(2): p. 94-95.

160. Lin, Y.S. and A.J. Burggraaf, *Preparation and Characterization of High-Temperature Thermally Stable Alumina Composite Membrane.* Journal of the American Ceramic Society, 1991. **74**(1): p. 219-224.

161. Gu, Y., et al., *Porous YSZ ceramics by water-based gelcasting.* Ceramics international, 1999. **25**(8): p. 705-709.

162. Rice, R., *Comparison of stress concentration versus minimum solid area based mechanical property-porosity relations.* Journal of materials science, 1993. **28**(8): p. 2187-2190.

163. Markaki, A.E., S.A. Westgate, and T.W. Clyne. *The Stiffness and Weldability of an Ultra-Light Steel Sandwich Sheet Material with a Fibrous Metal Core*. in *Processing and Properties of Lightweight Cellular Metals and Structures*. 2002. Seattle: TMS.

164. Cutler, W.A. *Overview of ceramic materials for diesel particulate filter applications*. in *28th International Conference on Advanced Ceramics and Composites A: Ceramic Engineering and Science Proceedings*. 2004. Wiley Online Library.

165. He, X., G.D. Doolen, and T. Clark, *Comparison of the lattice Boltzmann method and the artificial compressibility method for Navier–Stokes equations.* Journal of Computational Physics, 2002. **179**(2): p. 439-451.

166. Dwivedi, P.N. and S. Upadhyay, *Particle-fluid mass transfer in fixed and fluidized beds.* Industrial & Engineering Chemistry Process Design and Development, 1977. **16**(2): p. 157-165.

167. Engineering ToolBox. *Materials Properties*. 2019 [cited 2019 15/01/2019]; Available from: www.engineeringtoolbox.com.

168. Rhodes, M.J. and M. Rhodes, *Introduction to particle technology*. 2008: John Wiley & Sons.

169. McCabe, W.L., J.C. Smith, and P. Harriott, *Unit operations of chemical engineering*. Vol. 1130. 1993: McGraw-hill New York.

170. Kass, R.E. and A.E. Raftery, *Bayes factors.* Journal of the american statistical association, 1995. **90**(430): p. 773-795.

171. Krupke, W., et al., *Spectroscopic, optical, and thermomechanical properties of neodymium-and chromium-doped gadolinium scandium gallium garnet.* JOSA B, 1986. **3**(1): p. 102-114.

172. Rice, R.W., *Grain size and porosity dependence of ceramic fracture energy and toughness at 22 degrees.* Journal of Material Science, 1996. **31**: p. 1969-1983.

173. Cutler, W.A. and G. Merkel, *A new high temperature ceramic material for diesel particulate filter applications*, 2000, SAE Technical Paper.

174. Roy, R., D.K. Agrawal, and H.A. McKinstry, *Very low thermal expansion coefficient materials.* Annual Review of Materials Science, 1989. **19**(1): p. 59-81.

175. Price, R., *Properties of silicon carbide for nuclear fuel particle coatings.* Nuclear Technology, 1977. **35**(2): p. 320-336.

176. Benaqqa, C., et al., *Morphology, physical, thermal and mechanical properties of the constitutive materials of diesel particulate filters.* Appl. Therm. Eng., 2014. **62**(2): p. 599-606.

177. Slack, G.A., *Thermal Conductivity of Pure and Impure Silicon, Silicon Carbide, and Diamond.* J. Appl. Phys., 1964. **35**(12): p. 3460-3466.

178. Bolz, R.E. and G.L. Tune, *CRC Handbook of Tables for Applied Engineering Science*. 1973, Cleveland, Ohio, USA: CRC Press.

179. Nagarajan, A., *Ultrasonic Study of Elasticity-Porosity Relationship in Polycrystalline Alumina.* Journal of Applied Physics, 1971. **42**(10): p. 3693-3696.

180. Munro, R.G., *Evaluated Material Properties for a Sintered alpha-Alumina.* J. Am. Cer. Soc., 1997. **80**(8): p. 1919-28.